Geochemical and mineralogical studies of meteorite impact-generated hydrothermal systems on Earth and tracing sources of water: observations from the Rochechouart impact structure, France.

Sarah Lauren Simpson

Thesis presented for the degree of Master of Science in Earth Sciences

University of Glasgow

College of Science and Engineering
School of Geographical and Earth Sciences

September 2015

Abstract

Research within the last decade has revealed that meteorite impacts on our planet have the potential to create transient hydrothermal environments that are conducive to the development of extremophile microbial communities. Impact products also record the hydrologic and environmental history of a terrestrial body's surface, making them attractive targets in the search for water and exolife on other planets and satellites. The interpretation of geologic and surface processes observed on other terrestrial bodies is based on ground-truths we recognize on Earth. Due to the recycling of crust and an active surface environment, the direct study of hydrothermal activity in craters on our planet is often obscured by pre-impact fluid episodes and non-preservation at ambient surface conditions. As a result, detailed studies focusing on water-rock interactions during the post-impact cooling period are lacking. Many mysteries still surround the development and sustainability of impact-hydrothermal activity, such as the role of target composition and paleofluid reservoirs.

This study investigates post-impact hydrothermal activity within the complex, 23km diameter, marginal marine, late Triassic Rochechouart impact structure located in west-central France. Previous studies have noted a pervasive K-metasomatic overprint attributed to post-impact hydrothermal circulation; however, Rochechouart is highly weathered, and the target consists primarily of Hercynian quartzofeldspathic igneous and amphibolite facies metamorphic rocks which show evidence for aqueous alteration during pre-impact events. This thesis aims to overcome the complications arising from multiple fluid event overprinting in Rochechouart by documenting secondary alteration throughout all impactites using detailed petrography, scanning electron microscopy, energy dispersive X-ray and Raman analysis combined with carbon, oxygen and sulphur stable isotope techniques to place temperature and fluid constraints on secondary carbonate and sulphide minerals within lithic impactites.

Results from this study reveal that the intensity of alkali metasomatism directly correlates with host rock melt content; relatively impermeable melt rocks and melt-bearing breccias show evidence for pervasive K-metasomatism, with late-stage carbonate-sulphide mineralization concentrated in lithic breccias and autochthonous impact fractures. No pre-impact hydrothermal carbonates were detected isotopically. Isotopic data also supports the hypothesis that seawater, and possibly meteoric water, mixed with metamorphic fluids, were the contributing fluid reservoirs fueling hydrothermal circulation within the structure; this conclusion is further supported by the strongly biological signatures of secondary sulphide

minerals and the structure's marginal marine paleogeography.

The sequence of hydrothermal alteration within Rochechouart follows the following scheme; early stage alkali-saturated waters sourced from the quartzofeldspathic, impermeable melt rocks were responsible for the pervasive K-metasomatic overprint in all lithologies; intermediate stage alteration was dominated by chlorite-smectite assemblages with continued K-metasomatism, which decreases in intensity in melt-poor rocks; and relatively cool carbonate-sulphide assemblages dominate lithic impactites and basement fractures where hydrothermal fluid flow is concentrated well into the late stages of cooling. Results also reveal that the porous network of parautochthonous breccias and autochthonous impact fractures within the sub-crater environment of complex craters with a majority-crystalline target may host hydrothermal fluid circulation for relatively long periods of time. These sites may also provide an environment conducive to the development of thermophilic microbial communities.

Table of Contents

Chapter 3: Stable isotope studies and evidence for multi-phase aqueous alteration in the Rochechouart impact structure

List of Figures

Chapter 1

Chapter 2

Chapter 3

Chapter 4

List of Tables

Chapter 2

Chapter 3

List of equations

Acknowledgements

The author would like to thank the following people for their support and guidance throughout the course of this work.

The Barringer family, without whose generous support this project would not have been possible. Thank you!

Prof. Martin Lee and Dr. Paula Lindgren for their guidance, patience and encouragement throughout all of this. Thank you to all the staff and students in GES for your help and assistance, for listening to me rant about seagulls, and for tolerating my sometimes-annoying Southern American idiosyncrasies.

Thank you also to the examiners, Dr. James Darling and Dr. Daniel Koehn; your time and feedback on this thesis is very much appreciated.

Dr. Philippe Lambert for his unwavering support, kindness, patience and, most of all, enthusiasm and eccentricity. Philippe is living proof that not all experienced academics in the world of terrestrial impact cratering are unapproachable, grumpy, dinosaurs who stomp on terrified students new to planetary research.

Prof. Adrian Boyce and Mrs. Alison McDonald at the SUERC stable isotope facility for their patience and willingness to always stop and help with anything and everything, all the time, no matter what. You guys ROCK (get it?)

Thank you also to the staff at the Réserve Naturelle de l'Astroblème de Rochechouart-Chassenon for welcoming us to their park, their assistance in the field, and for granting us permission to sample from the structure.

Declaration

This thesis summarizes two years of independent research carried out at the University of Glasgow and the Scottish Universities Environmental Research Centre in East Kilbride.

This research was supervised by Prof. Martin Lee. Any published work not belonging to myself is given full acknowledgement in the text.

Sarah L. Simpson, 2015

Note to Examiners

Some content from Chapter 2 is repeated in Chapter 3; Chapter 3 is written in such a way to provide the foundation for a publication.

Chapter 1: Impact cratering: an overview of processes, products and how they shape our solar system

In this chapter

1.0 Impact cratering: an overview of processes, products and how they shape our Solar System

- 1.1 Intro to impacts
  - 1.1.1 The cratering record in our solar system: the LHB and impacts today
  - 1.1.2 Impact record on Earth
    - 1.1.2.1 The cratering record
    - 1.1.2.2 Extinction event
  - 1.1.3 Stages of crater formation
    - 1.1.3.1 Contact and compression
    - 1.1.3.2 Excavation
    - 1.1.3.3 Modification
  - 1.1.4 Types of craters
    - 1.1.4.1 Simple
    - 1.1.4.2 Complex
    - 1.1.4.3 Multi-ring
  - 1.1.5 Thermal effects of impact events
  - 1.1.6 How we find them
    - 1.1.6.1 Micro and mesoscopic shock features: PDF's, diaplectic glass, toasted quartz, ballen quartz and shatter cones.
    - 1.1.6.2 High pressure mineral polymorphs
    - 1.1.6.3 Gravity anomalies
  - 1.1.7 Economic significance
  - 1.1.8 Astrobiological implications
- 1.2 Impactite petrology and mineralogy
  - 1.2.1 Autochthonous
  - 1.2.2 Parautochthonous
  - 1.2.3 Allochthonous
    - 1.2.3.1 Crater-fill deposits and proximal ejecta
    - 1.2.3.2 Distal ejecta
  - 1.2.4 Impactite compositional variability with target type

1.0 Impact cratering: an overview of processes, products and how they shape our Solar System

1.1 Introduction to impacts

Impact cratering is one of the most ubiquitous processes in our solar system, affecting all terrestrial planets and satellites (French, 1998). By definition, impact cratering is "the excavation of a planet's surface when it is struck by a meteoroid" (LPI.USRA.EDU). A meteoroid is a fragment of a comet or asteroid; upon collision with Earth's surface is called a meteorite or projectile (French, 1998). Meteorite sizes vary from dust-sized particles to tens of kilometres-diameter asteroids, consisting of a mixture of rock, metal alloy, and volatiles (French, 1998; French and Koeberl, 2010). Less than 1% of the 100 tons of material entering the Earth's atmosphere every day strikes the surface (NASA/LPI); because of an active and dense atmosphere and mostly-water-covered surface, the bulk of this material quickly weathers at ambient conditions or is simply non-recoverable.

While impact events are notoriously devastating, citing responsibility for at least one mass extinction event, the long term effects may be beneficial. Impacts are economically significant; they can expose, produce or concentrate mineable deposits such as gold, uranium and hydrocarbons (French, 1998; Osinski and Pierazzo, 2012). Impacts provide an external source of energy and heat to tectonically inactive terrestrial planets,

and research within the last decade has revealed that on Earth, the long term effects of a collision event may be beneficial for the sustainability of extremophile life (Naumov, 2005; Osinski and Pierazzo, 2012; Osinski et al., 2013). Crater formation also reveals information on the sub-surface composition of rocky planets and satellites; on Earth this may be less important, but on inaccessible bodies it provides a means to study geology and geochemistry from afar.

1.1.1 The cratering record in our Solar System: the LHB and impacts today

Between 3.5 and 4 billion years ago, after the accretion of the terrestrial planets, the Solar System was bombarded by an anomalous influx of material resulting in an unusually high amount of collision events known as the "Late Heavy Bombardment", or LHB (Grieve, 1980; Koeberl, 2006; Johnson and Melosh, 2012). The LHB is a hypothetical period, and the origin of the projectile influx is debated; it has been suggested that a population of impactors came from outside the Solar System, or possibly sourced from the disturbance of the Kuiper and Inner asteroid belts by the accretion or migration of the gas giants to their current positions (Gomes et al. 2005; Koeberl, 2006). This event was initially controversial, as it was first evidenced only by the dating of melt rocks collected during the Apollo missions, which indicated a higher numbers of craters clustered around the Early Archean; but evidence for the LHB as a Solar System-wide event has since been recognized through the ages of impact materials on Earth (Goldin, 2012), as well as other terrestrial bodies (Fassett and Minton, 2013).

Since the formation of the Earth and the end of the LHB, the impact rate for larger projectiles has decreased significantly (Koeberl, 2006). Although catastrophic events no longer play as active a role in shaping our planet as they did during the early Earth, smaller collisions or air bursts still occur; the most recent of these events are the Chelyabinsk air burst in Russia in 2013 (Figure 1-2) and the Tunguska air burst in 1908 (De le Fuente Marcos and De le Fuente Marcos, 2014; McKinnon, 2015).

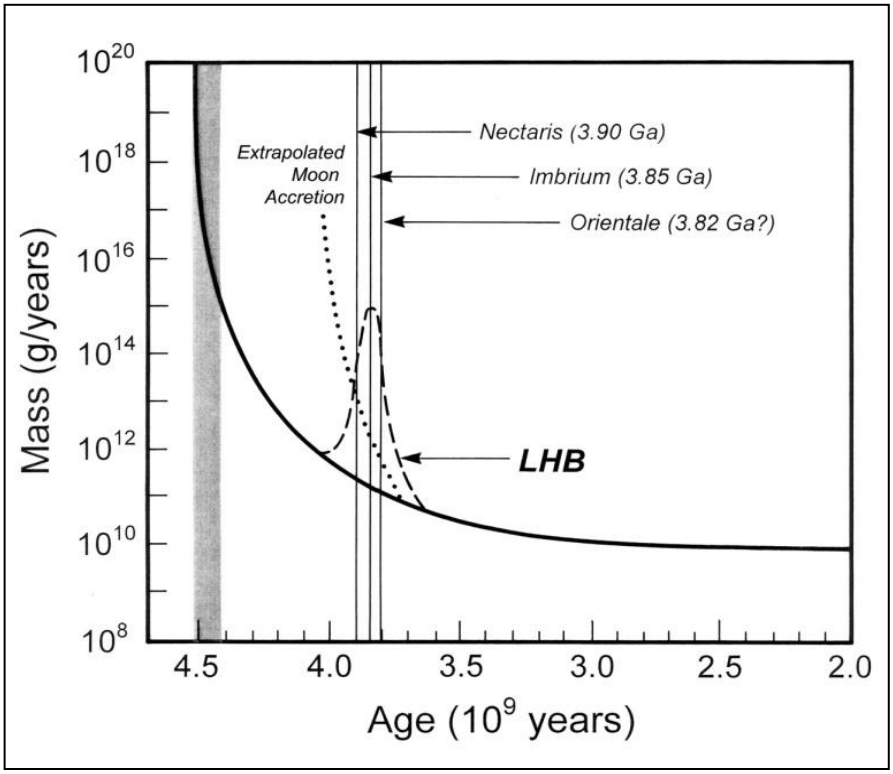

Figure 1-1: Diagram showing the flux in Lunar mass (accretion rate) during the LHB based on multiple interpretations (Koeberl, 2006). The solid line is an extrapolation of accretion based on current day; the dashed line labeled "LHB" indicates the short spike in accretion as a result of the LHB. The ages of the major Lunar impact basins is labeled as well.

Figure 1-2: The Chelyabinsk air burst over Russia in February 2013. The Chelyabinsk event was caused by the explosive breakup of an originally 20 meter diameter projectile 18 miles above the surface of the Earth; the resulting shock wave shattered windows and resulted in approximately 1500 injuries (McKinnon, 2015).

1.1.2 Impact record on Earth

Impacts craters are poorly preserved on Earth due to an active environment (e.g. surface weathering and erosion) and crust recycling (French, 1998). Though we may not be

able to study them directly, the subsequent effects of large impact events may be preserved, allowing them to be studied indirectly.

1.1.2.1 The cratering record

The cratering record on solid terrestrial planets and satellites is preserved very well on tectonically inactive bodies such as our moon and Mars. Over 300,000 impact craters larger than 1km in diameter have been indentified on Mars alone (Robbins and Hynek, 2012). Earth's impact record, however, consists of a mere 188 impact structures (Passc.net). Our planet's early history has been obscured by it's dynamic environment; active plate tectonics assures that the crust is constantly recycled, and an active atmosphere and erosional processes constantly modify surface features. The largest and oldest impact events on our planet are found fossilized in the oldest continental crust, or cratons.

Radiometric studies of impact events on Earth usually involve the most common minerals found throughout the crust, such as feldspars for Ar-Ar, zircons for U-Pb or apatite fission track (French, 1998).

1.1.2.2 Extinction event

Only one impact event has been directly linked to a mass extinction event; the Chicxulub impact at the Cretaceous-Paleogene boundary (~66 Ma), believed to be responsible for the demise of non-avian dinosaurs (Kring, 2007). Other mass extinctions, such as the Triassic-Jurassic, have previously been linked to collision events; this is currently under debate as the timing of the impact events is contested (Spray et al., 1998; Gallia et al, 2005; Saltzman and Thomas, 2012).

1.1.3 Stages of crater formation

There are three main stages recognized during crater formation: contact and compression; excavation; and modification (French, 1998). The effects of each of these stages with the target rock largely depend on the qualitative and quantitative parameters of the projectile, as well as target composition.

1.1.3.1 Contact and compression

The first stage is contact and compression, defined as the moment when the leading edge of the projectile comes into contact with the target (French, 1998; Osinski and Pierazzo, 2012). Immediately after contact, the projectile slows to a fraction of it's initial velocity and kinetic energy is transferred into the target as shock waves. The first wave

emanates from the projectile-target interface at the immediate moment of contact, and the second wave, the rarefaction wave produced by the reflection of the first shock wave by the trailing end of the projectile, comes shortly after. The second wave acts as an unloading mechanism to the projectile; the immense pressure from the impact is released resulting in extremely high temperatures that can potentially vaporize the projectile. The moment the rarefaction wave is transferred into the target rock marks the end of the first stage, and only lasts a few seconds.

1.1.3.2 Excavation

The second phase of crater formation is the excavation stage. The resulting shock waves radiate in a hemispherical shape through the target from a point directly below the point of impact. Shock wave pressures may reach up to hundreds of GPa, far exceeding those resulting from endogenic geological processes, which do not usually exceed 1 GPa (French, 1998; Osinski and Pierazzo, 2012; Koeberl, 2014). Some of this energy is directed upwards and intersects the original ground surface, at which point it is either reflected back downwards and outwards into the crater or can cause near surface rocks to be ejected. Within the lower levels of the crater, material moves down and outwards and is only displaced, not ejected. As outlined by French and Koeberl (2012), shock-induced melting of target rocks is believed to occur at pressures at and above 60 GPa; below this, selective mineral melting and diaplectic glass formation may occur between 30 and 60 GPa; and the production of high pressure mineral polymorphs and planar deformation features (PDF's) occurs between pressures from 10 to 30 GPa (Figure 1-8). (See Figure 8 for temps)

The projectile may or may not be recoverable, as often in larger craters (>4km), it is usually vaporized and ejected as part of the vapor plume. The shock waves can travel hundreds of kilometers and have the potential to eject material at a distance of twenty to thirty times the diameter of the projectile. As shock waves propagate out from the structure they become low pressure elastic waves, at which point the transient crater ceases to expand and the excavation stage ends. This process can last 2 to 6 minutes (French, 1998; Osinski and Pierazzo, 2012).

1.1.3.3 Modification

The last stage in this process is called the modification stage, which encompasses all processes affecting the structure after the excavation stage. Shortly after crater expansion ceases, gravity will counter any uplift and cause a "settling" of the structure, after which normal geologic and surficial processes take effect (i.e. sedimentation, erosion); there is no

defined “end” to this process (French, 1998; Osinski and Pierazzo, 2012; Koeberl, 2014).

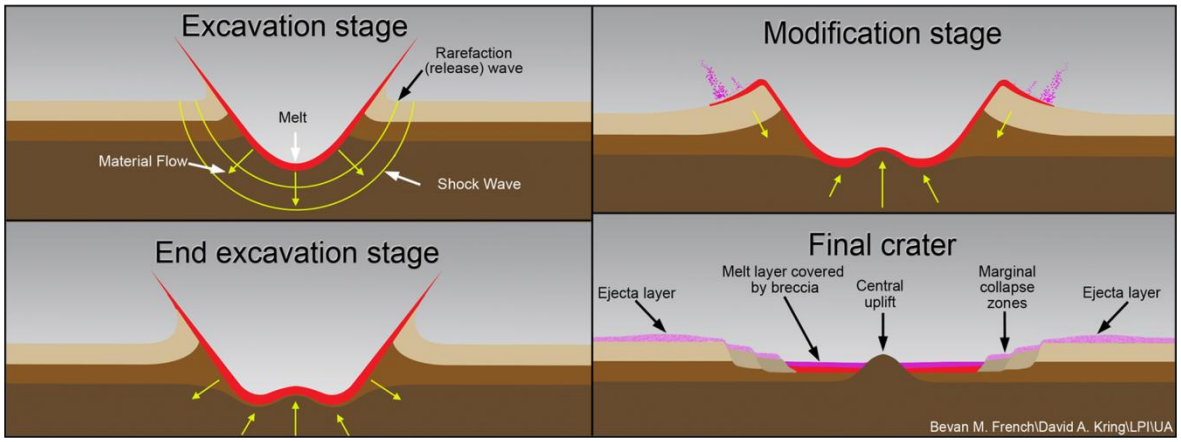

Figure 1-3: Stages of complex crater (Section 1.1.4.2) formation (LPI.USRA.EDU/Bevan M. French/David A. Kring).

1.1.4 Types of craters

There are three types of impact craters categorized based on size and morphology; simple, complex and multi-ring. The type of crater that forms during an impact event is a function of the amount of energy released, and therefore the size of the projectile and the acceleration due to gravity on a planet or satellite; the lower the gravity, the larger the crater must be in order to make the transition from more simple to complex structures (French, 1998; Osinski and Pierazzo, 2012). For example: on the Moon, the transition from a simple to complex structure is at ~20km, whereas on Earth it is 4 to 5km (French, 1998). Each type of crater has characteristically different structural and geologic features as a result of brittle and ductile processes; the types of rocks that form also depend largely on target composition (Section 1.2).

1.1.4.1 Simple craters

Simple structures are bowl-shaped and lack any morphological features except an outer transient rim; on Earth, they are between 2 and 4km in diameter (French, 1998; Osinski and Pierazzo, 2012). Their small size and absence of central uplift and rings contributes to preservation during the second stage of crater formation, as they are only modified slightly by collapse of the upper walls and infill of ejected material. In well-preserved structures, the crater diameter can be measured from the final outer rim (D); the true depth (d_t) of a simple crater is measured to the interface between the true crater cavity, also known as the transient crater cavity, and the top of the crater rim (French, 1998) (Figure 1-4).

The crater fill material, or allochthonous impactites (Section 1.2), of simple structures usually consists of a thin breccia lens of both shocked and unshocked material, a mixture of melted and non-melted target rocks, and possibly a crater lake sediment deposit. The target rocks immediately beneath the true floor of a simple crater are fractured and brecciated, but are generally not displaced, forming autochthonous and parautochthonous impactites (Figure 1-4) (Section 1.2). The most famous simple crater on Earth is the well-preserved Barringer crater in Arizona (Figure 1-6, A).

1.1.4.2 Complex craters

Complex structures on Earth are classified as those with a diameter over 4 to 5km, and contain a central uplift and outer ring structure (French, 1998; Osinski and Pierazzo, 2012). During the modification stage, isostatic rebound of the rocks results in the uplift of the central area; the total uplift of a structure does not exceed 10% of it's final diameter. As the size of the structure grows, the central uplift region becomes a series of concentric alternating rings and basins (French, 1998). As the central uplift forms, outer areas of the structure, at the rim, may experience collapse along concentric faults creating what are known as ring grabens. The resulting shape consists of a central uplift region, an annular trough and an outer rim (Figure 1-5).

The crater fill units of complex structures contain both lithic, unshocked target material and highly shocked rocks, minerals and glass; they may contain non-continuous melt bodies or coherent, continuous melt sheets within the annular trough and as ejecta (Figure 1-5) (Section 1.2). The sub-crater environment, those rocks beneath the true crater floor, are fractured and brecciated and may contain intrusions, or dikes, of allochthonous material from above or fine-crystalline frictional melt material known as pseudotachylite. The amount and distribution of impact melt in complex craters largely depends on the target composition (Section 1.2).

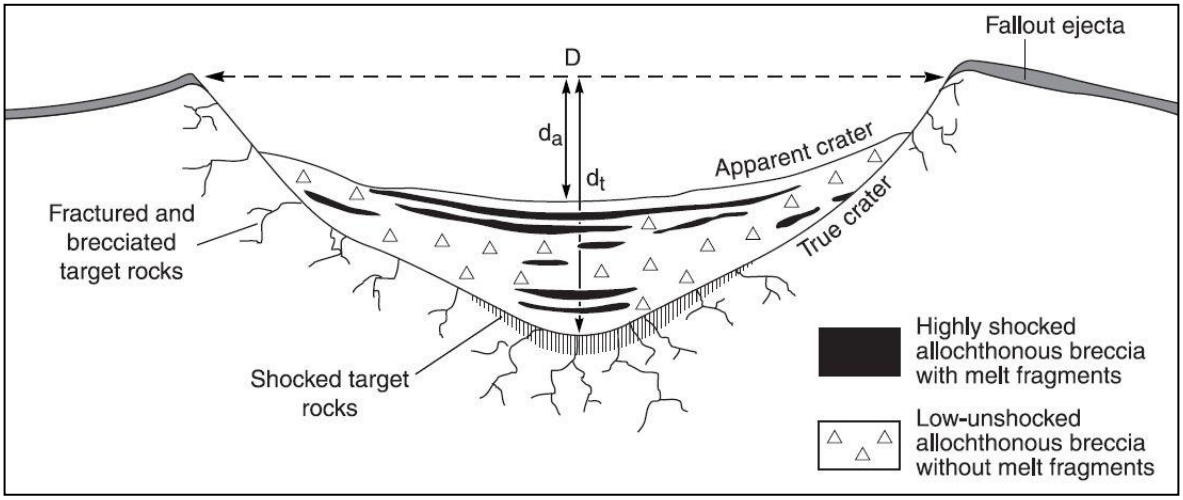

Figure 1-4: Cross-sectional view through a simple crater; the crater fill unit consists of a mixture of melted and non-melted target material, forming a breccia lens. The apparent depth (d_a) of simple craters extends from the horizon of the final rim diameter (D) to the top of the breccia lens, and the true depth (d_t) is measured to the bottom of the crater fill unit, at the interface between the lens and the true crater limit. Beneath the true crater floor, target rocks are fractured, sometimes brecciated, forming autochthonous and parautochthonous impactites (Section 1.2) (French, 1998).

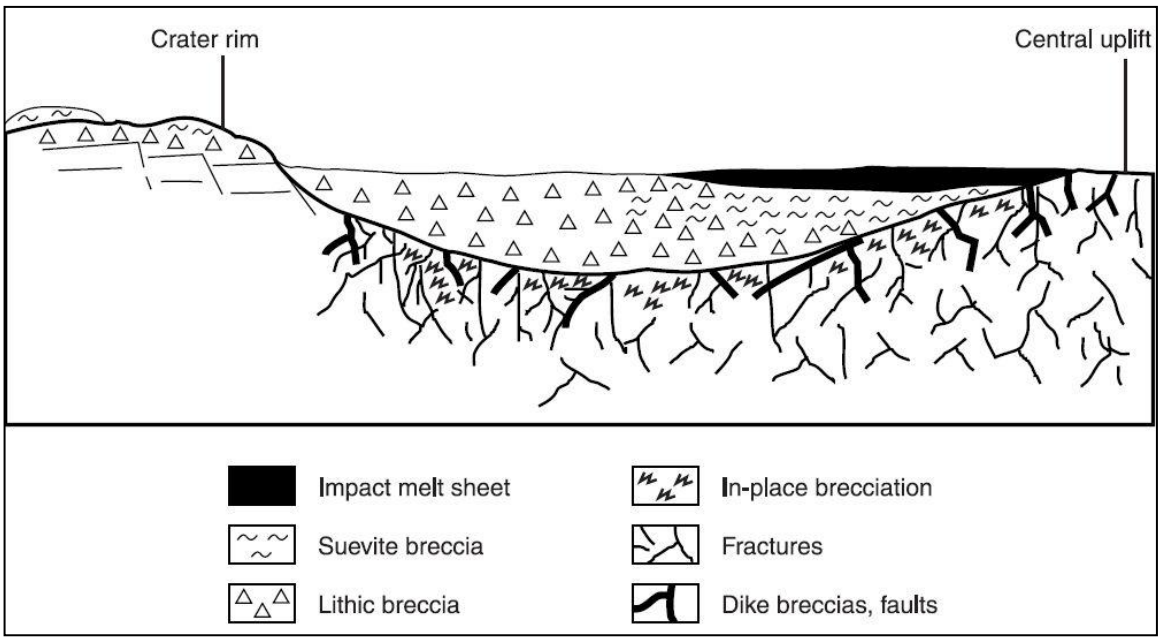

Figure 1-5: Radial cross section through a complex impact structure (central uplift, right); complex crater geology is diverse, containing a mixture of unshocked target material, moderately to highly shocked rocks and minerals with brittle shock features (Section 1.1.6), melt and glass. The distribution and proportion of melt to lithic (non-melted) material depends on the target type (Section 1.2). The sub-crater environment of complex craters, similar to simple craters, is fractured and brecciated and commonly contains intrusions of allochthonous impactite material from above, which may contain melt material (French, 1998).

1.1.4.3 Multi-ring structures

Multi-ring structures are made of sets of alternating uplifted rings and low-lying, faulted basins and can reach up to 1000km in diameter (French, 1998; Osinski and Pierazzo, 2012). Multi-ring structures are uncommon; they are associated with the very early stages of planetary accretion and cooling during the LHB and are thus are poorly preserved on Earth. They can be observed on the surfaces of other terrestrial planets and moons (Figure 1-6, B).

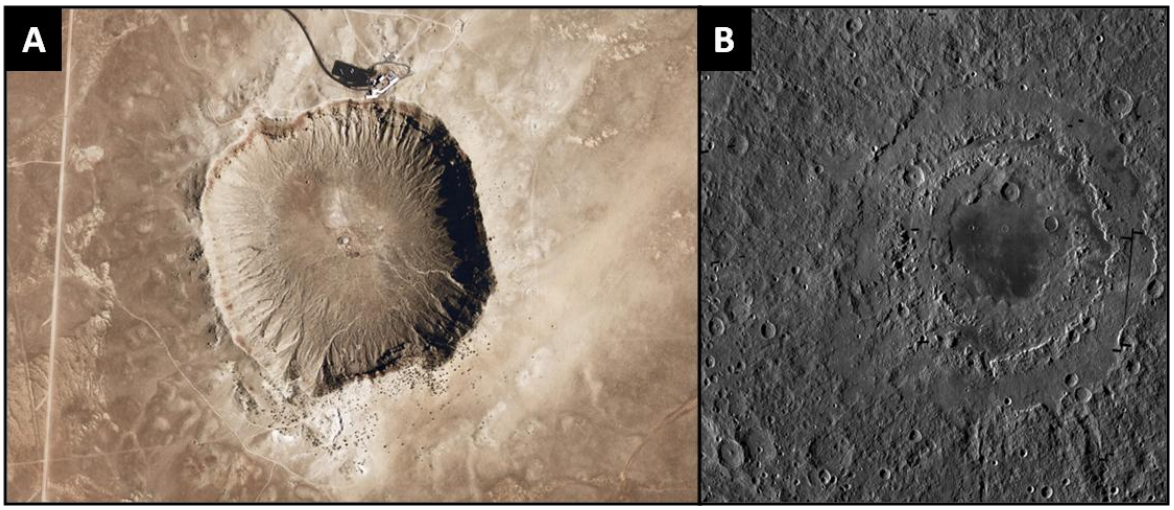

Figure 1-6: (A) The Barringer crater in Arizona, a young (50 Ka) simple, bowl-shaped crater with a diameter of ~1km (NASA). (B) The Orientale multi-ring basin on Earth's moon, with a diameter of ~930km (NASA/GSFC/University of Arizona).

1.1.5 Thermal effects of impact events

Impact events may temporarily disturb the geothermal gradient, causing it to elevate closer to the surface than normal (Figure 1-7). Though transient, combined with the presence of impact melt, the thermal anomaly generated by an impact has the potential to last several thousands to millions of years in the largest craters (Abramov and Kring, 2004; Naumov, 2005). The residual heat produced during an impact event can have unique effects on shocked rocks and minerals (Section 1.2); if water is also present, the heat may generate temporary hydrothermal environments (Figure 1-7, 1-17) (Section 1.3).

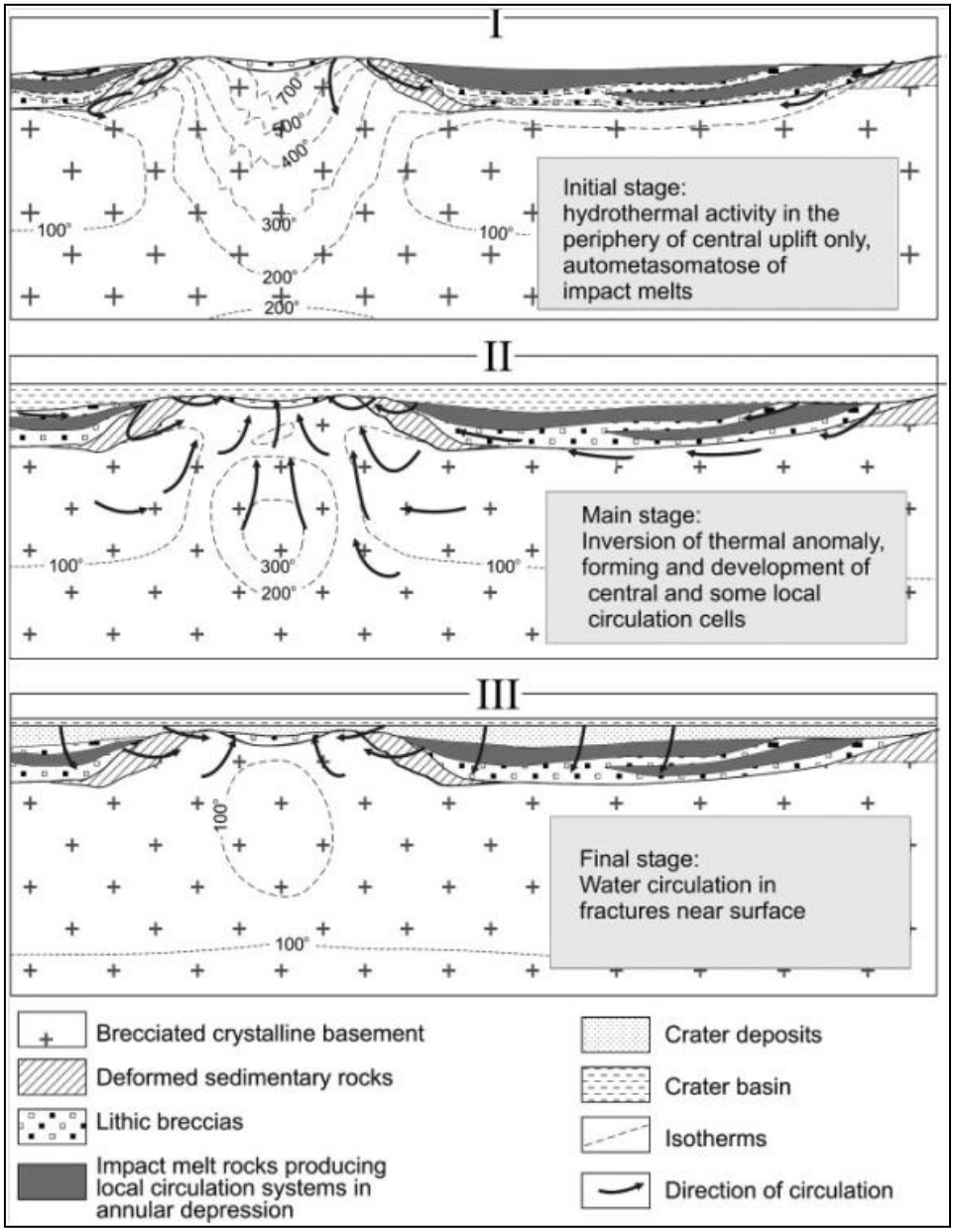

Figure 1-7: Cross-sectional view through a complex impact structure, showing the generation and evolution of hydrothermal circulation relative to the thermal anomaly and impactite type (Naumov, 2005).

1.1.6 How we find them: shock metamorphism

In well preserved structures, geomorphology is often the first clue leading to the discovery of a new crater; a topographic central uplift and concentric outer rim are characteristic features of complex impact structures. The finding of melt rocks and breccias may also allude to an impact site, but are certainly not definitive evidence without further investigation (French, 1998; French and Koeberl, 2010; Osinski and Pierazzo, 2012; Koeberl, 2014).

There are other geologic formations on Earth resembling impact sites such as

collapsed salt diapirs or volcanic calderas, and similarly, other igneous and sedimentary rocks produced from endogenic processes might resemble impactites (Osinski and Pierazzo, 2012). Before ascribing an impact origin to a potential site, supplemental tests must be implemented including the identification of meso- and microscopic shock features in minerals such as planar deformation features, diaplectic glass, shatter cones or high pressure mineral polymorphs, coesite, stishovite or possibly diamonds. Geophysical data may also provide evidence in the form of a gravity anomaly produced from lower density impactites overlying dense, unshocked target rock (French, 1998; Osinski and Pierazzo, 2012; Koeberl, 2014).

Shock stage	Pressure (GPa)	Temperature (°C)	Shock Effects
0			Fractured minerals
	5 to 10	100	
Ia			Quartz with planar fractures and planar deformation features
	20	170	
Ib			Quartz and feldspar with planar deformation features and reduced refractive index; stishovite and minor coesite
	35	300	
II			Diaplectic quartz and feldspar glass; coesite and traces of stishovite; cordierite glass
	45	900	
III			Normal feldspar glass (vesiculated) and diaplectic quartz glass; coesite; cordierite glass
	60	1500	
IV			Rock glasses or crystallized melt rocks (quenched from whole melt rocks)
	80 to 100	>2500	
V			Rock glasses (whole rock melts condensed from silicate vapour)

Figure 1-8: IUGS shock levels and their corresponding features in quartzofeldspathic minerals (Stöffler and Grieve, 2007).

1.1.6.1 Meso- and microscale shock metamorphism: PDF's, diaplectic glass, toasted quartz, ballen quartz and shatter cones.

Shock metamorphism is manifested as shock features in rocks and minerals over a wide range of pressures and temperatures (Figure 1-8); in well preserved craters, the identification of these features is the most widely used evidence for the confirmation of an impact origin for a suspected site (French, 1998; Stöffler and Grieve, 2007; French and Koeberl, 2010; Osinski and Pierazzo, 2012).

Planar deformation features (PDF's) are sets of straight, parallel planes of glass less than 2µm thick spaced 2 to 10µm apart; they form most commonly in quartz and more rarely in feldspars (Stöffler and Langenhorst, 1994; French, 1998). PDF's form as a result of mechanical shock deformation at a range of pressures, from 5 to 35 GPa and may contain small fluid inclusions, sometimes with oxide minerals such as hematite, resulting from post-impact aqueous alteration and annealing. PDF's are a definitive shock feature, and are not formed by any endogenic processes (French and Koeberl, 2010). PDF's are not to be confused with planar fractures (PF's), which are open, planar fissures also following crystallographic planes (French, 1998; Stöffler and Grieve, 2007; Osinski and Pierazzo, 2012).

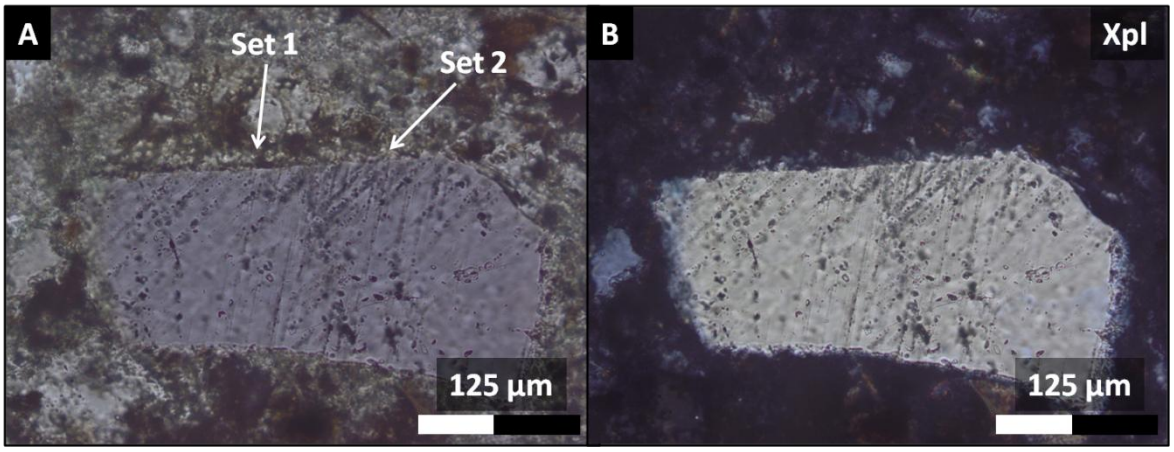

Figure 1-9: Two sets of PDF's in a quartz grain from the melt-bearing impact breccia, type Chassenon, from the Rochechouart impact structure, France.

Diaplectic glass forms by solid state transformation of quartz and feldspar minerals (maskelynite). In crystalline rocks these transformations take place at 28GPa for An-plagioclase and 35GPa for quartz; in more porous sedimentary rocks, transformation begins as low as 5GPa for quartz (French, 1998; French and Koeberl, 2010; Osinski and Pierazzo, 2012). Annealing and devitrification of glass may begin at temperatures above 1200ºC, commonly forming α-quartz or cristobalite, or clay minerals at lower temperatures during early stage hydrothermal alteration (Section 1.3).

Toasted quartz is a post-impact thermal feature; the name comes from it's distinct brown-yellow, dirty, "toasted" appearance in transmitted light, which results from a high density of inclusions (Ferrière et al., 2009). Toasted quartz has a high albedo; in hand sample, grains are visible to the naked eye as bright white, opaque mineral grains.

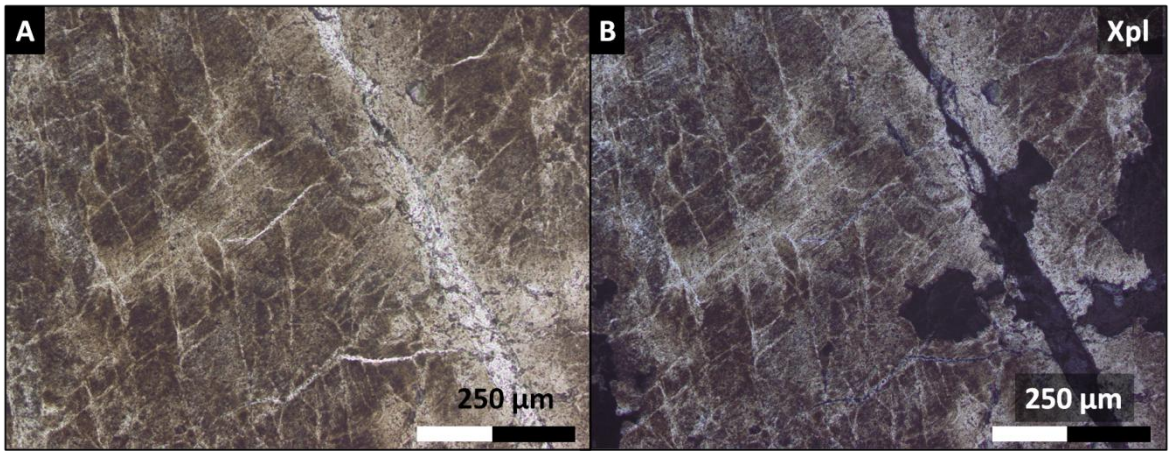

Figure 1-10: Characteristic dirty, opaque brown color of toasted quartz in the melt-bearing impact breccia (type Chassenon) from the Rochechouart impact structure in France.

Grains of ballen quartz have a spherical to hemispherical "ballen" texture that forms as a result of post-impact recrystallization of higher temperature polymorphs and glass to more stable phases such as α-quartz or α-cristobalite (Ferrière et al., 2009) (Figure 1-11). Because ballen quartz is a post-impact thermally mediated texture forming from glass, it is believed to form at pressures above ~35 GPa (Ferrière et al., 2009). There are five types of ballen quartz categorized based on their textural and compositional properties.

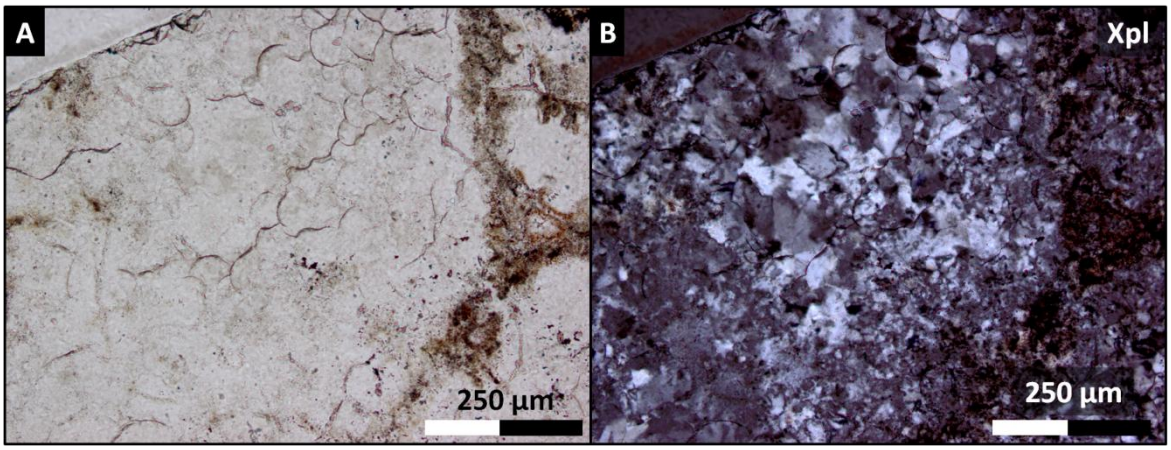

Figure 1-11: Type IV ballen quartz, ballen quartz with intraballen recrystallization, in the particulate impact melt rock (type Montoume) from the Rochechouart impact structure in France; type IV ballen quartz contains heterogeneous extinction within individual ballen in transmitted light (Ferrière et al., 2009).

Shatter cones are conical, radiating striations forming on fracture surfaces of fine-grained sedimentary and fine-crystalline igneous target rocks at pressures between 2 and 10 GPa (French, 1998; French and Koeberl, 2010). There are other endogenic processes which may create features resembling shatter cones, such as slickenlines or cone-in-cone

structures; shatter cone striations radiate from a single point and form at various angles in a host rock. Shatter cones are a definitive impact feature; no other process on Earth has been discovered which results in their formation (French, 1998; French and Koeberl, 2010; Osinski and Pierazzo, 2012.)

Figure 1-12: Well-formed shatter cones in limestone from the Steinheim crater in Germany, showing both negative (left) and positive (right) cones at different angles (Impact-structures.com).

1.1.6.2 High pressure mineral polymorphs: coesite, stishovite and diamonds

Metastable high pressure quartz polymorphs form in crystalline rocks at pressures from 30 to 60 GPa for coesite and 12 to 45 for stishovite, and are usually found as inclusions in diaplectic glass or PDF's (French and Koeberl, 2010). Stishovite is the only high pressure quartz polymorph that forms solely from impact processes; coesite can be found in other high pressure endogenic environments, such as associated with kimberlites (French, 1998; Osinski and Pierazzo, 2012).

Diamonds form from solid-state transformation of graphite in carbon-rich target rocks; in the Ries crater, they are estimated to have formed at peak pressures of 30 to 40 GPa. Impact diamonds, similar to coesite, are not a definitive shock feature.

1.1.6.3 Gravity anomalies (Bouguer anomaly)

The brecciation and fracturing of target rocks as a result of impact processes results in a decrease in density of the impact site and surrounding area, forming a gravity anomaly (French, 1998; French and Koeberl, 2010). Impact craters are associated with a circular,

negative anomaly; in structures with a central structural uplift, a positive anomaly may exist within the center.

1.1.7 Economic significance

Impact cratering may also produce, concentrate or expose economically viable precious metal, mineral or hydrocarbon deposits. Resource deposits are categorized as progenetic, syngenetic or epigenetic; those that existed prior to the impact event within the target and were redistributed as a result, those that formed during or shortly after the impact event, and those which formed as a result of topographic modification (Grieve and Masaitis, 1994; Pirajno, 2009; Osinski and Pierazzo, 2012).

A famous example of a progenetic deposit is the Vredefort dome in South Africa, from which 40 to 50% of gold ever mined has originated; as a by-product of gold mining, 150,000 t of uranium have also been extracted (Osinski and Pierazzo, 2012 and references therein). Syngenetic deposits include impact diamonds and ore deposits formed as a result of post-impact hydrothermal activity. The 130 km diameter Sudbury structure in Ontario, Canada (PASSC) is well-known for it's Cu-Ni sulphides and platinum group element deposits; the total worth of metals produced by mining of the Sudbury basin is over USD 300 billion (Osinski and Pierazzo, 2012, and references therein). Similarly, heavy hydrothermal sulphide mineralization has been discovered within smaller structures, such as the 23km diameter Haughton crater, also in Canada (Osinski et al., 2005). Epigenetic deposits form as a result of the modification of underground fluid flow due to the formation of localized topographic basins; this commonly includes the formation of hydrocarbon deposits.

1.1.8 Astrobiological significance

The astrobiological implications for impact cratering are numerous; impacts bring an immense amount of heat and energy to their targets, and as a result, when coupled with volatiles such as H_2O, moderate to large impact events can generate temporary hydrothermal systems (Cockell and Bland, 2005; Osinski et al., 2013) (Section 1.3). On Earth, colonies of extremophilic microbes have been formed by post-impact hydrothermal processes (Osinski et al., 2005; Muttik et al., 2010; Osinski et al., 2012; Sapers et al., 2014). Hydrothermal systems in other endogenic environments on Earth such as black smokers at mid-ocean ridges are favorable habitats for bacterial communities to thrive, as they contain an abundance of bioavailable nutrients and heat. This finding has lead scientists to explore impact sites (e.g. NASA Curiosity rover currently at Gale Crater on

Mars) on other terrestrial bodies, namely Mars, as cratering is a ubiquitous geologic process in our solar system.

1.2 Impactite petrology and mineralogy

“Impactite” is the term used to describe any rock that has been affected by impact metamorphism (French and Koeberl, 2010); this process encompasses a wide range of effects from complete destruction or melting of a rock to localized fractures in the basement beneath and outside the crater cavity. The classification of impact rocks is based on their abundance of melt and lithic (non-melted) material, and relative location within the structure (Stöffler and Grieve, 2007; French and Koeberl, 2010).

Impactites are first subdivided into three main categories; autochthonous, those found in their original pre-impact location; parautochthonous, which have been moved or brecciated, but appear to be in their original place; and allochthonous, which originate from beyond their current location. Allochthonous impactites are further divided into proximal and distal; those within and nearby the structure and those further away, respectively. This classification scheme may become problematic when we consider that many impact structures are highly eroded, and contextual relationships based on structural relationships cannot be determined. The most recent IUGS classification scheme for impact rocks is outlined in Figure 1-8.

1.2.1 Autochthonous fractures

Autochthonous impactites are coherent target rocks that have not experienced brecciation, mixing or melting; they have undergone brittle deformation as fracturing and faulting resulting from dissipated shock wave pressures and usually preserve their original pre-impact relationships. Autochthonous fractures have been found to extend three crater radii outwards from the structure center within affected targets (French, 1998). Autochthonous impact fractures may resemble those produced by other endogenic processes, and without other contextual information an impact origin cannot be conclusively demonstrated.

1.2.2 Parautochthonous

Parautochthonous impactites are target rocks that have been fractured, faulted or brecciated, but have not been significantly mixed, melted or relocated within the structure, remaining mostly in their pre-impact stratigraphic position (French, 1998; French and Koeberl, 2010; Osinski and Pierazzo, 2012). In simple and complex structures,

parautochthonous impactites may be found as discontinuous units within and beneath the transient crater cavity floor; these may be uplifted to near-surface conditions, particularly within the central area of complex craters.

Parautochthonous brecciated and fractured target rocks form discontinuous, irregular bodies, are usually monomict, depending on the local geology, may or may not record shock metamorphic effects, are poorly sorted with angular clasts, and grade downward into unshocked target rocks (Osinski and Pierazzo, 2012). Parautochthonous breccias resemble those produced as a result of other endogenic processes (i.e. fault breccias); if no shock features are present and contextual information is unavailable, they cannot be distinguished as impact products.

Figure 1-13: Monomict lithic breccia from the Rochechouart impact structure, France.

1.2.3 Allochthonous

Allochthonous impactites are subdivided into proximal and distal; those found inside the crater and within five crater radii outside the rim (crater fill and proximal ejecta), and those more than five radii from the rim (distal ejecta), respectively (French, 1998).

1.2.3.1 Crater-fill deposits and proximal ejecta

Allochthonous crater-fill and proximal impactites differ in their melt, glass and lithic content, forming a wide variety of impact breccias and melt rocks.

Those that are free of melt are termed lithic breccias and are composed of poorly sorted, angular target lithic fragments in a fine clastic matrix; they may record a range of subsolidus shock pressures, but rarely contain melt fragments (French, 1998; Osinski and

Pierazzo, 2012). In complex craters, lithic breccias form between the continuous melt sheet and crater floor; in simple craters they constitute the bulk of the breccia lens. Allochthonous breccias may form dikes in the sub-crater environment, beneath the true crater floor.

Lithic breccias may continuously grade into melt-bearing breccias; a recent scheme outlined by Sapers et al. (2014) has termed impactites with a mixture of melt, glass and lithic material as ‘particulate impact melt’ or simply ‘melt-bearing impact breccias’. Melt-bearing breccias record a wide range of shock pressures, occurring as crater-fill lithologies or dikes below the transient crater floor within both simple and complex structures, and may be found above or below continuous melt bodies (French, 1998; French and Koeberl, 2010; Osinski and Pierazzo, 2012; Sapers et al., 2014).

Impactites whose matrix is dominated by melt are generally categorized as melt rocks; these usually constitute continuous or semi-continuous melt bodies, and are further subdivided based on the amount of lithic clasts as ‘clast-rich’, ‘clast-poor’ or ‘clast-free’, as well as vesicular or non-vesicular (French, 1998; French and Koeberl, 2010; Osinski and Pierazzo, 2012; Sapers et al., 2014). Lithic and mineral fragments within melt rocks display a wide range of shock features, including glass, and partial to complete melting. Melt rocks are emplaced at various locations throughout the impact structure; they may be found above parautochthonous units, separated by a layer of melt-bearing breccia, or as dikes within the crater floor (Lambert, 1981). The lower and upper contacts of melt sheets contain more lithic material and are the first to cool; in thick melt sheets, this cooling rate difference may result in a more coarsely-crystalline interior.

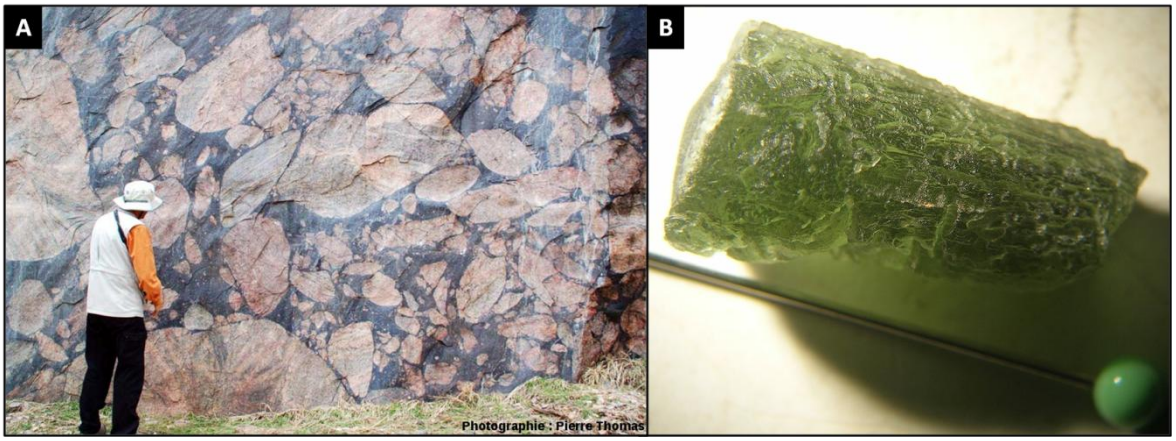

Figure 1-14: (A) Pseudotachylite, fine crystalline frictional melt, from the Vredefort crater in South Africa (Pierre Thomas, Planet-terre.ens-lyon.fr) and (B) moldavite-type tektite from the Central European strewn field (Figure 1-15).

1.2.3.2 Distal ejecta

Distal impact ejecta is poorly studied on Earth due to it's loss by erosional processes; ejecta from large impacts may be preserved in sedimentary units that can be traced chronostratigraphically or compositionally by the presence of shocked minerals and tektite beds (French, 1998; French and Koeberl, 2010; Osinski and Pierazzo, 2012). Tektites are mm to cm-size spheres of impact glass that form from shock melting; they are generally spherical or aerodynamically shaped, and black or greenish in color. There are four tektite strewn fields on Earth that can be linked to the respective impact events responsible for their formation (Figure 1-15) (Koeberl, 1994).

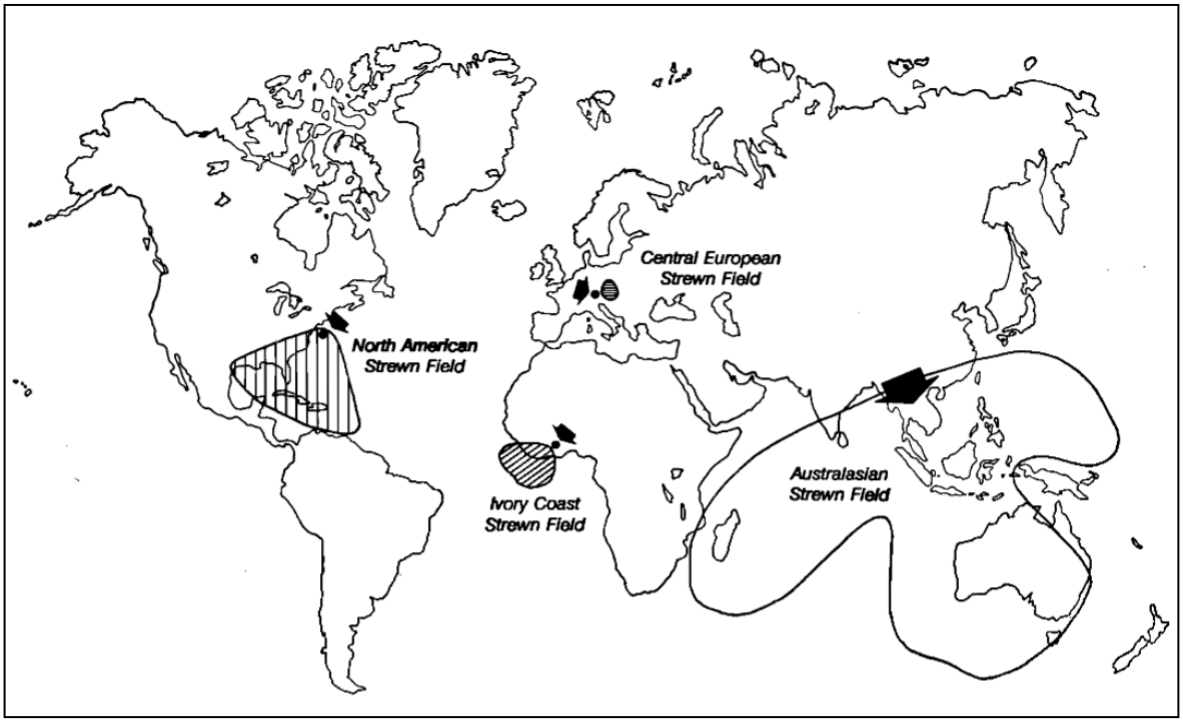

Figure 1-15: Map of tektite strewn fields across the world (Koeberl, 1994). The North American strewn field is linked to the Chesapeake Bay impact in (34 Ma), the Ivory Coast is linked to the Bosumtwi impact in Ghana (1 Ma) and the European field is linked to the Ries crater in Germany (15 Ma); the source of the Australian field (<1 Ma) has yet to be identified.

1.2.4 Impactite compositional variability with target type

Both sedimentary and crystalline targets produce impact melt, but the products of impacts into sedimentary targets differ substantially due to higher amounts of volatiles such as H_2O.

Impacts in largely crystalline targets produce large, thick, coherent continuous or semi-continuous silicate melt sheets (Osinski and Pierazzo, 2012). Silicate melts in crystalline targets are compositionally homogenous when compared to their targets, and

generally melt at pressures above 50 GPa (French, 1998; French and Koeberl, 2010; Osinski and Pierazzo, 2012). Sedimentary targets melt at considerably lower pressures, beginning at around 30GPa for a majority sandstone composition. Impacts into mixed majority sedimentary targets will produce heterogeneous immiscible silicate and carbonate melts as clast-rich impact melt rocks. It was previously believed that carbonate-rich targets did not produce melt; this has since been disproven (Osinski and Spray, 2001; Osinski and Pierazzo, 2012).

Mixed targets are those that comprise a crystalline basement overlain by a sedimentary package. In contrast to strictly crystalline targets, mixed targets do not produce continuous, large coherent melt sheets, but instead form irregular bodies and lenses.

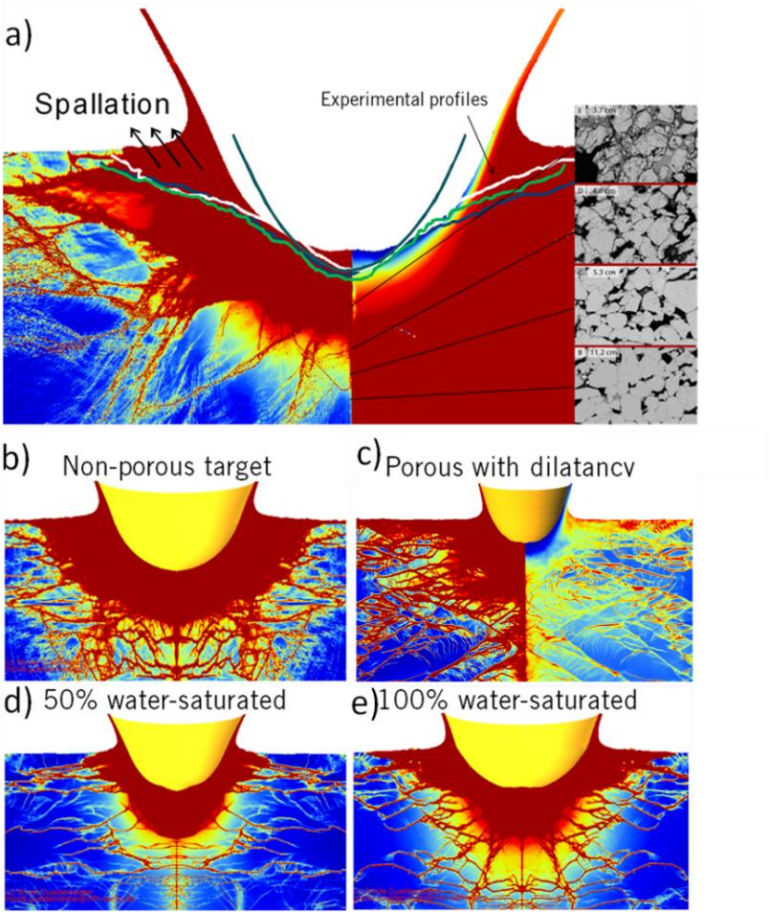

Figure 1-16: Results from experimental impacts into different target types with varying amounts of water saturation. Blue areas are undamaged material, and red is completely damaged (Memin.de).

1.3 Impact hydrothermal systems

Hydrothermal systems form as a result of an impact event if: (i) enough energy is released as heat (melt generation and uplifted geothermal gradient); (ii) sufficient volatiles

are present within the target and paleoenvironment, such as liquid water or ice; (iii) if there is sufficient porosity to support fluid flow (impact breccias, fractured and faulted target) (Naumov, 2005; French and Koeberl, 2010; Osinski and Pierazzo, 2012; Osinski et al., 2013). Approximately 1/3 of impact structures on Earth show evidence for post-impact hydrothermal activity, and it has recently been confirmed on Mars (Marzo et al., 2010).

The pervasiveness and nature of hydrothermal alteration within an impact structure is largely controlled by the distribution of the heat sources, and to a lesser degree target rock type (Naumov, 2005). Impact hydrothermal geochemistry is reminiscent of other endogenic hydrothermal systems on Earth, with the exception that shocked minerals are generally metastable and break down easily, and impact hydrothermal systems are retrograde. Osinski et al. (2013) identified six locations within a complex impact structure which are favorable for the development of hydrothermal circulation (Figure 1-17). Three main stages and facies of hydrothermal alteration have been outlined by Naumov et al. (2005) and Osinski et al. (2013) (Section 1.3.3).

In addition to forming, remobilizing or concentrating economically viable metals, minerals or hydrocarbons, the implications of impact-generated hydrothermal activity for the search for extra-terrestrial life is significant. Because impacts are such a ubiquitous process in our solar system they are being explored as potential harbors for current or fossilized life on volatile-bearing terrestrial planets and satellites (Gale and Toro craters, Mars) (Marzo et al., 2010; Osinski et al., 2013).

1.3.1 Distribution of hydrothermal environments in complex impact structures

There are six areas within a complex impact structure which are conducive to the development of hydrothermal circulation, and coincide with areas of high permeability and heat; the interior of central uplifts; the outer margin of the central uplift; surrounding continuous and discontinuous melt bodies and melt-bearing impact breccias; in crater rim faults as fumaroles and springs; and in crater lake-fill sediments, if a crater lake forms.

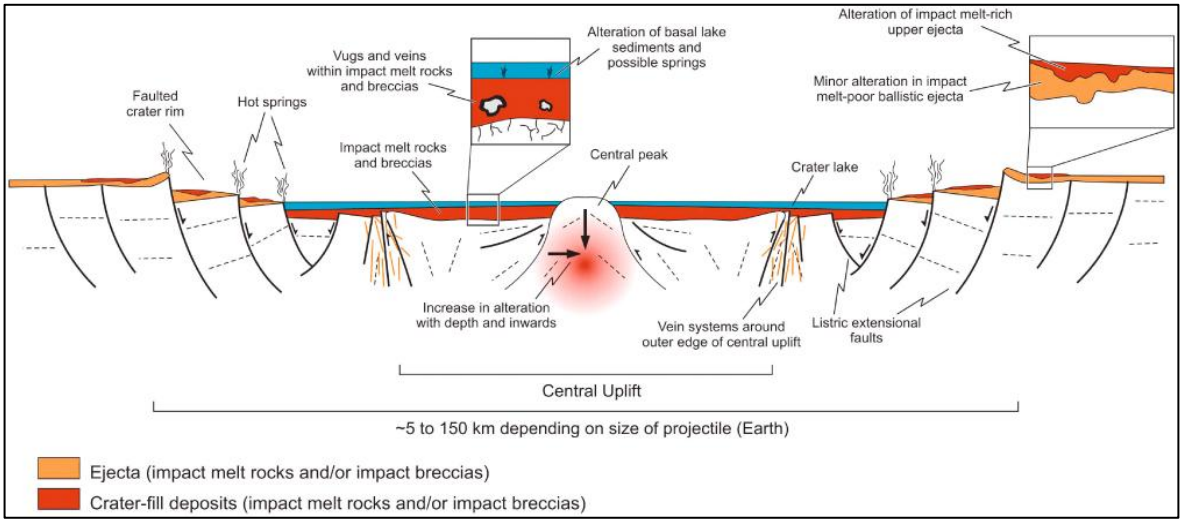

Figure 1-17: Areas within a complex impact structure which exhibit favorable conditions for the development of hydrothermal circulation (Osinski and Pierazzo, 2012).

The longevity of this activity is not well understood, but is believed to be largely controlled by the heat source; in larger structures with thick, coherent melt sheets, it has been suggested hydrothermal activity may last as long as one million years (Abramov and Kring, 2004). The longevity of the systems are also controlled by host rock permeability and self-sealing; studies have shown that crater fill impact breccias are generally impermeable (on average <1mD) (Parnell et al., 2010). Because of the low permeability, allochthonous impactites act as barriers to hydrothermal waters and cause fluids to concentrate in autochthonous fractures.

1.3.2 Sources of volatiles in targets

On Earth, it is easy to imagine a sufficient supply of water on the surface capable of fuelling hydrothermal activity in an impact structure. The most common reservoirs have been identified as meteoric water and seawater, but may also come from groundwater or basinal brines; fluid inclusion studies have not found any involvement from magmatic fluids to date (Naumov, 2005; Osinski and Pierazzo, 2012). The paleogeography of an impact site must be taken into account when studying impact-related hydrothermal alteration; in highly eroded structures, it is possible that surface processes completely erase post-impact mineral assemblages.

Hydrothermal fluid chemistry depends on the reservoir and host rock type; meteoric waters generally have a low salinity, whereas seawater is saturated in ions such as magnesium, calcium and sulphate (Pirajno, 2009). An influx of meteoric water into a hydrothermal system can lower the pH, resulting in moderate to advanced H^+ metasomatism (Pirajno, 2009). In most cases, post-impact hydrothermal fluid salinity is

low to moderate (up to 13% NaCl) with low CO_2 content (Naumov, 2005; Osinski and Pierazzo, 2012). Fluids evolve upon reactions with host rocks and system self-sealing; the loss of volatiles such as H_2S or CO_2, and the uptake of H^+ and release of cations during early stage silicate hydrolysis will affect fluid pH, and subsequently, the types of mineral assemblages that precipitate during later stages (Naumov, 2005; Pirajno, 2009).

On planets other than Earth, the question of what potential fluid reservoirs are available is slightly more difficult to answer. The modern-day surface of polar regions on Mars contain ground ice, and geomorphological and mineralogical evidence suggests liquid water was present on the surface in the past; the surface of Mars is also sulphate-rich as a result of early volcanic outgassing (Pirajno, 2009; Flauhaut et al., 2015). The Jovian moon system, particularly Europa, also contains liquid and solid water but is currently significantly more difficult to study than Mars owing to it's distance from Earth (Rhoden et al., 2015).

1.3.3 Heat sources and controls on alteration and major stages

There are three major heat sources driving hydrothermal activity in complex impact structures: impact melt, an uplifted geothermal gradient and residual heat imparted to rocks within the central basement uplift (Naumov, 2005; Osinski et al., 2013). The pervasiveness of alteration in both crystalline and sedimentary targets is controlled by heat; early hydrothermal circulation is initiated by volatiles within melt or interaction of fluid reservoirs in the paleoenvironment with hot areas of the structure.

During the early stages of cooling, hydrothermal circulation begins first within and around silicate melt sheet in crystalline targets; in structures where little to no coherent melt sheet is generated, circulation will begin around the central uplift region, where temperatures can reach 1000ºC (Naumov, 2005; Osinski and Pierazzo, 2012; Osinski et al., 2013). Similar to endogenic plutonic and volcanic activity, volatiles in a silicate impact melt result in subsolidus reactions during cooling (also called autometasomatism); in crystalline targets, this process enriches early fluids in K^+ or Na^+ (Naumov, 2005; Pirajno, 2009). Subsequent reactions combined with a vapor-dominated hydrothermal environment at temperatures from 300 to 500ºC and ion-undersaturated early fluids result in H^+ metasomatism and acid leaching of silicate minerals cooled from the melt. These reactions produce K-feldspar and smectite-dominated mineral assemblages within melt-rich impactites (Naumov, 2005). Alkali metasomatism also releases iron and titanium, which may form Fe-Ti-oxide inclusions in feldspars or neoblastic minerals in intracrystalline voids and vesicles (Naumov, 2005; Pirajno, 2009).

The intermediate stage of impact hydrothermal circulation is liquid-vapor dominated as temperatures continually decrease to between 300 and 150ºC; fluid neutralize and become enriched in ions as a result of H^+ uptake during silicate hydrolysis (Naumov, 2005; Pirajno, 2009; Osinski et al., 2013). During this stage, K or Na-metasomatism may continue to affect all lithologies, but chlorite-smectite-zeolite assemblages dominate in silicate targets; in sedimentary targets, this stage is dominated by carbonate-sulphate mineralization (Naumov, 2005; Osinski and Pierazzo, 2012). The intermediate stage is the longest and most pervasive.

The last stage of alteration is liquid dominated at temperatures below 150 to 100ºC. Fluid geochemistry and target rock type determines the types of minerals that precipitate, but they are generally dominated by carbonates, zeolites, sulphates and sulphides (Naumov, 2005; Osinski and Pierazzo, 2012. The end of this stage is arbitrary; as the geothermal gradient returns to normal and temperatures decrease to diagenetic conditions, the precipitation of secondary minerals is controlled by host rock permeability and the kinetics of water-rock interaction (Naumov, 2005; Osinski and Pierazzo, 2012).

Because the hydrothermal system is retrograde, higher temperature assemblages may be overprinted by later stage alteration; ambient condition diagenesis complicates matters even further, as surficial weathering may completely obliterate beginning and intermediate stage alteration in poorly preserved structures.

1.4 Techniques in impact-hydrothermal studies on Earth and Mars

Similar to other endogenic hydrothermal environments on Earth, the study of fossil impact-hydrothermal systems begins with field investigations and sample return; in structures that are less-accessible, this initial stage is often done by drilling. The difficulty in impact hydrothermal studies, particularly in older eroded structures, arises from the overprinting of multiple fluid events. In mixed or purely crystalline targets, pre-impact hydrothermal products can be incorporated into lithic impactites. Many of the assemblages produced in metamorphic, magmatic and impact-hydrothermal environments are texturally and compositionally identical, and cannot be distinguished from each other solely by descriptive analyses, such as conventional optical microscopy or SEM investigation.

In order to decipher multiple aqueous alteration events at an impact site, previous studies have utilized a set of techniques to constrain fluid events, such as determining bulk rock changes in impactites resulting from pervasive alteration by XRF or XRD analysis (Lambert, 2010; Sapers et al., 2014); using stable isotopes for physiological constraints such as temperature or fluid source (Muttik et al., 2010; Parnell et al., 2010); and fluid

inclusion analysis to determine fluid chemistry and source fluid reservoirs (Osinski et al., 2001; 2005).

Studies on terrestrial impact-hydrothermal environments employing both field and analytical lab methods are lacking; two sites whose hydrothermal systems have been extensively explored using a combination of isotopes, fluid inclusions, bulk rock geochemistry and field studies are the Haughton and Ries craters in Canada and Germany, respectively. Impact hydrothermal activity is being explored on Mars (Marzo et al., 2010), and is currently limited to what can be observed at the immediate and shallow surface.

1.4.1 Case studies highlighting approaches for studying impact-hydrothermal systems: Haughton and Ries craters

Two notable craters which show evidence for well-developed post-impact hydrothermal environments are the Haughton and Ries structures, in Canada and Germany, respectively. Both sites have been studied in depth and previous authors have successfully identified hydrothermal environments and mineral phases using a combination of field observations, analytical methods and lab techniques.

1.4.1.1 Haughton impact structure, Devon Island, Canada

The Haughton impact crater in the Canadian arctic has been dated to approximately 39 Ma. The target consists of ~1800 m of lower Paleozoic sedimentary units, dolostones and limestones with minor shales and sandstones, overlaying Precambrian metamorphic basement (Osinski et al. 2001, 2005).

The impact-hydrothermal environment has been well-studied within the Haughton structure; cavity-filling secondary calcite, Fe-sulphide and sulphate mineralization is recorded within the melt breccias, which intensifies towards the basal contact with the underlying target rock (Figure 1-18, A). Secondary quartz cemented lithic breccias are found within the outer margins of the central uplift and cylindrical hydrothermal pipe structures, or gossans, containing carbonate and Fe-sulphide-cemented breccias, are found at the outer margins (outer rim) of the crater.

Using fluid inclusion techniques on secondary carbonates and quartz, authors have identified the primary hydrothermal fluid reservoirs within the structure. Today, ground waters are sulphate-rich with the Paleozoic pore water salinities at 17% wt NaCl equivalent, and were likely so at the time of the impact event (Osinski et al. 2001, 2005); however, fluid inclusion data reflects low salinities (<3% wt NaCl equivalent), supporting the likelihood that surface and meteoric waters were the main fluids circulating within the

system.

A three-phase hydrothermal model for Haughton has been outlined by Osinski et al (2005) based on fluid inclusion and analytical studies. The first phase was a hot (>200°C) vapor dominated stage driven by melt; the second was vapor-liquid dominated and characterized by intermediate temperatures (200 to 80°) and the development of a convection system resulting in the precipitation of quartz, calcite and marcasite; and the last was a cooler, fluid dominated stage (<80°C) resulting in the precipitation of low-temperature vein forming and cavity-filling calcite, quartz and selenite gypsum.

Extremophile microbial colonization directly related to the development of a post-impact hydrothermal environment is also a notable feature of the Haughton structure, as evidenced by sulphur stable isotope analysis of Fe-sulphide and sulphate minerals (Parnell et al., 2010).

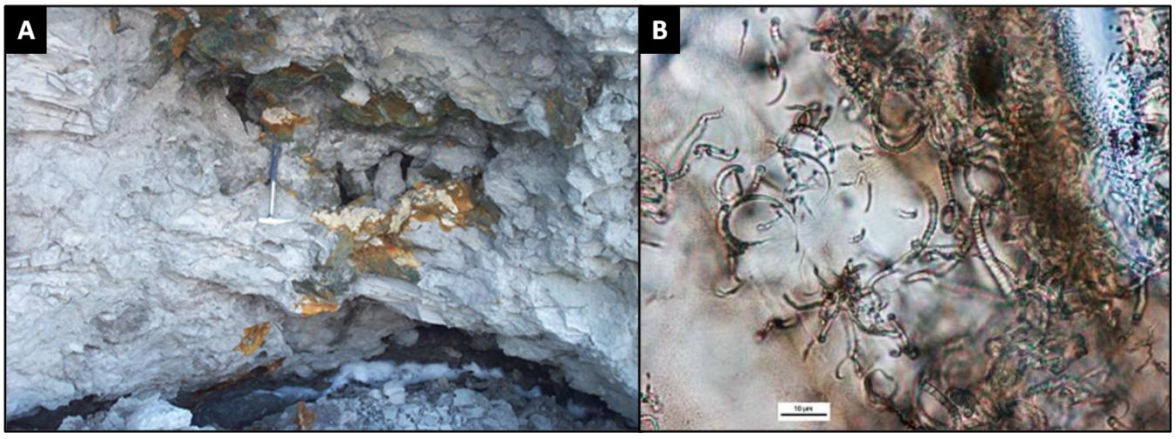

Figure 1-18: (A) Sulphide mineralization (orange, rusty color) lining a cavity within the melt-bearing impact breccias at the Haughton impact structure in Canada (Gordon Osinski, University of Western Ontario/PSI) and (B) tubular features in impact glass of the Ries crater in Germany, attributed to the colonization by thermophilic microbes during the post-impact hydrothermal period (Sapers et al., 2014a).

1.4.1.2 Ries crater, Germany

Ries crater is a well-preserved 14.3 Ma, 24km-diameter complex impact crater located in Bavaria, Germany. The target consists of 600 m of Triassic sandstones, marlstones and siltstones overlying Variscan plutonics and Pre-Variscan crystalline metamorphic units (Vennemann et al., 2001).

Post-impact hydrothermal alteration and mineralization within Ries has been identified within the groundmass of the surficial suevites, also referred to as the proximal impactites, as vesicle, fracture and cavity fillings, and alteration fronts along fractures within glass clasts consisting of clays, montmorillonite and zeolites (Vennemann et al.,

2001; Muttik et al., 2010). Secondary vesicle-lining chalcedony (quartz) has also been documented within glass clasts of the surficial suevite. Fracture and cavity-filling calcite is the dominant alteration mineral within non glass-bearing impactites. Ries impact melt rocks are distinctly red due to hematite and goethite lining vesicles and fractures. It is unclear whether the Fe-oxides/oxyhydroxides formed as high temperature vapor phase or low temperature hydrothermal product.

The crater fill suevites, those impactites within the central inner ring, exhibit much more pervasive and distinctly different alteration assemblages from their proximal counterparts. Secondary K-feldspar partially to completely replaces plagioclase phases within lithic clasts and as irregular masses within the groundmass of suevites. Montmorillonite and illite also replace both groundmass and lithic clasts of suevites. Chlorite occurs in minor amounts, and increases in abundance with depth into the underlying target. Using a combination of $\delta^{18}O$ and δD isotopes, and XRD analysis, secondary clays that have precipitated as a result of hydrothermal alteration have been distinguished from clays formed by surface weathering (Muttik et al., 2010).

The colonization of impact glass by thermophilic microbes during the post-impact hydrothermal period in the Ries crater has been evidenced by tubular structures (Sapers et al., 2014a) (Figure 1-18, B).

1.4.2 Hydrothermal activity associated with craters on Mars

Impact-generated hydrothermal activity has been confirmed in the complex Toro crater on Mars (Marzo et al., 2010); spectroscopic data has revealed the presence of hydrous phyllosilicates (chlorite + smectites) in and around the central uplift region, which is complimented by volatile release mounds geomorphically expressed on the surface (Figure 1-19). Currently, researchers only have access to qualitative geologic information on the immediate to shallow surface of Mars through spectroscopic data obtained through instruments such as CRISM on the Mars Reconnaissance Orbiter (MRO) (NASA/JPL) and the ChemCam instrument on the Curiosity rover (NASA/JPL).

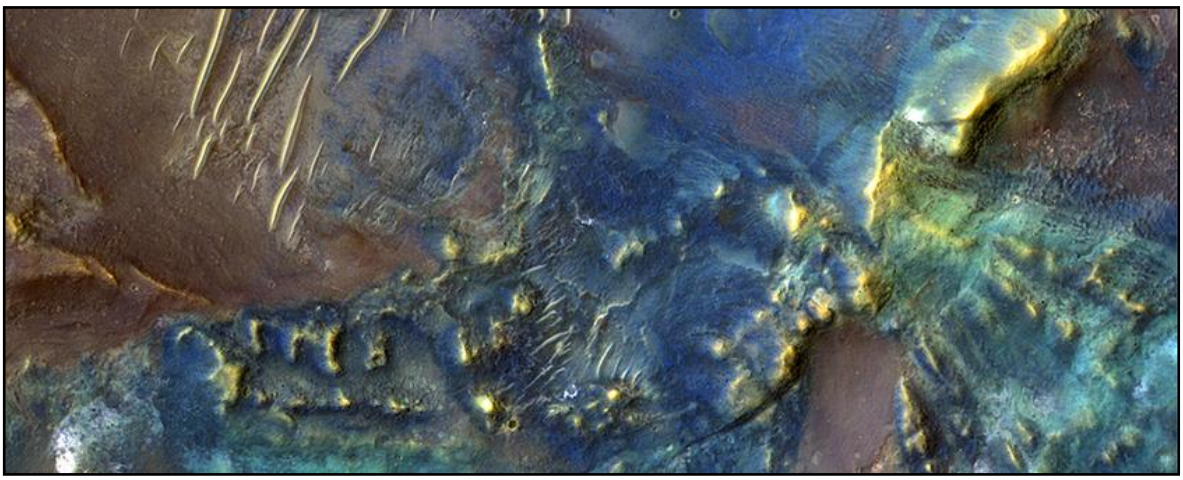

Figure 1-19: HiRise image of the floor of Toro crater on Mars. Blue colors represent anhydrous mineral phases such as pyroxene and olivine, and warmer colors represent hydrous mineral phases such as clay (NASA/JPL/University of Arizona).

1.5 Outstanding questions in impact hydrothermal studies: project purpose and overview

Previous studies on complex impact structures (Section 1.4.1) have revealed well-developed hydrothermal systems capable of supporting extremophile life during the post-impact cooling period. Many parameters surrounding the development of hydrothermal circulation remain undefined, such as the roles of target type and palaeofluid reservoirs, as well as further exploring their ability to host microbial communities, particularly in relatively dry targets. In addition to environmental factors leading to the initiation of hydrothermal circulation, the conditions and type of alteration relative to location within the structure, heat source and impactite type are not well-explored.

The lifetime of hydrothermal activity is contingent on the cooling rate of the structure (Osinski et al. 2013); no active systems currently exist on Earth's surface, and the reconstruction of hydrothermal environments in craters is limited to what can be determined from the alteration products fossilized therein. Direct evidence for life may be sought out in impact products, such as the microfossils found within the silicate glass of the Ries crater in Germany (Sapers et al. 2014); however, the identification of such evidence can be hindered by diagenesis. In highly eroded structures, parautochthonous impactites and the radial fracture network within the underlying and surrounding target rock may be all which remains.

1.5.1 Exploring hydrothermal activity within the sub-crater environment

Previous authors have outlined areas within complex craters conducive to the development of hydrothermal circulation, as well as controls on impactite porosity on fluid flow within a crater (Parnell et al., 2010; Osinski et al., 2012). They hypothesized that

hydrothermal circulation is largely controlled by impact fractures; while coherent melt-bearing impactites stay hotter for longer periods of time due to heat transfer by conduction rather than convection, they also contain low porosity (Parnell et al., 2010). As a result of low matrix permeability in impact breccias, hydrothermal fluids focus along impact fracture systems; hydrothermal waters carry nutrients and heat, both of which are conducive to the development of extremophile microbial communities.

1.5.2 The Rochechouart impact structure

Following the methods of previous studies (Section 1.4.1), this thesis is a case study on the late-Triassic Rochechouart impact structure located in the Limousin region of west-central France. It combines field observations, microscale mineralogical investigations and isotopic analyses to reconstruct post-impact hydrothermal environments in a mixed, marginal-marine target. Rochechouart is a 23km-diameter complex impact structure; although highly eroded it is sufficiently well-preserved to provide a full suite of impactites representing a continuum of melt-rich to melt-poor lithologies, with access points cross-cutting allochthonous crater-fill impactites into the sub-crater environment (Lambert, 1977; 2010; Sapers et al., 2014b). Rochechouart represents a marginal marine, coastal impact site; the majority of the target consists of Variscan quartzofeldspathic igneous and metamorphic rocks of the Central Massif. Rochechouart was also proximal to the then-transgressing Aquitaine basin. Previous researchers have identified rare sedimentary elements within Rochechouart impactites as limestone clasts in breccias (Sapers et al., 2009), as well as a K-metasomatic overprint attributed to post-impact hydrothermal processes affecting the entire structure (Spray et al., 1997; Tagle et al., 2009; Lambert, 2010; Schmeider et al., 2010; Sapers et al., 2014b).

The first aim of study is to evaluate the post-impact hydrothermal environment in Rochechouart to determine whether conditions were suitable to host extremophile life. Previous studies have identified isotopic evidence for bacterial sulphate reduction within secondary sulphide minerals in breccia matrices and impact fractures; findings by Parnell et al. (2010) suggest that autochthonous impact fractures focus hydrothermal fluid flow and host conditions conducive to the development of extremophile microbial communities during the cooling period. Heavy carbonate-sulphide mineralization is commonplace in lithic impactites at and below the transient crater floor in Rochechouart, which will be the focus for sulphur isotope comparison.

The second aim of this study is to constrain the hydrothermal fluid reservoirs within the structure. Observations presented by previous authors (Lambert, 1977, 2010; Sapers et

al., 2014b) provide evidence that Rochechouart hosted a pervasive hydrothermal system. The paleogeography of the target, as marginal marine, suggests hydrothermal activity may have been influenced by the infiltration of seawater from outside the structure. Secondary carbonate mineralization is found throughout the parautochthonous impact breccias and autochthonous impact fractures; the carbon isotope signature preserved therein may reveal clues on the origin of the fluids from which they precipitated.

The third main objective of this thesis is to provide a thorough overview of the types and pervasiveness of secondary alteration in impactites and target material. In addition to fluid chemistry, the conditions and extent of hydrothermal activity on a smaller scale, and relative to host rock and heat source, are poorly known in Rochechouart; the sub-crater environment of Rochechouart hosts a variety of carbonate and sulphide mineralized breccias and basement fractures, which are rare to absent in melt-bearing lithologies, and while K-metasomatism has affected all lithologies, it is most pervasive in melt-rocks and melt-bearing breccias.

Following the methods of previous authors (Muttik et al. 2010; Parnell et al. 2010), this study will employ a set of techniques to characterize aqueous alteration assemblages throughout the structure. Stable isotope analysis provides a powerful tool in constraining temperatures, fluid sources and origin of secondary minerals within a fossilized impact-hydrothermal system; this study will use $\delta^{18}O$, $\delta^{13}C$ and $\delta^{34}S$ of secondary carbonate and sulphide minerals to compliment petrography, scanning electron microscopy, energy dispersive X-ray analyses and Raman mineral phase data.

Results from this study will highlight the extent and effects of hydrothermal circulation beneath the transient crater floor within a marginal marine, complex impact structure with a majority crystalline target and determine whether the post-impact environment in Rochechouart was conducive to the development of extremophile life. Isotopic analysis will also distinguish between pre-impact metamorphic hydrothermal alteration within the basement, post-impact hydrothermal alteration and surficial weathering and diagenesis.

1.6 References

Abramov, O., Kring, D., 2004, Numerical modeling of an impact-induced hydrothermal system at the Sudbury crater, *Journal of Geophysical Research*, Vol. 109.

Cockell, C. S., Bland, P. A., 2005, The evolutionary and ecological benefits of asteroid and

comet impacts, *Trends in Ecology and Evolution*, Vol. 20 No. 4.

De le Fuente Marcos, C., De le Fuente Marcos, R., 2014, Reconstructing the Chelyabinsk event: pre-impact orbital evolution, *Monthly Notices of the Royal Astronomical Society*, 443, L39-L43.

Fassett, C. I., and Minton, D. A., 2013, Impact bombardment of the terrestrial planets and the early history of the Solar System, *Nature Geoscience 6,* 520-524.

Ferrière, L., Koeberl, C., Reimold, W. U., 2009, Characterisation of ballen quartz and cristobalite in impact breccias: new observations and constraints on ballen formation, *European Journal of Mineralogy,* 21, p. 203-217.

Flahaut, J., Carter, J., Poulet, F., Bibring, J. P., van Westrenen, W., Davies, G. R., Murchie, S. L., 2015, Embedded clays and sulfates in Meridiani Planum, Mars, *Icarus*, 248, p 269-288.

French B. M., 1998, Traces of Catastrophe: A Handbook of Shock-Metamorphic Effects in Terrestrial Meteorite Impact Structures. *LPI Contribution No. 954, Lunar and Planetary Institute, Houston. 120 pp.*

French, B. M., Koeberl, C., 2010, The convincing identification of terrestrial meteorite impact structures: What works, what doesn't, and why, *Earth Science Reviews*, 98, 123-170.

Galli M. T., Jadoul F., Bernasconi S. M., Weissert H., 2005, Anomalies in global carbon cycling and extinction at the Triassic/Jurassic boundary: evidence from a marine C-isotope record, *Palaeogeography, Palaeoclimatology, Palaeoecology*, 216, p. 203 – 214.

Goldin, T., 2012, Planetary science; Earth’s ancient catastrophes, *Nature Geoscience* 5, 309.

R. Gomes, R., Levison, H. F., Tsiganis, K., Morbidelli , A., 2005, Origin of the cataclysmic Late Heavy Bombardment period of the terrestrial planets, *Nature letters* 435.

Grieve, R. A. F., 1980, Impact bombardment and it’s role in proto-continental growth on

the early Earth, *Precambrian Research,* 10, p. 217-247.

Grieve, R. A. F., and Masaitis, V. L., 1994, The Economic Potential of Terrestrial Impact Craters, *International Geology Review,* Vol. 36, pp. 105-151.

Impact-structures.com, 2015, *The shatter cone page ERNSTSON CLAUDIN IMPACT STRUCTURES – METEORITE CRATERS* (online) Available at: http://www.impact-structures.com/impact-rocks-impactites/the-shatter-cone-page/ (Accessed 2 Sep. 2015).

Koeberl, C., 1994, Tektite origin by hypervelocity asteroidal or cometary impact: target rocks, source craters and mechanisms, *Geological Society of America Special Paper 293.*

Koeberl, C., 2006, The record of impact processes on the early Earth: A review of the first 2.5 billion years, *Geological Society of America Special Paper 405.*

Koeberl, C., 2014, The geochemistry and cosmochemistry of impacts, *Planets, Asteroids, Comets and The Solar System, Volume 2 of Treatise on Geochemistry, 2nd edition*. Elsevier, p.73-118.

Kring, D., 2007, The Chicxulub impact event and its environmental consequences at the Cretaceous–Tertiary boundary, *Palaeogeography, Palaeoclimatology, Palaeoecology*, 255, p. 4–21.

Lambert P., 1977, The Rochechouart Crater: Shock Zoning Study, *Earth and Planetary Science Letters*, 35 p. 258-268.

Lambert, P., 1981, Breccia dikes - Geological constraints on the formation of complex craters Multi-ring basins: Formation and evolution; *Proceedings of the Lunar and Planetary Science Conference, Houston, TX, November 10-12 1980,* p. 59-78.

Lambert, P., 2010, Target and impact deposits at Rochechouart impact structure, France *Geological Society of America,* Special Paper 465.

Lpi.usra.edu, 2015, *Impact Cratering*, (online) Available at: http://www.lpi.usra.edu/education/explore/shaping_the_planets/impact_cratering.shtml

(Accessed 2 Sep. 2015).

Lpi.usra.edu, 2015, *Impact Crater Formation*, (online) Available at: http://www.lpi.usra.edu/exploration/training/illustrations/craterFormation/ (Accessed 7 Mar. 2015).

Marzo, G. A., Davila, A. F., Tornabene, L. L., Dohm, J. M., Fairén, A. G., Gross, C., Kneissl, T., Bishop, J. L., Roush, T. L., McKay, C. P., 2010, Evidence for Hesperian impact-induced hydrothermalism on Mars, *Icarus*, 208, 667-683.

McKinnon, M., 2015, *Here's Everything We Know About The Chelyabinsk Meteor*, (online) Earth & Space. Available at: http://space.io9.com/heres-everything-we-know-about-the-chelyabinsk-meteor-1637134445 (Accessed 2 Sep. 2015).

Muttik, N., Kirsimäe, K., Vennemann, W. T., 2010, Stable isotope composition of smectite in suevites at the Ries crater, Germany: Implications for hydrous alteration of impactites, *Earth and Planetary Science Letters*, 299, 190–195.

Naumov, M., 2005, Principal features of impact-generated hydrothermal circulation systems: mineralogical and geochemical evidence, *Geofluids*, 5, p 165-184.

NASA, (2015). *Asteroid Fast Facts*. (online) Available at: http://www.nasa.gov/mission_pages/asteroids/overview/fastfacts.html (Accessed 2 Sep. 2015).

Osinski, G. R., Spray, J. G., 2001, Impact-generated carbonate melts: evidence from the Haughton structure, Canada, *Earth and Planetary Science Letters*, 194, p. 17-29.

Osinski G. R., Spray, J. G., and Lee, P., 2001, Impact-induced hydrothermal activity within the Haughton impact structure, arctic Canada: Generation of a transient, wet warm oasis. *Meteoritics and Planetary Science*, 36, No. 731-745.

Osinski, G. R., Lee, P., Parnell, J., Spray, J. G. and Baron, M., 2005, A case study of impact-induced hydrothermal activity: The Haughton impact structure, Devon Island, Canadian High Arctic, *Meteoritics and Planetary Science*, Vol. 40, No. 12, pp. 1859-1877.

Osinski, G. R. and Pierazzo, E., 2012, Impact Cratering: Processes and Products, *John Wiley & Sons, Ltd*, Chichester, UK. doi: 10.1002/9781118447307.ins

Osinski, G. R., Tornabene, L. T., Banerjee, N. R., Cockell, C. S., Flemming, R., Izawa, M. R., McCutcheon, J., Parnell, J., Preston, L. J., Pickersgill, A. E., Pontefract, A., Sapers, H. Southam, G., 2013, Impact-generated hydrothermal systems on Earth and Mars, *Icarus*, 347-363.

Memin.de, (2015), *Results TP-5 - MEMIN - Multidisciplinary Experimental and Modeling Impact Research Network*, (online) Available at: http://www.memin.de/results-tp-5.html (Accessed 20 Aug. 2015).

Parnell, J., Boyce, A., Thackrey, S., Muirhead, D., Lindgren, P., Mason, C.,Taylor, C., Still, J., Bowden, S., Osinski, G. R., and Lee, P., 2010, Sulfur isotope signatures for rapid colonization of an impact crater by thermophilic microbes, *Geology*, Vol. 38, No. 3, pp. 271-274.

Passc.net, 2015, *Earth Impact Database*, (online), Available at: http://www.passc.net/EarthImpactDatabase/ (Accessed 12 Aug. 2014).

Pirajno, F., 2009, Hydrothermal processes and mineral systems, 1st edn., *Springer & Geological Survey of Western Australia.*

Planet-terre.ens-lyon.fr, (2015). - *Planet-Terre*, (online) Available at: http://planet-terre.ens-lyon.fr/image-de-la-semaine/Img437-2013-10-14.xml (Accessed 2 Sep. 201).

Rhoden, A. R., Hurford, T. A., Roth, L., Retherford, K., 2015, Linking Europa's plume activity to tides, tectonics, and liquid water, *Icarus*, 253, p 169-178.

Robbins, S. J., Hynek, B. M., 2012, A new global database of Mars impact craters ≥ 1km: 2. Global crater properties and regional variations of the simple-to-complex transition diameter, *Journal of geophysical research*, vol. 117.

Galli M. T., Jadoul F., Bernasconi S. M., Weissert H., 2005, Anomalies in global carbon cycling and extinction at the Triassic/Jurassic boundary: evidence from a marine C-isotope record, *Palaeogeography, Palaeoclimatology, Palaeoecology*, 216, p. 203 – 214.

Sapers, H. M., Osinski, G. R., Banerjee, N., 2009, Re-evaluating the Rochechouart impactites: petrographic classification, hydrothermal alteration and evidence for carbonate bearing target rocks, *40th Lunar and Planetary Science Conference, Abstract # 1284.*

Sapers, H. M., Osinski, G. R., Banerjee, N. R., Preston, L. J., 2014a, Enigmatic tubular features in impact glass, *Geology*.

Sapers H. M., Osinski G. R., Banerjee N. R., Ferriere L., Lambert P., Izawa M. R., 2014b, Revisiting the Rochechouart impact structure, France, *Meteoritics and Planetary Science*, 1-17.

Schmeider M., Buchner E., Schwarz W. H., Trieloff M., Lambert P., 2010, A Rhaetian $^{40}Ar/^{39}Ar$ age for the Rochechouart impact structure (France) and implications for the latest Triassic sedimentary record, Meteoritics & Planetary Science 45, Nr 8, 1225-1242.

Spray J. G., Kelley S. P., and Rowley D. B., 1998, Evidence for a late Triassic multiple impact event on Earth, *Nature*, vol. 392.

Stöffler, D., Langenhorst, F., 1994, Shock metamorphism of quartz in nature and experiment: I. Basic observation and theory, Meteoritics 29, 155-181.

Stöffler, D, and Grieve, R. A. F., 2007, A systematic nomenclature for metamorphic rocks: Chapter 11: Impactites. *Recommendations by the IUGS Subcommission on the Systematics of Metamorphic Rocks*. Web version 01.02.07.

Vennemann, T. W., Morlok, A., Von Engelhardt, W. V., Kyser, K., 2001, Stable isotope composition of impact glasses from the No¨rdlinger Ries impact crater, Germany, Geochimica et Cosmochimica

Chapter 2: The Rochechouart impact structure

In this chapter

2.0 The Rochechouart impact structure

2.1 Introduction: location, parameters and current state

The Rochechouart impact structure is a 23 km diameter, highly eroded complex impact crater located in west-central France, with the center at latitude 45°48'48.37" N and longitude 0°46'32.19" E (Lambert et al.,1977; 2010) (Figure 2-1 A). The most recently proposed age of the structure is 201 ± 2 Ma (Schmeider et al., 2010). The bulk impactite geochemistry is granitic, reflective of it's Variscan granitic igneous and metamorphic crystalline target (Lambert et al., 1977; 2010). Almost all of the structure has been eroded and is lacking any surficial expression characteristic of complex craters (i.e., central uplift, crater rim). The Rochechouart field area covers a large, rural expanse of densely vegetated forest and fields, in what is today a temperate climate and receives an average of 1022 mm of rainfall per year (Weather Online Ltd).

In 1833, Rochechouart impactites were first described as volcanic or man made in origin, and were extracted for building material (Manes, 1833; Kraut, 1935) (Figure 2-1 B). Today, impactites can be seen in much of the original infrastructure throughout villages in the area, as well as in 4th century Roman geothermal baths excavated in the Cassinomagus archaeological park (Lambert, 2010; Departmental Council of Charente Registered for Historical Monuments). In the 1960's, investigations by Francois Kraut lead to the discovery of PDF's and shatter cones. Rochechouart was officially recognized as an impact structure in 1969 (Kraut et al., 1969; Kraut and French, 1971).

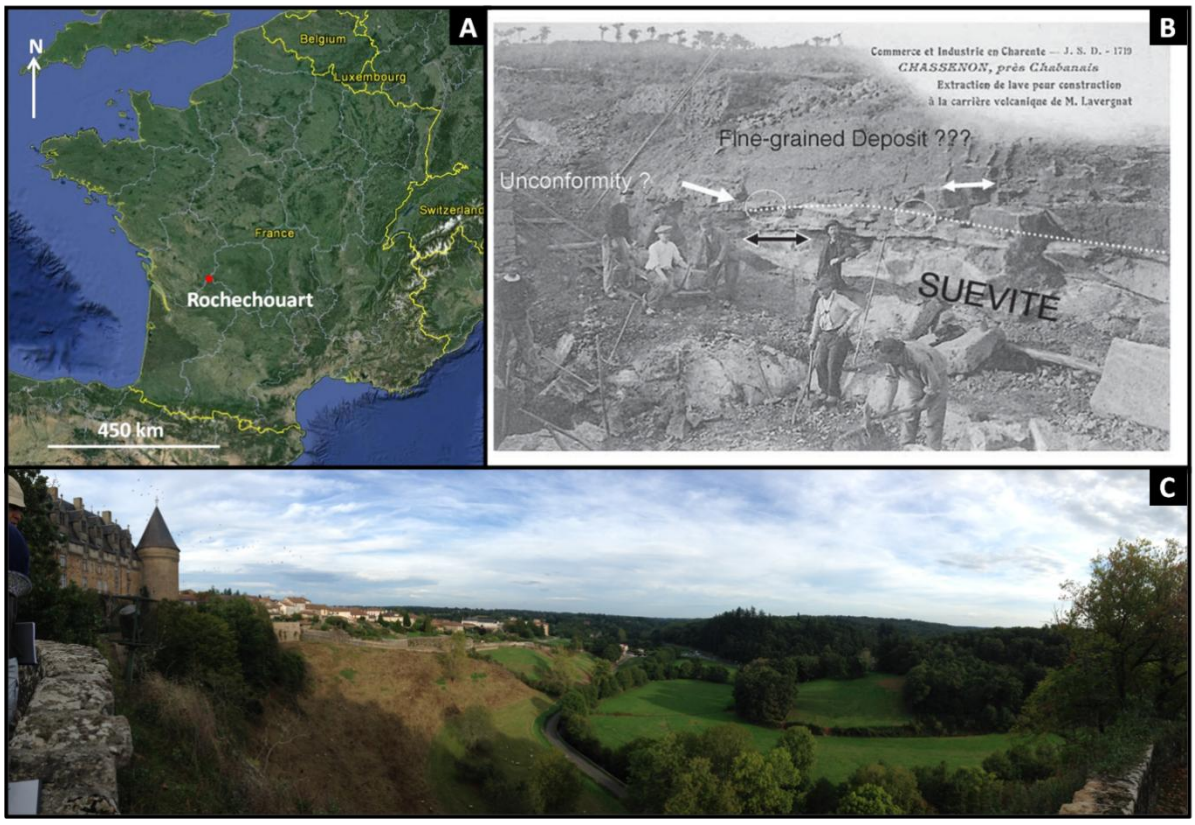

Figure 2-1: (A) A map showing location of the Rochechouart impact structure (Google Earth, 2014). (B) A postcard dated to the early 1900's with a picture of men working in a quarry in Rochechouart, with the title stating "Chassenon, near Chabanais, Extraction of lava flow material for construction at the volcanic quarry of Monsieur Lavergnat" (Lambert, 2010). (C) A panoramic view from the top a cliff next to the Rochechouart Chateau.

In 2008, the Réserve Naturelle de l'Astroblème de Rochechouart-Chassenon was formed to protect the area as both an archaeological heritage site and to preserve what little of the impact structure remained; collection of rocks within the area is now strictly regulated (Réserve Naturelle de l'Astroblème de Rochechouart – Chassenon). Permission to collect within the area may be obtained following approval by application to the reserve's scientific board. The area today is the second-least populated region in metropolitan France, with the majority of habitants being cattle farmers. There is a thirteenth-century castle found in the village of Rochechouart, which is a landmark historic monument protected by the French ministry of culture, (Departmental Museum of Contemporary Art in Rochechouart) currently being utilized as a modern art museum.

2.2 History of research on Rochechouart

Research on Rochechouart is lacking in comparison to other impact structures found in mainland Europe, likely due to it's poor state of preservation. The most extensive

work has been done by Philippe Lambert, focusing on impactite petrology and geochemistry (Lambert 1977, 1986 and 2010; Janssens 1977). A revision in Rochechouart impactite nomenclature was recently published, and is based on the ratios of melt and lithic material as opposed to the impactite origin relative to location within the structure (Stoffler and Grieve, 2007; Sapers et al., 2014a). This recent revision has been executed in order to allow impactite classification within poorly preserved craters, such as Rochechouart, where impactite origin-crater morphology relationships are difficult to establish.

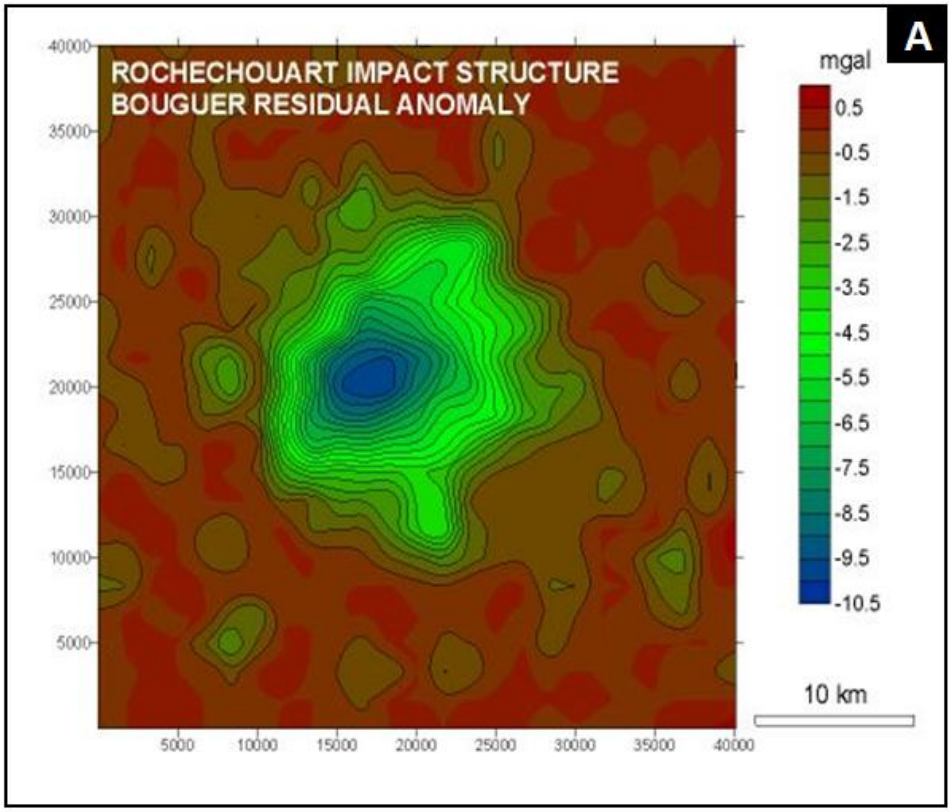

B

Date	Authors	Age (Ma)	Methods
2010	Schmeider et al.	201 ± 2	$^{40}Ar/^{39}Ar$ gneiss K-feldspar
1997	Kelley & Spray	214 ± 8	$^{40}Ar/^{39}Ar$ laser pseudotachylite
1987	Reimold & Oskierski	186 ± 5	Rb-Sr melt rock
1975	Wagner & Storzer	206 ± 39	Glass fission track Chassenon
1975	Wagner & Storzer	198 ± 25	Apatite fission track Chassenon
1974	Lambert	165 ± 5	K-Ar glass
1971	Kraut and French	154 ± 8	K-Ar melt rock

Figure 2-2: (A) Bouguer residual anomaly, common known as a gravity anomaly, within the Rochechouart area, characteristic of meteorite impacts. Brecciated rocks are less dense than surrounding unshocked material (Schmidt et al., 1984). (B) Summary of history of dating attempts in Rochechouart, with corresponding ages, authors and methods (modified after Schmeider et al., 2010).

There have been several attempts at dating the impact event, the earliest in 1977 (Lambert 1977) and the most recent (Schmeider et al., 2010) placing it at the currently accepted age of 201 ± 2 Ma using $^{40}Ar/^{39}Ar$ dating techniques on K-feldspar extracted from shocked basement gneiss (Schmeider et al., 2010) (Figure 2-2 B). The most recent age is also concomitant with the Triassic-Jurassic global marine extinction event, as well as a world-wide $\delta^{13}C$ excursion recorded in the marine carbonate record (Gallia et al., 2005; Saltzman and Thomas, 2012). Recent evidence suggests CAMP (Central Atlantic Magmatic Province) volcanism and outgassing during the late Triassic ultimately lead to a global CO_2 increase, and is likely the cause of the extinction (Whiteside et al., 2010).

There are other impact structures of similar age to Rochechouart; the Manicouagan structure at 214 Ma and the Red Wing crater in North Dakota at 200 Ma. Some have previously suggested that they may have formed a chain of impacts in the late Triassic related to the breakup of an asteroid (Spray et al., 1998).

There have been several attempts to determine the projectile composition. The most recent in 2009 using platinum group element patterns and Ni/Cr/Ir ratios within melt rocks, found the projectile to be of non-magmatic iron (IA and IIIC) composition (Tagle et al., 2009).

A recent study attempted to determine whether a magnetic reversal was recorded in grains of titanohematite within the melt rocks (Eitel et al, 2014). The study found no reversal resulted from the impact.

A Bouguer residual anomaly, also known as a gravity anomaly, is observed within the Rochechouart area (Schmidt et al., 1984) (Figure 2-2, A).

Several authors have noted secondary mineral assemblages related to hydrothermal alteration and weathering within the structure (Lambert, 1977, 2010; Spray et al., 1998; Tagle et al., 2009; Sapers et al., 2014a). A recent publication outlined the major alteration assemblages (Sapers et al., 2014a), but a comprehensive study on the origin, relationship and timing of these assemblages relative to each other and the target material remains to be undertaken.

2.3 Tectonic and depositional history of the target

Basement rocks in Rochechouart consist of a variety of granitic metamorphic and plutonics of the Variscan orogeny, originating from a series of deformation events related to continental-continental collision and rifting episodes beginning in the Devonian (Faure et al., 2009; Lambert, 2010; Le Carlier de Veslud et al., 2013). The closing of the Iapetus

ocean and collision of several microcontinents and islands has formed the complex geologic history observed in the Central Massif (Faure et al., 2009). Collision events during this period resulted in the subduction of the leading edge of the Gondwana plate; this subducted continental slab is what forms a large part of the metamorphic basement in the Rochechouart target.

A small portion of subducted oceanic crust forms a unit of serpentinized peridotites, called the Merly serpentinites, which can be found in the Rochechouart field area (Faure et al., 2009; Lambert 2010).

The last major tectonic event occurred around 300 Ma, and is represented by various granite and granodiorite bodies found throughout the Central Massif (Figure 2-3, Section 2.5.2.2 and 2.5.2.3).

The burial and erosion history of Rochechouart is not well known; the coastal paleogeography might suggest the then-transgressing Aquitaine basin may have contributed to the poor preservation of the structure, but at present, the marine limestones syngenetic with the impact event are found 5 km outside the accepted crater limit.

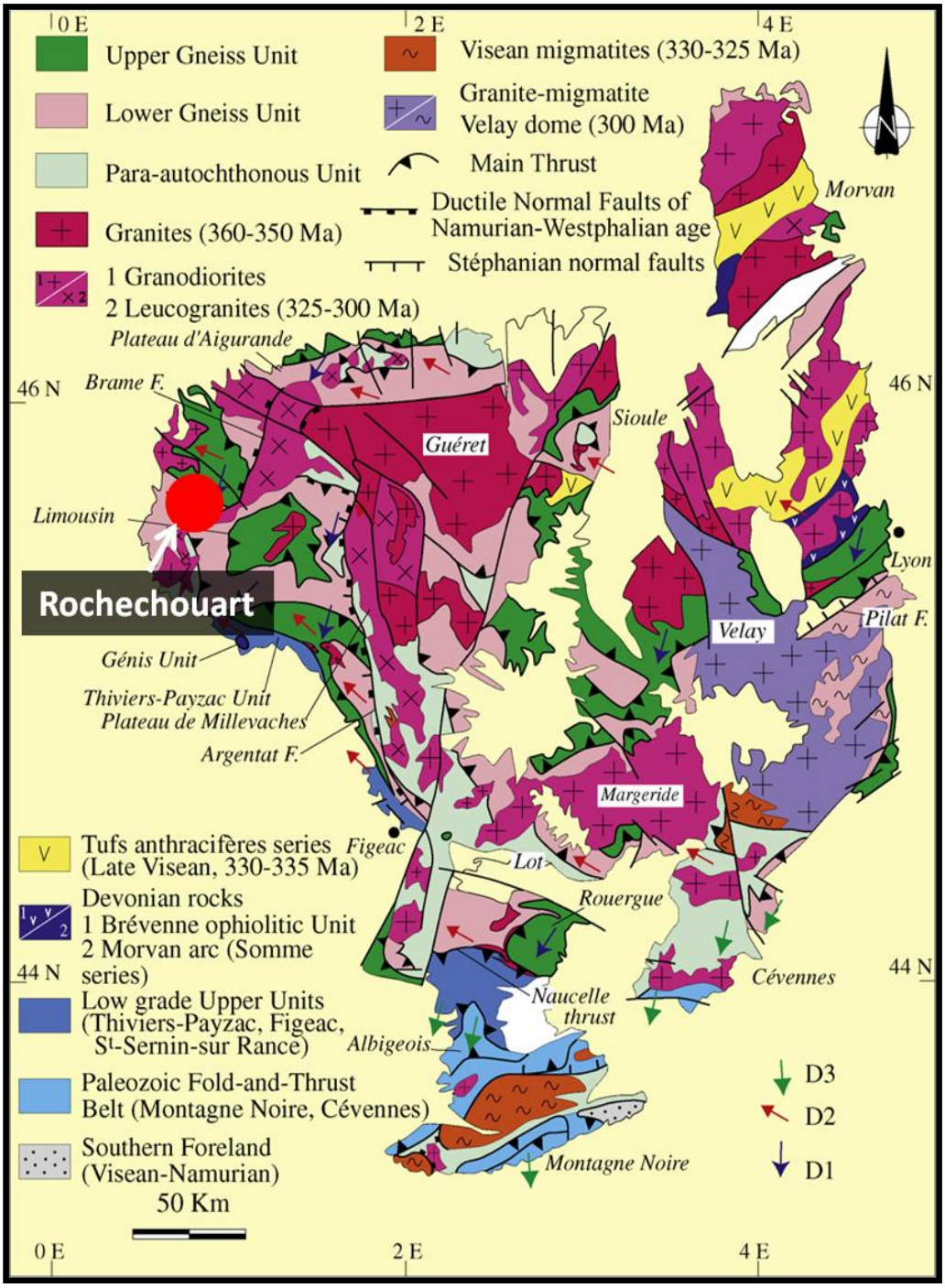

Figure 2-3: Geologic map of the crystalline basement of the Central Massif, with Rochechouart for context (modified from Faure et al., 2009).

Around 250 Ma the Mesozoic sea, which today is recognized as the Aquitaine basin, began to deposit platform carbonates directly over the crystalline basement forming an unconformity which can be traced north into the Paris Basin (Lambert, 2010; Cathelineau et al., 2012).

The infiltration of seawater into basement fractures in Variscan plutonics along the unconformity is recognized as a significant event by some researchers, and has been dated between 146 to 156 Ma (Boiron et al., 2002; Cathelineau et al., 2012). This process is

evidenced by isotopic and fluid inclusion studies of what is proposed to represent multiple generations of carbonate-fluorite-silicate mineralization within basement fractures formed during cooling of plutons (Fourcade et al., 2002; Boiron et al., 2002; Cathelineau et al., 2012).

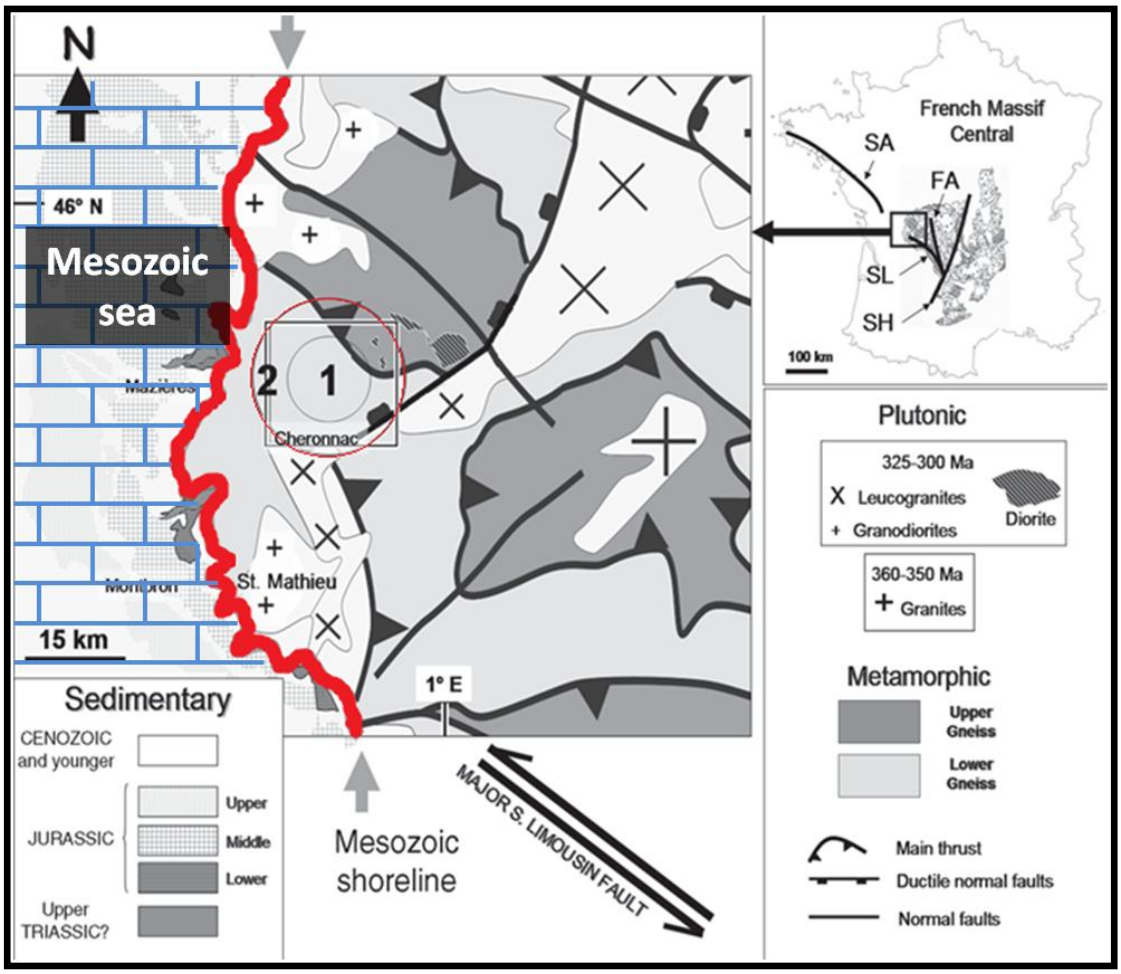

Figure 2-4: Simplified geologic map of the main units within and surrounding the Rochechouart impact structure. Shown is what is left preserved of the Aquitaine shoreline (modified after Lambert, 2010).

2.4 Rochechouart impactites

Rochechouart is located at the boundary between the Aquitaine basin and Central Massif, classifying it as a marginal marine impact (Lambert 1977, 2010). Although today Mesozoic carbonates can be found in outcrop only 5km outside the perimeter of the structure, the impactite petrology and geochemistry unambiguously supports the majority target contribution as crystalline granitic plutonics and metamorphics of the Central Massif (Lambert 2010; Sapers et al., 2014a).

The discovery of a limestone clast in a melt-bearing impactite, coupled with the

paleogeography, has lead to the hypothesis that a thin sedimentary cover may have been present at the time of the impact (Sapers et al., 2009).

2.4.1 Impactite classification and nomenclature

The nomenclature of Rochechouart impactites has evolved since the structure's discovery in the 1960's. The most recent update to this scheme was in 2014, and is based on the composition of the groundmass of the impactite. This new scheme allows for the classification of highly eroded impact sites with limited geological context, as opposed to a classification scheme based on the location of the impactite relative to the transient crater cavity (Stöffler and Grieve, 2007). The original rock names first used in the 1960's (Kraut et al., 1969) are based on the geographic locations in which the rock types were found.

Table 2-1: Evolution of Rochechouart impactite nomenclature

Sapers et al. 2014	**Lambert 2010**	**Lambert 1977**	**Kraut 1969**
Shock fractured basement	Shocked basement	(A) Fractured basement rock	N/A
Monomict lithic breccia	Monomict lithic breccia	(B) Monomict breccia	Rochechouart breccia
Lithic impact breccia	Polymict lithic breccia	(C) Polymict breccia, no glass	Rochechouart breccia
Melt-bearing impact breccia	Melt-poor suevite	(D) Polymict breccia, with glass	Chassenon suevite
Melt-rich impactite	Melt-rich basal suevite	N/A	N/A
Particulate impact melt rock	Impact melt	(E) Melt	Montoume breccia
Impact melt rock	Impact melt rock	Impact melt rock	Babaudus melt

2.4.2 Impactite cover and preservation

Very little allochthonous impactite material is preserved in Rochechouart, and collection of samples has therefore been regulated since the opening of the reserve in 2008 (Figure 2-5 and 2-6). Based on field observations by Lambert, 2010, the estimated amount of allochthonous impactite remaining covers an area of 47.7km^2. Further, it estimated that the volume of this material amounts to only 1.18km^3, with only 0.02km^3 of that being melt (Figure 2-5 and 2-6). Most impactite outcrops suitable for sampling in Rochechouart are either obscured and located on private property, or in active and/or abandoned quarries, both which are gated off and require special permission from either the landowner or

natural reserve to collect.

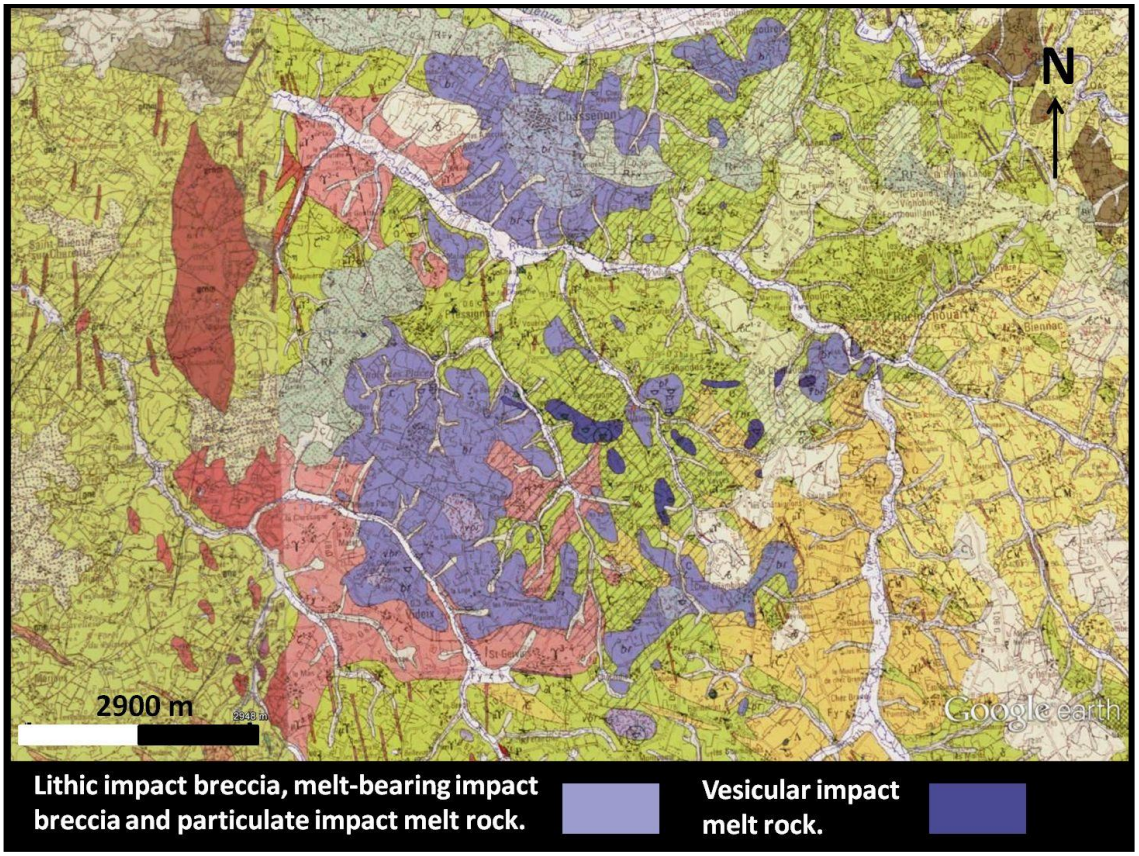

Figure 2-5: Geologic map of Rochechouart, showing current cover of melt-bearing and polymict lithic impactites (BRGM overlay and Google Earth, 2014).

A

Exposed Today	Area (km^2)	Thickness (m)		Volume (km^3)	Melt	
		Average	Maximum		Fraction (%)	Volume (km^3)
Polymict lithic breccias	40.9	26	40	1.1	0	0
Suevite	4.9	15	20	0.07	1–38	0.01
Impact melt rocks	1.9	7	20	0.01	50–95	0.01

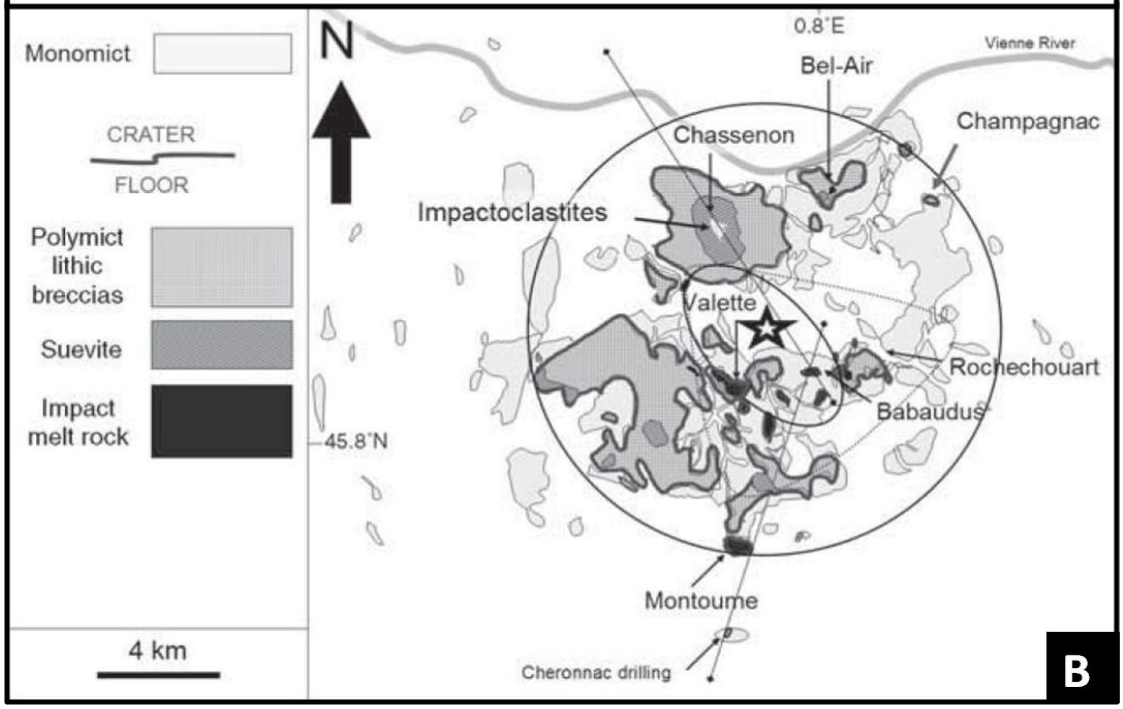

Figure 2-6: (A) Field based estimates of impactite material cover, volume and thickness in Rochechouart (Lambert, 2010), and (B) simplified geologic map of impactite cover in Rochechouart, including monomict lithic breccias (Lambert, 2010), both using Lambert's earlier impactite classification scheme (Table 2-1).

Section 2.4.3 XRF studies (Lambert, 2010)

All Rochechouart impactites (melt rocks, melt-bearing breccias, lithic breccias and coherent basement) are granitic in composition, reflective of their crystalline target units; there is no evidence for significant target contribution from the nearby marine carbonates. Bulk XRF analysis performed by Lambert (2010) shows impactites on average contain between 2 to 4 wt% ± 0.5 Fe and between 0 to 1.5 wt% Mg, with the exception of the particulate impact melt and melt-bearing impact breccia, which are slightly more mafic at 6.5 wt% Fe and about 2% wt % Mg (Figure 2-7, A).

Overall, Rochechouart impactites plot closer to the orthoclase pole on the orthoclase-albite-quartz ternary diagram. There is a slight K-metasomatic overprint in the target material, which is observed both mineralogically and through whole rock XRF data. This K-metasomatism is even more pronounced in the Rochechouart impactites; all are

enriched in K_2O relative to Na_2O and CaO. In impact melt rocks, this enrichment is as much as 15 times that of the target rocks for K/Na and 10 times for the lithic clasts in impact melt (Lambert, 2010).

The K/Ca ratio in impact melt is around 10. Alteration and K-enrichment in impactites has been noted by previous authors, and is attributed to post-impact hydrothermal activity (see chapters 1 and 3). It is unsure if K-enrichment observed in unshocked basement rocks is related to post-impact hydrothermal activity or fluid circulation during the collision and metamorphic event.

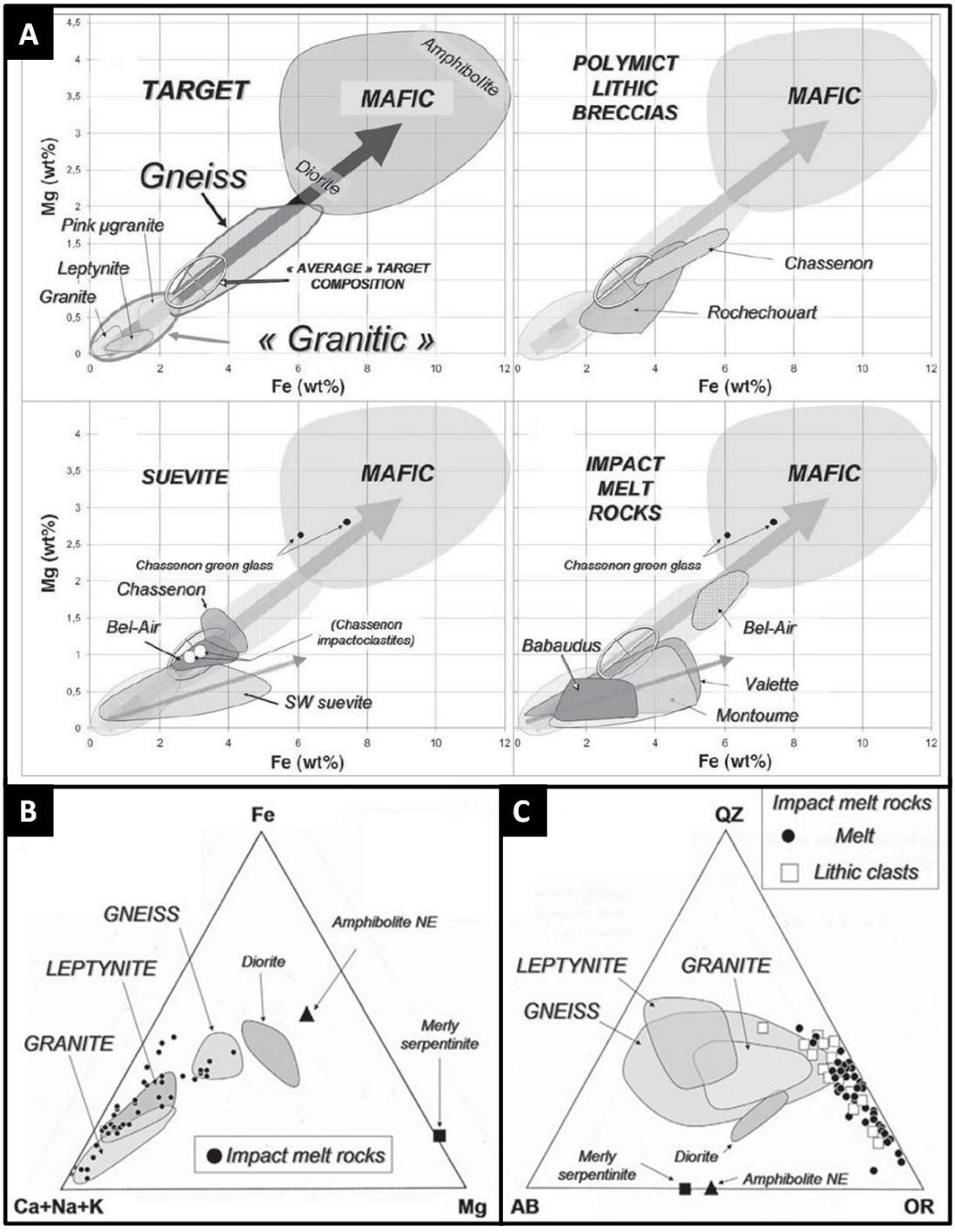

Figure 2-7: (A) Fe-Mg bulk chemical (XRF) data for Rochechouart impactites, with comparison to target rock geochemistry, (B) Fe:Mg:Ca+Na+K and (C) orthoclase:albite:quartz ternary diagrams, comparing bulk chemistry of the Rochechouart melt-bearing impactites to that of the unshocked target material. All Rochechouart impactites are enriched in K^+ relative to the target material, and therefore plot closer to the Or pole.

2.5 Lithologic descriptions

2.5.1 Methods: sample collection, petrography, SEM/EDX and Raman

Material was collected from the study site over the course of two field campaigns. Coated and non-coated polished thin sections and the surfaces of fractured samples were prepared for petrography, high-resolution SEM imaging, qualitative EDX analysis and Raman spectroscopy at the University of Glasgow at the Imaging Spectroscopy and Analysis Center. Following detailed petrographical and mineralogical characterization isotopic analysis of carbonate and sulphide minerals was performed at the Scottish Universities Environmental Research Center in East Kilbride.

2.5.1.1 Sample collection and return

Two field campaigns, one in October 2013 and the second in August 2014, were undertaken in order to determine field relationships and collect material with permission from the Reserve Naturel de Rochechouart-Chassenon and with the guidance and assistance of Dr. Philippe Lambert, Dr. Paula Lindgren and Prof. Martin Lee.

A suite of hand samples representing the main impactite lithologies was collected as well as unshocked basement material within the structure and marine carbonates representing the Mesozoic sea at the time of the impact outside the structure (Figure 2-8; Table 2-2).

Samples were stored in plastic bags and coordinates were recorded at outcrops and collection sites. Material was either returned to Glasgow by the author or shipped by the reserve at a later date (marked with * in Table 2-2).

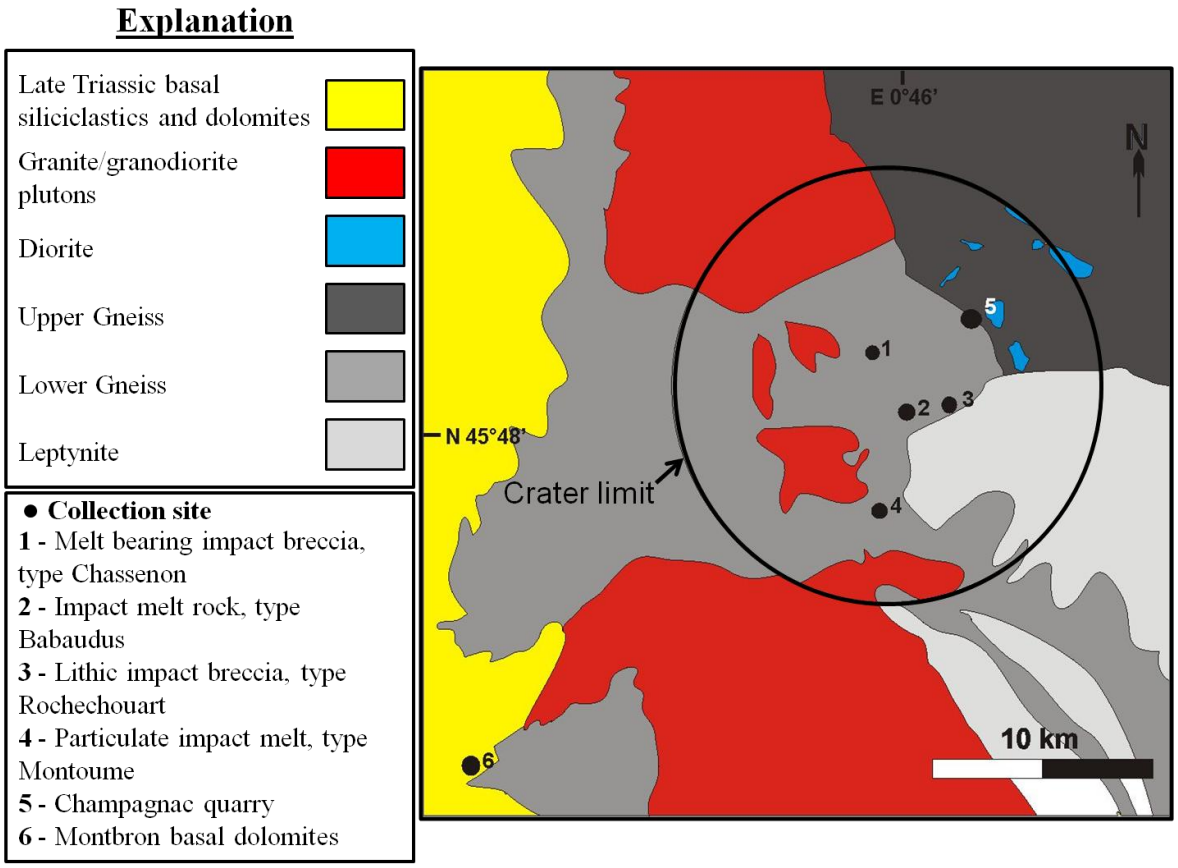

Figure 2-8: Simplified geologic map of Rochechouart target rocks and sampling localities, modified after Lambert (2010) and BRGM map numbers 686 (La Rochefoucauld) and 687 (Rochechouart).

Table 2-2: Summary of material collected during the 2013 and 2014 field seasons in the Rochechouart impact structure.

Rock type		Location	Season
Impactites	Impact melt rock, type Babaudus	Near central area of Valette, and Reserve archive	2013
	Particulate impact melt rock, type Montoume	Montoume quarry, outside Montoume village	2013
	Melt-poor suevite, type Chassenon* and impactoclastite sub-unit	Chassenon quarry	2013
	Polymict lithic breccia, type Rochechouart*	Rochechouart village, base of Chateau	2013
	Monomict lithic breccia, type Champagnac	Champagnac quarry	2013 and 2014
	Autochthonous impactite	Champagnac quarry	2013 and 2014
	Polymict melt-bearing breccia	Champagnac quarry	2014

	dike		
Basement	Champagnac diorite/granodiorite	Champagnac quarry	2013 and 2014
	Upper Gneiss	Champagnac quarry	2013

Note: Not all basement lithologies could be sampled during this study.

2.5.1.2 Petrography, SEM, EDX and Raman analysis

Thirty-three 30 µm-thick polished thin sections (Table 2-3) were prepared from nine representative lithologies (Table 2-2) for transmitted and reflected light petrographic studies.

An Olympus DP25 5-megapixel microscope camera attached to an Olympus BX41 laboratory microscope coupled with Cell^B FIVE version 5.0.1233 image processing software was used for transmitted and reflected light microscopy and image capture.

Image exposure times ranged from 30 ms to 5 seconds in polarized, plane polarized (XPL) and reflected light.

Table 2-3: List of thin sections

Rock type	**ID**	**Rock type**	**ID**	**Rock type**	**ID**
Impact melt rock	M-B-1	Polymict lithic breccia	L-R-1	Autochthonous	CA-1
	M-B-2		L-R-3	Unknown	CU-1
	M-B-3		L-R-4		CU-2
Melt-bearing breccia	S-C-1		L-R-5		CU-3
	S-C-2	Particulate melt	PM-1	Champagnac dike	CP-1
	S-C-3		PM-2		CP-2
	S-C-5		PM-3		CP-3
	S-C-6		PM-4	Basement	BT-1
	S-C-7		PM-5		BT-2
	F-C-1		PM-6		BT-3
				Parautochthonous	CB-1
					CB-2
					CB-3

SEM and EDX analyses were performed using a Carl Zeiss Sigma variable pressure analytical SEM with Smart SEM version 5.05 software, and an FEI Quanta 200F

environmental SEM with EDAX Genesis version 6.35 software. For secondary electron imaging (SE) and angle selective backscattered electron imaging (AsB), polished thin sections were coated with 10 nm of carbon using an Agar Scientific automatic SEM carbon coater. Five samples of four lithologies were broken to approximately 1cm x 1cm x 1cm dimensions, coated with 10 nm of Au using an Agar Scientific automatic sputter coater and grounded using Agar Scientific silver paint. Energy dispersive X-ray (EDX) mapping and qualitative analysis was performed using AzTec 2.2 SP1 software on the carbon-coated polished thin sections. Maps were acquired at 1024 x 768 resolution with pixel dwell times ranging from 25µs to 40µs for acquisition periods ranging from 5 minutes to 5 hours.

EDX analyses were performed in high-vacuum (2.6×10^{-6} torr) at a working distance of approximately 8.5 to 11.5mm, with a beam current of 20.00 keV and aperture size ranging from 30µm to 60 µm.

Table 2-4: List of Au-coated fractured samples

Description	ID
Vesicular impact melt rock	2013-1-F
Champagnac melt-bearing dike	2014-1-F
Montbron Limestone	2014-4-F
Champagnac monomict breccia, clast with cement	2014-13-Fa
Champagnac monomict breccia, clast	2014-13-Fb

A Renishaw InVia Raman microscope equipped with 514nm and 785nm laser sources and WiRE version 4.1 software was used to investigate minerals in non-coated polished thin sections.

Static and extended scans were performed at exposure times ranging from 1 to 5 seconds, at laser power ranging from 20% to 100% and accumulation times of 1 to 20 seconds. Spectra were checked against the Renishaw inorganic library (2010) and the RRUFF Raman spectra database (LaFuente et al., 2015).

2.5.2 Basement and Target material

Basement material is composed of a variety of granitic crystalline metamorphic and plutonics of the Variscan orogeny (Faure et al., 2009; Lambert, 2010). Aquitaine carbonate sequences directly overlying crystalline basement as little as 5km outside the currently accepted impact diameter, which overlap in age with the impact, are arguably a component of the target (see section 2.3.2.4); they may therefore have been incorporated into the

impactites (Sapers et al., 2009).

Table 2-5: Major target rock types in the Rochechouart field area

Rock Type	Age (Ma)	Origin and context
Late Triassic/Early Jurassic marine carbonates, "Montbron limestones"	210 to 190	Hettangian/Sinemurian/Infra-Toarcian basal series, siliciclastics and dolomites (Boiron et al., 2002). These units lack fossils, concomitant with the late Triassic marine extinction, and their exact age is poorly constrained. The Bureau de Recherches Géologiques et Minières (BRGM) maps them as Lias, Hettangian-Sinemurian (L1-4), or Late Triassic-Early Jurassic basal siliciclastics and dolomites.
Dikes - Microgranite - Microdiorite	300	Last stage of Variscan metamorphism, these formed as a result of the Variscan belt collapse, and are oriented N-S, the same as local wrench faults (Lambert 2010). Microgranites are more prevalent in the eastern area of the structure, and micrograbbros/microdiorites in the west.
Granite and diorite plutonics	325 to 300	Large plutons are found mostly in the western region of the structure cross-cutting metamorphic units. There are smaller bodies of diorite found in the eastern area near Champagnac. All plutonics are related to exhumation during the late stages of the Variscan orogeny (Lambert, 1977, 2010).
Upper Gneiss	385 to 350	Upper slab of continental crust, similar protolith to Lower Gneiss unit, but slightly more mafic. Locally contains blocks or lenses of amphibolite, which derives from retrograde metamorphosed eclogite facies rocks which did not melt.
Lower Gneiss	385 to 350	Orthogneiss, or leptynites, derived from metamorphosed pre-Variscan alkaline granitoid intrusions of Early Ordovician and Early Cambrian (550 to 480 Ma) age. Unit as a whole is interpreted as the Paleozoic remnants of the Northern Gondwana margin (Faure et al., 2009; Le Carlier de Veslud et al, 2013).

2.5.2.1 Upper Gneiss and Lower Gneiss

Rock type: Variscan basement, amphibolite to granulite facies ortho- and paragneiss.

Hand sample description: The Lower Gneiss unit is a mixture of grey to dark grey,

plagioclase-rich paragneiss (sedimentary origin) and lighter colored orthogneiss, also known as leptynite. The Lower Gneiss is composed primarily of metagreywackes, metapelites and metarhyolites (Faure et al., 2009; Lambert, 2010; Le Carlier de Veslud et al., 2013). Serpentinized peridotites, also known as the Merlis serpentinites, may be found as local intercalations in the southern area of the structure (Lambert, 2010). The Upper Gneiss is a dark grey-blue to light grey, well indurated, fine-crystalline, amphibolite facies paragneiss with localized intercalations of lighter orthogneiss, known as the "leptynites-amphibolite sequence". A biotite-garnet-staurolite metamorphic assemblage is observed by some authors, characteristic of amphibolite facies Barrovian metamorphism of a majority pelitic protolith (Faure et al., 2009).

Composition: Upper gneiss: Anhedral quartz, albite and potassically altered K-feldspar with minor muscovite replacement; euhedral, Fe-rich chlorite, also found partially replacing biotite and minor sub-mm thick veins of pyrite; trace molybdenite + calcite + Fe-Ti oxides oriented along fabric planes and filling veins, and minor accessory up to 0.1mm apatite and zircon (Figures 2-9, 2-10 and 2-11).

Table 2-6: XRF data (wt%) for crystalline metamorphic basement in Rochechouart, from Lambert (2010).

	SiO_2	Al_2O_3	Fe_2O_3	MgO	CaO	Na_2O_3	K_2O	TiO_2	P_2O_5
Gneiss	66.19	16.21	5.79	2.76	1.84	2.94	3.28	0.82	0.16
Amphibolite	44.50	18.68	12.82	8.71	9.55	1.95	1.88	1.75	0.16
Leptynite	75.18	13.58	2.09	0.56	1.28	3.56	3.56	0.03	0.03

Coordinates of sampling area and outcrop: Upper Gneiss: 45° 51' 15.15" N, 0° 49'52.91" E**.** Outcrops can be found in the lower levels of the active Champagnac quarry. The Lower Gneiss unit was not collected during this study.

Comments and identification techniques: The Upper Gneiss and Lower Gneiss have similar protoliths; both derive from a mixture of pelitic material and acidic lavas and tuffs, intruded by alkaline granitoids during the Cambrian to early Ordovician (Faure et al., 2009; Lambert 2010). The Upper Gneiss has a slightly more mafic origin, consisting of a mixture of basalt, gabbro and locally ultramafic material. The Upper Gneiss forms the overlying, upper part of the subducted continental Gondwana margin, and may also locally reach eclogite-granulite facies. The Lower Gneiss is the dominant rock type in Rochechouart, while the Upper Gneiss is found only in the north-northeastern area of the structure, most notably near the area of Champagnac (Lambert, 2010).

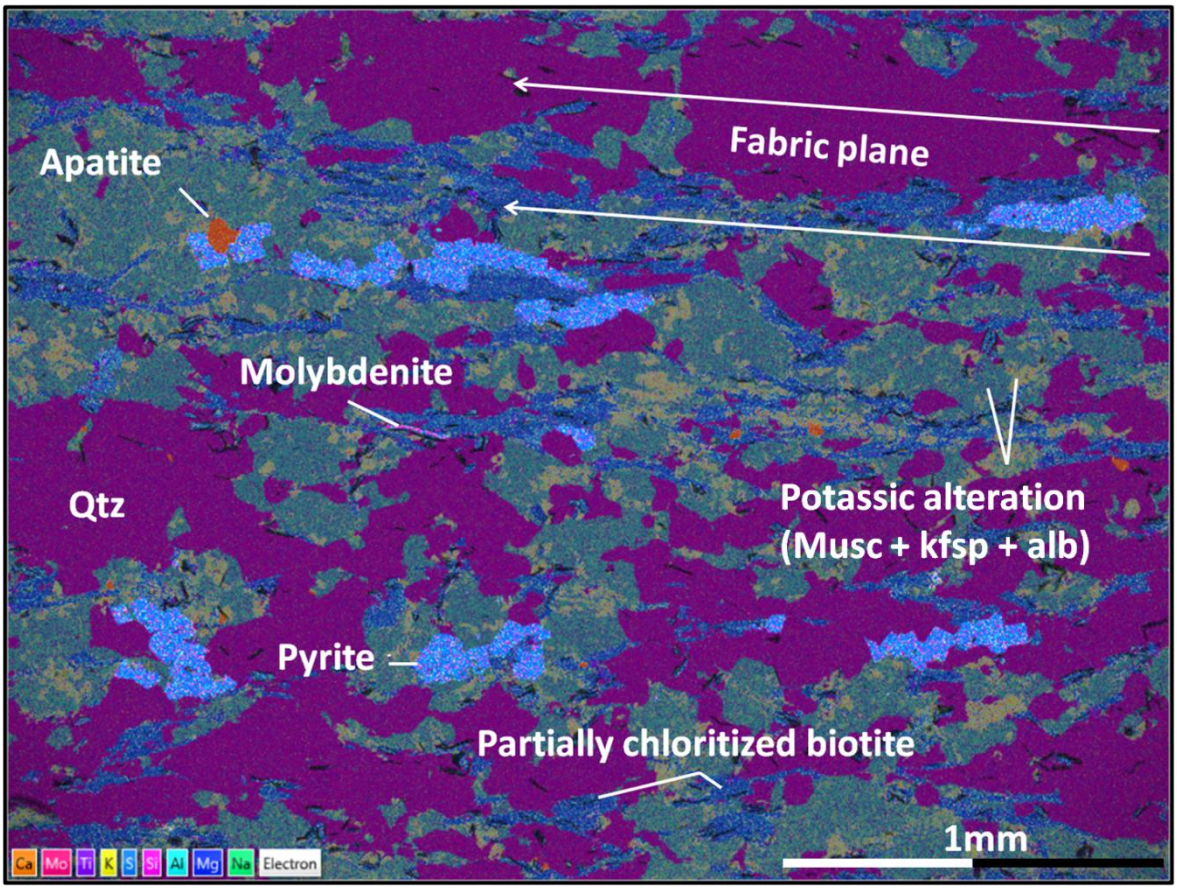

Figure 2-9: Element map (EDS) of the Upper Gneiss, showing Na and K-feldspar partially altered to muscovite (potassic alteration), partially to completely chloritized biotite, anhedral quartz, pyrite, and minor apatite and molybdenite. All basement lithologies in Rochechouart display some level of alteration attributed to fluid circulation during the main metamorphic event. Section BT-U-6, hand sample B1.

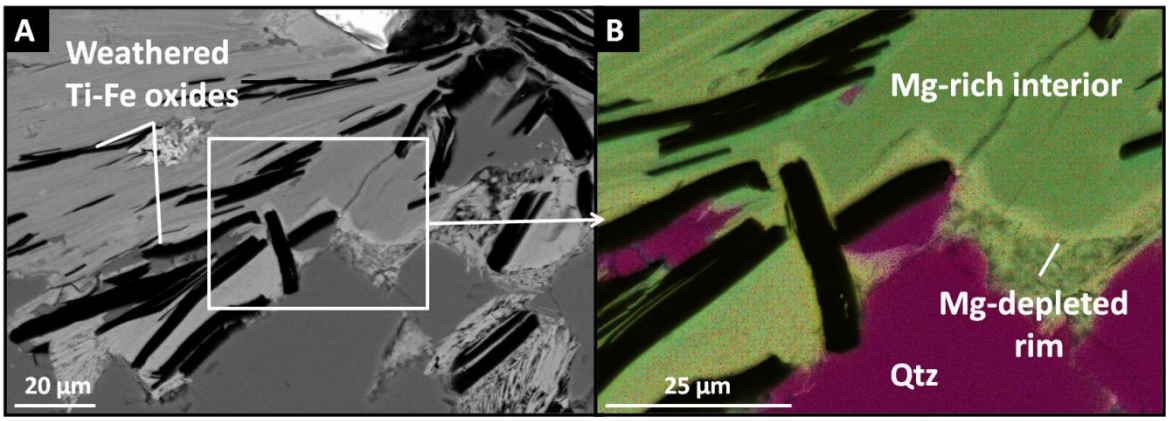

Figure 2-10: (A) SEM image and element map (B) of Fe-Mg phyllosilicates, exhibiting varying levels of biotite altered to chlorite within the Upper Gneiss. Phyllosilicates contain rectangular vugs, which are interpreted as relict crystals of Fe-Ti oxides and are predominantly associated with sericite and chlorite-biotite. The outer rims of the phyllosilicates are also Fe-rich and Mg depleted.

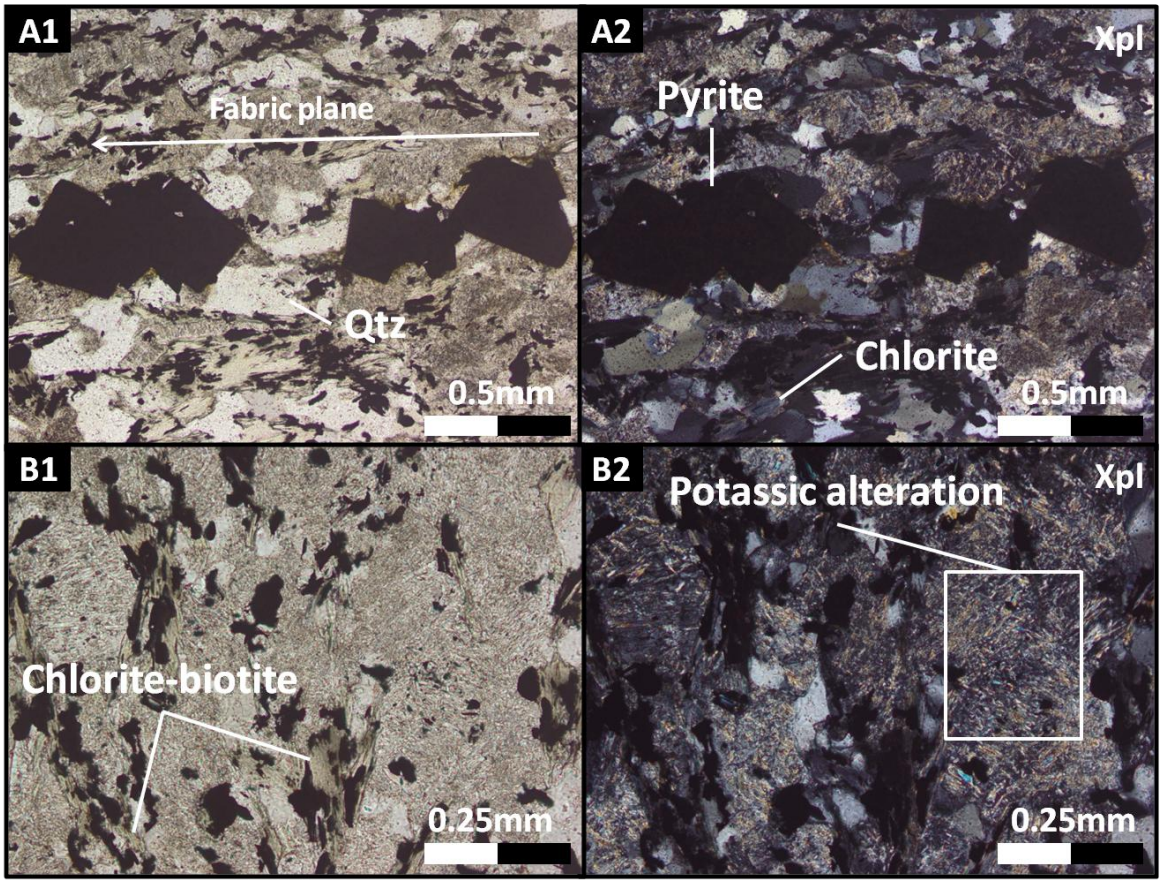

Figure 2-11: (A1 and B1) Optical microscope images of Upper Gneiss thin section in plane polarized light and (A2 and B2) crossed polars. Opaque areas, where not labeled, are a mixture of Ti-Fe oxides, and relict oxide crystals which have been weathered, as seen in Figure 2-10 A and B. The "Berlin blue" color observed in chloritized biotite is characteristic of high-Fe chlorite.

2.5.2.2 Champagnac site diorite; Chabanais granodiorite

Rock type: Variscan basement, plutonic to sub-plutonic diorite/granodiorite.

Hand sample description: Massive, well-indurated, aphanitic to porphyritic/phaneritic, light grey (fresh) to orange-grey (weathered) diorite.

Composition: Phaneritic, anhedral grey quartz; phaneritic, light pink to red k-feldspar replacing micro-scale albite (potassic alteration); euhedral, phaneritic, dark grey-green biotite and chlorite; aphanitic, anhedral, light grey to white "dusty" at hand scale, white mica (potassic alteration); accessory euhedral, 0.5 to 1mm pyrite and dolomite coating fracture surfaces (Figure 2-12, B1 and B2), and minor, mm-size veins of dolomite; 1 to 2mm relict/skeletal sphene crystals replaced by rutile and pyrite; minor apatite and zircon.

Table 2-7: XRF data (wt%) for diorite, from Lambert (2010).

SiO_2	Al_2O_3	Fe_2O_3	MgO	CaO	Na_2O_3	K_2O	TiO_2	P_2O_5
59.37	18.57	6.86	4.08	1.79	3.01	5.23	0.83	0.27

Coordinates of sampling area and outcrop: 45° 51’ 15.15” N, 0° 49’52.91” E; Found at lowest level of Champagnac quarry, material is generally fresh and can be collected from rubble piles or quarry walls.

Comments and identification techniques: Material has been altered by moderate temperature hydrothermal activity; Ca-plagioclase has been completely sericitized and calcitized (Lambert, 2010), and feldspars are partially to completely replaced by muscovite (potassic alteration) (Figure 2-12, A1 and A2). Evidence for fluid circulation and infiltration inwards from fracture surfaces can be seen within the rock, characterized by alteration “fronts” of bright red-orange K-feldspar. Myrmekite is common, and in some places feldspar has been naturally etched and weathered, with only xenomorphic “worm” shaped quartz remaining (Chapter 3, Section 3.3.1.2). Euhedral, 1-2mm diamond shaped relict crystals of sphene are common (Figure 2-12, C and D), as well as large 1-3mm crystals of biotite at various stages of chloritization.

There are other larger igneous plutonic bodies in the area; the Cherronac and Chabanais intrusions in the western area of the structure and two smaller bodies, the Bouloux and St. Gervais, between (Figure 2-14). The Chabanais intrusion in the north, which is considered the main body from which the smaller outcrops of diorite originate, is a calc-alkaline granodiorite with quartz, K-feldspar, plagioclase and biotite, and the Cherronac to the south, is a light colored leucogranite, bearing orthoclase, muscovite and biotite, with the two smaller regional bodies in the structure a mixture of the two larger plutons (Lambert, 2010).

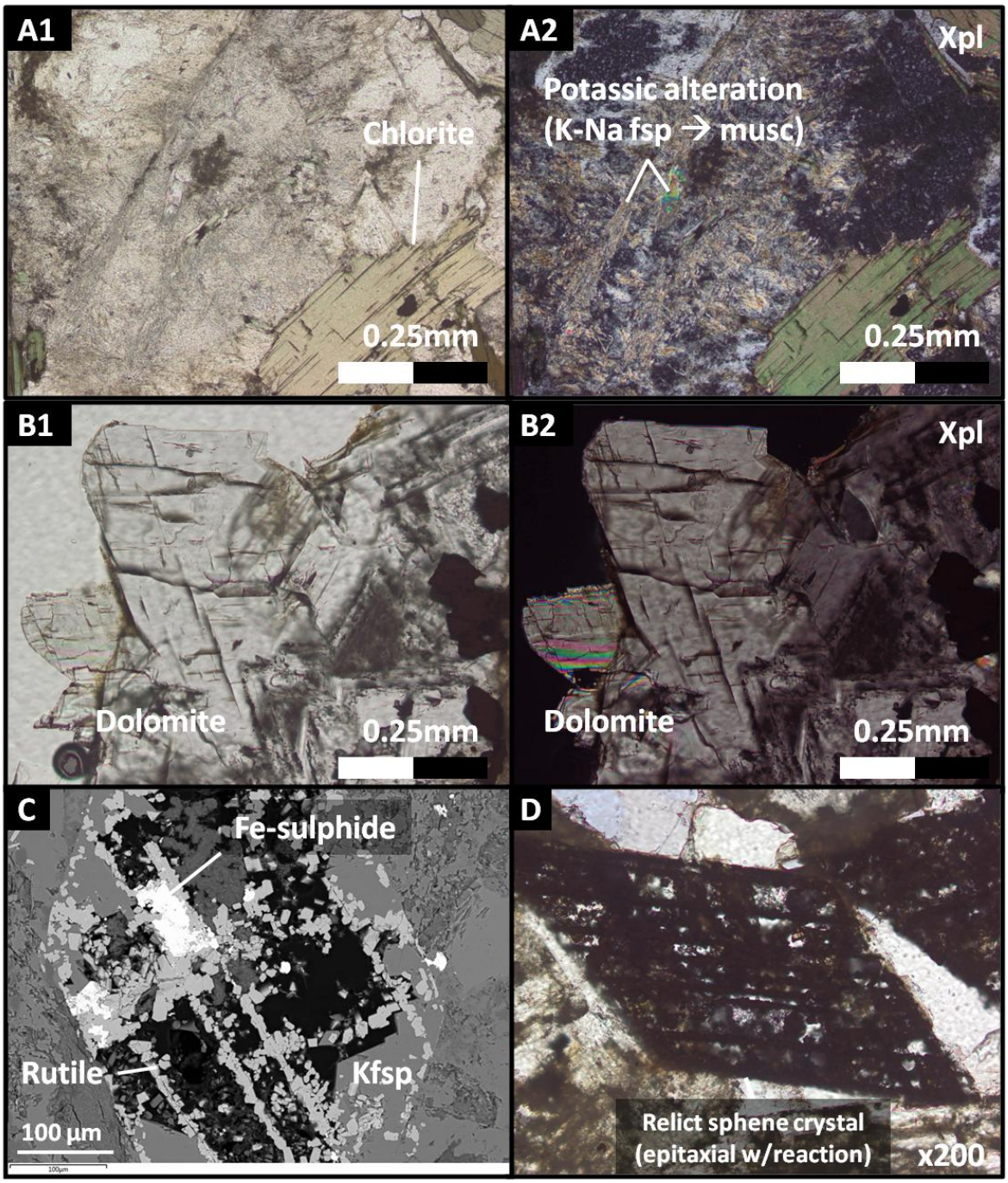

Figure 2-12: (A1 to B2, D) Transmitted light microscope images and SEM AsB image of various minerals, both primary and secondary, in Champagnac diorite. The majority of the primary Na-K feldspars, albite and orthoclase, have been partially to completely altered to muscovite (A1, A2 and Figure 2-6 A, B), and all Ca-plagioclase has been completely calcitized or sericitized, as also noted by Lambert, (2010). Large, 1-2mm euhedral crystals of biotite can also be observed; in some cases they have been either partially or completely replaced by chlorite, a common feature of basement rocks in the Rochechouart area (A1, A2). Secondary dolomite is also observed coating fracture surfaces (B1, B2). Relict diamond-shaped sphene crystals are observed, which have been subjected to epitaxial mineral growth with reaction to rutile and pyrite (C and D).

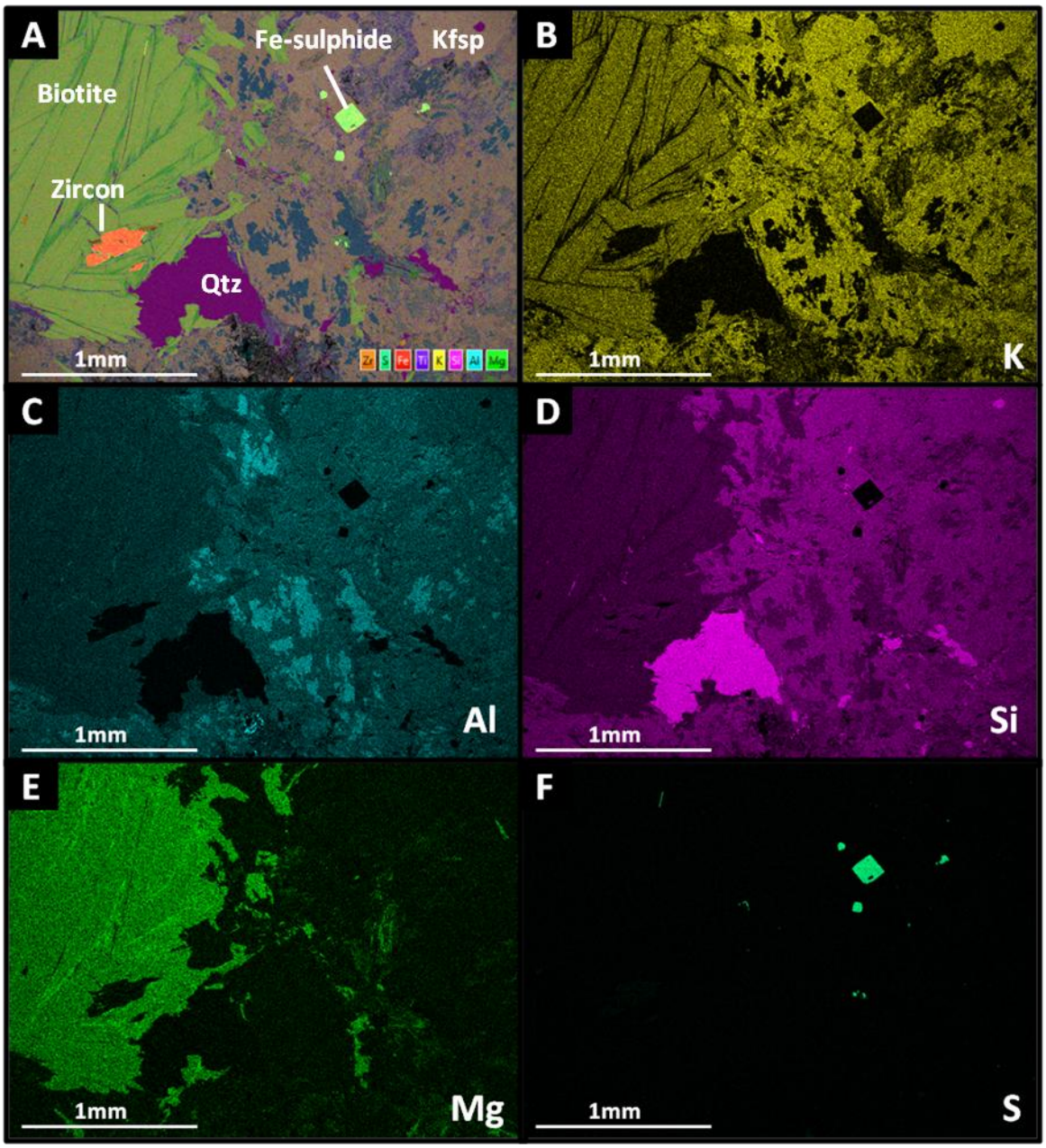

Figure 2-13: Element maps of Champagnac diorite. Overall, the diorite has been enriched in potassium (B), and depleted in calcium (not shown), except for minor carbonates coating fracture surfaces and apatites; this chemical profile is consistent with potassic alteration. Feldspars are partially or completely replaced by muscovite (B, C, D and Figure 2-11 A2). Biotite has often been altered to chlorite (B and E). Chloritization of mafic minerals such as biotite releases K and Mg, which may be a contributing source for the K-metasomatism observed in all Rochechouart rock types, both basement and impactite (Chapter 3). Xenomorphic quartz and zircon can also be observed (A, D), as well as small, euhedral pyrite crystals (F).

2.5.2.3 Microgranite and microgabbro dikes

Rock type: Basement, late stage Variscan igneous intrusions

Hand sample description: Microgranite "pink" dikes and more mafic, gabbroic "black"

dikes, both containing 1mm to 1cm phenocrysts in aphanitic fine-crystalline groundmass (Lambert 2010).

Composition: Orthoclase, albite, quartz, plagioclase, pyroxene, amphibole, rare olivine.

Table 2-8: XRF data (wt%) for black microgabbro dikes, from Lambert (2010)*.

SiO_2	Al_2O_3	Fe_2O_3	MgO	CaO	Na_2O_3	K_2O	TiO_2	P_2O_5
60.47	16.77	7.74	5.97	1.45	1.95	4.59	1.00	0.11

* = no XRF data for microgranite.

Coordinates of sampling area and outcrop: Coordinates: This lithology was not a component of this study, but can be collected from the lower levels of Champagnac quarry and elsewhere in the Rochechouart area (Figure 2-14).

Comments and identification techniques*:* Microgranite dikes are more prevalent in the eastern area of the structure, whereas the more mafic microgabbros and microdiorites are more common in the west (Lambert, 2010) (Figure 2-14). Dikes are oriented N-S, same as wrench faults in the area. No material was collected for this study.

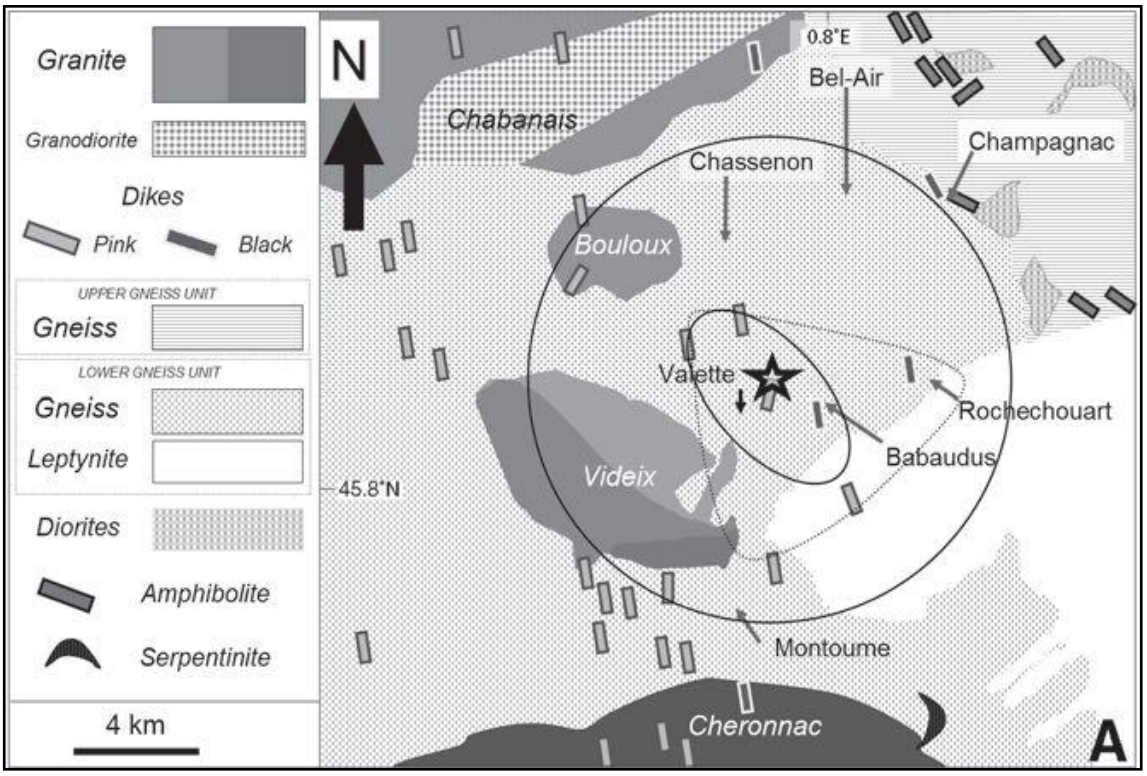

Figure 2-14: Simplified geologic map of the Rochechouart field area basement, showing N-S oriented microgranite and microgabbro dikes (Lambert, 2010).

2.5.2.4 Late Triassic/Early Jurassic basal siliciclastics and dolomites; "Montbron limestone"

Rock type: Aquitaine Lias or Hettangian to Sinemurian dolomitized limestones/platform carbonates.

Hand sample description: Light (fresh) to dark grey (weathered), massive, well indurated, fine crystalline, non-laminated/non-bedded dolomitized limestones (Figure 2-15 C). This unit is generally non-fossiliferous; it may contain very rare microfossils (Figure 2-15, A).

Composition: Fine crystalline (0.01mm) euhedral dolomite, calcite and quartz with rare Fe-sulphides (Figure 2-15 B).

Coordinates of sampling area and outcrop: 45° 40' 6" N, 0° 30' 37" E; Outcrop on main road at eastern entrance to the village of Montbron, covered in moderate to heavy vegetation (Figure 2-16 A and B).

Comments and identification techniques: Can be found outside structure from 5km west of the crater diameter, overlying crystalline basement. The most common sampling localities are in the villages of Montbron and Mazieres (Figure 2-16 A and B). This unit part of the basal siliciclastic series directly overlying Variscan crystalline basement. The sub-unit directly above this, belonging also to the Lias, and also a massive marine carbonate, contains large (up to 6cm) euhedral geodic calcite and dolomite (Fourcade et al., 2002) and can be collected along the same road cut as the massive, non-bedded limestone. The exact dating of this unit is debated, as it lacks fossils; however, the late Triassic is marked by a global marine extinction, and is therefore generally mapped as late Triassic.

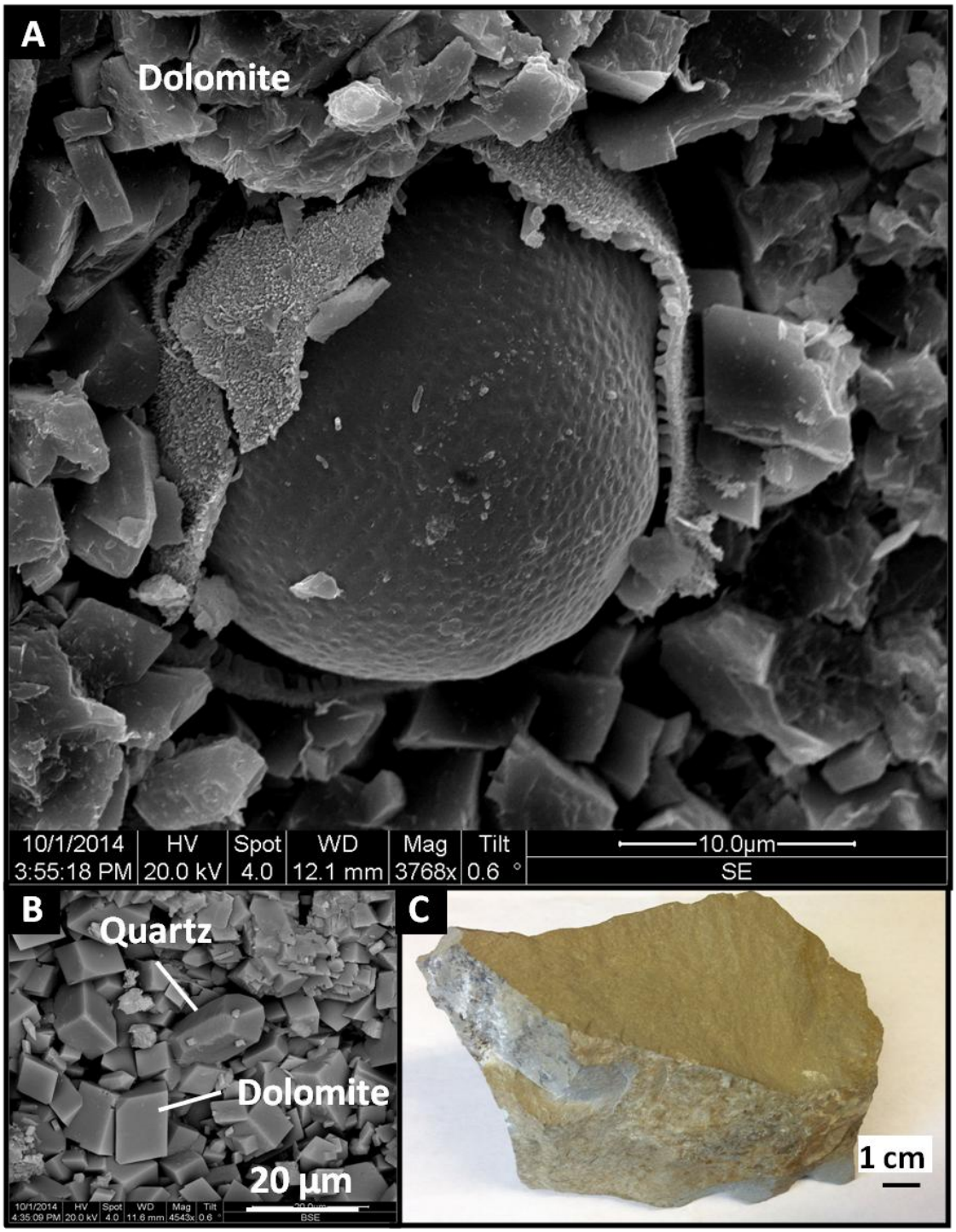

Figure 2-15: (A) Secondary electron image of unknown microfossil found in the Montbron basal carbonates, (B) secondary electron image of Montbron carbonates, showing single crystal of quartz and (C) hand sample taken from road cut outside the village of Montbron. The lack of fossils present in this limestone support the dating of this unit as very late Triassic, as there was a global marine extinction event around 200 Ma resulting from CAMP volcanism and the increase of atmospheric CO_2 (Gallia et al., 2005; Saltzman and Thomas, 2012).

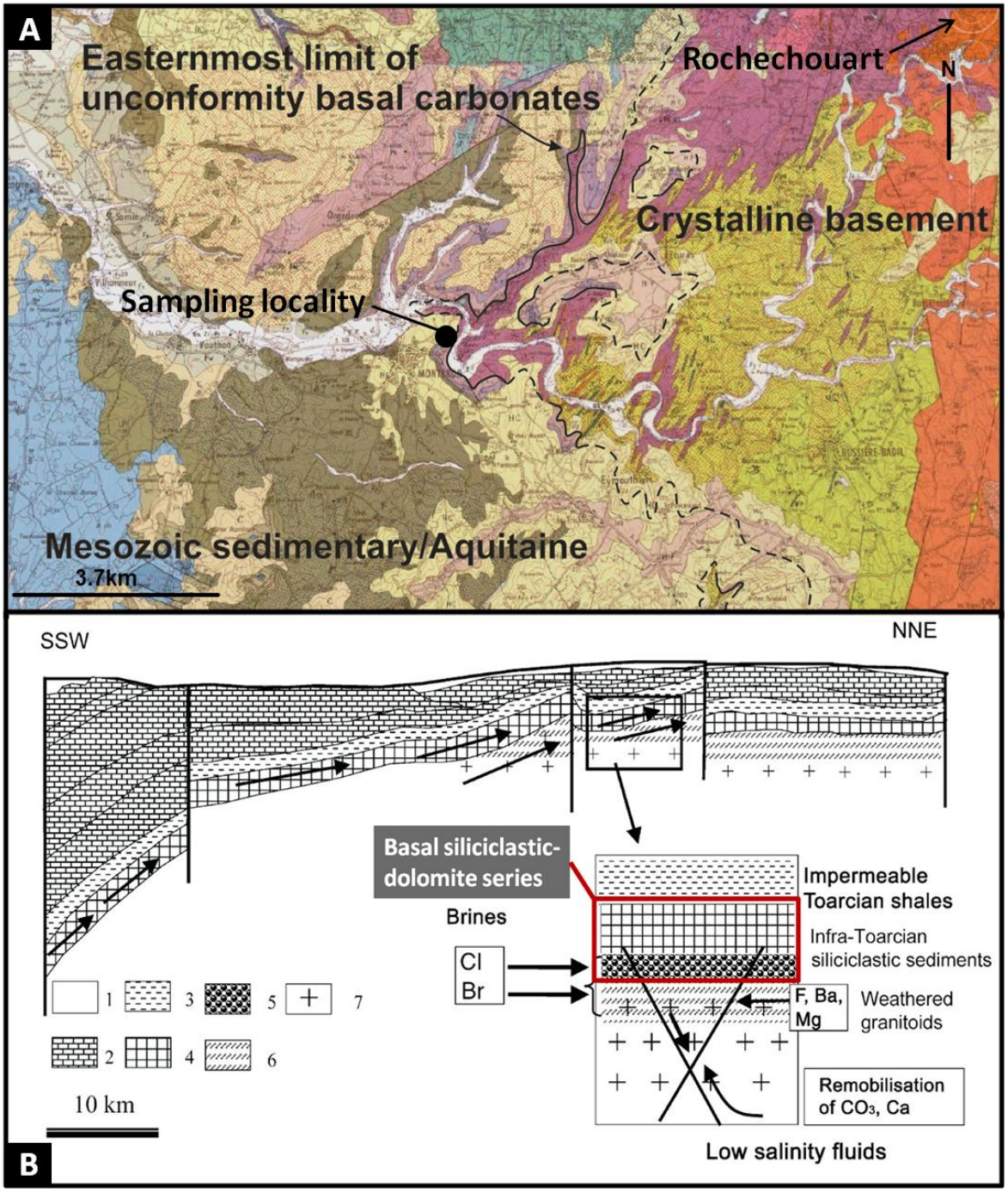

Figure 2-16: (A) Modified BRGM geologic map showing limit of Mesozoic Aquitaine unconformity carbonates and (B) schematic cross section through Aquitaine unconformity above the Charroux-Civray plutonic complex, 26km west of the Montbron sampling locality, modified after Boiron et al., 2002. Units 4 and 5 correspond to the basal Hettangian-Sinemurian siliciclastic-dolomite series overlying the Upper Gneiss and Cherronac granite from 5km outside the structure the west, use in this study.

2.5.3 Impactites

2.5.3.1 Shock-fractured basement; Autochthonous impactite

IUGS Impactite classification: Massive basement rocks; non-coherent, highly altered, basement granodiorite with cm-wide heavily mineralized shock fractures and post-impact veins. Locally may be considered "crackle breccia", where material has been separated by planes of fracture but does not show any major displacement or rotation.

IUGS Shock level: 0: fractured minerals; little to no shock observed

Shocked minerals: none

Description hand sample: Light grey-green (fresh) to brown-grey (weathered), phaneritic/medium to coarse crystalline, highly altered/sericitized, poorly indurated granodiorite.

Composition: Lithic material: Euhedral sub-mm chlorite, minor muscovite and paragonite as individual, larger crystals and as smaller, anhedral alteration products in feldspar minerals; anhedral albite with euhedral K-feldspar overgrowths and rims, and anhedral quartz, accessory apatite and zircon (Figures 2-18 and 19). **Mineralized fractures**: 0.5cm-thick euhedral, cubic and pyritahedron-shaped pyrite overgrown by minor euhedral, 2-3mm, orange-white dolomite rhombs (Figure 2-17 C and 2-18).

Major rock forming minerals in order of decreasing abundance (XRD, Sapers et al 2014): N/A

Bulk chemistry (XRF Lambert 2010): N/A

Coordinates and outcrop: 45° 51' 15.15" N, 0° 49'52.91" E; Champagnac quarry, Champagnac. Outcrops form ~5m steep cliffs in quarry terraces with no vegetation cover.

Comments and identification techniques: Weathered samples with heavy sulphide mineralization may be covered by dusty orange-brown Fe-oxides, commonly known as "gossan" in economic deposits. Pervasive fractures related to pre-impact Barrovian metamorphism and exhumation can also be found throughout the Central Massif, making autochthonous impact fractures arguably the most difficult impact product to identify in Rochechouart. Autochthonous material can only be identified as impact-related by it's context within the rest of the impactite deposits and outcrop, and by carefully establishing field relationships. Several fractures within larger blocks of basement within an established "shock zone" can be identified as impact origin (communication with Philippe Lambert).

There is also a later, much younger fluid event documented throughout the Central Massif – Aquitaine unconformity (Cathelineau et al., 2012). It is attributed to the infiltration of seawater into cooling fractures in granite and diorite plutons, to the north of

Rochechouart. This also must be considered as a potential source for the mineralization observed in some of these fractures. Carbon and oxygen isotope studies have been carried out to attempt to determine the provenance and relationship between the many mineralized fractures and veins found in the field area (Chapter 3).

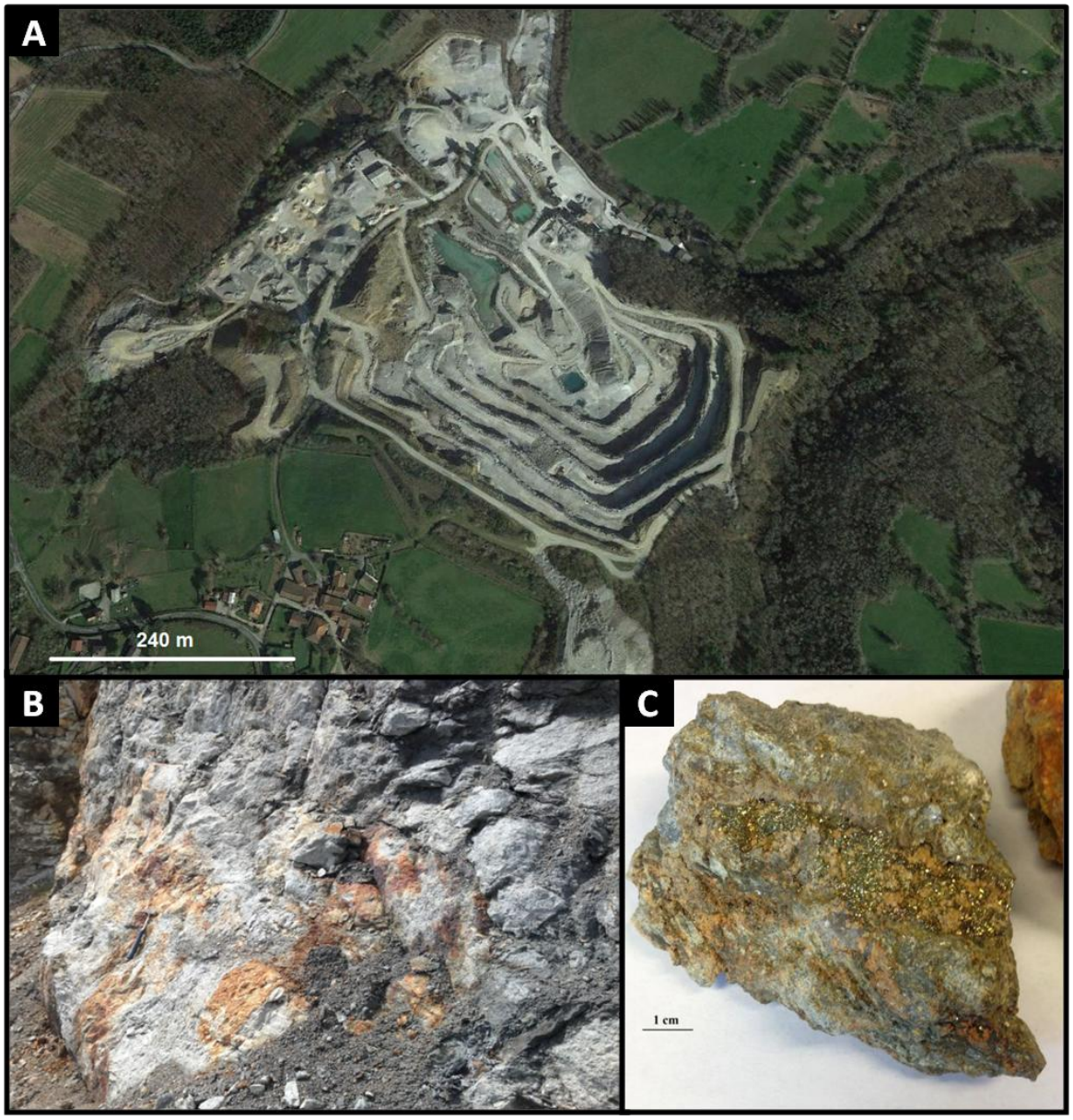

Figure 2-17: (A) Aerial photo of Champagnac quarry (Google Earth, 2014), which cuts directly through the transient crater floor, and showcases the complexities involved in impact processes and below the crater-basement interface. (B) Picture of autochthonous impactite outcrop in field area and (C) hand sample of Fe-sulphide mineralization coating autochthonous impact fracture. Dusty orange-brown coating observed at the macroscale (outcrop) and mesoscale (hand sample) is due to oxidation of Fe-sulphides, or "gossan", commonly observed economic iron ore deposits.

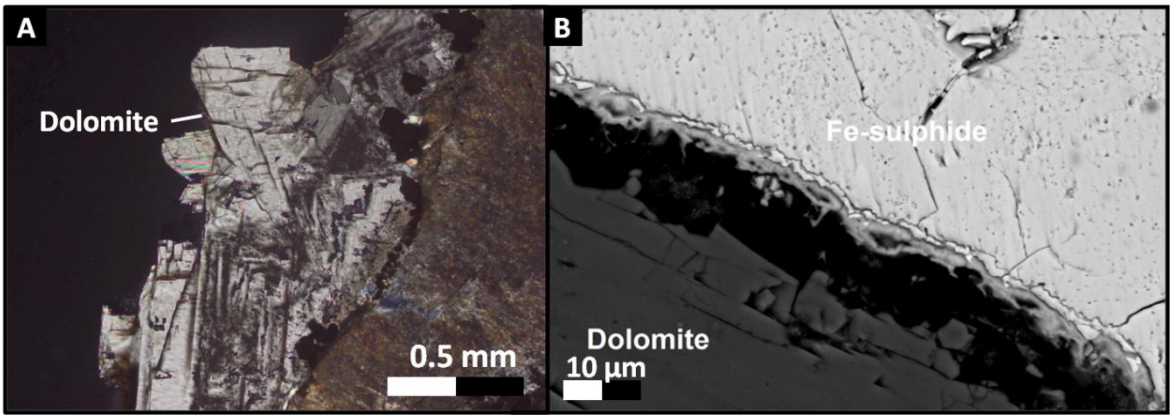

Figure 2-18: (A) Transmitted light microscope image (XPL) of carbonate mineralized fracture of unknown origin in highly altered basement diorite and (B) SEM image of a sulphide-carbonate mineralized autochthonous impact fracture. Distinguishing the two fracture types is difficult without radiometric dating studies, and currently can only be identified by their field relationships and context within the rest of the crater deposits.

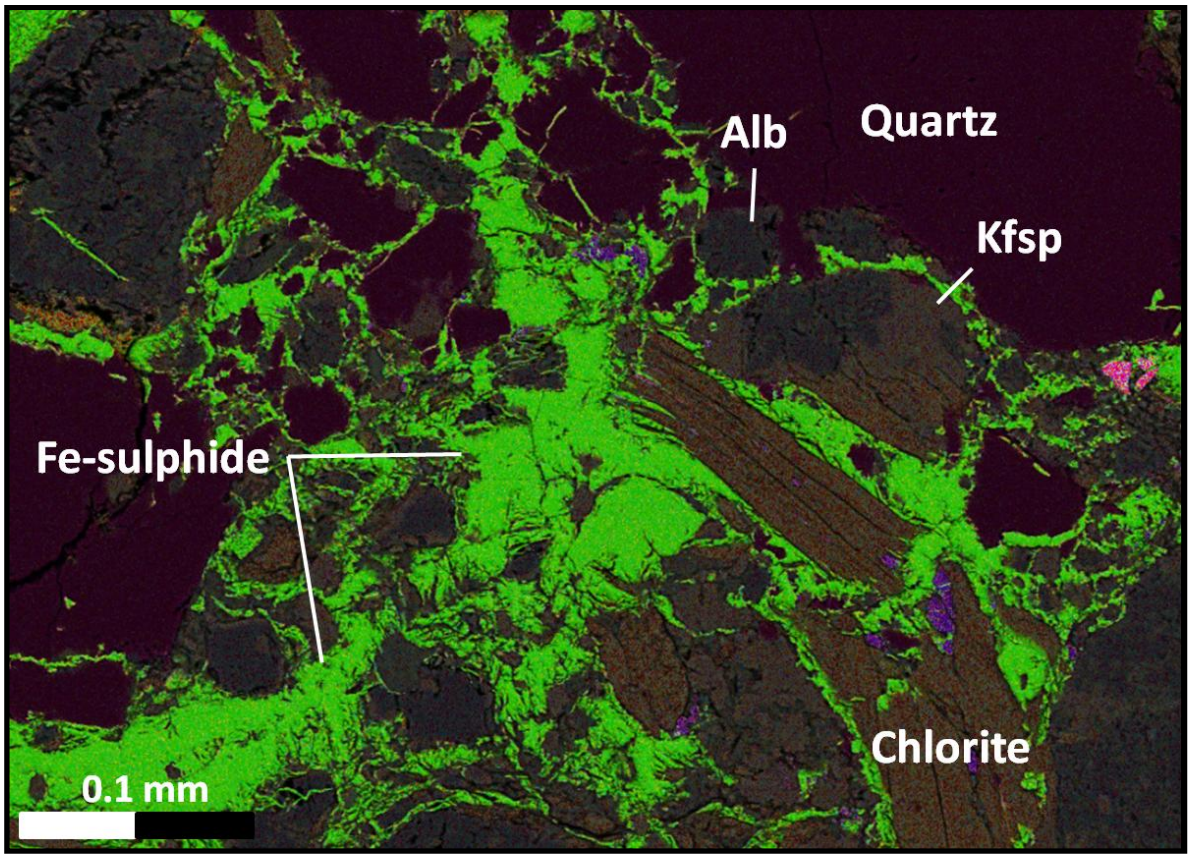

Figure 2-19: EDS layered element map of autochthonous fractured material showing heavy sulphide mineralization (bright green), chlorite and and K-feldspar replacing albite due to potassic alteration. Alb = albite, Kfsp = K-feldspar.

2.5.3.2 Monomict lithic impact breccia, type Champagnac

IUGS Impactite classification: Monomict lithic impact breccia.

IUGS shock level: 0 to 1a: little to no shock observed.

Shocked minerals: Rare to none; potential ballen silica and kink bands.

Description hand sample: Angular to sub-angular, clast supported, orthobreccia (clast supported) para- and orthogneiss clasts within a fine-clastic matrix of similar material which has been locally replaced by secondary carbonate-silicate-sulphide cement (Figure 2-21, A, B and C and Figure 2-22). Well-indurated, dark grey-green to blue-green (fresh) to yellow-brown/grey (weathered), angular, 1 to 4cm clasts of basement orthogneiss and paragneiss of the Upper Gneiss unit, poorly to moderately sorted, locally very porous monomict breccia. Locally, some clasts may display dark-grey high-temperature reaction rims and weathered clay interiors with small specks of black-brown biotite along fabric planes throughout.

Composition: **Clasts:** potassically altered 1 to 4cm ortho and paragneiss clasts of the Upper Gneiss unit; ≤ 500 micron crystals of biotite, high Fe chlorite and clays (Figure 2-23), ≤ 250 micron xenomorphic quartz, anhedral albite at various stages of potassic alteration to orthoclase, overgrown and replaced by euhedral ≤ 250 micron K-feldspar and muscovite are aligned on gneiss fabric plan. Clasts are overgrown by 100 to 125 µm thick layer of euhedral k-feldspar, adularia with minor anhedral apatite (Figure 2-21, A, B). Minor accessory dolomite, pyrite, Fe-Ti oxides, apatite and zircon and garnets are found throughout lithic clasts. Matrix: Lithic clasts to matrix ratio varies, but fine grained clastic matrix generally constitutes no greater than 20% of the rock, leaving around 80% of lithic breccia clasts; clastic/lithic <1mm matrix 10%. Locally, the matrix can be completely replaced by coarse-crystalline, pale pink (fresh) to pink-orange (weathered) 1 to 5mm rhombohedral Fe-Ca-Mg carbonates (dolomite + calcite + siderite + ankerite) and minor amounts of euhedral, coarse crystalline 3 to 5mm pyrite.

Major rock forming minerals in order of decreasing abundance (XRD, Sapers et al, 2014): N/A

Bulk Chemistry (XRF Lambert, 2010):

Table 2-9*: XRF data (wt%) for monomict lithic leptynite breccia, from Lambert (2010).

SiO_2	Al_2O_3	Fe_2O_3	MgO	CaO	Na_2O_3	K_2O	TiO_2	P_2O_5
75.69	13.82	1.26	0.32	0.19	2.98	5.77	0.11	n/a

* Data from monomict leptynites breccia collected from drill core 10 km south of the structure's center.

Coordinates and outcrop: 45° 51’ 15.15” N, 0° 49’52.91” E; the most accessible outcrop is located in Champagnac quarry, Champagnac. This lithology is non-continuous and forms irregular bodies and lenses in the field area at and below the transient crater floor (Figure 2-20). The maximum thickness of this unit is 90 to 100 meters, underlying allochthonous material.

Comments and identification techniques: Monomict lithic impact breccias are notoriously difficult to distinguish from normal endogenic tectonic breccias, as they usually contain very little to no shock indicators (see section x in chapter 1). In Rochechouart, monomict material is found up to 15km west of the center and may rarely be observed to be cross cut by polymict lithic and melt-bearing dikes. There are multiple generations of hydrothermal alteration recorded in this rock type; this study has found secondary mineral assemblages representative of both potassic alteration (K-feldspar + biotite + muscovite + sericite, K-rich fluids) and propylitic alteration (chlorite + pyrite + Ti-Fe oxides, Fe-Mg rich fluids). Reaction rims on clasts indicate proximity to an overlying or adjacent heat source. Monomict breccias from Champagnac contain the heaviest hydrothermal alteration and mineralization of all Rochechouart impactites in this study, likely due to their locally high porosity and localized fracturing facilitating hydrothermal fluid flow.

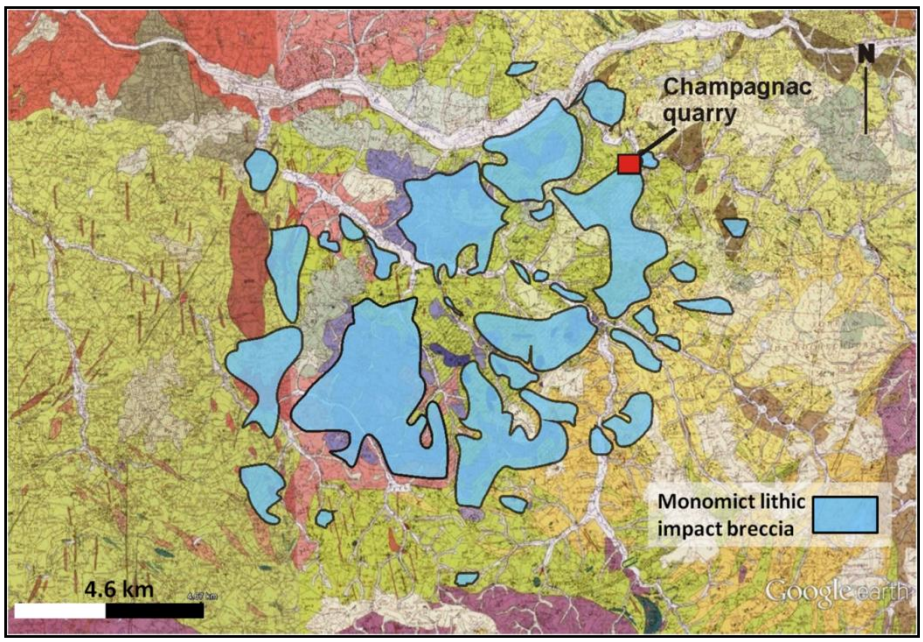

Figure 2-20: Simplified map of monomict lithic breccia distribution in Rochechouart (after Lambert, 2010) (underlay base map BRGM; Google Earth, 2014).

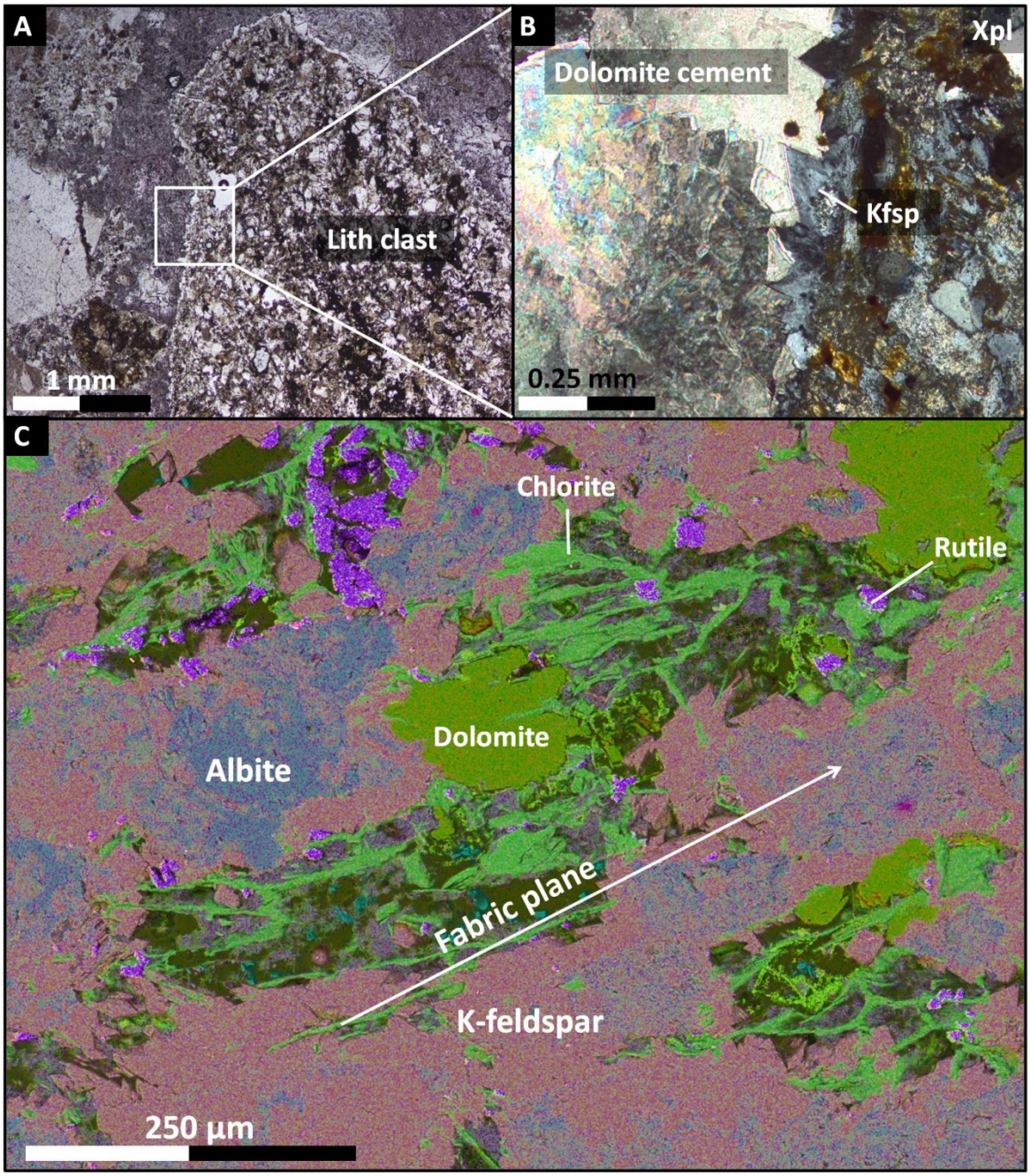

Figure 2-21: (A and B) Transmitted light microscope images of lithic clast, secondary carbonate and K-feldspar matrix cement in monomict lithic breccia, and (C) EDS element map of a monomict lithic clast showing distribution and habit of rock forming minerals. Champagnac monomict breccia displays a range of degrees of hydrothermal alteration. Subtle differences in protolith geochemistry, the orthogneiss-paragneiss sequence of the Upper Gneiss unit, are reflected in the alteration product, with some breccia clasts slightly more mafic than others. These differences can also be seen in the clean cut image (Figure 2-22, A), as some clasts are darker than others.

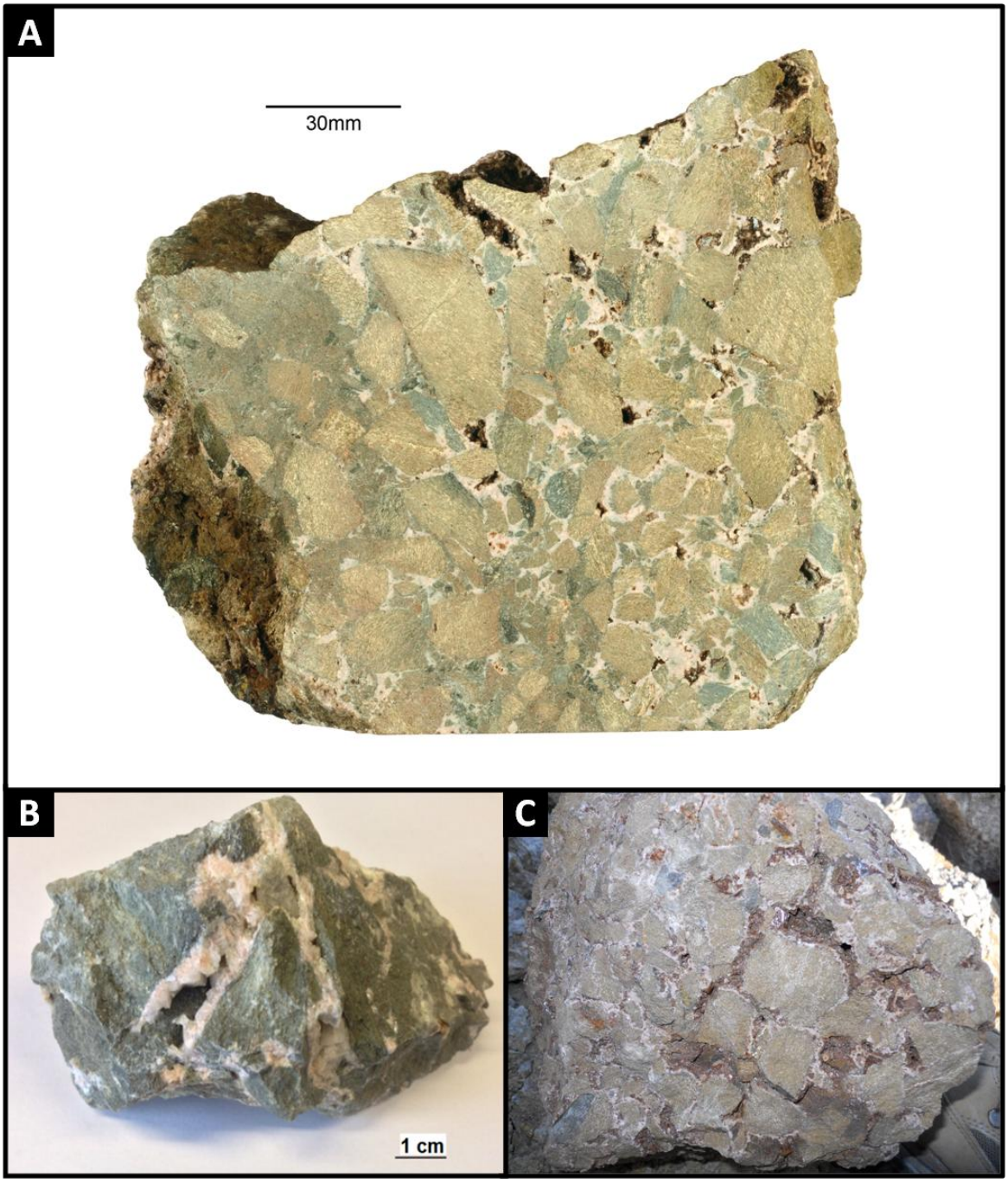

Figure 2-22: Photos of clean-cut (A), rough mesoscale (B) and field (C) samples of monomict lithic impact breccia. Coarse crystalline pink and white cement is a mixture of dolomite and calcite (also see Figure 2-21, A and B). Photo A courtesy of Les Hill, University of Glasgow.

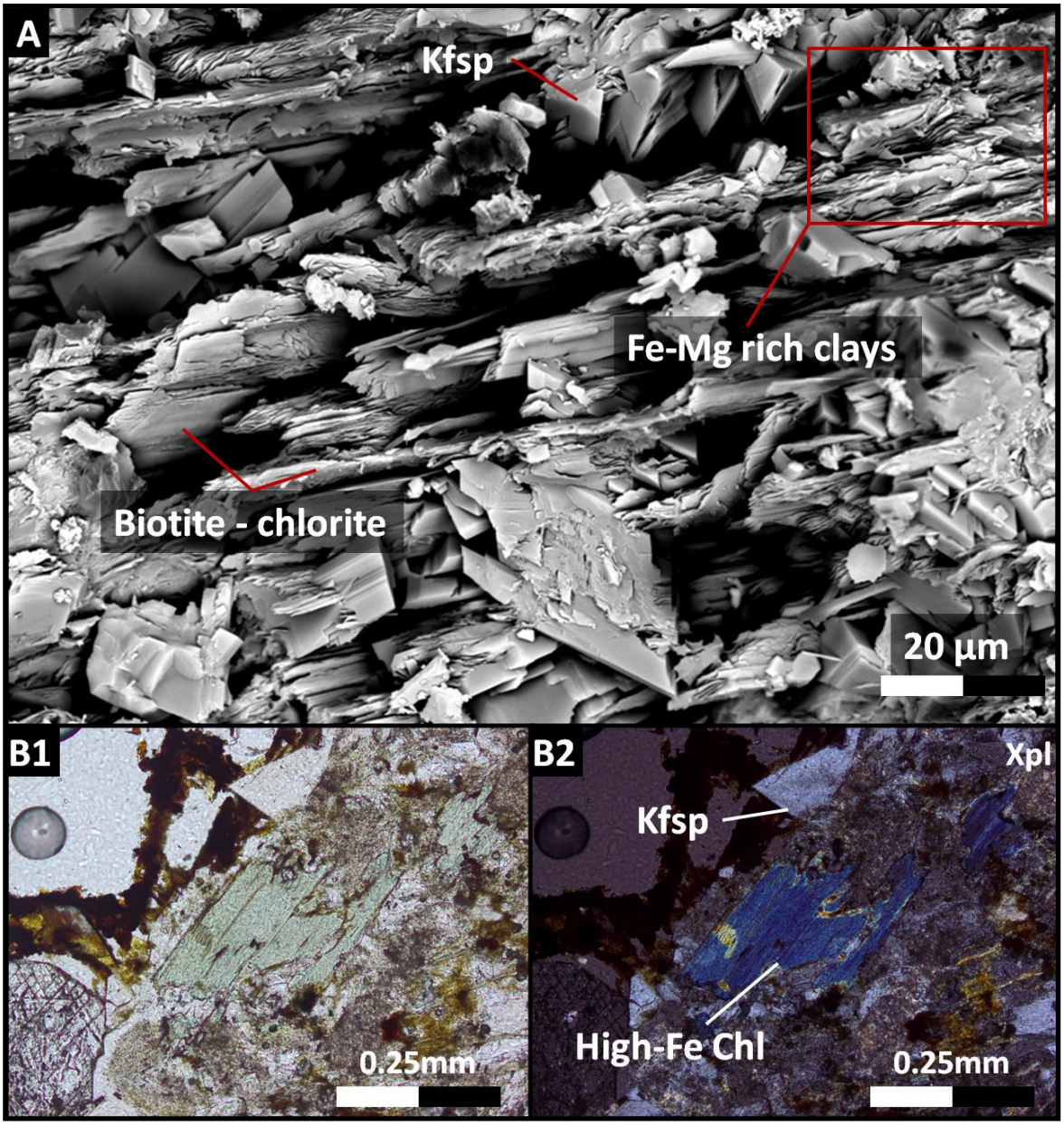

Figure 2-23: (A) Secondary electron image of a fracture surface in a monomict breccia clast, showing various phyllosilicates, biotite, chlorite and diagenetic Fe-Mg rich diagenetic clays, and authigenic k-feldspar crystals aligned and layered along fabric plane. (B1 and B2) Transmitted light microscope images of dark blue interference colors characteristic of high-Fe chlorite, and secondary K-feldspar in a clast of monomict breccia.

2.5.3.3 Champagnac polymict melt-bearing intrusion and surrounding host rock

IUGS impactite classification: Complex, multiple generation intrusion divided into zones based on compositional differences in material; Zones 1-3: monomict lithic impact breccia and Zone 4: melt-bearing breccia dike (Figure 2-24).

IUGS Shock level: 0 to possibly IV (see comments and identification section).

Shocked minerals: Possible ballen silica (Figure 2-27).

Description hand sample: Melt-bearing intrusion: Massive, moderately indurated melt-

bearing impact breccia, with various angular 0.5 to 1cm angular lithic and mineral fragments in a very fine grey-green clastic matrix.

Composition: Zone 1: Monomict lithic impact breccia: Moderately sorted, dark-blue to grey1 to 2cm clasts of mafic amphibolite gneiss of the Upper Gneiss unit in a matrix of sub-mm clastic material which has been locally replaced by secondary dolomite cement, as observed in the semi-continuous unit of monomict lithic breccia. **Zone 2: Monomict lithic impact breccia:** Poorly to moderately sorted, tan to light brown-green, angular 2 to 5cm clasts of more felsic basement orthogneiss of the Upper Gneiss unit with a coarse-crystalline matrix of dolomite cement, slightly larger lithic clasts and more poorly sorted than the semi-continuous monomict lithic breccia unit. **Zone 3: Monomict lithic impact breccia:** Poorly sorted dark red-grey to dark blue 0.5 to 2cm, sub-angular to angular clasts of Upper Gneiss unit with high temperature dark grey to dark red reaction rims of authigenic K-feldspar, and clast interiors composed of soft clays. Lithic matrix is composed of a mixture of angular to sub-angular ≤500 micron dark red K-feldspar rich gneiss clasts, quartz and pink to tan dolomite. **Zone 4: Melt-bearing breccia intrusion:** 0.5 to 1cm angular clasts of various mineral and crystalline lithic fragments in a very fine matrix. The matrix is composed of ≤5mm cryptocrystalline, quartzofeldspathic melt clasts (Figure 2-25, B1 and B2), angular crystalline basement lithic fragments at various stages of potassic alteration (orthoclase and albite to muscovite), angular to sub-angular fragments of bright red K-feldspar and quartz, and various phyllosilicates, paragonite, muscovite and chlorite. Vug –filling dolomite can be found in very small amounts in the matrix.

Major rock forming minerals in order of decreasing abundance (XRD, Sapers at al 2014): N/A

Bulk geochemistry (XRF Lambert 2010): N/A

Coordinates and outcrop: 45° 51’ 15.15” N, 0° 49’52.91” E; In Champagnac, outcrops of 1 to 3 meter wide breccia dike can be found cross-cutting parautochthonous impactite and autochthonous basement material at higher elevations within the quarry.

Comments and identification techniques: Multiple generations of breccias are represented in this intrusion, and the exact relationships between the different rock types and zones are unknown. The fine clastic, green melt-bearing impact breccia cross-cuts both lighter and darker monomict lithic breccia, zones 1, 2 and 3, with zone 3 believed to represent a thermal “reaction zone”, as evidenced by the high temperature reaction rims on clasts and isotopic evidence (Chapter 3). Optical and SEM observations reveal the dark red-grey reaction rims on breccia clasts in zone 3 to be authigenic, K-feldspar, with the interiors of clasts decomposed to smectite clay (Figure 2-26) (also see Chapter 3). This

alteration and reaction pattern suggests an incomplete reaction throughout the clasts. The bright red area marked "???" is K-feldspar replacing albite with cross-cutting veins of dolomite (Chapter 3). Minor clasts of ballen-like quartz can also be found (Figure 2-27). Breccia dikes are a feature of Rochechouart noted by previous authors (Lambert, 1981; 2010).

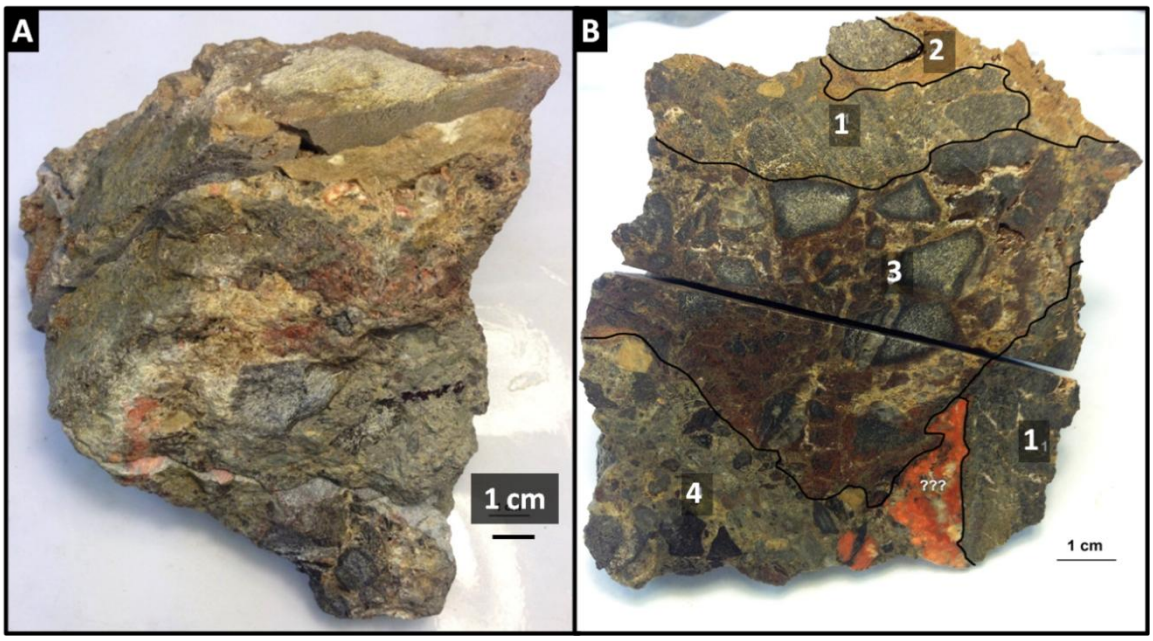

Figure 2-24: Hand samples of polymict melt-bearing intrusion and surrounding host rock. Numbers 1-4 denote generations of breccias/differences in geochemistry/ alteration "zones".

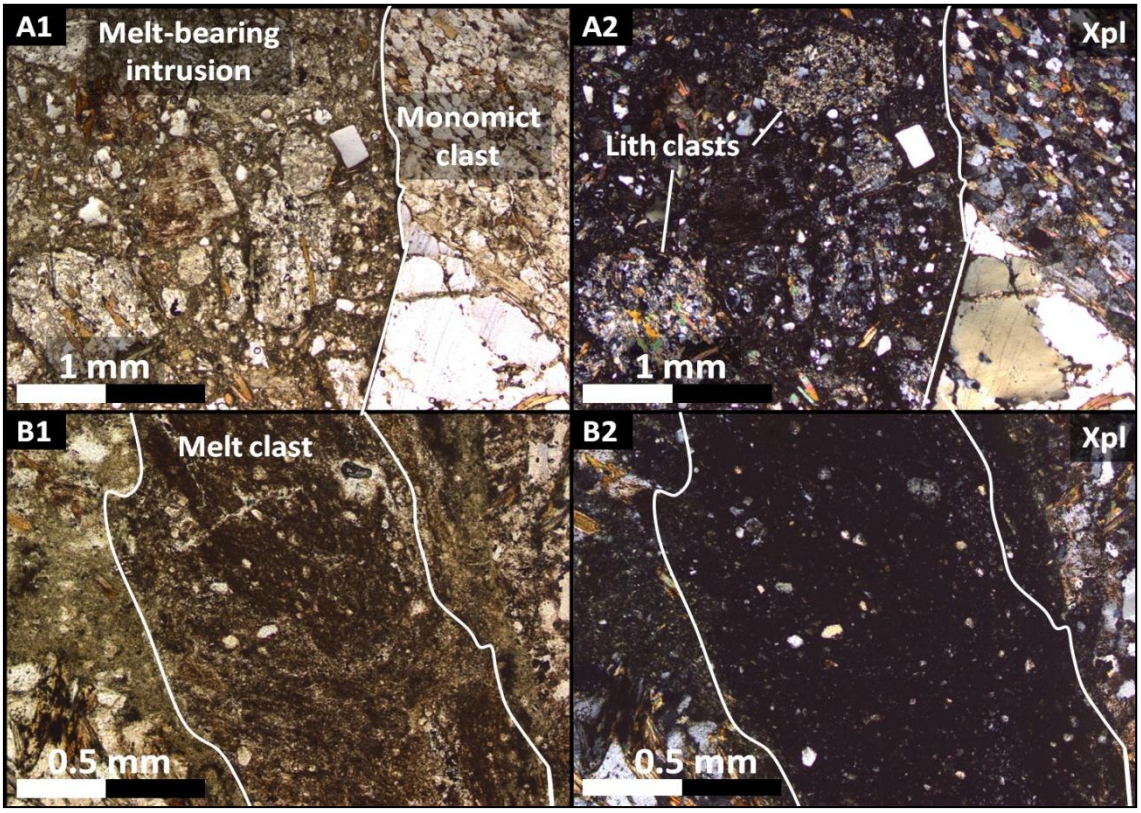

Figure 2-25: Transmitted light microscope images of the contact of melt-bearing impact breccia intrusion (zone 4) with monomict lithic breccia (zone 3), showing several sub-mm sub-angular lithic clasts and angular mineral fragments in fine green-grey clastic matrix (A1 and A2), as well as a ~2mm crystalline quartzofeldspathic melt clast (B1 and B2), also in zone 4 matrix.

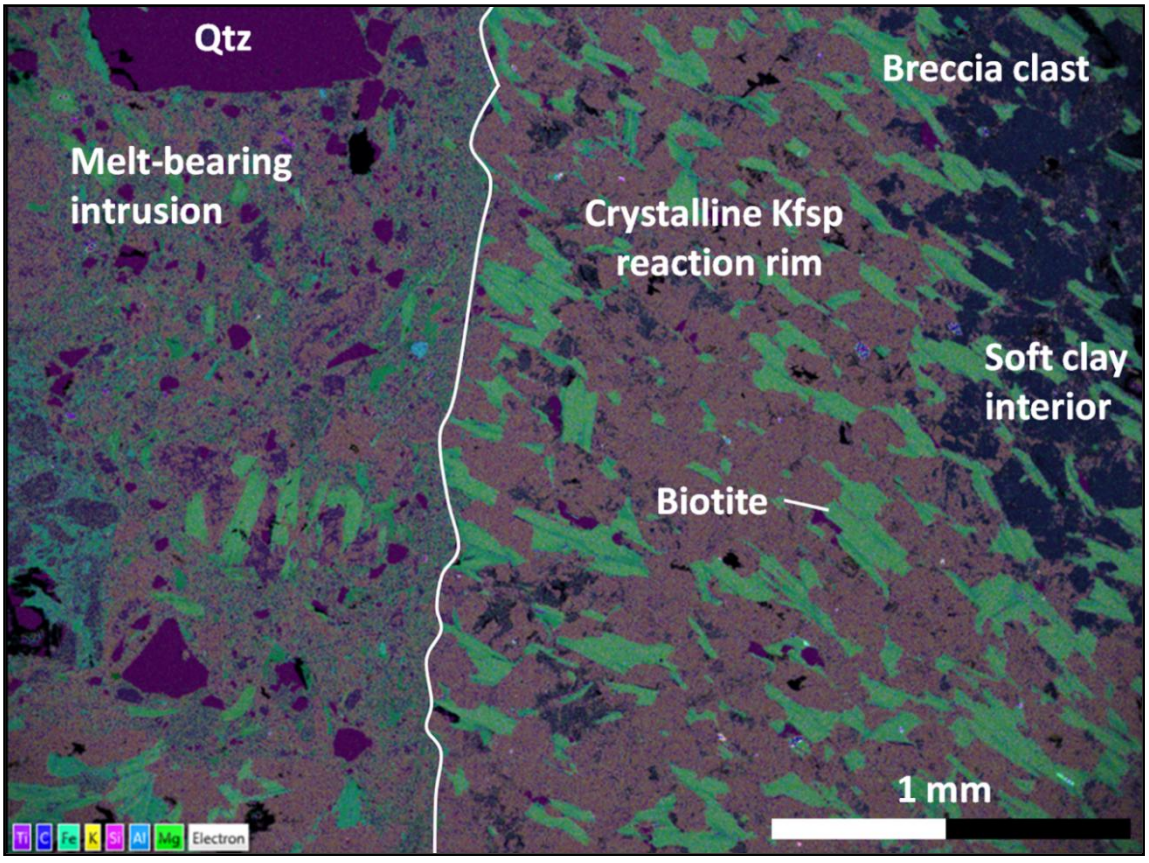

Figure 2-26: EDS element map of the contact between fine-grained melt-bearing impactite

intrusion and monomict lithic breccia clast showing reaction rim of K-feldspar and clay-rich weathered interior. See chapter 3 for further details.

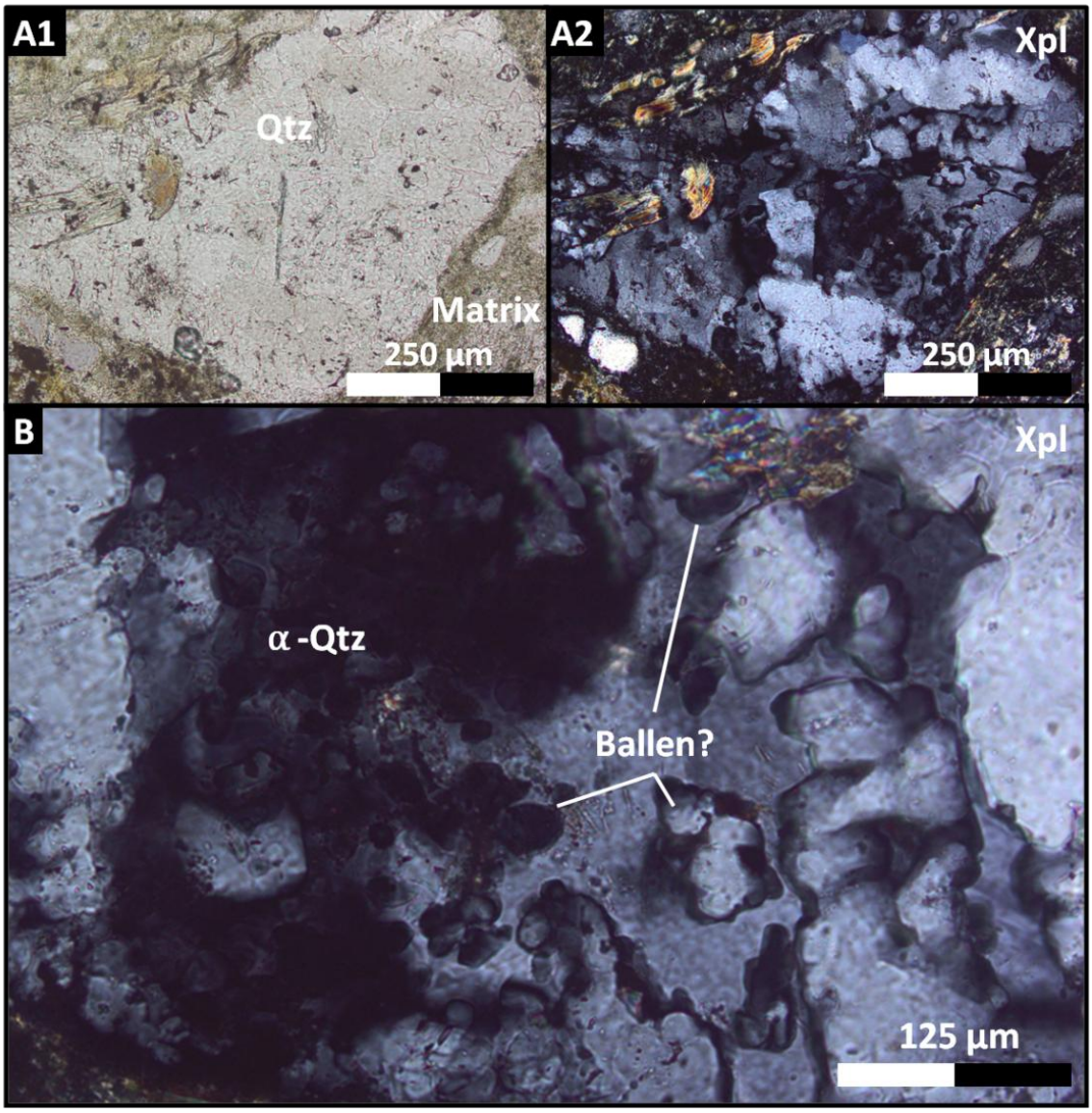

Figure 2-27: Transmitted light microscope images of clast of ballen-like quartz in fine-clastic, green, melt-bearing intrusion (zone 4, Figure 2-24). Raman spectroscopy reveals both ballen-like crystals and non-ballen areas are α-quartz.

2.5.3.4 Polymict lithic impact breccia, type Rochechouart

IUGS impactite classification: Clast-rich impact melt rock or lithic impact breccia.

IUGS Shock level: 1a; Quartz with planar fractures and planar deformation features.

Shocked minerals: Planar deformation features (PDF's) and planar fractures in quartz, kink bands in phyllosilicates and rare melt clasts.

Description hand sample: Massive, very well indurated, dark brown to tan (weathered) to light brown-yellow (fresh) lithic breccia with 0.5cm to decimeter sized angular to sub-

angular lithic fragments of crystalline basement gneiss, granite and granodiorite in a fine clastic quartzofeldspathic matrix (Figure 2-28, A and B).

Composition: Clasts: Approximately 30% of clasts are larger than 5mm (Lambert, 2010) and consist of all representative crystalline basement lithologies in the Rochechouart area; diorite, granodiorite, orthogneiss and paragneiss. Sedimentary clasts have been found previously, but are very rare (Sapers et al., 2009). Lithic clasts commonly display bright pink to red reaction rims of authigenic K-feldspar. Lithic clasts larger than 10cm have been reported, but are uncommon (Lambert, 2010). **Matrix:** Clastic matrix consists of a variety of quartzofeldspathic angular mineral and lithic fragments with 50% of material ranging from 1mm to <50 µm. Mineral fragments, angular quartz, feldspar, muscovite, paragonite, biotite and chlorite, display various shock features; decorated PDF's, planar fractures and kink bands (Figure 2-29, A1, A2 and D). Very rare 1 to 2mm melt clasts occur (Figure 2-29, B1 and B2), and minor Fe-Ti oxides, hematite can be found filling in secondary porosity. Secondary hydrothermal K-feldspar can be found infilling fractures.

Major rock forming minerals in order of decreasing abundance (XRD Sapers et al., 2014): Quartz + chlorite + mica + alkali feldspar + plagioclase + pyroxene.

Bulk chemistry (XRF Lambert, 2010): Full bulk data not reported; 2 to 5wt% Fe and 0.5 to 1.5 wt% Mg.

Coordinates and outcrop: 45°49'12.00" N 0°48'36.00" E; The most well-known and outcrop is located in a field at the base of the Rochechouart Chateau, forming an approximately 5m high wall (Figure 2-28, C and D). It may be covered at the base by dense vegetation. The maximum thickness of the unit is approximately 40 meters (Lambert, 2010).

Comments and identification techniques: The Rochechouart lithic breccia is the most abundant impactite in the area covering approximately 41km^2, directly overlying the crystalline basement. Faint bedding has also been reported within this unit, striking and dipping parallel with the crater floor (Lambert 2010). The Rochechouart lithic breccia has high secondary porosity; it contains vugs lined with iron oxides, relic lithic fragments that have been weathered (Figure 2-28 B). Bright red-orange k-feldspar reaction rims, similar to those in the monomict breccia, may be observed on clasts, and is likely a result of heat and potassium-rich fluid circulation, as seen throughout all Rochechouart impactites.

Geochemically, the Rochechouart breccia is the closest in composition to the crystalline basement than all other impactites; it is only slightly higher in iron content than the target (Figure 2-7).

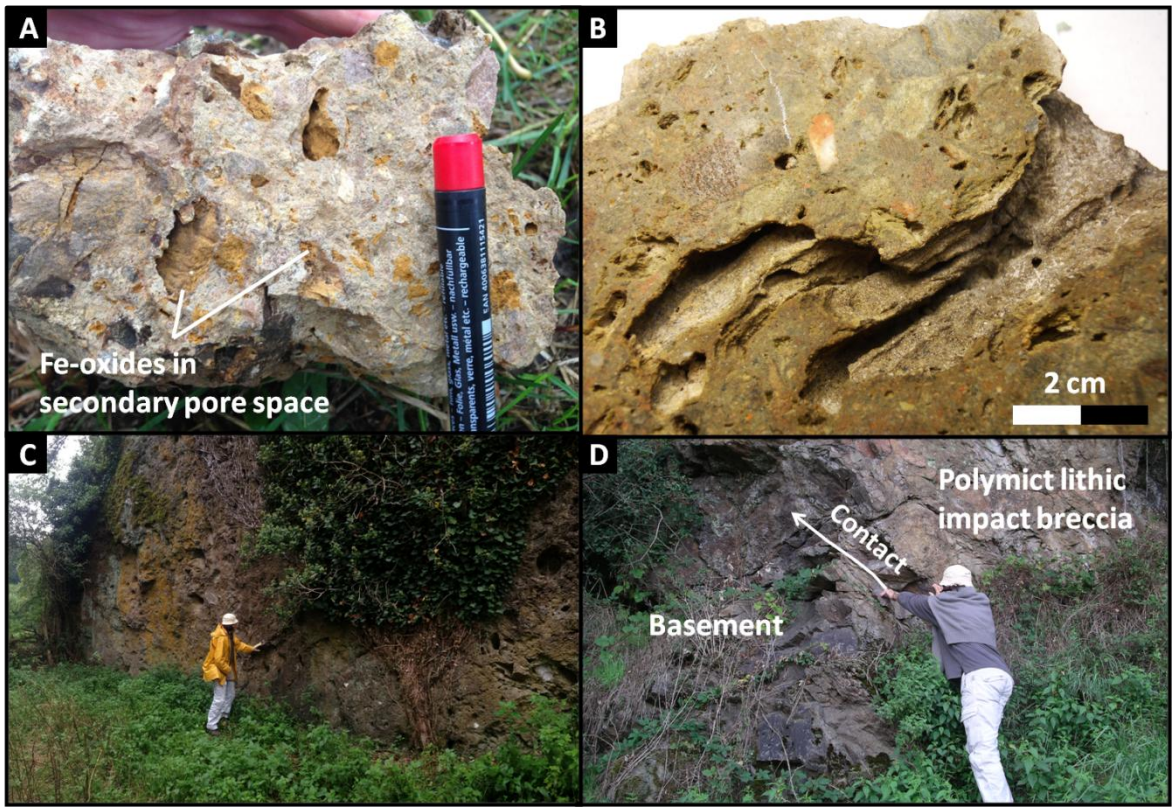

Figure 2-28: (A) Photos of the Rochechouart type polymict lithic impact breccia; hand sample from field showing Fe-Ti oxide and oxyhydroxide filling and staining secondary porosity created from weathered rock and mineral clasts. (B) Large vug created from weathered material. (C) Outcrop beneath the chateau in the village of Rochechouart, and (D) a contact between underlying crystalline basement and overlying polymict lithic impact breccia (photo c/o Dr. Paula Lindgren).

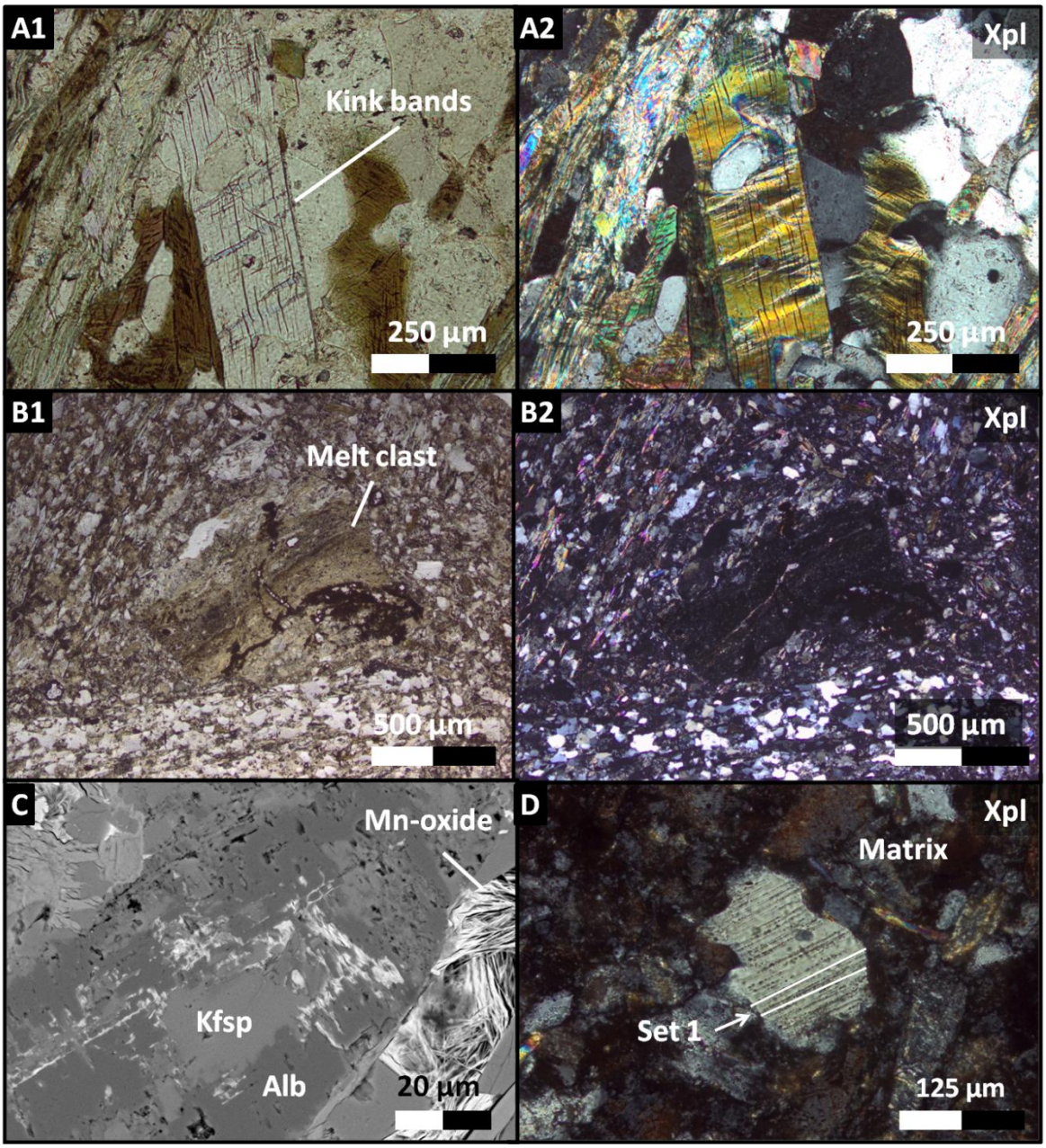

Figure 2-29: Transmitted light microscope (A1, A2, B1, B2 and D) and SEM (C) images of the Rochechouart type polymict lithic breccia; kink bands in a muscovite crystal (A1 and A2), melt clast in matrix (B1 and B2), Mn-Ca oxide weathering in albite (C) and a single set of decorated planar fractures in a quartz crystal within the fine clastic matrix (D).

2.5.3.5 Melt-bearing impact breccia type Chassenon and impactoclastite sub-unit

IUGS Impactite classification: Crater fill suevite.

IUGS Shock level: 0 to IV; Rock glasses or crystallized melt rock.

Shocked minerals: Diaplectic quartz glass at various levels of devitrification, planar deformation features and planar fractures in quartz, kink bands in phyllosilicates and toasted quartz.

Description hand sample: Massive, moderately to well indurated, dark grey to green

(fresh), to light grey (weathered), melt and glass-rich impact breccia, with up to 2cm angular to sub-rounded clasts of green-blue, soft devitrified glass and partially to completely melted basement lithic fragments in a fine clastic matrix. Light-yellow to tan vesicular melt material similar to the impact melt rock, type Babaudus, may rarely be found within the matrix.

A thin, very fine-grained, stratified, "fall-back" sub-unit can be found at the top of the massive melt-bearing unit. It is a poorly to moderately indurated, dark red fresh to grey weathered "impactoclastite" as termed by Lambert (2010), and may locally display flow textures. It may also be found forming dikes within the main massive unit (Lambert, 2010). **Composition**: **Main unit clasts**: Angular to sub-rounded, 0.5 to 2cm partially to completely melted lithic fragments representative of all crystalline basement lithologies. On average, melt constitutes 12% vol or less of the whole rock, but can vary from 0.1 to 38% vol (Lambert, 2010). Dark green, soft clasts of 0.5 to 1cm weathered, friable Fe-Mg-K rich and quartz impact glass at various levels of devitrification and decomposition can also be found, and is very characteristic of the lithology. Weathered glass is generally unresolved under an optical microscope, but careful inspection may reveal thin overgrowths of fibrous α-quartz and aggregates of rutile (Figure 2-31, C1 and C2). **Matrix**: Very fine, angular fragments of lithic and mineral fragments, quartz, feldspar, muscovite, paragonite and chlorite up to 10 µm in size (Figure 2-30, B1 and B2). Quartz with decorated PDF's and toasted quartz are observed, as well as kind bands in phyllosilicates oriented perpendicular to the cleavage. Larger quartz fragments may contain aggregates of apatite. **Sub-unit:** Approximately 2 to 3 meters thick, the unit forms a gradational contact with the underlying main, massive unit (Lambert, 2010). It consists of approximately 5% sub-mm lithic clasts within a very fine matrix of quartzofeldspathic mineral fragments; Quartz, K-feldspar, muscovite, paragonite and biotite (Figure 2-32, B1 and B2). While the matrix is unresolved under the optical microscope, stratification can be observed as well as turbulent flow structures (Figure 2-32, A1 and A2), also noted by previous authors (Lambert, 2010).

Major rock forming minerals in order of decreasing abundance (XRD Sapers 2014): Quartz + clays + alkali feldspar + mica + pyroxene.

Bulk chemistry (XRF Lambert, 2010): Reported bulk data for main unit: 3 to 4.5 wt% Fe and 1 to 1.5 wt% Mg.

Table 2-10*: XRF data (wt%) for impactoclastite*, from Lambert (2010).

SiO_2	Al_2O_3	Fe_2O_3	MgO	CaO	Na_2O_3	K_2O	TiO_2	P_2O_5
73.24	12.65	3.03	1.00	0.46	1.38	6.12	0.63	0.09

* Data reported for impactoclastite sub-unit only.

Coordinates and outcrop description: 45°50’35.71” N, 0°46’20.50 E; Material can be collected from a Roman quarry near the village of Chassenon and the Cassinomagus archaeological park, with permission. The outcrop surface is very well exposed and excavated. Very little of the impactoclastite sub-unit remains, and sampling is discouraged.

Comments and identification techniques: The Chassenon type melt-bearing impact breccia can be identified it’s dark-green, friable devitrified glass clasts, seen at hand scale (Figure 2-30), and the overall green-grey appearance of the rock. It has been compared morphometrically to the Rochechouart type lithic impact breccia by previous researchers, with the exception of the presence of glass and melt fragments in the Chassenon-type suevite (Lambert, 2010). The Chassenon suevite sits on top of the polymict lithic breccia, at 20 to 30 meters thick and 1.2km wide.

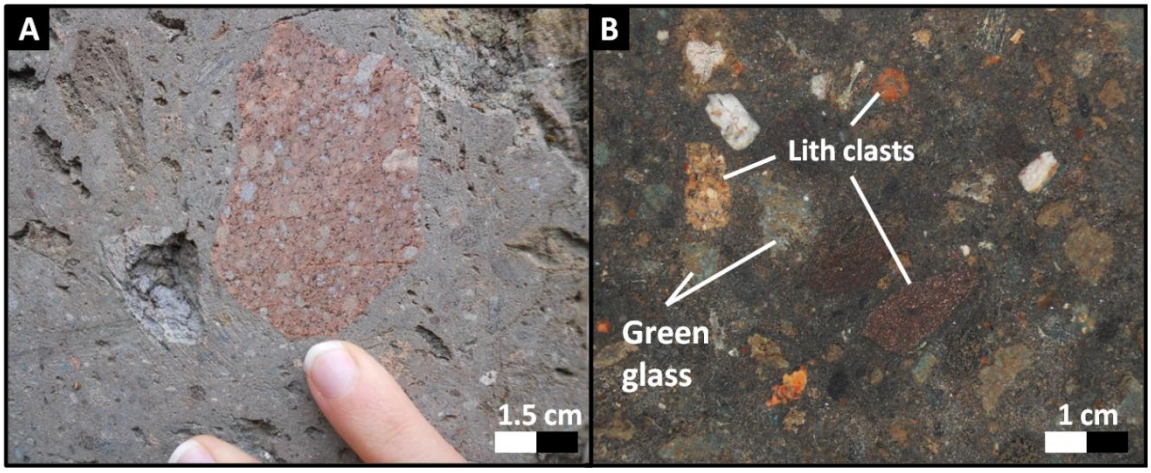

Figure 2-30: Photographs of partially melted lithic fragment in outcrop (A) and clean-cut surface of the Chassenon type melt-bearing breccia showing partially devitrified green glass and lithic fragments in a fine clastic matrix (B).

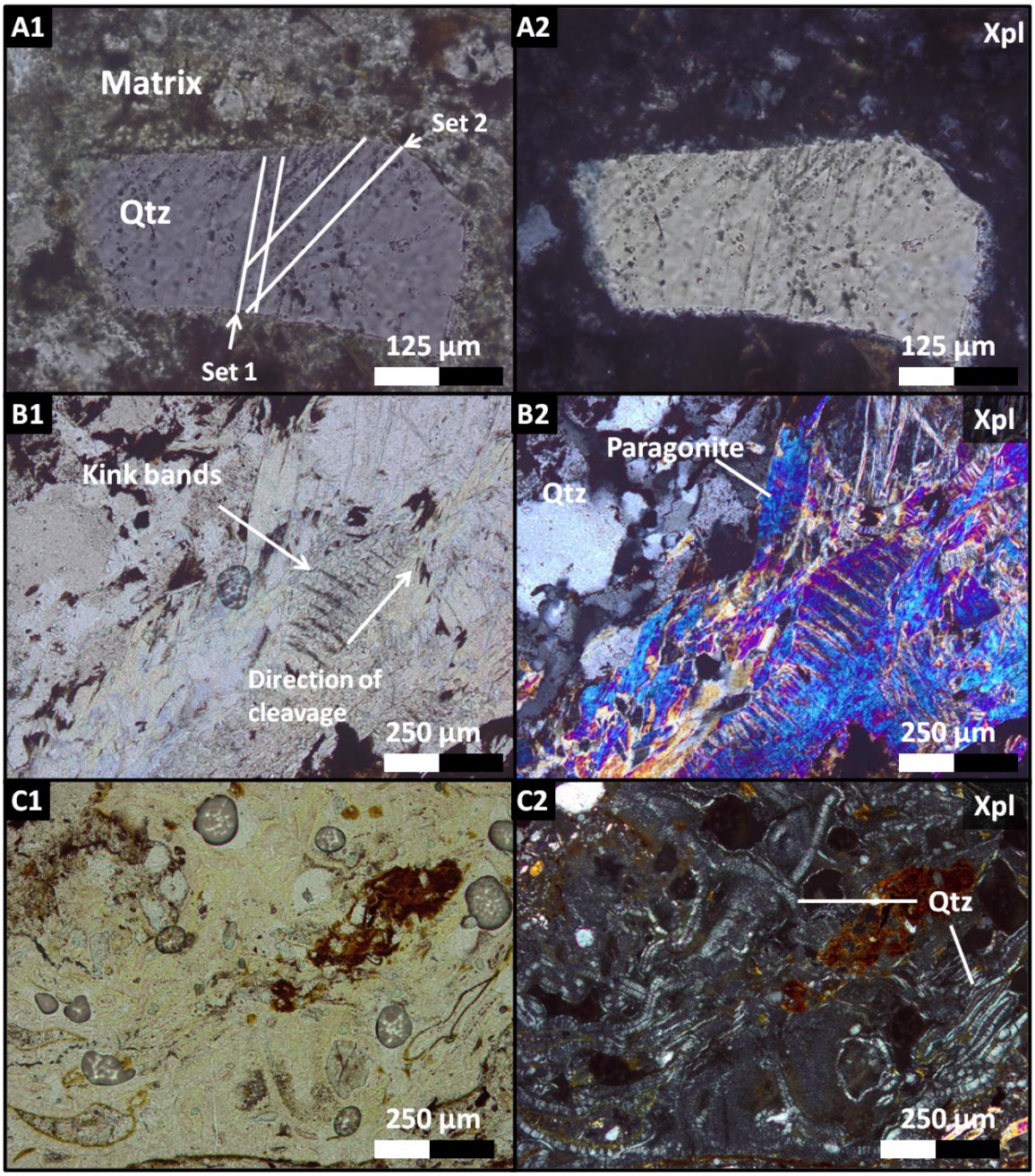

Figure 2-31: Transmitted light microscope images of shock features in the Chassenon type melt-bearing breccia; two sets of PDF's in a quartz fragment within the matrix (A1 and A2), kink bands perpendicular to the cleavage plane in paragonite (bright blue mineral in xpl, B2) within a lithic fragment (B1 and B2) and isotropic quartz glass which has been partially devitrified to fibrous α-quartz (C1 and C2).

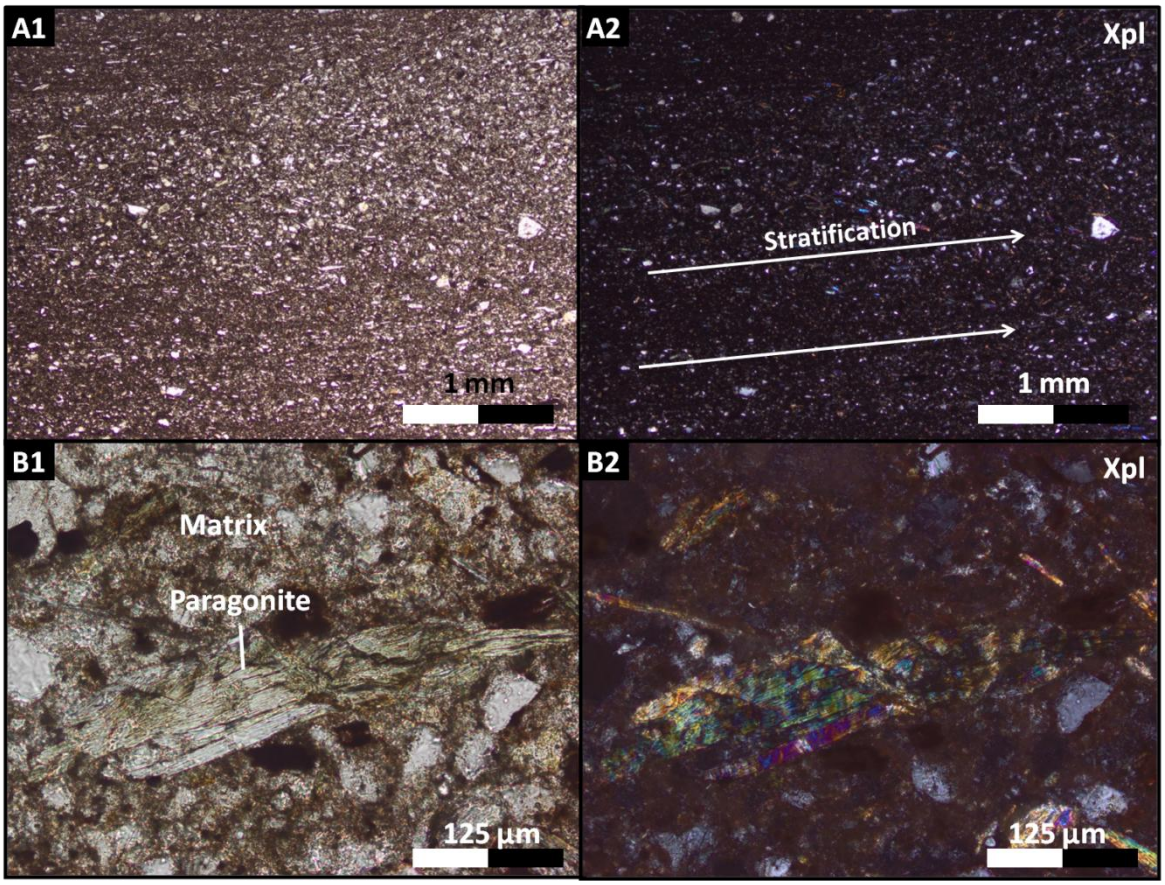

Figure 2-32: Transmitted light microscope images of fine-grained impactoclastite sub-unit in the Chassenon melt-bearing breccia unit; The faint stratification is caused by phyllosilicate-rich layers (Lambert, 2010).

2.5.3.6 Particulate impact melt rock, type Montoume.

IUGS Impactite classification: Crater fill suevite or clast-rich impact melt rock.

IUGS shock stage: IV; Rock glasses or crystallized melt rock.

Shocked minerals: Rare planar deformation features and planar fractures in quartz (Figure 2-34, B), toasted quartz (Figure 2-34, D1 and D2), type IV ballen silica (Figure 2-34, A, C1 and C2) and kink bands in phyllosilicates.

Description hand sample: Very well indurated, massive, dark red-brown weathered to pink-red fresh quartzofeldspathic, crystalline melt matrix with 25 to 40 vol% basement lithic fragments greater than 0.5mm at various stages of melting; commonly exhibits flow textures, is rarely vesicular and displays columnar jointing in outcrop. Lithic clasts represent all crystalline basement lithologies in the Rochechouart field area. Secondary mineralization at the mesoscale is rare; vesicles may be found with a thin, drusy sub-mm coating of quartz, adularia or iron oxides/hydroxides, hematite and goethite.

Composition: **Clasts:** Sub-angular to rounded, 0.5mm to 4 cm quartzofeldspathic mineral fragments and lithic clasts representing all crystalline basement lithologies. Lithic clasts

are found at various stages of melting and incorporation into the matrix. Secondary K-feldspar and hematite is commonly found as vein fillings cross-cutting both clasts and matrix (Figure 2-35, A1, A2 and B). **Matrix:** Crystalline melt matrix consists of 0.5mm to 5 micron K-feldspar crystallites and mineral fragments, quartz, K-feldspar, Fe-Ti oxides, and various phyllosilicates (Figure 2-34, D1 and D2, and Figure 2-35, B and C). In many cases, the matrix cannot be resolved under the optical microscope. Quartz displays a variety of high shock and thermal features (Figure 2-34).

Major rock forming minerals in order of decreasing abundance (XRD Sapers 2014): Quartz + alkali feldspars + mica + clays + pyroxene.

Bulk chemistry (XRF Lambert 2010): Reported bulk data for Montoume: 5% wt Fe and 1% wt Mg.

Table 2-11*: XRF data (wt%) for impact melt rocks from Lambert (2010).

SiO_2	Al_2O_3	Fe_2O_3	MgO	CaO	Na_2O_3	K_2O	TiO_2	P_2O_5
66.60	16.24	4.22	1.29	0.25	0.34	10.19	0.76	n/a

*Data reported for impact melt rocks as a whole.

Coordinates and outcrop: 45°46'32.2"N 0°46'28.6"E; The largest outcrop which remains today can be found 7.5km south of the center of the structure in an abandoned quarry (Figure 2-33). High walls of the quarry are exposed and display columnar jointing. The area is covered by dense vegetation. The thickness based on this outcrop is approximately 25 meters (Lambert, 2010).

Comments and identification techniques: Originally called “red-welded breccia” (Kraut, 1969), this impactite displays a distinct red coloring due to a mixture of high quantities of K-feldspar melt crystallites (Figure 2-33, A and Figure 2-35, B and C) and K-metasomatism, which also produces large amounts of iron oxides (Chapter 3).

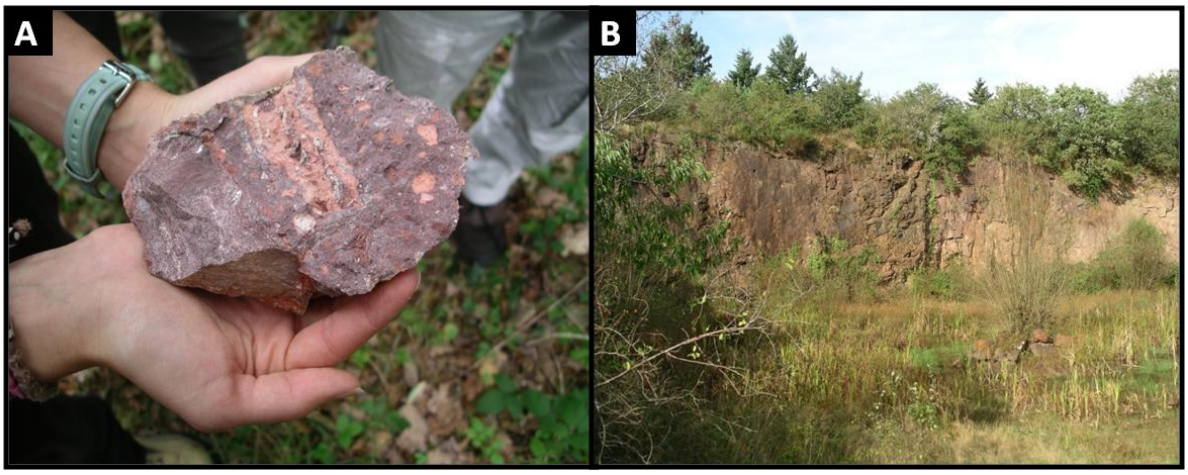

Figure 2-33: (A) Montoume type particulate impact melt rock as found in the field, from an abandoned quarry near the village of Montoume approximately 7.5km south of the center of the structure (B). The deep reds and pinks are characteristic of this lithology, and are a result of high amounts of iron oxides and K-feldspar crystallites in the melt and partial melting of orthoclase-rich granitic basement clasts.

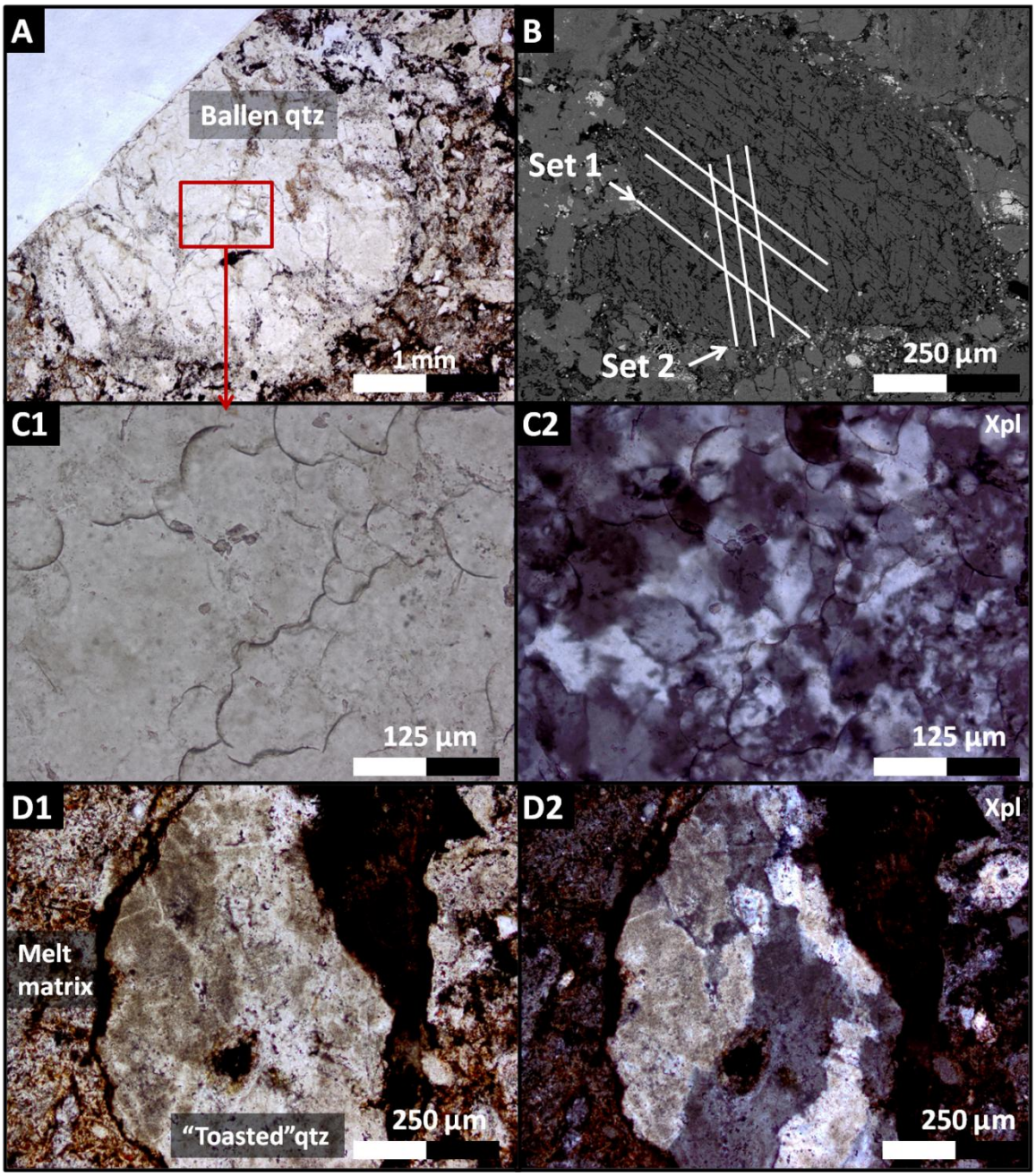

Figure 2-34: Transmitted light microscope and secondary electron images of various shock features found within the Montoume type particulate impact melt rock; type IV ballen silica (A, C1 and C2) (Ferrière et al., 2009), planar fractures in a quartz clast within the melt matrix (B) and "toasted" quartz, also within the melt matrix (D1 and D2).

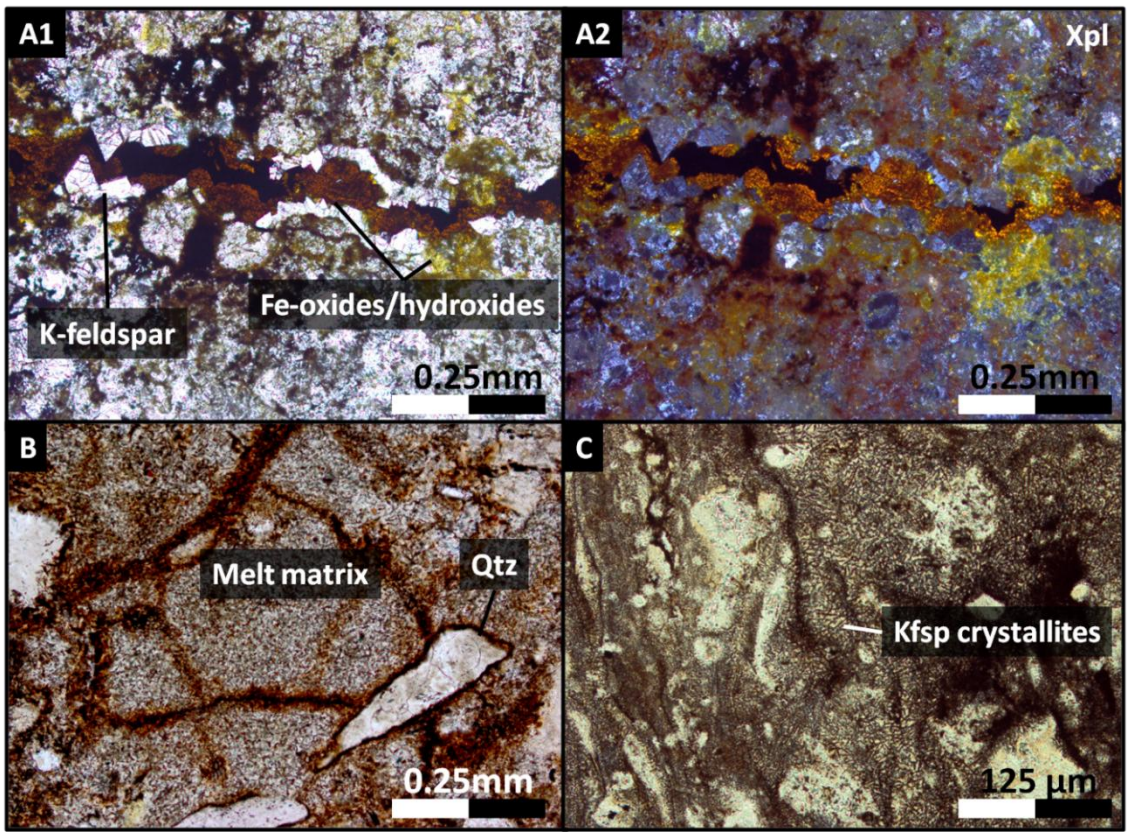

Figure 2-35: Transmitted light microscope images of the Montoume impact melt rock; fracture-filling, euhedral secondary K-feldspar and red and yellow iron oxides and hydroxides, hematite and goethite (A1 and A2), dark red K-feldspar crystallites and fracture filling hematite within the melt matrix (B and C) and flow features within the melt matrix (C). Hematite is often a by-product of K-metasomatism (Pirajno, 2009); combined with the k-feldpsar rich quartzofeldspathic melt rocks is responsible for the characteristic red coloring of the Montoume melt.

2.5.3.7 Impact melt rock, type Babaudus.

IUGS Impactite classification: Clast-poor to clast-free impact melt rock or suevite

IUGS Shock level: Level IV; Rock glasses and/or crystallized melt rock.

Shocked minerals: Planar deformation features and planar fractures in quartz (Figure 2-37 D1 and D2).

Description hand sample: Moderately indurated, light yellow fresh to orange-yellow weathered, crystalline vesicular melt rock with less than 10% rounded to well-rounded, partially to completely melted and assimilated quartzofeldspathic lithic clasts (Figure 2-37). Vesicles may be elongated and exhibit flow textures, and may be lined with fine-crystalline drusy adularia, grains of metallic exsolved Fe-Ti oxides and smectite clays (Figure 2-37, B and C).

Composition: Matrix: The crystalline melt matrix is very high in silica content and consists almost completely of two phases of or-feldspar; the first phase composed of thin,

sharp, elongated crystallites (Figure 2-38) and a second phase of flat, euhedral, blocky crystals with interlocking margins and euhedral rhombohedral crystal aggregates infilling vesicles (Figure 2-38). The first phase contains abundant heavy and light REE's surrounding vesicles, and Fe-Ti oxides. Where filling vesicles and forming veins, the second phase can also be found with abundant smectite replacing or-feldspar, amygdaloidal chlorite lining vesicles (Figure 2-38, B), minor euhedral Fe-Ti oxides, rutile, ilmenite and hematite, and rarely barite (Chapter 3). Both phases are difficult to resolve under transmitted or reflected microscope. Clasts: Clasts are partially to completely assimilated into the melt, and consist of individual quartz grains or highly altered quartzofeldspathic crystalline basement clasts (Figure 2-38, A). In areas where clasts have been completely melted, brown or red patches of melt with vesicles forming rotational flow textures are observed (Figure 2-38, A). In most cases, lithic clasts do not retain any of their original textures and are unrecognizable.

Major rock forming minerals in order of decreasing abundance (XRD Sapers 2014):

Bulk chemistry (XRF Lambert, 2010): see table 2-9; 1 to 3 wt% Fe and 0.25 to 0.75 wt % Mg (XRF Lambert 2010).

Coordinates and outcrop: 45°49'00.63"N, 0°47'31.04" E; Material can be found near the central area of Valette (Figure 2-14). The Babaudus type melt forms a very small body, and is only 1 to 2 meters thick and a few hundred meters wide (Lambert, 2010). Material collected from outcrop is very weathered and in poor condition (Figure 2-36, A); fresh material can be loaned from the reserve.

Comments and identification techniques: The Babaudus melt is easily identifiable by it's bright yellow color and highly vesicular texture (Figure 2-36, B). It consists almost completely of crystalline K-feldspar with very few mineral and lithic fragments. Quartz clasts are the most common recognizable clasts, and are often found with a "toasted" brown appearance and contain planar fractures or PDF's (Figure 2-37, A1, A2, D1 and D2). Vesicles are often occluded by smectite and can be found with a drusy lining of K-feldspar (adularia) and dusty orange-red hematite and goethite. This lithology weathers very easily, and fresh samples are difficult to find in the field.

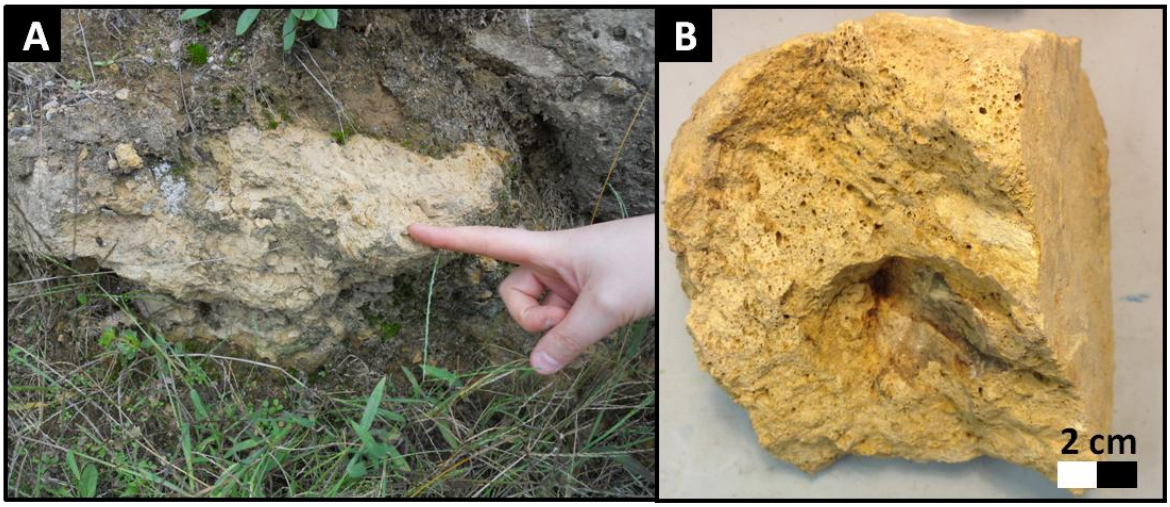

Figure 2-36: Photo of the Babaudus type impact melt rock in outcrop (A) and a hand sample from the collection at the reserve (B).

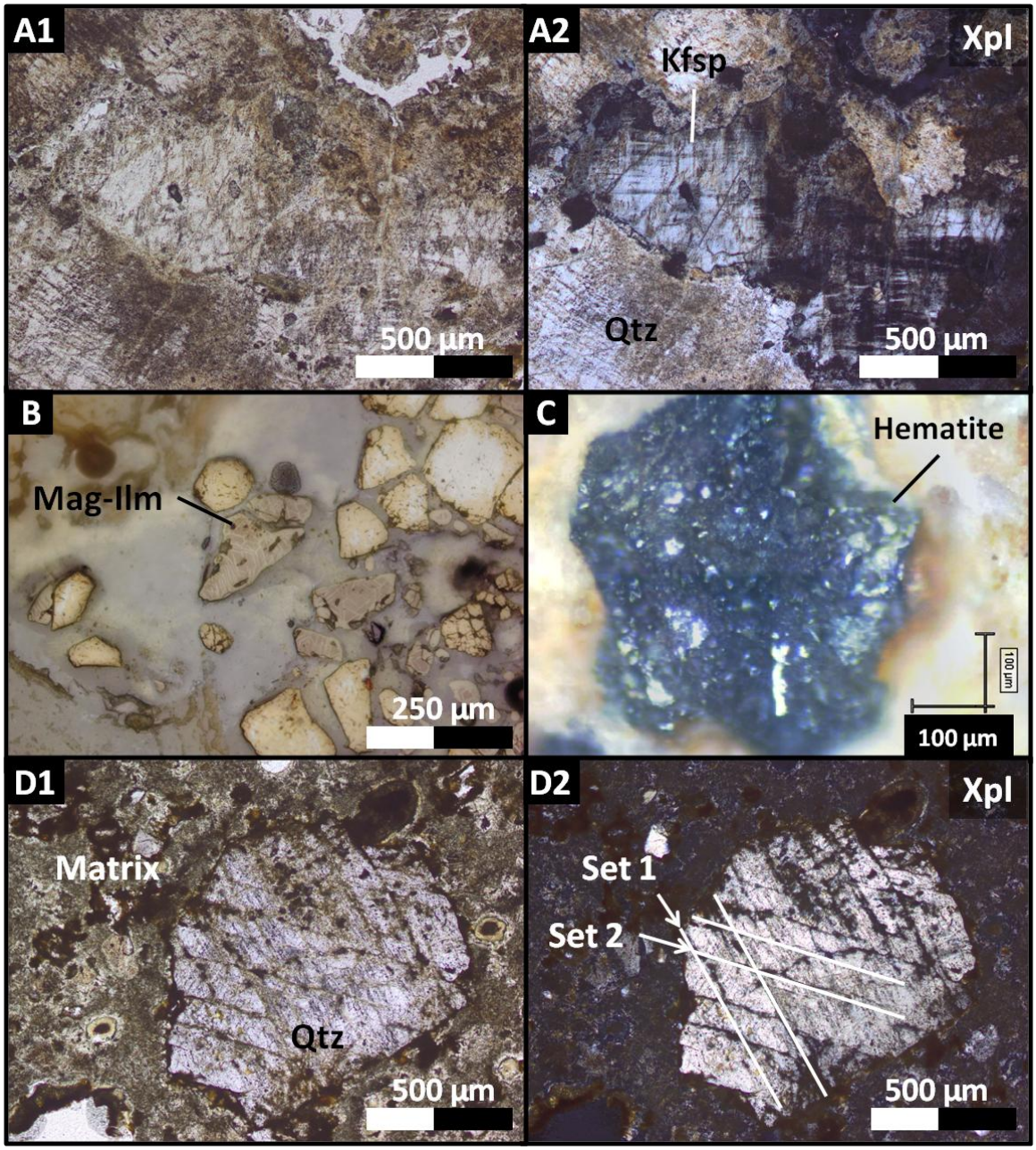

Figure 2-37: Transmitted light microscope images of the Babaudus-type impact melt rock; highly altered lithic fragment within the matrix, showing quartz with a "toasted" appearance (A1 and A2), reflected light microscope image of magnetite and ilmenite grains within a vesicle showing faint exsolution patterns (B), photograph of metallic hematite grain within a vesicle (C) and a quartz grain with two sets of planar fractures (D).

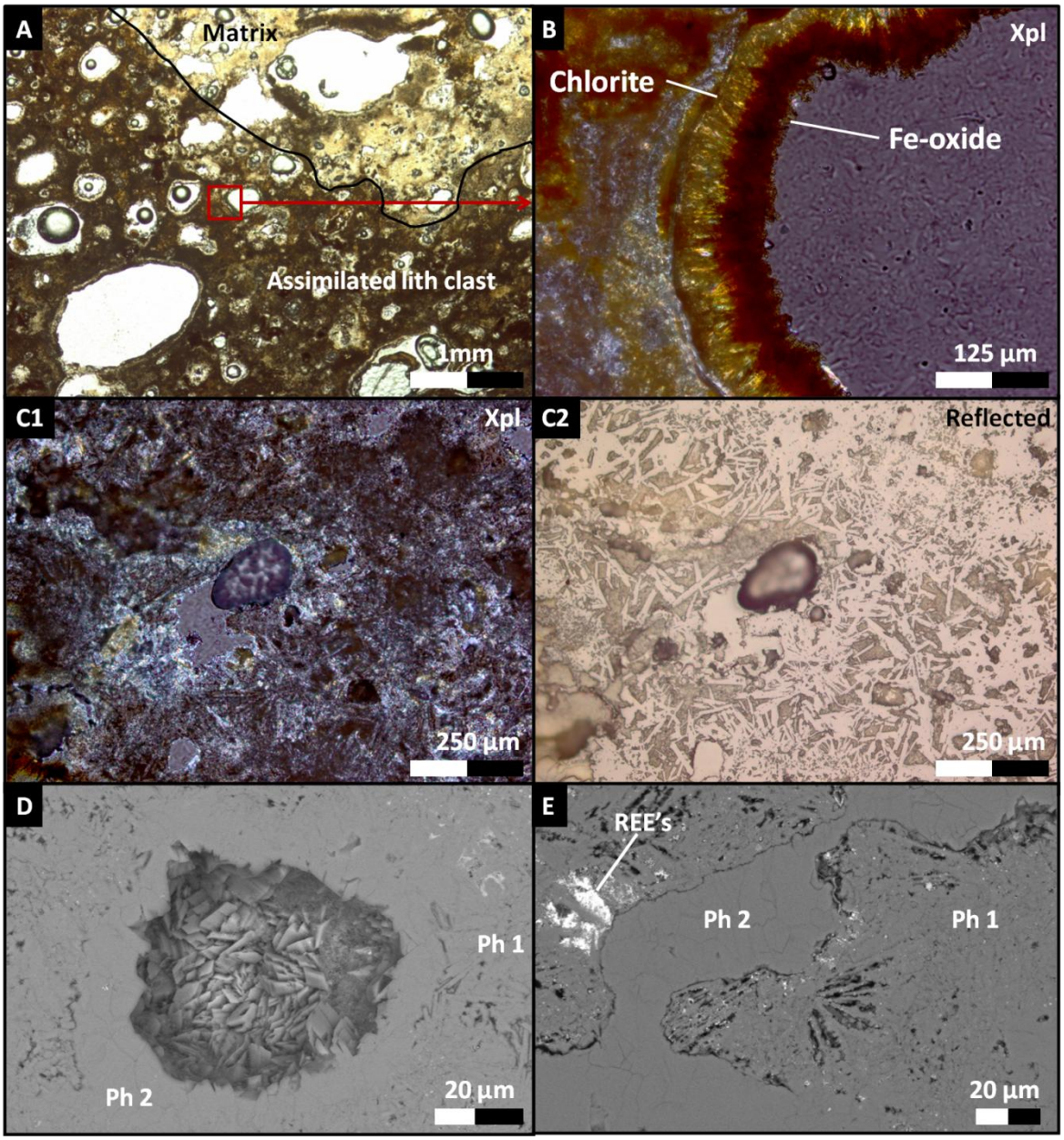

Figure 2-38: (A) Transmitted light microscope images of an assimilated melt clast (brown melt), (B) amygdaloidal chlorite and Fe-oxide lining vesicle and orthoclase crystallites in phase 1 (Ph1) of the melt matrix, (C1) transmitted and (C2) reflected light microscope images of melt, showing texture of sanidine crystallites, and (D and E) SEM images of the melt matrix showing both the sharp crystallite-bearing phase (Ph1) and the flat, euhedral, rhombohedral orthoclase phase (Ph2), and an accumulation of rare earth elements in intracrystalline voids within phase 1.

2.5.3.8 Shatter cones

The best specimens of shatter cones in Rochechouart are found within the microgranite dikes beneath the transient crater floor (Figure 2-39). They are not well-formed in the gneiss or main plutonic bodies. Shatter cones may be found within 7km of the structure's center, according to Lambert (2010).

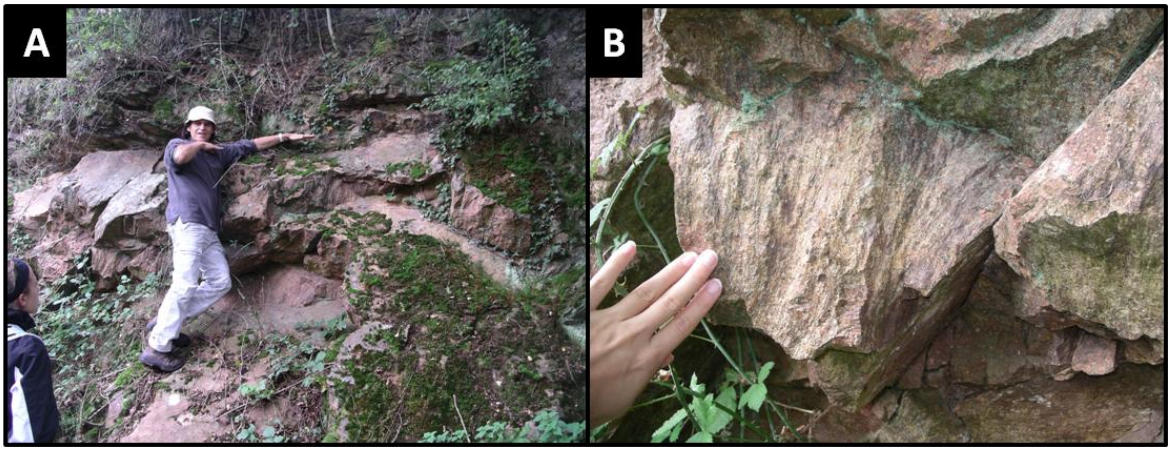

Figure 2-39: (A) Outcrop of shatter-cone bearing microgranite and (B) a close up of striated shatter cone surface. Photos courtesy of Dr. Paula Lindgren.

2.6 High pressure quartz polymorphs

To date, no coesite or stishovite has been found within the Rochechouart impact structure.

2.7 Post-impact hydrothermal activity within Rochechouart

Previous authors have noted a pervasive hydrothermal overprint in all impactites manifested as a general absence of Ca-Na plagioclase, enrichment in K-feldspar, aqueous alteration of impact glasses and the precipitation of secondary K-feldspar within voids and fractures (Lambert, 1977, 2010; Spray et al., 1998; Tagle, et al., 2009; Sapers et al., 2014); these observations are consistent with early stage aqueous alteration as outlined by Naumov (2005) within well-developed hydrothermal systems in complex craters with crystalline targets. However, due to the poor state of preservation, studies dedicated to exploring the hydrothermal system in Rochechouart are lacking; because of Earth's active environment, multiple fluid events and surficial weathering often convolute the direct investigation of impact-hydrothermal activity in older structures. Previous authors have also found impact-hydrothermal environments host conditions conducive to the development of extremophile microbial communities (Osinski et al., 2005, 2013; Osinski and Pierazzo, 2012; Parnell et al., 2010a, 2010b); this may also be the case with

Rochechouart.

This thesis aims to overcome the difficulties arising from aqueous alteration overprinting in Rochechouart by coupling stable isotope analysis to place temperature and fluid constraints on select minerals, with detailed petrography, SEM, EDX and Raman studies. There are three major fluid events which have affected all rocks within the Rochechouart area; pre-impact hydrothermal processes and metasomatism related to Variscan orogenesis and crustal rifting, hydrothermal circulation related directly to the impact event, and late-stage diagenesis at ambient conditions (Faure et al., 2009; Lambert, 2010; Cathelineau et al., 2012; Sapers et al., 2014). Secondary carbonate and sulphide mineralization is a common feature of lithic impactites, but is rare to absent in melt-bearing and melt-rich lithologies; carbon, oxygen and stable isotope analysis may allude to heat controls on the types, pervasiveness and timing of these minerals, as well as identify the fluid sources pervading the structure. Previous authors have predicted hydrothermal fluid flow is focused in autochthonous impact fractures, as impact breccias have generally low permeability and porosity (Parnell et al., 2010a); the Champagnac site in Rochechouart cross-cuts the transient crater floor, and provides access to parautochthonous, autochthonous and unshocked basement material for comparison. This thesis also aims to provide a comprehensive review of secondary alteration in all impactites.

Results from this study will reveal (i) information on fluid reservoirs and heat controls on impact-hydrothermal activity in complex structures with a majority crystalline, marginal marine target and (ii) evaluate the structure's potential to host extremophile microbial life during the post-impact cooling period.

2.8 References

Boiron, M. C., Cathelineau M., Banks D. A., Buschaerta S., Fourcade S., Coulibaly Y., Michelot J. L., Boyce A., 2002, Fluid transfers at a basement/cover interface Part II. Large-scale introduction of chlorine into the basement by Mesozoic basinal brines, *Chemical Geology*, 192 p. 121– 140.

Bureau de recherché géologiques et minières, Maps: number 686: La Rochefoucauld, 1982; number 687: Rochechouart, 2012. 1:50,000. BRGM.

Le Carlier de Veslud, C., Alexander, P., Ruffet, G., Cuney, M., Cheilletz, A., 2013, A two-stage exhumation in Western French Massif Central: new geochronological evidences of

syn-collisional extension, *Lithos,* 175–176, pp. 1–15.

Cathelineau M., Boiron M. C., Fourcade S., Ruffet G., Clauer N., Belcourt O., Coulibaly Y., Banks D. A., Guillocheau F., 2012, A major Late Jurassic fluid event at the basin/basement unconformity in western France: $^{40}Ar/^{39}Ar$ and K–Ar dating, fluid chemistry, and related geodynamic context, *Chemical Geology*, 322–323, p. 99–120.

Departmental Council of Charente Registered for Historical Monuments, 2015, Cassinomagus Archaeological Park Homepage, [electronic] Available at: www.cassinomagus.fr.

Departmental Museum of Contemporary Art in Rochechouart, 1985 to 2015, Museum Homepage, (electronic), Available at: www.musee-rochechouart.com.

Eitel M., Gilder S. A., Kunzmann T., Pohl J., 2014, Rochechouart impact crater melt breccias record no geomagnetic field reversal, Earth and Planetary Science Letters Vol 387, p. 97–106.

Faure M., Lardeaux J. M., Ledru P., 2009, A review of the pre-Permian geology of the Variscan French Massif Central *Geoscience Tectonics,* 341, 202–213.

Fourcade S., Michelot J. L., Buschaert S., Cathelineau M., Freiberger R., Y. Coulibalyc,f, J.F. Aranyossy, 2002, Fluid transfers at the basement/cover interface Part I. Subsurface recycling of trace carbonate from granitoid basement rocks (France), *Chemical Geology*, 192, p. 99– 119.

Galli M. T., Jadoul F., Bernasconi S. M., Weissert H., 2005, Anomalies in global carbon cycling and extinction at the Triassic/Jurassic boundary: evidence from a marine C-isotope record, *Palaeogeography, Palaeoclimatology, Palaeoecology*, 216, p. 203 – 214.

Google Earth version 7.1., 2014, 45.8239° N, 0.8217° E, www.google.com/earth/index.html, (accessed Jan 20, 2015).

Imperial College London, 2013, Glossary: Folk Classification (electronic)Available at: www.imperial.ac.uk/earthscienceandengineering/rocklibrary/viewglossrecord.php?gID=00000000290 (accessed May 13, 2015).

Imperial College London, 2013, Glossary: Dunham Classification (electronic) Available at:www.imperial.ac.uk/earthscienceandengineering/rocklibrary/viewglossrecord.php?Term=dunham%20classification (accessed May 13, 2015).

Janssens M. J., Hertogen J., Takahashi H., Anders E., Lambert P., 1977, Rochechouart Meteorite Crater' Identification of Projectile, *Journal of Geophysical Research,* Vol 82 No 5.

Kraut, F., 1935, Sur l'origine des breches de Chassenon (Charente), *Comptes Rendus de l'Academie des Sciences*, v. 20, p. 221.

Kraut, F. and French B., 1971, The Rochechouart meteorite impact structure, France: Preliminary Geological Results, *Journal of Geophysical research,* Vol 76 No 23.

Kraut, F., Short, N.M., and French, B.M., 1969, Preliminary report on a probable meteorite impact structure near Chassenon, France: Meteoritics, v. 4, p. 490.

Lafuente, B., Downs, R. T., Yang, H., Stone, N., (2015) The power of databases: the RRUFF project. *Highlights in Mineralogical Crystallography*, T Armbruster and R M Danisi, eds. Berlin, Germany, W. De Gruyter, pp 1-3.

Lambert P., 1977, The Rochechouart Crater: Shock Zoning Study, Earth and Planetary Science Letters, 35 p. 258-268.

Lambert, P., 1981, Breccia dikes - Geological constraints on the formation of complex craters Multi-ring basins: Formation and evolution; *Proceedings of the Lunar and Planetary Science Conference, Houston, TX, November 10-12 1980*, p. 59-78.

Lambert P., 2010, Target and impact deposits at Rochechouart impact structure, France *Geological Society of America,* Special Paper 465.

Manes, G., 1833, Description Geologique et Industrielle du Departement de la

Haute-Vienne: Limoges, Ducourtieux, 140 p.

Osinski, G. R., Lee, P., Parnell, J., Spray, J. G. and Baron, M., 2005, A case study of impact-induced hydrothermal activity: The Haughton impact structure, Devon Island, Canadian High Arctic, *Meteoritics and Planetary Science,* Vol. 40, No. 12, pp. 1859-1877.

Osinski, G. R. and Pierazzo, E., 2012, Impact Cratering: Processes and Products, *John Wiley & Sons, Ltd*, Chichester, UK. doi: 10.1002/9781118447307.ins

Osinski, G. R., Tornabene, L. T., Banerjee, N. R., Cockell, C. S., Flemming, R., Izawa, M. R., McCutcheon, J., Parnell, J., Preston, L. J., Pickersgill, A. E., Pontefract, A., Sapers, H. Southam, G., 2013, Impact-generated hydrothermal systems on Earth and Mars, *Icarus*, 347-363.

Parnell, J., Taylor W. C., Thackrey, S., Osinski, G. R., Lee, P., 2010a, Permeability data for impact breccias imply focussed hydrothermal fluid flow, *Journal of Geochemical Exploration,* 106, p. 171-175.

Parnell, J., Boyce, A., Thackrey, S., Muirhead, D., Lindgren, P., Mason, C.,Taylor, C., Still, J., Bowden, S., Osinski, G. R., and Lee, P., 2010b, Sulfur isotope signatures for rapid colonization of an impact crater by thermophilic microbes, *Geology*, Vol. 38, No. 3, pp. 271-274.

Réserve Naturelle de l'Astroblème de Rochechouart - Chassenon, CCPM Mairie-Place-du-Chateau, 87600, Rochechouart, France.

Saltzman M. R., and Thomas E., 2012, Carbon Isotope Stratigraphy, *The Geologic Time Scale,* p. 207 to 232.

Sapers H. M., Osinski G. R., Banerjee N., 2009, Re-evaluating the Rochechouart impactites: petrographic classification, hydrothermal alteration and evidence for carbonate bearing target rocks, *40th Lunar and Planetary Science Conference.*

Sapers H. M., Osinski G. R., Banerjee N. R., Ferriere L., Lambert P., Izawa M. R., 2014a, Revisiting the Rochechouart impact structure, France, *Meteoritics and Planetary Science*, 1-17.

Schmeider M., Buchner E., Schwarz W. H., Trieloff M., Lambert P., 2010, A Rhaetian $^{40}Ar/^{39}Ar$ age for the Rochechouart impact structure (France) and implications for the latest Triassic sedimentary record, Meteoritics & Planetary Science 45, Nr 8, 1225-1242.

Schmidt, T, 1984, Bearbeitung und Auswertung von Schweremessungen im Gebiet der Impakt-Struktur von Rochechouart (Massif Central, Frankreich). *Diploma thesis, University of Munich.*

Spray J. G., Kelley S. P., and Rowley D. B., 1998, Evidence for a late Triassic multiple impact event on Earth, *Nature*, vol. 392.

Stöffler, D, and Grieve, R. A. F., 2007, A systematic nomenclature for metamorphic rocks: Chapter 11: Impactites. *Recommendations by the IUGS Subcommission on the Systematics of Metamorphic Rocks*. Web version 01.02.07.

Whiteside J. H., Olsen P. E., Eglinton T., Brookfield M. E., and Sambrotto R. N., 2010, Compound-specific carbon isotopes from Earth's largest flood basalt eruptions directly linked to the end-Triassic mass extinction, *Proceedings of the national academy of sciences of the united states of America*, vol. 107 no. 15.

Tagle R., Schmitt R. T., Erzinger J., 2009, Identification of the projectile component in the impact structures Rochechouart, France and Saaksjarvi, Finland: Implications for the impactor population for the earth, *Geochimica et Cosmochimica Acta*, vol 73 p. 4891–4906.

Weather Online Ltd. 1999 to 2015, Climate of the World: France, (electronic), Available at: http://www.weatheronline.co.uk/reports/climate/France.htm (accessed May 23, 2015).

University of Glasgow, University Ave, Glasgow, Scotland, United Kingdom, G12 8QQ.

Chapter 3 Stable isotope studies and evidence for multi-phase aqueous alteration in the Rochechouart impact structure

In this Chapter

3.0 Stable isotope studies and evidence for multi-phase aqueous alteration in the Rochechouart impact structure

3.1 Introduction

3.1.1 Review of previous work on hydrothermal alteration in Rochechouart

Previous authors have identified post-impact hydrothermal alteration in Rochechouart from (i) bulk changes in impactite and underlying basement whole rock geochemistry and mineralogy through XRF and XRD studies, (Lambert, 2010; Sapers et al., 2014) (Section 3.1.1.1) (Table 3-1), (ii) authigenic mineral precipitation in veins, fracture coatings, and vesicles and pore space fillings (Spray et al., 1998; Tagle et al., 2009; Lambert, 2010; Schmeider et al., 2010; Sapers et al., 2014) (3.1.1.2), and (iii) aqueous alteration of primary impact products, namely impact glass and melt (Lambert, 2010;

Sapers et al., 2014) (Section 3.1.1.3).

3.1.1.1 Whole rock geochemistry and mineralogy; XRF and XRD studies

XRF work by Lambert (2010) documents an enrichment in K_2O and a depletion in Na_2O and CaO in all Rochechouart lithologies relative to target rocks. Impactites are the most enriched, by as much as 40 times more K_2O than CaO than the crystalline basement (Table 3-1).

Table 3-1: Summary of K_2O/Na_2O and K_2O/CaO ratios of Rochechouart impactites and basement lithologies (XRF) (modified after Lambert, 2010)

Rock type		K_2O/Na_2O	K_2O/CaO
Unshocked target	Gneiss	1.2	1.8
	Granite	1.6	7.2
Impactites	Monomict lithic	3.4	n/a
	Polymict lithic	6.9	n/a
	Melt rocks	21.6	40.7
	Impactoclastite	18	40.8

In impact melt rocks and the impactoclastite sub-unit of the Chassenon type melt-bearing impact breccia, albite content has been reduced significantly with An-rich plagioclase rare to absent, while both are observed in significantly higher quantities in the unshocked basement. Lithic impact breccias are less depleted in Na_2O than the once-hotter melt-bearing and melt-rich impactites. This pervasive enrichment of potassium and depletion of calcium and sodium has been attributed to post-impact hydrothermal processes (Lambert, 2010).

XRD data in Sapers et al. (2014) documents significant amounts of muscovite, illite, montmorillonite/smectite, glauconite, chlorite, calcite and Fe-Ti oxides within both impactites and unshocked basement material. They attributed this mineralogy to aqueous secondary alteration related to post-impact hydrothermal activity.

3.1.1.2 Vesicle, vein and pore space mineralization

Previous authors have noted a pervasive K-metasomatic overprint in all impact and unshocked target lithologies as well as varying amounts of secondary carbonate, argillic, chlorite, and sulphide mineralization (Lambert, 1977, 2010; Spray et al., 1998; Tagle et al., 2009; Schmeider et al., 2010; Sapers et al., 2009, 2014).

Vein and void filling mineralization has previously been reported, the most common being adularia, quartz and Fe-Ti oxides (Spray et al., 1998; Lambert, 2010; Schmeider 2010; Sapers et al., 2014). In melt-rich impactites, vesicles can contain adularia, Fe-Ti oxides and amygdaloidal chlorite (Lambert, 2010; Sapers et al., 2014), and in the mesostasis, clays, zeolites and carbonates are the dominant alteration products (Spray et al., 1998). Secondary calcite been reported from within the polymict lithic impact breccia (Sapers et al., 2014).

3.1.1.3 Devitrification of impact glasses and fluid inclusions

Devitrification of impact glasses to carbonate and clay minerals has been reported (Lambert, 2010; Sapers et al., 2014). Tectosilicates at shock level 1b and higher have been altered or recrystallized, and PDF's in quartz may be decorated with fluid inclusions (Lambert, 2010).

3.1.2 Evidence for multiple fluid event overprinting

The direct study of impact-generated hydrothermal activity within Rochechouart is complicated by the overprinting of multiple geologic and fluid events pre-dating and post-dating the impact event.

3.1.2.1 Pre-impact Variscan metamorphism

The first hydrothermal event recorded in the Rochechouart area is related to pre-impact metamorphism of the crystalline basement during continental collision and rifting associated with the Variscan orogeny (Chapter 2, Section 2.3) (Boiron et al., 2002; Cathelineau et al., 2012). Using stable isotope and fluid inclusion data, temperature constraints of 170 to 400°C have been placed on early to late Hercynian-age carbonate and silicate fracture fillings within crystalline basement 30km north of Rochechouart (Fourcade et al., 2002); many of these fracture fillings exhibit textural and compositional similarity to those observed in Rochechouart unshocked basement rocks.

3.1.2.2 Impact hydrothermal activity

The second fluid event is associated with the impact event and subsequent hydrothermal activity during the cooling period. Previous studies on impact-generated hydrothermal systems within other structures (Chapter 1, Section 1.4) have recorded a wide range of temperatures; in craters of comparable size to Rochechouart, temperatures are generally no higher than 300°C during the early stages of fluid circulation (Naumov,

2005). Impact-hydrothermal activity is retrograde; new minerals may be precipitated and as the system cools, those inherited from the target may be altered or erased.

3.1.2.3 Surface diagenesis and unconformity fluid event

The last fluid phase coincides with processes affecting the structure after the cooling stage; late stage diagenesis related to burial and surface weathering. Previous studies have also identified a major "fluid event" related to infiltrated seawater mixing with basinal brines and meteoric waters in Hercynian crystalline basement fractures along the Aquitaine unconformity (Figure 3-1) (Boiron et al., 2002; Fourcade et al., 2002; Cathelineau et al., 2012). This "event" is evidenced as fracture-filling carbonate, sulphide, sulphate, halide and silicate minerals, with carbonates precipitating at temperatures similar to those we might expect within the mid to late stage of impact generated hydrothermal systems (25 to 100°C). Within the Charroux-Civray plutonic complex, approximately 30km north of Rochechouart, this infiltration has been dated to 156 to 146 Ma using Ar-Ar on secondary adularia. It is unknown how this activity may have affected the impact structure.

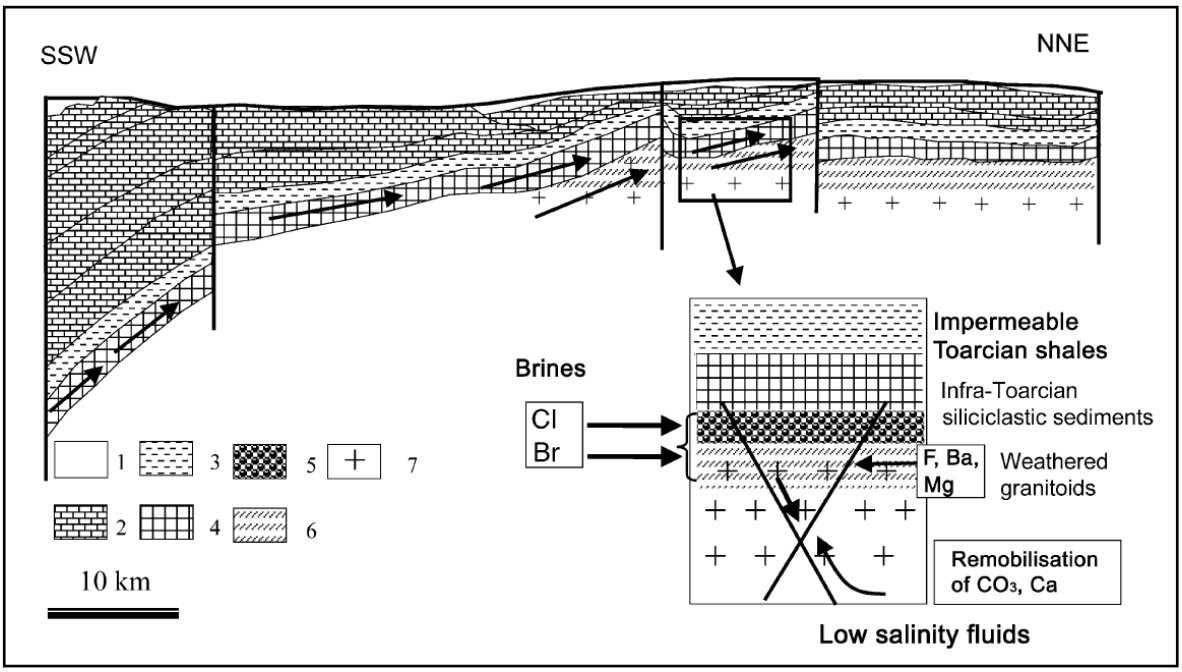

Figure 3-1: Cross-section through the crystalline Hercynian Charroux-Civray plutonic complex and Aquitaine unconformity, ~30km north of Rochechouart (Boiron et al., 2002). The authors have identified a late fluid event along the unconformity related to the percolation and mixing of seawater with meteoric and metamorphic fluids, which may also have affected Rochechouart.

3.1.3 Project purpose

It is well established that transient hydrothermal circulation was a feature of the post-impact environment in Rochechouart (Section 3.1.1) (Spray et al., 1998; Tagle et al., 2009; Lambert 2010; Schmeider et al., 2010; Sapers et al., 2014); however, an in-depth study of this activity within the impact structure, as well as the identification of pre and post-impact fluid events, is lacking.

This project will focus on two components: documenting and comparing the distribution of secondary mineral assemblages within all Rochechouart lithologies to determine how they have been affected by hydrothermal activity, and constraining hydrothermal fluid temperatures and reservoirs. Previous authors have hypothesized that impact-generated hydrothermal fluid flow is controlled by autochthonous fractures as opposed to impermeable impact breccias (Parnell et al., 2010); this study will also focus on sub-crater lithologies to investigate whether they may have hosted conditions conducive to the development of microbial communities during the cooling period.

3.1.3.1 Distribution and comparison of secondary alteration in impactite and basement lithologies

Previous studies have outlined the principal secondary mineral assemblages in Rochechouart impactites (Section 3.1.1) (Sapers et al., 2014). While some assemblages are pervasive, such as those associated with potassic metasomatism, others are more localized such as carbonates, sulphides and clays. The relationship and context of alteration assemblages relative to host rock type and heat source has yet to be outlined, and so is the focus of this thesis.

3.1.3.2 Constraining hydrothermal fluid reservoirs

As evidenced by isotopic and fluid inclusion studies in other impact structures, hydrothermal fluids may be sourced from a variety of reservoirs (Osinski et al., 2005; Muttik et al., 2010) (Chapter 1, Section 1.4). The Rochechouart target is classified as marginal marine; today it is close to a major unconformity. Marine platform carbonates coeval with the impact event are found only 5km outside the perimeter of the structure. Impacts are capable of producing fractures within their targets a distance of 3 crater radii outside the structure (Chapter 1, Section 1.2); therefore it is possible that seawater was a major constituent of Rochechouart hydrothermal fluids. Metamorphic fluids are also present within the Variscan crystalline basement throughout the Central Massif (Fourcade et al., 2002) and meteoric waters have been recorded as a major constituent of other

impact-hydrothermal systems (Chapter 1, Section 1.4).

3.1.4 Project approach and outline

Following the approach of previous studies on impact hydrothermal systems (Chapter 1, Section 1.4), this study uses a combination of field observations, microscopic and spectroscopic analysis and stable isotope studies to provide an overview of alteration assemblage distribution throughout the structure, the identification of selected pre-impact mineral phases, and the construction of a general hydrothermal cooling model.

3.1.4.1 Methods selection

The first component of this study classifies and documents the various secondary mineral assemblages in all Rochechouart lithologies using a combination of optical and electron microscopy and Raman spectroscopy. This work is complimented by $\delta^{13}C$, $\delta^{18}O$ and $\delta^{34}S$ stable isotope analysis of selected carbonate and sulphide mineral assemblages found throughout impactite and target material within and outside of the structure. Combining these two datasets will allow us to constrain temperature and fluid properties in different areas of the structure and compare and contrast how hydrothermal activity has affected primary impact products. Stable isotope studies of both target and impactite material will enable the differentiation of pre-impact from post-impact and diagenetic alteration phases, and determine the degree to which post-impact hydrothermal activity might have altered target rocks below the transient crater cavity. This work will also test the hypothesis that seawater was a contributing fluid reservoir by using isotope data to compare marine carbonates representing the Mesozoic sea at the time of the impact and secondary carbonates within the structure.

3.1.4.2 Site selection

In order to preserve what little allochthonous impactite material remains in Rochechouart, sampling sites for many lithologies are limited and under discretion from the reserve staff. Notable collection sites are Champagnac quarry, 7.5km north-east of the structure's center, and Montbron village, which is located on the Aquitaine unconformity outside the structure (Figure 3-7).

Champagnac quarry is a unique site in that it cross-cuts the continuous allochthonous unit, discontinuous parautochthonous material and autochthonous impactites, and underlying unshocked target lithologies. It thus showcases the complexities involved in impact cratering at and beneath the transient crater floor. The sub-transient-

crater environment as observed in Champagnac was highly fractured by the impact, forming a network of conduits ideal for fluid flow (Parnell et al., 2010; Chapter 1 Section 1.3). Autochthonous fractures and parautochthonous breccias with intense carbonate and sulphide mineralization are preserved in excellent condition, as is unshocked crystalline target material containing carbonate and sulphide mineralization within primary rock fabrics and secondary fractures and veins, whose origin is unknown (Also see Chapter 2). The accessibility, quality and condition of material make Champagnac an ideal locality to study the multiple generations of orogenesis and alteration overprinted in Rochechouart.

The second notable sampling locality is the village of Montbron, located at the Aquitaine unconformity (Figure 3-7). Limestones exposed in this area are mapped as basal late Triassic/early Jurassic siliciclastic rocks and dolostones, representing Mesozoic seawater ~201 Ma.

3.1.4.3 Material selection

All lithologies collected were studied for evidence of secondary alteration. $\delta^{13}C$, $\delta^{18}O$ and $\delta^{34}S$ stable isotope analyses focus on carbonates and sulphides found within allochthonous, parautochthonous, autochthonous and target lithologies. Multiple phases of hydrothermal alteration are recorded in Rochechouart, and where the amount of material is sufficient to enable extraction, all instances of carbonate and sulphide mineralization were analyzed. Carbon stable isotope analysis of the unconformity limestones from Montbron will reveal the marine carbon isotopic composition of seawater at the time of the impact, and will be used for comparison to secondary carbonates found within the structure.

3.1.5 Carbon stable isotopes

One of the most versatile elements, carbon is found in a variety of organic and inorganic compounds on Earth. Naturally occurring ratios vary as much as 120‰, with the heaviest at >+20‰ and the lightest at < -100‰. Carbon has two stable isotopes (Hoefs, 2009); ^{12}C (98.93%) and ^{13}C (1.07%). Carbon isotopes are generally measured against the Pee Dee Belemnite standard, and expressed as VPDB, or variation relative to PDB.

3.1.5.1 Carbon isotopes and the global carbon cycle

There are two major carbon reservoirs on Earth; biogenic organic carbon and inorganic, or marine, carbon. The organic reservoir is controlled by the recycling and distribution of plant and animal based material, such as coal or methane. The inorganic reservoir is represented by various carbon species found throughout the atmosphere,

hydrosphere and lithosphere, such as atmospheric CO_2 and carbonate minerals. The two reservoirs are marked by distinctly different $\delta^{13}C$ signatures; plants preferentially metabolize ^{12}C during photosynthesis leading to a decrease in the $^{12}C/^{13}C$ ratio, and are isotopically light, averaging around -25‰. Contrastingly, inorganic marine carbonates are heavier, averaging around 0‰ (Hoefs, 2009). The oxidation of organic matter in water may result in carbonate mineral precipitation with intermediate $\delta^{13}C$ values, falling between the range of organic and inorganic reservoirs (Boiron et al., 2002).

3.1.5.2 Fractionation mechanisms

The organic and inorganic carbon reservoirs fractionate distinctly differently, by kinetic processes during photosynthesis and by a series of equilibrium exchange reactions between carbon compounds, respectively.

Fractionation mechanisms in the organic carbon reservoir are kinetic, resulting from differences in metabolic processes involved in photosynthesis between plant species. The uptake and diffusion of atmospheric CO_2 is the primary isotope discriminating step (Hoefs, 2009); due to differences in the permeability of cells involved in regulating CO_2 input during photosynthesis, C_3 plants are more depleted in $\delta^{13}C$ than C4 plants relative to atmospheric CO_2.

The isotopic composition of inorganic carbon is regulated by a series of linked equilibrium exchange reactions between atmospheric CO_2, dissolved bicarbonate species in water and solid carbonate minerals (Equations 3-1 through 3-3) (Hoefs 2009). Each of these equilibrium equations is associated with an isotopic fractionation; the differences in ^{13}C of each species are dependent on temperature, and the abundance of each species is dependent on the pH of the system (Zhang et al., 1995; Hoefs, 2009).

Equation 3-1: Equilibrium exchange reaction 1: dissolution of atmospheric CO_2 into liquid water to form carbonic acid.

$$CO_2 + H_2O \rightarrow H_2CO_3 \text{ (carbonic acid)}$$

Equation 3-2: Equilibrium exchange reaction 2: carbonic acid dissociation into hydrogen and bicarbonate.

$$H_2CO_3 \text{ (carbonic acid)} \rightarrow H^+ + HCO_3^- \text{ (bicarbonate)}$$

Equation 3-3: Equilibrium exchange reaction 3: formation of carbonate species by dissociation of a bicarbonate molecule.

$$HCO_3^-\ (\text{bicarbonate}) \rightarrow H^+ + CO_3^{2-}\ (\text{carbonate})$$

The resulting carbonate ion then bonds with cations such as calcium and magnesium to form solid minerals. The fractionation factors (α) resulting from equilibrium exchange reactions between CO_2 gas and various carbon-bearing compounds commonly found in geologic materials at set temperatures have been determined experimentally (Figure 3-2).

3.1.5.3 Late Triassic $\delta^{13}C$ excursion

The Triassic-Jurassic boundary (at 201.3 Ma) is marked by a global mass extinction event attributed to the onset of Central Atlantic Margin Province, or CAMP, volcanism (Galli et al., 2005). The eruption of CAMP CO_2 into the atmosphere resulted in ocean acidification, which lead to a biocalcification crisis, sea level rise and carbonate platform collapse. This extinction event eliminated approximately 80% of all species, affecting both land and marine organisms. Globally, there is an absence of continuous marine sections and fossils, making the Triassic-Jurassic boundary difficult to investigate.

In addition to sea level rise, CAMP outgassing lead to the destabilization and release of $\delta^{13}C$-depleted methane hydrates, resulting in a global negative isotope anomaly. With the age of the event at 201.3 Ma, and Rochechouart at 201 +/- 2 Ma, it is possible that if seawater was circulating within the structure during the post-impact cooling period secondary carbonates may record the isotope excursion.

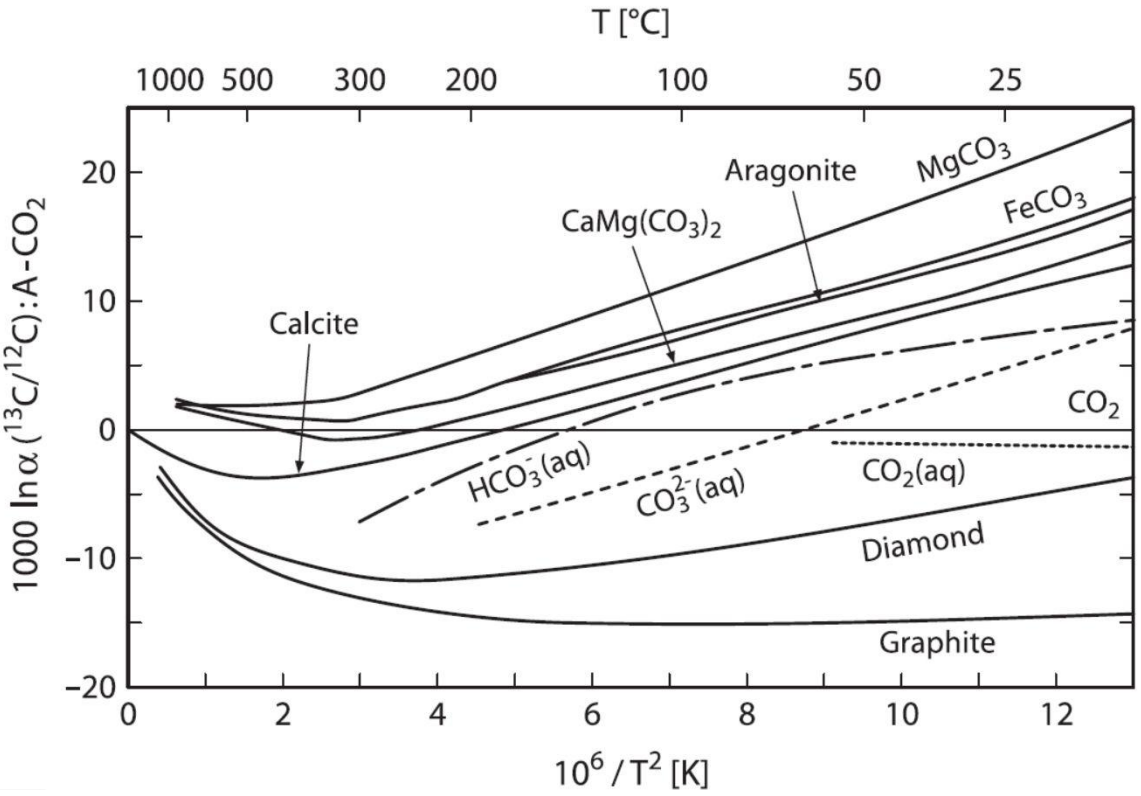

Figure 3-2: Carbon isotope fractionations associated with equilibrium exchange reactions between carbon-bearing species and gaseous CO_2 in common geologic materials (Hoefs, 2009).

3.1.6 Oxygen stable isotopes

The most abundant element on our planet, oxygen is found in numerous solid, liquid and gaseous compounds, making it one of the most common elements used in isotope studies (Hoefs, 2009). Oxygen has three stable isotopes; ^{16}O (99.757%, ^{17}O (0.038%) and ^{18}O (0.205%) and may be measured against the Pee Dee Belemnite (PDB) standard or Vienna Standard Mean Ocean Water (SMOW).

There are multiple environmental factors which may cause oxygen to fractionate; this study will focus on applications as a paleothermometer in the inorganic H_2O-carbonate system.

3.1.6.1 Fractionation mechanisms

Oxygen isotope fractionation is mass dependent; changes in the size of the atom resulting from differences in the number of neutrons leads to behavioural changes throughout fluxes in temperature, pressure and pH of an environment (Hoefs, 2009). For example, if a body of water at room temperature and atmospheric pressure were to heat up and boil, the resulting water vapour would be enriched in the lighter isotope, ^{16}O, and liquid water remaining would be depleted. The fractionation factor between liquid water

and water vapour as a function of temperature has been determined experimentally (Figure 3-3).

3.1.6.2 Oxygen isotope variability in sea and surface water

Spatial and temporal oxygen isotope variability in oceans and meteoric water is intimately linked to fractionation processes throughout the hydrologic cycle (Hoefs, 2009; Gradstein et al., 2012). Water vapour becomes enriched in ^{16}O as it travels to colder regions due to the preferential condensation and precipitation of the heavier isotope, ^{18}O, as rainfall over time and distance from source. Sea ice and polar latitudes are more depleted in the heavier isotope and conversely, warmer, lower latitudes closer to the equator are enriched in ^{18}O (Figure 3-4). This effect is referred to as Rayleigh distillation, and forms the basis of palaeoclimate studies involving global temperature fluctuations recorded in polar ice (Hoefs, 2009; Gradstein et al., 2012).

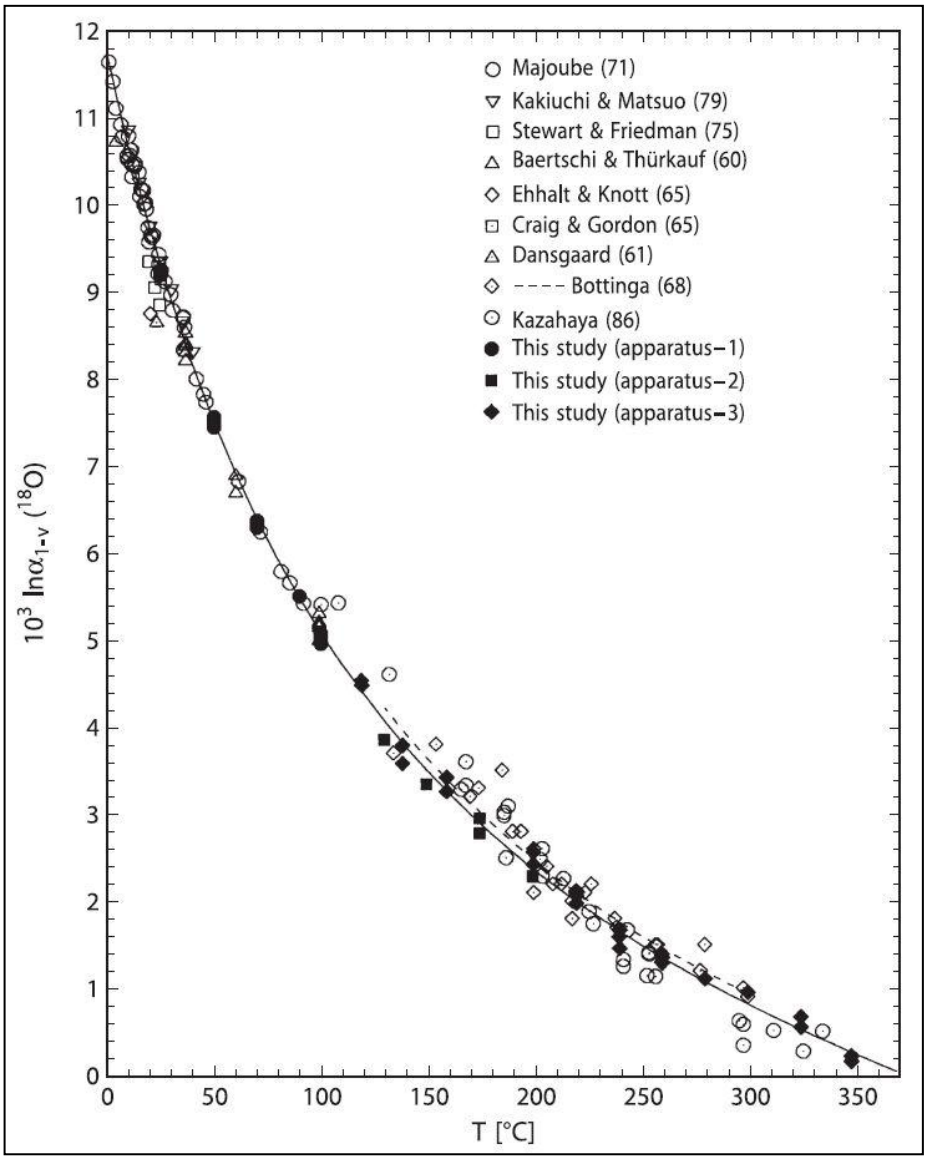

Figure 3-3: Fractionation factor between liquid water and water vapour as a function of temperature (Hoefs, 2009).

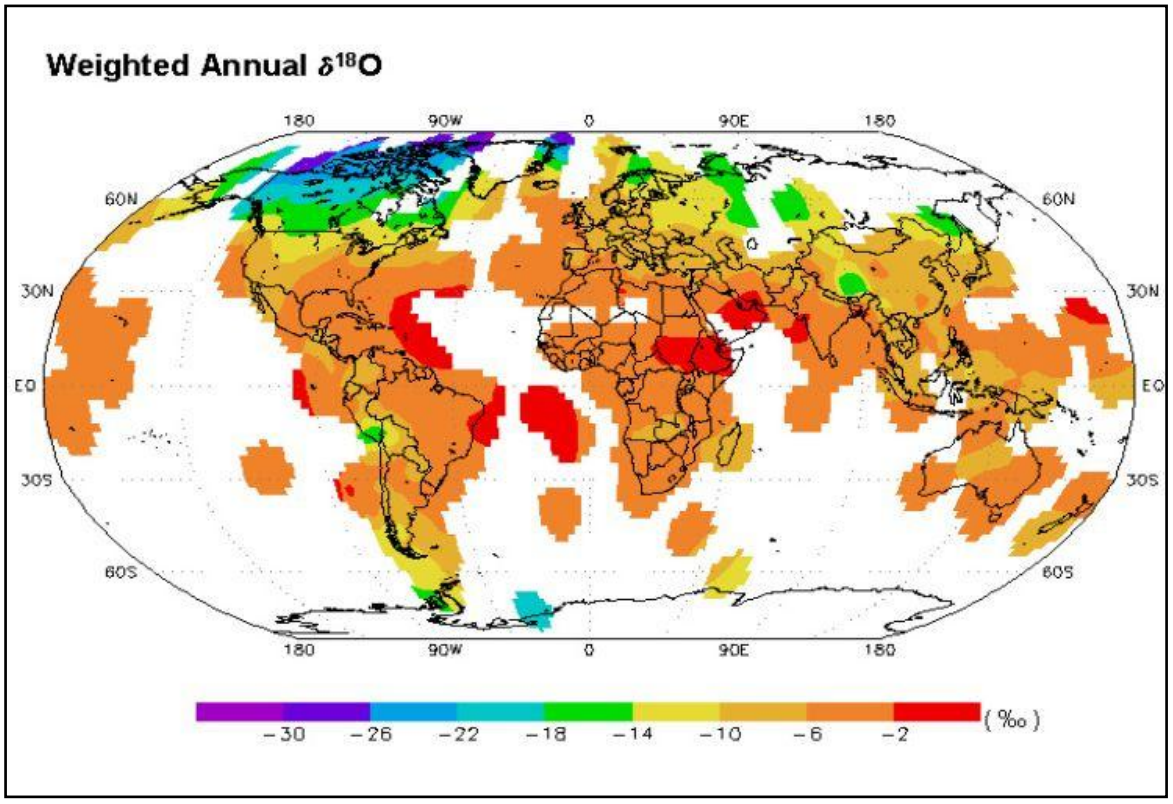

Figure 3-4: Weighted annual $\delta^{18}O$ variability in global sea and surface water from 1961 to 1999 (IAEA, 2001). Warmer, mid latitude regions are enriched in the heavier isotope, while the colder, northern latitudes are depleted.

3.1.6.3 Applications in carbonate-H_2O systems and diagenetic carbonate precipitation

Oxygen isotope ratios in secondary minerals record the thermal and fluid history of hydrothermal and metamorphic events. In oxygen isotope studies involving fluid-rock interactions, it is most useful to know the $\delta^{18}O$ of the starting fluid; unfortunately this is not always the case, and temperatures may then only be constrained using models (3.2.3.5) (Vasconcelos, 2005; Hoefs, 2009). The fractionation factor, α, between various carbonate minerals and volatile compounds has been determined experimentally for decades; these equations can be used to model temperatures where the $\delta^{18}O$ of a mineral is known but the fluid is unknown (Figure 3-5).

The formation of carbonate minerals is represented by the reaction of a cation, most commonly calcium, magnesium or iron, with a carbonate anion (Equation 3-4). Positively charged metals and alkali earth metals are often present within a system as chloride complexes, resulting from preceding or concomitant hydrothermal reactions within host rocks or originating from the parent fluid reservoir (i.e. calcium or magnesium chlorides in

seawater) (Pirajno, 2009). Chloride complexes destabilize as a result of pH neutralization over the course of the lifetime of a hydrothermal system; if sufficient bicarbonate species are present, a neutralized pH will allow for carbonate mineral precipitation (Pirajno, 2009).

Equation 3-4: Reaction of positively charged divalent metal (Me) with negatively charged carbonate molecule to form a solid carbonate mineral (Pirajno, 2009).

$$Me^{2+} + CO_3^{2-} \rightarrow MeCO_3 \text{ (carbonate mineral)}$$

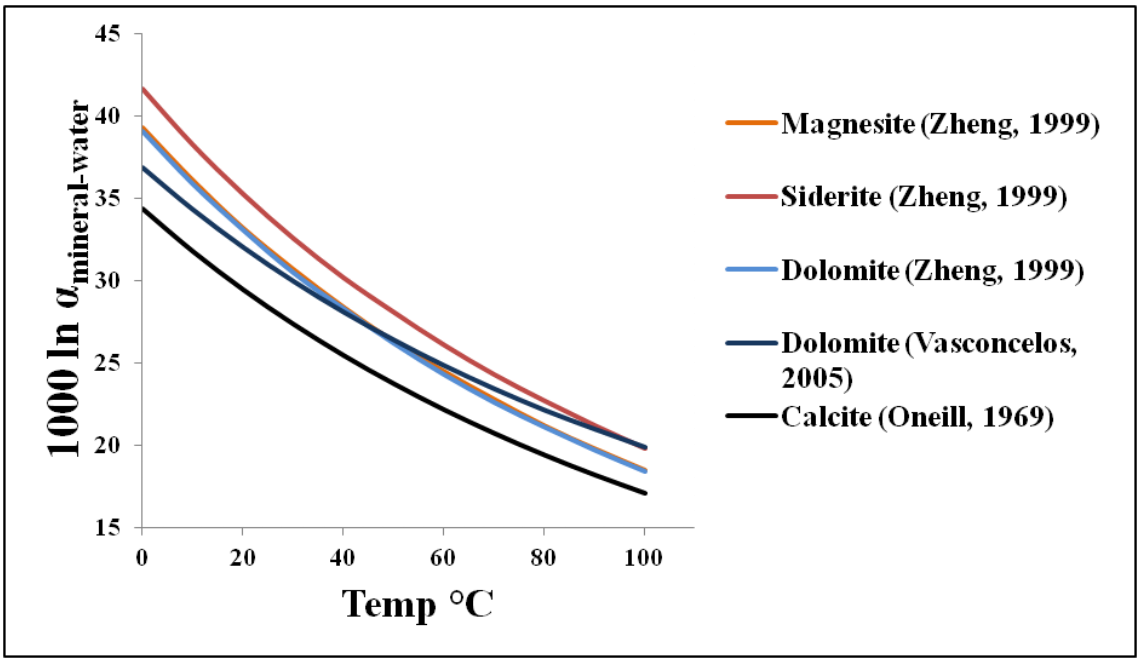

Figure 3-5: Fractionation factors (1000 ln α) between various carbonate minerals and water as a function of temperature. As temperature increases, the fractionation factor between mineral species and water decreases (Oneill, 1977; Zheng 1999; Vasconcelos, 2005).

3.1.7 Sulphur stable isotopes

Sulphur has five stable isotopes; ^{32}S (94.93%), ^{33}S (0.76%), ^{34}S (4.29%) and ^{36}S (0.02%), and is measured against the Canyon Diablo Troilite (CDT) standard (Seal et. al (2006; Hoefs, 2009). Naturally occurring sulphur isotope ratios vary by approximately 180‰, with the heaviest sulphates at +120‰, and the lightest sulphides at -65‰ (Hoefs, 2009). Isotope variations throughout the sulphur cycle are regulated by kinetic processes and exchange reactions between mineral pairs.

3.1.7.1 Sulphur isotope variability in major geologic reservoirs

The most common naturally occurring inorganic sulphur-bearing compounds are

sulphides (H_2S) and sulphates (SO_4^{2-}), and the largest reservoirs are the mantle, seawater and sediment (Figure 3-6) (Hoefs, 2009). Overall, seawater sulphate and evaporates are isotopically heavy, sulphides cooled from a melt are near 0 and sedimentary and hydrothermal sulphides cover a wide range, tend to be isotopically light, and may form as a by-product of thermochemical or biological sulphate reduction in diagenetic environments.

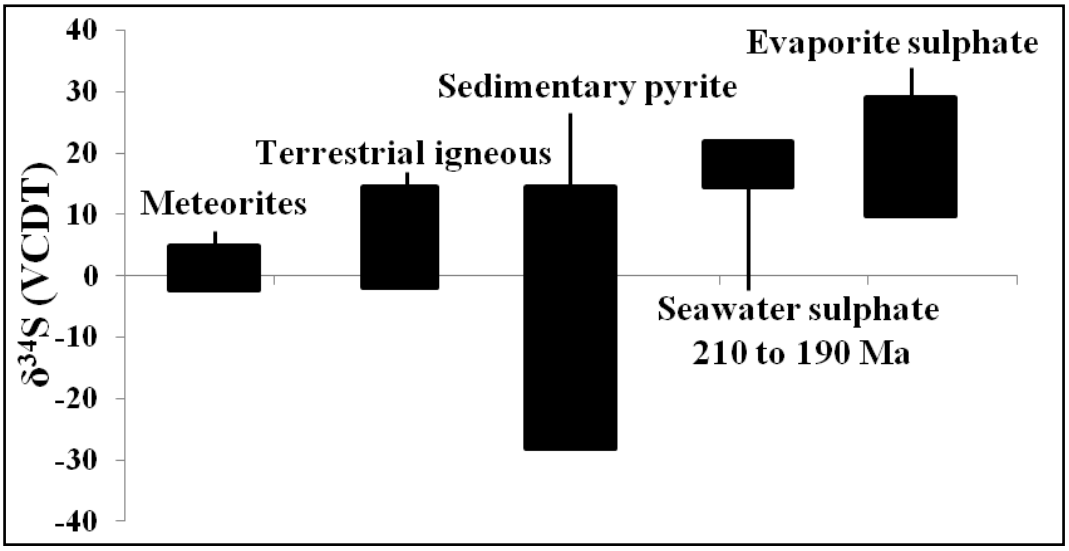

Figure 3-6: Major sulphur geologic reservoirs and representative $\delta^{34}S$ values, including seawater sulphate at during the late Triassic/early Jurassic, modified from Seal et. al (2006) and Hoefs (2009).

3.1.7.2 Biological and thermochemical sulphate reduction

Sulphur isotopes may fractionate kinetically, through biological and thermochemical redox reactions between sulphides and sulphates (Machel, 2001; Hoefs, 2009). Biological sulphate reduction, or BSR, is the process by which certain types of bacteria obtain energy by using sulphate as an electron accepter during metabolism of organic compounds; in the process of "breathing" and stripping the oxygen attached to sulphate (SO_4^{2-}), hydrogen sulphide is created as a byproduct (H_2S) (Equation 3-5) (Machel, 2001). BSR is common in diagenetic settings up to around 100ºC where sufficient organic material is present and often where conditions are anoxic, and the sulphur produced is characteristically isotopically light (Machel, 2001). Sulphate-reducing bacteria are some of the oldest-known organisms; they are found in a wide range of habitats, from hostile mid-ocean ridge vents on the seafloor to the bottom of calm, shallow lakes. Chemosynthesizers, or organisms which live solely off energy produced by chemical reactions, are of significant astrobiological interest; scientists have discovered colonies of sulphur reducers thriving in environments once thought uninhabitable, and it has been

hypothesized that they may exist in inhospitable environments on other rocky planets and satellites (Cockell and Bland, 2005; Osinksi et al., 2013).

Thermochemical sulphate reduction (TSR) is the process by which sulphate is reduced thermally in the presence of organic compounds, rather than metabolically by bacteria. It is common in high temperature diagenetic geologic environments from approximately 100 to 180ºC and is a slow process (Machel, 2001). TSR produces much smaller fractionations than biological reduction; it is only capable of reducing parent sulphate by as much as 20‰ and due to the longer reaction rate, fractionations in resulting sulphides are generally homogenous over a small scale (Machel, 2001).

The mineralogical products of BSR and TSR are very similar and it may be difficult to distinguish unless the $\delta^{34}S$ of the parent sulphate is known, or precise thermal constraints are possible. Large, inhomogeneous fractionations on a small scale are indicative of bacterial sulphate reduction.

The precipitation of metal sulphide minerals in a hydrothermal solution is usually limited by the amount of hydrogen sulphide available (Machel, 2001). As H_2S concentration increases, pH neutralizes and/or temperature decreases, certain ionic compounds will destabilize and sulphide minerals may precipitate as a result (Equation 3-5).

Equation 3-5: Metal sulphide produced as a result of bacterial sulphate reduction (1) and destabilization of chloride complexes (2) due to fluxes in temperature, pH and H_2S concentration (Pirajno, 2009).

$$(1)\ \text{Organic} + SO_4^{2-} + H^+ \rightarrow 2CO_2 + H_2S + 2H_2O$$

$$(2)\ \text{MeCl (metal chlorides)} + H_2S \rightarrow \text{MeS (metal sulphides)} + 2H^+ + Cl^-$$

3.1.7.3 Isotope exchange reactions between co-existing sulphide minerals

Co-existing sulphide pairs in isotopic equilibrium will have difference isotopic signatures depending on the temperature of an environment. The most common sulphide minerals are pyrite, galena and sphalerite; pyrite is always the most enriched in $\delta^{34}S$, galena the most depleted and sphalerite displays intermediate values. Further information may be found in Hoefs (2009).

3.2 Materials and methods

Material was collected from the study site over the course of two field campaigns.

Coated and non-coated polished thin sections and the surfaces of fractured samples were prepared for petrography, high-resolution SEM imaging, qualitative EDX analysis and Raman spectroscopy at the University of Glasgow at the Imaging Spectroscopy and Analysis Center. Following detailed petrographical and mineralogical characterization isotopic analysis of carbonate and sulphide minerals was performed at the Scottish Universities Environmental Research Center in East Kilbride.

3.2.1 Field sessions and material collection

Two field campaigns, one in October 2013 and the second in August 2014, were undertaken in order to determine field relationships and collect material with permission from the Reserve Naturel de Rochechouart-Chassenon and with the guidance and assistance of Dr. Philippe Lambert, Dr. Paula Lindgren and Prof. Martin Lee.

A suite of hand samples representing the main impactite lithologies was collected as well as unshocked basement material within the structure and marine carbonates representing the Mesozoic sea at the time of the impact outside the structure (Figure 3-7) (Table 3-2).

Samples were stored in plastic bags and coordinates were recorded at outcrops and collection sites. Material was either returned to Glasgow by the author or shipped by the reserve at a later date (marked with * in Table 3-2).

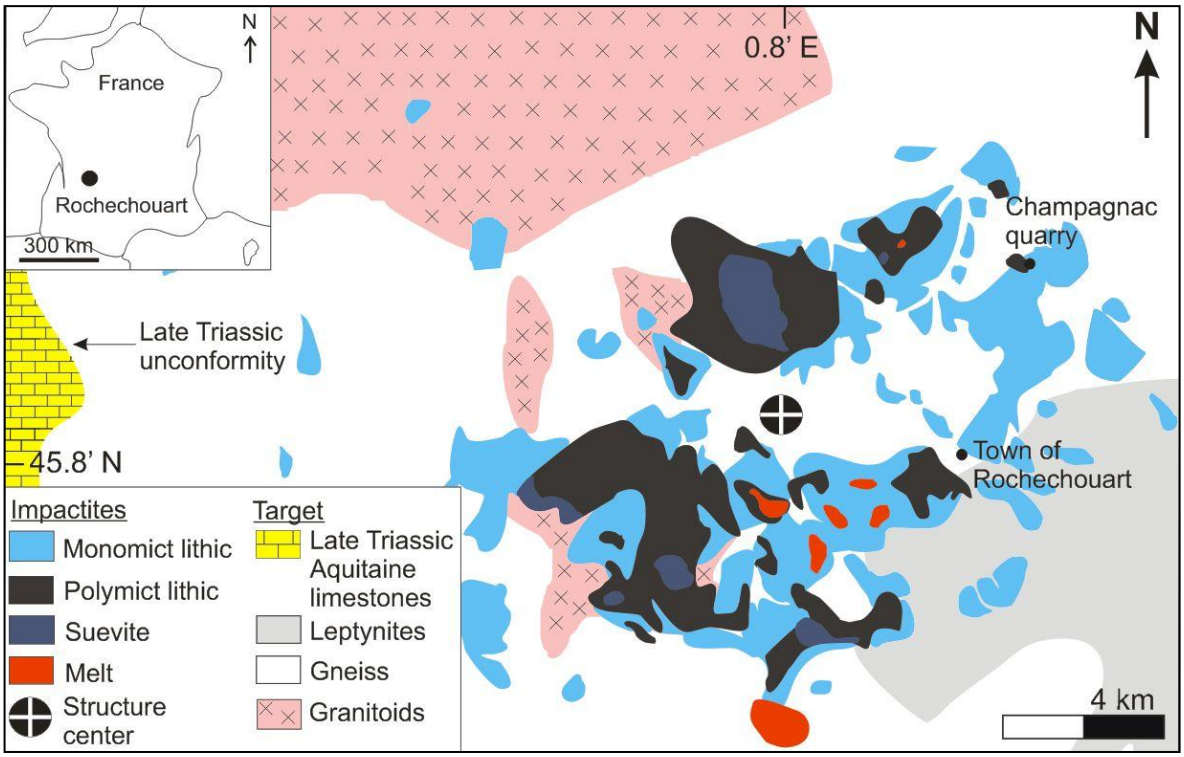

Figure 3-7: Simplified geologic map of Rochechouart target rocks and impactite cover, modified

after Lambert (2010) and BRGM map numbers 686 (La Rochefoucauld) and 687 (Rochechouart).

Table 3-2: Summary of material collected during the 2013 and 2014 field seasons in the Rochechouart impact structure.

Rock type		Location	Season
Impactites	Impact melt rock, type Babaudus	Near central area of Valette, and Reserve archive	2013
	Particulate impact melt rock, type Montoume	Montoume quarry, outside Montoume village	2013
	Melt-poor suevite, type Chassenon* and impactoclastite sub-unit	Chassenon quarry	2013
	Polymict lithic breccia, type Rochechouart*	Rochechouart village, base of Chateau	2013
	Monomict lithic breccia, type Champagnac	Champagnac quarry	2013 and 2014
	Autochthonous impactite	Champagnac quarry	2013 and 2014
	Polymict melt-bearing breccia dike	Champagnac quarry	2014
Basement	Champagnac diorite/granodiorite	Champagnac quarry	2013 and 2014
	Upper Gneiss	Champagnac quarry	2013

Note: Not all basement lithologies could be sampled during this study.

3.2.2 Petrography, SEM, EDX and Raman studies

Thirty-three 30 µm-thick polished thin sections (Table 3-3) were prepared from nine representative lithologies (Table 3-2) for transmitted and reflected light petrographic studies.

An Olympus DP25 5-megapixel microscope camera attached to an Olympus BX41 laboratory microscope coupled with Cell^B FIVE version 5.0.1233 image processing software was used for transmitted and reflected light microscopy and image capture.

Image exposure times ranged from 30 ms to 5 seconds in polarized, plane polarized (XPL) and reflected light.

Table 3-3: List of thin sections

Rock type	ID	Rock type	ID	Rock type	ID
Impact melt rock	M-B-1	Polymict lithic breccia	L-R-1	Autochthonous	CA-1
	M-B-2		L-R-3	Unknown	CU-1
	M-B-3		L-R-4		CU-2
Melt-bearing breccia	S-C-1		L-R-5		CU-3
	S-C-2	Particulate melt	PM-1	Champagnac dike	CP-1
	S-C-3		PM-2		CP-2
	S-C-5		PM-3		CP-3
	S-C-6		PM-4	Basement	BT-1
	S-C-7		PM-5		BT-2
	F-C-1		PM-6		BT-3
				Parautochthonous	CB-1
					CB-2
					CB-3

SEM and EDX analyses were performed using a Carl Zeiss Sigma variable pressure analytical SEM with Smart SEM version 5.05 software, and an FEI Quanta 200F environmental SEM with EDAX Genesis version 6.35 software. For secondary electron imaging (SE) and angle selective backscattered electron imaging (AsB), polished thin sections were coated with 10 nm of carbon using an Agar Scientific automatic SEM carbon coater. Five samples of four lithologies were broken to approximately 1cm x 1cm x 1cm dimensions, coated with 10 nm of Au using an Agar Scientific automatic sputter coater and grounded using Agar Scientific silver paint. Energy dispersive X-ray (EDX) mapping and qualitative analysis was performed using AzTec 2.2 SP1 software on the carbon-coated polished thin sections. Maps were acquired at 1024 x 768 resolution with pixel dwell times ranging from 25µs to 40µs for acquisition periods ranging from 5 minutes to 5 hours.

EDX analyses were performed in high-vacuum (2.6×10^{-6} torr) at a working distance of approximately 8.5 to 11.5mm, with a beam current of 20.00 keV and aperture size ranging from 30µm to 60 µm.

Table 3-4: List of Au-coated fractured samples

Description	ID
Vesicular impact melt rock	2013-1-F
Champagnac melt-bearing dike	2014-1-F
Montbron Limestone	2014-4-F
Champagnac monomict breccia, clast with cement	2014-13-Fa
Champagnac monomict breccia, clast	2014-13-Fb

A Renishaw InVia Raman microscope equipped with 514nm and 785nm laser sources and WiRE version 4.1 software was used to investigate minerals in non-coated polished thin sections.

Static and extended scans were performed at exposure times ranging from 1 to 5 seconds, at laser power ranging from 20% to 100% and accumulation times of 1 to 20 seconds. Spectra were checked against the Renishaw inorganic library (2010) and the RRUFF Raman spectra database (LaFuente et al., 2015).

3.2.3 $\delta^{13}C$, $\delta^{18}O$ and $\delta^{34}S$ stable isotope analysis

Carbonate and sulphide minerals were extracted from impactite and basement rocks for $\delta^{13}C$, $\delta^{18}O$ and $\delta^{34}S$ analysis at the Scottish Universities Environmental Research Center (SUERC) (Table 3-6 and 3-7).

Carbon isotope compositions were measured from CO_2 gas extracted from reacted calcite and dolomite, and calculated relative to Pee Dee Belemnite (PDB) and Standard Mean Ocean Water (SMOW).

Oxygen isotope compositions, also measured from CO_2 gas extracted from reacted calcite and dolomite, are expressed relative to Standard Mean Ocean Water (SMOW).

Individual crystals of calcite and dolomite were too small and intimately intergrown to be physically separated, thus the method of sequential acid extraction of mixed carbonates as outlined by Al-Aasm et al. (1990) was utilized.

Sulphur isotope compositions were measured from SO_2 gas extracted from Fe-sulphides and calculated relative to the Canyon Diablo Troilite standard (CDT). For samples large enough to yield at least 4mg of powdered separate, the extraction of SO_2 gas was performed using conventional techniques outlined by Robinson and Kusakabe (1975) (Section 3.2.3.3). Deposits whose size was insufficient to yield at least 4 mg of powder separate were analyzed using in situ laser combustion techniques outlined by Wagner et al. (2002) (Section 3.2.3.2) (Appendix).

Five sets of standards were run before sample analysis; NBS123 sphalerite, IAEAS-3 argentite, and an internal lab standard, CP1 chalcopyrite, for $\delta^{34}S$, and an internal lab standard, MAB-2 medium marble (calcite) for $\delta^{13}C$, $\delta^{18}O$ (Table 3-5) (Appendix).

Table 3-5: Summary of isotope standards

Sample ID	Mineral
NBS123	Sphalerite
IAEAS-3	Argentite
CP1 (internal)	Chalcopyrite
MAB-2 (internal)	Calcite

3.2.3.1 Sample selection

A sample set representative of carbonate and sulphide mineralization within impactites, unshocked and unbrecciated target material, and Triassic marine carbonates was used for comparative isotopic studies. Mineralized fractures of unknown origin from within unshocked basement were also analyzed; these fractures were hosted within unshocked granodiorite found throughout Champagnac quarry.

3.2.3.2 Sequential acid extraction of CO_2 from mixed carbonates (Al-Aasm, 1990)

Following the methods of Al-Aasm et al. (1990), 10 to 20 mg powdered samples of calcite plus dolomite were reacted in sealed glass digestion tubes *in vacuo* with 3.5 ml of 100% H_3PO_4. Digestion vessels were then placed in a 25°C water bath for 3 hours for the dissolution of calcite (Equation 3-6; Table 3-6). CO_2 produced from this reaction was then removed, measured and transferred to a mass spectrometer tube (Appendix).

Equation 3-6: Reaction of calcite with 100% phosphoric acid

$$Ca(CO_3)\ (calcite) + H_3PO_4\ (phosphoric\ acid) \Rightarrow CaHPO_4 + CO_2 + H_2O$$

Vessels with remaining phosphoric acid and dolomite were then vacuum pumped, sealed and placed in a 100°C metal hotplate for overnight reaction of remaining dolomite (Equation 3-7). Extractions were measured on a SIRA II mass spectrometer.

Equation 3-7: Reaction of dolomite with 100% phosphoric acid

$$3CaMg(CO_3)_2\ (dolomite) + 8H_3PO_4\ (phosphoric\ acid) \Rightarrow Ca_3(PO_4)_2 + 6H_2O$$

$$+ 6CO_2(g) + 3Mg(H_2PO_4)_2$$

3.2.3.3 Conventional SO_2 extraction from sulphide species (Robinson and Kusakabe, 1975)

Powdered separates of pyrite, marcasite and chalcopyrite were extracted manually from hand samples using an electric hand drill. 200mg of an oxidizing agent, Cu_2O, was combined with between 4 and 14mg of powdered metal sulphide, placed in a glass tube with quartz fiber and combusted at 1075°C *in vacuo* for 25 minutes. This reaction releases CO_2 and SO_2 gas. SO_2 is then isolated from the mixture using a combination of a CO_2 ice trap and an n-pentane trap, and then transferred to a mass-spectrometer sample tube for analysis. Extractions were run on a Thermo Fisher Scientific MAT 253 mass spectrometer. Pyrite and marcasite species were extracted simultaneously and analyzed together for $\delta^{34}S$.

3.2.3.4 In-situ laser combustion extraction of SO_2 from metal sulphides (Wagner et al. 2002)

Hand samples were cut to 2cm x 3cm blocks and polished. Metal sulphides were combusted in situ with a Spectron Lasers 902Q Nd:YAG laser in a vacuum chamber with excess oxygen, and the released SO_2 gas was measured using an on-line VG SIRA II mass spectrometer.

3.2.3.5 Oxygen isotope temperature modeling equations

Because the $\delta^{18}O$ of the starting fluid is unknown, temperatures are modeled over a range of fluid ^{18}O values using the equations outlined by O'Neill et al. (1969) for calcite-H_2O (Equation 3-8) and Vasconcelos et al. (2005) for dolomite-H_2O (Equation 3-9).

Equation 3-8: Fractionation factor between calcite and water as determined by O'Neill et al. (1969).

$$1000 \ln \alpha_{\text{calcite-water}} = 2.78(10^6 T^{-2}) - 3.39$$

Equation 3-9: Fractionation factor between dolomite and water as determined by Vasconcelos et al. (2005).

$$1000 \ln \alpha_{\text{dolomite-water}} = 2.73(10^6 T^{-2}) + 0.26$$

Table 3-6: Summary of samples selected for calcite and dolomite $\delta^{13}C$ and $\delta^{18}O$ determinations

Sample ID	Rock type	Description	Sample wt (mg)	Assc. Secondary minerals
	Late Triassic basal dolomites			
TC-1		Massive marine carbonates	13.4	N/A
TC-2		Massive marine carbonates	12.0	N/A
	Monomict lithic breccia			
MC-1		Secondary matrix cement	17.1	Pyr, Ort
MC-2		Secondary matrix cement	21.0	Pyr, Ort
MC-3		Secondary matrix cement	2.80	Pyr, Ort
MC-4		Secondary matrix cement	32.1	Pyr, Ort
MC-5		Secondary matrix cement	23.6	Pyr, Ort
MC-6		Secondary matrix cement	22.4	Pyr, Ort
MC-7		Secondary matrix cement	21.3	Pyr, Ort
	Polymict dike			
PC-1		Massive matrix cement, zone 1	48.3	N/A
PC-2		Massive matrix cement, zone 1	15.8	N/A
PC-3		Massive matrix cement, zone 3	52.1	N/A
	Autochthonous			
AC-1		Euhedral, 2-3mm, individual rhombs	21.2	Pyr

	Unknown			
UC-1		Mineralized fracture surface in granodiorite	36.2	Cpy, Ort
UC-2		Mineralized fracture surface in granodiorite	36.1	Cpy, Ort
UC-3		1cm vein in granodiorite	21.9	Pyr
UC-4		4 to 5cm veins in granodiorite	23.6	Qtz
UC-5		4 to 5cm veins in granodiorite	21.5	Qtz

Abbreviations: Cpy = chalcopyrite; Ort = orthoclase; Pyr = pyrite; Qtz = quartz.

Table 3-7: Summary of samples analyzed for $\delta^{34}S$

Sample	Rock type	Description	Mineral	Analysis type	Sample wt (mg)	Assc. secondary minerals
	Monomict lithic breccia					
MS-1		Secondary matrix cement; indv. 3mm cubic crystal	Pyr	Con	5.10	Cal, Dol, Ort
MS-2		Secondary matrix cement; indv. 3mm cubic crystal	Pyr	Con	4.00	Cal, Dol, Ort
MSL-1		Sub-mm vein in clast fabric	Pyr	Laser	N/A	Dol, Qtz
MSL-2		Sub-mm vein in clastic matrix	Pyr	Laser	N/A	N/A
	Autochthonous fractures					
AS-1		Massive, mineralized fracture coatings in granodiorite	Pyr, Mar	Con	9.80	Cal, Dol, Qtz, Phy, Ort
AS-2		Massive, mineralized fracture coatings in granodiorite	Pyr, Mar	Con	11.5	Cal, Dol, Qtz, Phy, Ort
AS-3		Massive, mineralized fracture coatings in granodiorite	Pyr, Mar	Con	8.30	Cal, Dol, Qtz, Phy, Ort
AS-4		Massive, mineralized fracture coatings in granodiorite	Pyr, Mar	Con	13.8	Cal, Dol, Qtz, Phy, Ort
AS-5		Massive, mineralized fracture coatings in granodiorite	Pyr, Mar	Con	10.1	Cal, Dol, Qtz, Phy, Ort
AS-6		Massive, mineralized fracture coatings in granodiorite	Pyr, Mar	Con	8.40	Cal, Dol, Qtz, Phy, Ort
AS-7		Massive, mineralized fracture coatings in granodiorite	Pyr, Mar	Con	9.20	Cal, Dol, Qtz, Phy, Ort
ASL-1		Secondary cement, brecciated basement quartz veins	Pyr	Laser	N/A	N/A
ASL-2		Secondary cement, brecciated basement quartz veins	Pyr	Laser	N/A	N/A
ASL-3		Secondary cement, brecciated basement quartz veins	Pyr	Laser	N/A	N/A
	Basement					
BS-1		2 to 3mm crystal assc. w/ primary K-feldspar melt in gneiss	Pyr	Con	6.50	N/A
BS-2		2 to 3mm gneiss vein, cross-cutting fabric	Pyr	Con	5.50	Dol

BSL-1		Sub-mm crystals in gneiss fabric	Pyr	Laser	N/A	N/A
BSL-2		Sub-mm crystals in gneiss fabric	Pyr	Laser	N/A	N/A
BSL-3		2 to 3mm vein cross-cutting gneiss fabric	Pyr	Laser	N/A	N/A
	Fractures of unknown origin					
US-1		1 to 2 mm fracture coatings, ind. crystals	Cpy	Con	9.00	Cal, Dol, Ort
US-2		1 to 2 mm fracture coatings, ind. crystals	Cpy	Con	6.20	Cal, Dol, Ort
US-3		4 to 5mm fracture cubic aggregates	Pyr	Con	8.00	Cal, Dol, Ort
US-4		4 to 5mm fracture cubic aggregates	Pyr	Con	7.40	Cal, Dol, Ort

Abbreviations: Cal = calcite; Con = conventional; Cpy = Chalcopyrite; Dol = dolomite; Mar = marcasite; Ort = orthoclase; Phy = various phyllosilicates; Pyr = pyrite; Qtz = quartz.

3.3 Results

3.3.1 Aqueous alteration of Rochechouart lithologies

3.3.1.1 Amphibolite gneiss

The Upper and Lower Gneiss units within the basement show evidence for minor K-metasomatism. The dominant secondary mineral is sericite (muscovite), with minor chlorite, biotite, carbonates and sulphides (Table 3-8).

Muscovite: Partially replaces albite and orthoclase within the gneiss fabric, forming "dirty" yellow-white sericitic texture in transmitted light (Figure 3-9). *Chlorite:* Fe-Mg phyllosilicates have been partially replaced by biotite; high Fe-chlorite is not as common within the gneiss as other lithologies, but some crystals may show a dull blue color in transmitted light. Chlorite and biotite contain rectangular voids where Ti oxides have weathered, and Fe-rich rims with K-depleted interiors (Figure 3-9, A1). *Carbonate:* Dolomite mineralization is sparse, forming secondary veins within and cross-cutting gneiss fabric, usually associated with iron sulphides. *Sulphide:* Iron sulphide mineralization is moderate, forming euhedral, cubic crystals within fabric and veins, and may be associated with carbonate mineralization (Figure 3-8, B; Figure 3-9, B1 and B2). *Ti-oxides:* Small amounts of oxide minerals are associated with Fe-Mg phyllosilicates and quartz; in many cases the oxides are weathered, leaving only rectangular, elongated voids (Figure 3-8, A; 3-9, A1 and A2).

Table 3-8: Secondary minerals in basement gneiss

Mineral	Occurrence	Description
Muscovite	Fabric; partial replacement of feldspars.	Very fine, less than 20 μm, sericitic texture.
Chlorite-biotite	Fabric; partial replacement of chlorite.	Euhedral to subhedral, up to 0.5 mm, brown to blue in crossed polars, light green-brown in plane light.
Dolomite	Veins cross-cutting and along fabric plane.	250 to 400 μm veins; may be associated with pyrite.
Sulphide	Veins cross-cutting and along fabric plane.	Up to 0.5 mm thick veins, may be associated with carbonate.
Ti-Fe oxides	Fabric; often weathered, forming rectangular	Subhedral to anhedral, 10 μm

voids within Fe-Mg phyllosilicates and quartz. to 0.25mm crystals.

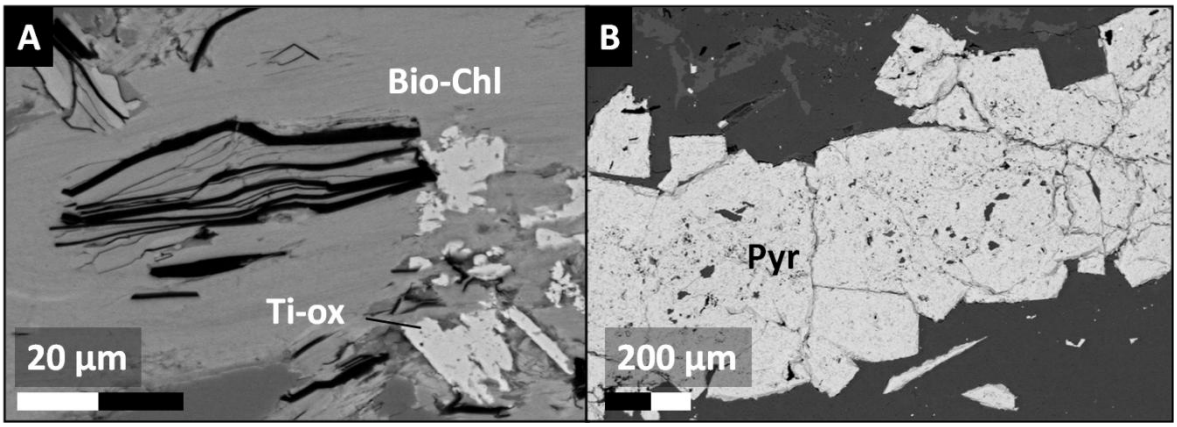

Figure 3-8: (A) SEM AsB images of alteration within amphibolite gneiss, showing rectangular voids with Fe-Mg phyllosilicates. (B) Pyrite mineralization along the gneiss fabric. (Bio-Ch= biotite-chlorite; Pyr = pyrite; Ti-ox = titanium oxides).

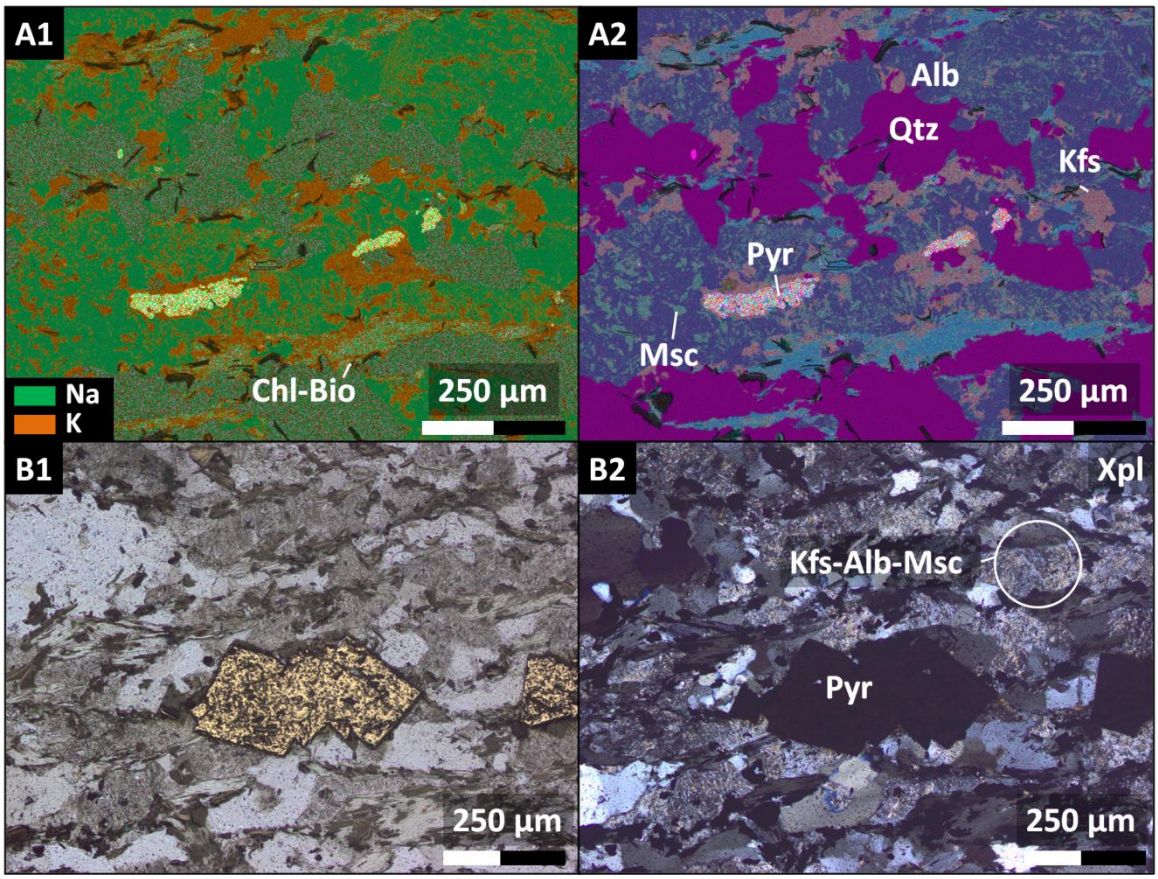

Figure 3-9: (A1 and A2) EDS element maps of amphibolite gneiss. A1 shows the distribution of Na and K, and alteration of Fe-Mg phyllosilicates. Mafic phyllosilicates, chlorite, have K-rich rims as a result of potassic alteration. (B1 and B2) Transmitted + reflected light microscope images of pyrite within the fabric of amphibolite gneiss and sericitic texture of feldspars (Kfs-Alb-Msc). (Alb = albite; Bio = biotite; Chl = chlorite; Kfs = K-feldspar; Msc = muscovite; Pyr = pyrite; Qtz =

quartz).

3.3.1.2 Champagnac granodiorite

The Champagnac granodiorite has been pervasively affected by potassic and propylitic alteration; K-feldspar, white mica, biotite and chlorite are the main alteration products affecting the primary igneous fabric. Myrmekite is a common texture, and is not observed in Rochechouart impactites. Carbonate and sulphide mineralization along fracture surfaces and within veins is not uncommon.

K-feldspar: K-feldspar overgrows and replaces albite, and has precipitated within intercrystalline voids; also replaces plagioclase in myrmekite (Figure 3-11, A and B).*White mica*: feldspars may show a sericitic texture due to alteration to muscovite and paragonite (Figure 3-10, A). *Biotite:* Dark green-brown porphyroblastic biotite can be seen at the hand specimen scale as large, platy, black crystals; locally it may be partially replaced by chlorite (Figure 3-10, B). *Dolomite:* Dolomite has precipitated along fracture surfaces; in concordance with other non-melt bearing lithologies. Crystals are large (0.5 to 1.5mm), well formed, are iron-rich, and may be associated with Fe-sulphides (Figure 3-10, C; 3-11 C1 and C2). *Fe-Ti oxides*: Found as large relict crystals within the fabric. Calcium has been removed from precursor anatase and rutile has precipitated in it's place, forming a skeletal texture (Figure 3-11, D and E), and may also be associated with sulphide minerals. *Sulphide:* Cubic pyrite is found within the primary fabric, associated with dolomite in fractures and within relict sphene crystals.

Table 3-9: Secondary minerals in Champagnac granodiorite

Mineral	Occurrence	Description
K-feldspar	Groundmass and fractures; replacement and overgrowth of albite and precipitated within voids.	Euhedral to anhedral, up to 250 µm crystals, first order grey, often "dirty" due to sericitic texture or Fe-ox inclusions.
Biotite	Porphyroblasts; large, unaltered crystals in groundmass.	Euhedral, 100µm to 2mm, black-brown crystals, seen at hand scale.
Dolomite	Fractures; crystallized along fracture surfaces.	Euhedral to Subhedral, 0.5 to 1.5mm Fe-rich, associated with Fe
Fe-Ti oxides	Replacement and reaction of large sphene	Euhedral, 20 to 30µm crystals,

	crystals with rutile.	opaque in transmitted light (Figure 3-11, D and E).
Sulphide	Minor; commonly associated with carbonates and other Fe-Ti oxide minerals.	Euhedral to Subhedral, 0.5 to 1 mm crystals of chalcopyrite and pyrite (Figure 3-10, C).

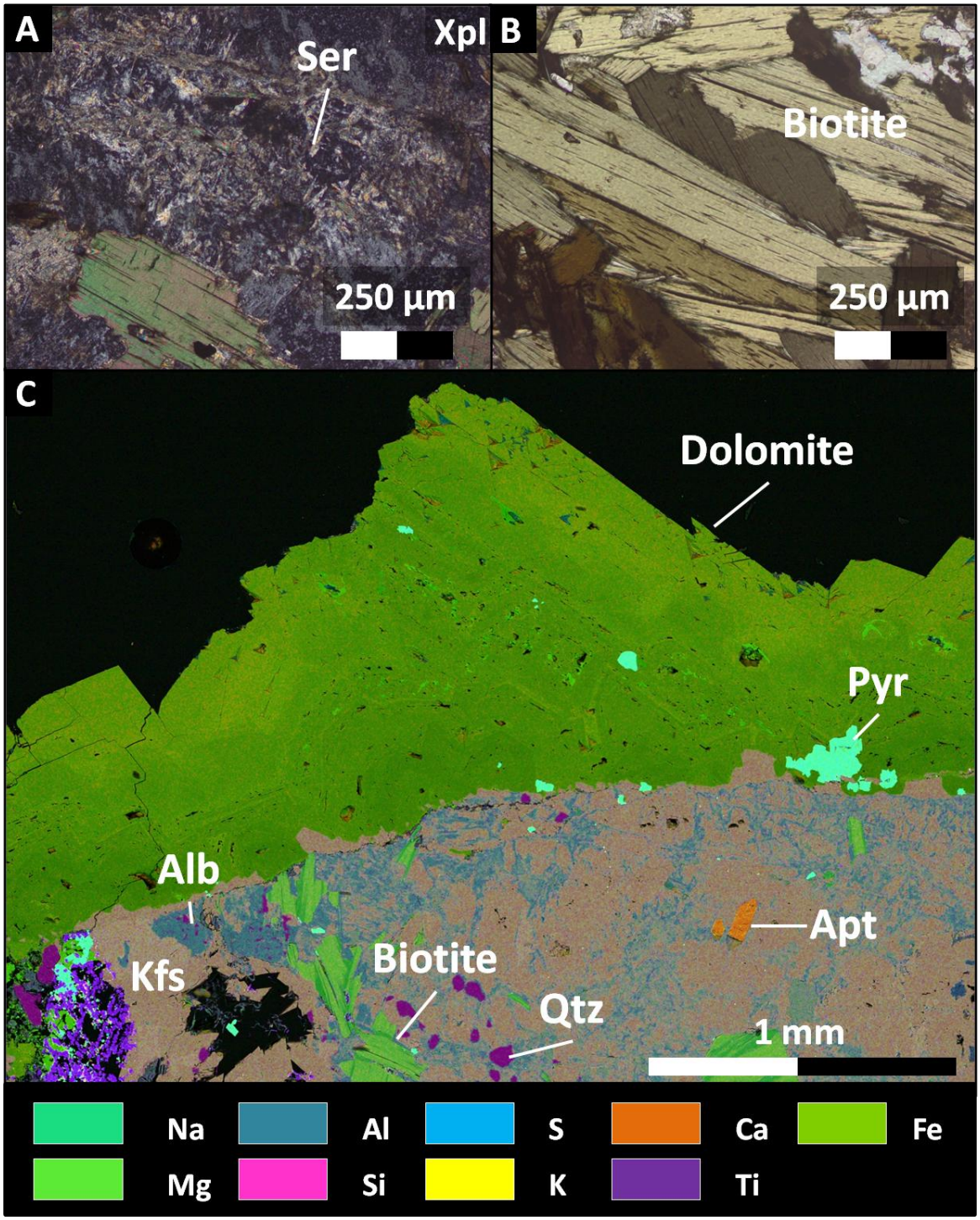

Figure 3-10: (A) Crossed polarized transmitted light microscope image of sericitic texture of felspars in the Champagnac diorite. (B) Large phenocrysts of biotite in plane polarized transmitted light. (C) EDS element map of carbonate mineralization along fracture surface; quartz and

feldspars are sericitized and secondary K-feldspar is common in secondary porosity created by aqueous alteration (Kfs). (Alb = albite; Apt = apatite; Kfs = K-feldspar; Pyr = pyrite; Qtz = quartz; Ser = sericite).

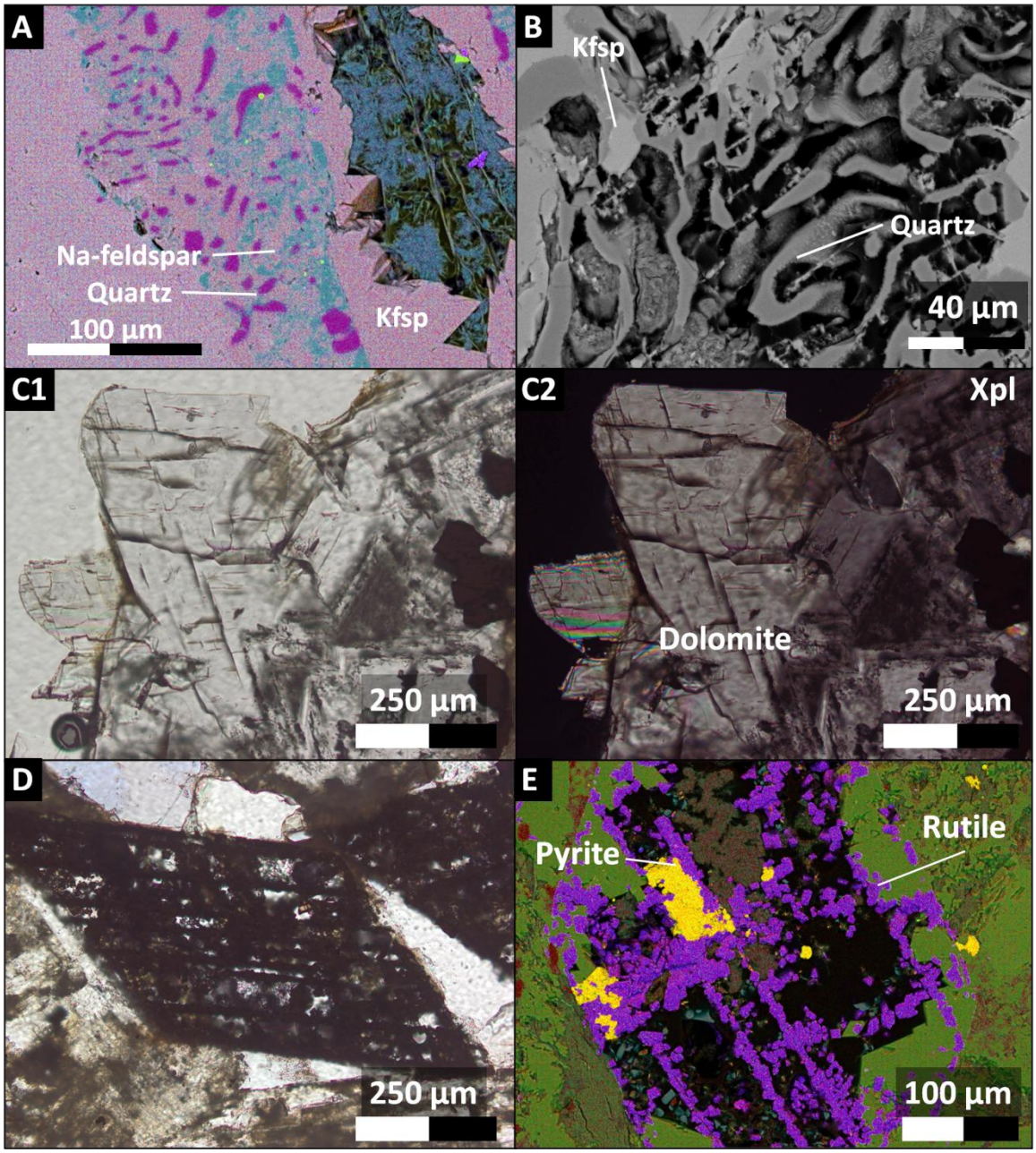

Figure 3-11: (A and B) EDS map and SEM AsB image of myrmekite, a common alteration product associated with metasomatism in igneous rocks. (C1 and C2) Transmitted light microscope images of dolomite precipitation on fracture surface. (D and E) Transmitted light image and EDS map, respectively, of epitaxial growth and reaction of sphene to rutile with secondary iron sulphide mineralization (colors in E: yellow = S; purple = Ti; green = K; red = Si).

3.3.1.3 Autochthonous fractures

Autochthonous fractures within the granodiorite basement at Champagnac have considerable sulphide and carbonate mineralization, more than any other impactite or target lithology. There is also evidence for K-metasomatism within the host rock, but it is not as extensive as in melt-bearing lithologies.

Sulphides: Marcasite and pyrite form fracture coatings and veins within metasomatized basement diorite (Figure 3-14). Small, anhedral iron sulphide veins cross-cut all other minerals within host rock (Figure 3-13). Where sulphide mineralization is intense, iron oxide staining occurs in and around fractures in outcrop, forming gossan (Figure 3-12). *Carbonates:* Euhedral dolomite crystals co-precipitated with and post-date Fe-sulphide; dolomite in all cases has a high Fe content, and may be very weathered (Figure 3-14, C). *K-feldspar*: similar to melt-bearing lithologies, albite is partially replaced and overgrown by K-feldspar (Figure 3-14, B). *Chlorite:* Chlorite is associated with intense sulphide mineralization (Figure 3-13), and is also found in the host rock. *White mica:* Potassic alteration has affected the host rock, as evidenced by the sericitic texture of framework silicates and as observed by previous authors (Lambert, 2010). *Quartz:* Anhedral quartz crystals have precipitated with sulphides, chlorite and feldspars. *Barite:* Very minor amounts of barite may be found within thick, Fe-sulphide veins and fracture coatings.

Table 3-10: Secondary minerals in autochthonous

Mineral	Occurrence	Description
Pyrite + marcasite	Fracture surfaces and veins in basement.	Light-yellow to brown , euhedral to anhedral, 20µm to 0.5cm-thick veins and fracture coatings; larger, well-formed crystals display a variety of geometry. Fracture surfaces may be coated in dusty-orange iron oxides.
Dolomite	Fracture surfaces; pre, syn and post-genetic precipitation with Fe-sulphides.	Euhedral to anhedral, 400 µm to 3mm rhombs; where acts as substrate for sulphides, very weathered.
K-feldspar	Host rock and fractures; partially replaces albite phases.	Euhedral, up to 5 to 10µm overgrowths on Na-phases

		(Figure 3-14).
Chlorite-biotite	Host rock and fractures; may be dispersed throughout heavy sulphide mineralization or found within host rock.	Euhedral, up to 150µm individual crystals (Figure 3-13).
White mica	Host rock and fractures; minor, found within host rock as large, individual crystals or replacing feldspar minerals.	Euhedral to anhedral, 10 to 200µm crystals; forms sericitic texture in silicates.
Quartz	Fractures; associated with heavy sulphide mineralization.	Anhedral, 20 to 100µm, usually associated with intense sulphide mineralization.
Barite	Fractures; rare, isolated occurrences, precipitated with sulphides.	Anhedral, 20 to 50µm crystals.

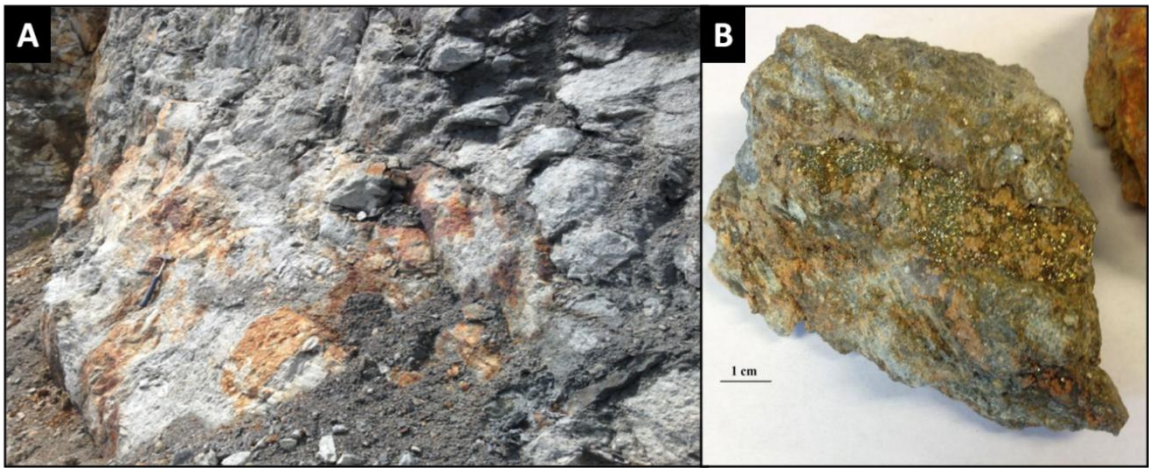

Figure 3-12: (A) Field photo of autochthonous impact fractures in Champagnac, showing orange iron oxide staining, or gossan, where fractures contain heavy sulphide mineralization. (B) Hand specimen of heavy sulphide mineralization, with orange dolomite crystals.

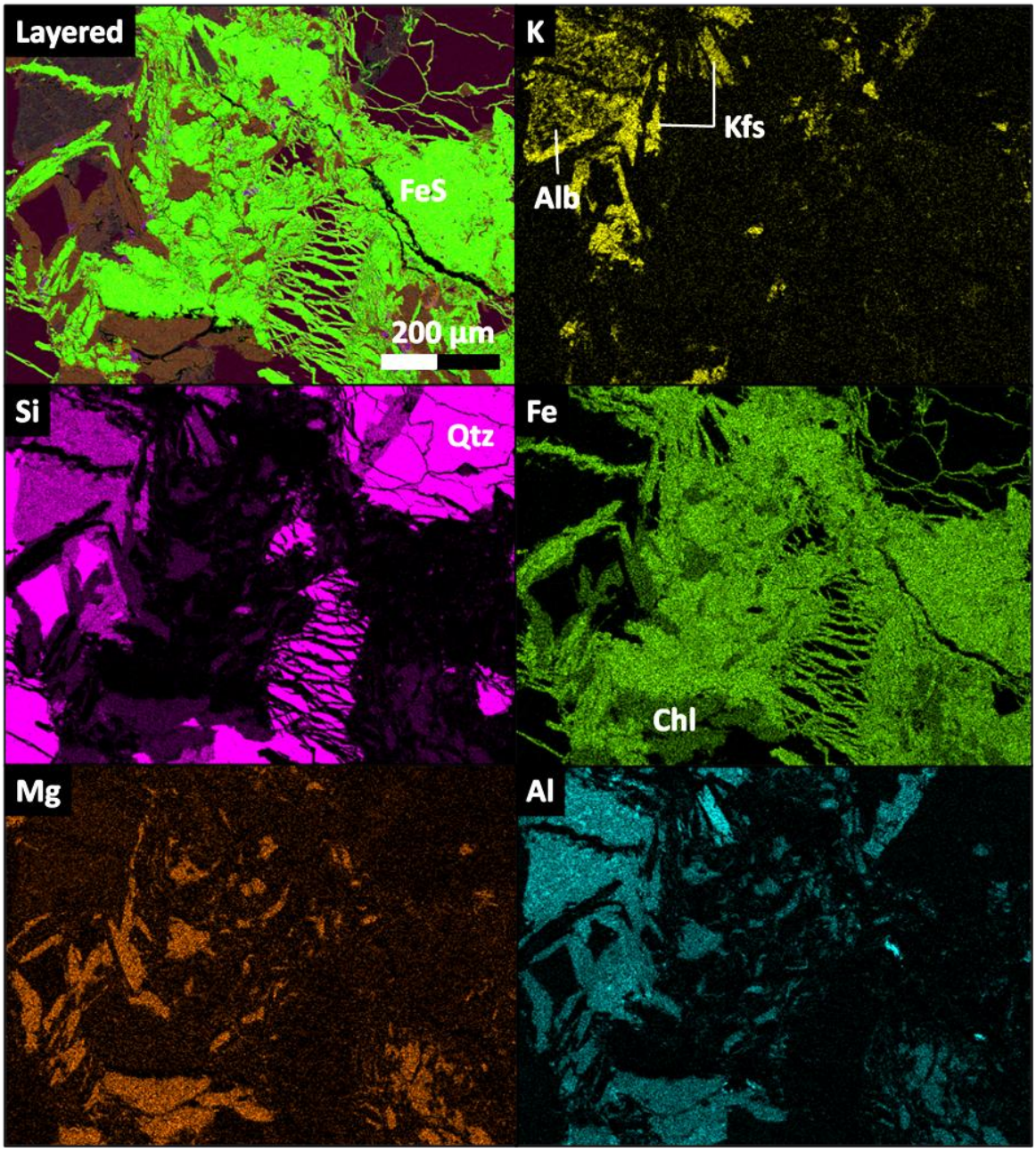

Figure 3-13: EDS element maps of heavy sulphide mineralization in autochthonous basement fractures. Like all other Rochechouart impactites, K-feldspar is seen replacing and overgrowing Na-phases (K map). Anhedral quartz is cross-cut by sulphides (Si map) and chlorite is abundant. (Alb = albite; Chl = chlorite; FeS = iron sulphide; Kfs = K-feldspar; Qtz = quartz).

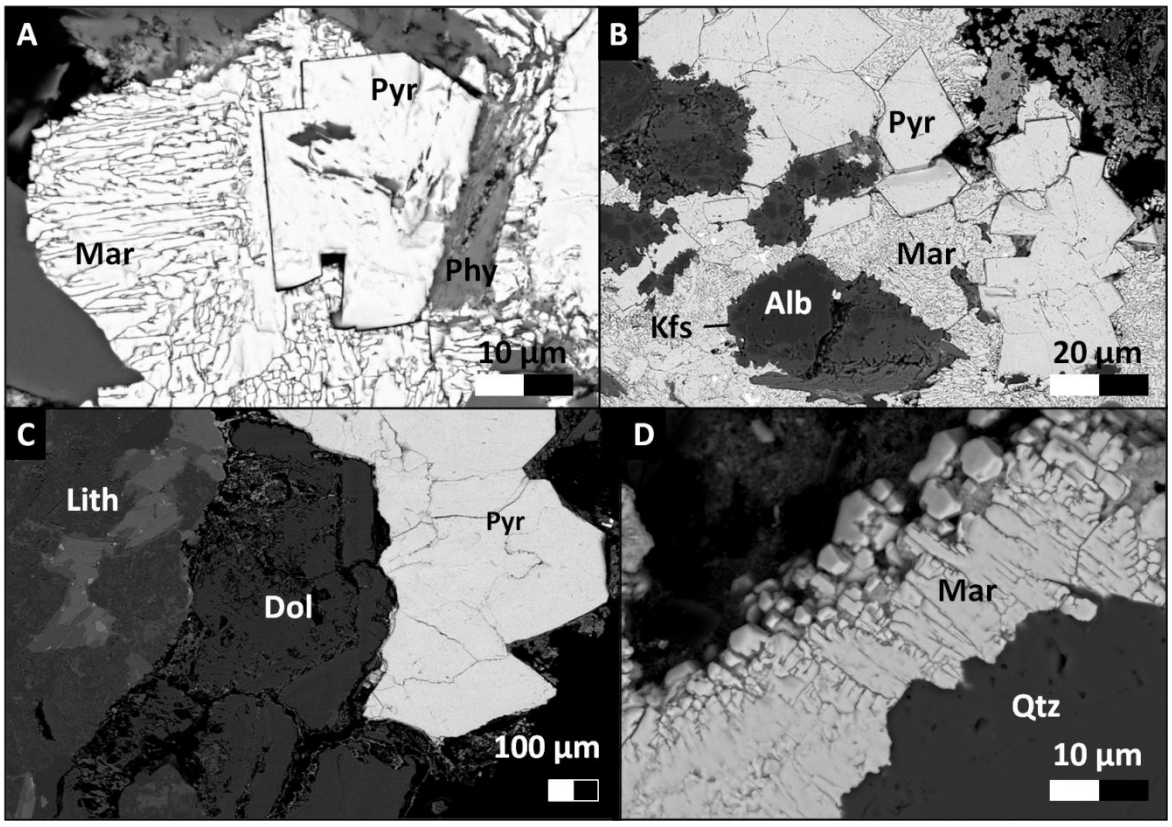

Figure 3-14: SEM AsB images of pyrite and marcasite textures in autochthonous fractures, showing a variety of crystal geometry. Minor phyllosilicates, chlorite and white mica, and feldspars are intergrown with sulphides (A, B and D). Dolomite which has precipitated before Fe-sulphides is very weathered (C). (Alb = albite; Dol = dolomite; Kfs = K-feldspar; Lith = host rock; Mar = marcasite; Phy = phyllosilicates; Pyr = pyrite).

3.3.1.4 Champagnac monomict lithic breccia

The Champagnac-type monomict breccia has been less affected by K-metasomatism (Lambert, 2010) than melt-bearing lithologies, but has been pervasively chloritized and locally, the clastic matrix has been replaced by dolomite, calcite and pyrite.

Carbonates: Dolomite and calcite may completely replace the clastic matrix; vuggy, coarse pink dolomite is often overgrown by clean, white crystals of calcite (Figure 3-15). Carbonates have also precipitated within the void space of lithic clasts, and may also form small veins along fabric planes; Mn and Fe-rich ankerite are found in minor amounts. *K-feldspar:* Coarse K-feldspar crystals form rims on and may crystallize within intercrystalline voids and fractures of breccia clasts. K-feldspar also partially replaces grains of albite within lithic fragments. *Chlorite and biotite:* High Fe-chlorite partially to completely replaces biotite within lithic fragments. Euhedral crystals of biotite are also found within the fabric plane of breccia clasts; even within clasts which display reaction rims, biotite crystals remain well formed and unaffected by alteration into weathered clast

interiors. *Sulphide:* Pyrite post-dates carbonate mineralization within the matrix, and may form up to 5mm cubic crystals; it may also that are not associated with carbonate form small veinlets and crystals within the clastic matrix. Pyrite may also be found within the fabric plane of clasts. *Apatite:* Minor amounts of authigenic apatite occur within both the lithic fragments and have crystallized within the secondary adularia rims.

Table 3-11: Secondary minerals in monomict lithic impact breccia, type Champagnac

Mineral	Occurrence	Description
Dolomite and calcite	Matrix and clasts; matrix locally replaced by carbonates, and may also be found localized within the fabric of lithic clasts (Figures 3-15, 16, 17 and 18).	Euhedral, 1 to 5mm, pink to white at hand scale, rhombohedral crystals; sparry dolomite cement, often overgrown by clean calcite.
K-feldspar	Matrix and clasts; precipitated within voids of lithic clasts and replacing albite, and forms dark red-grey reaction rims on clasts.	Euhedral to subhedral, 100 to 125 µm; first order grey in transmitted xpl light.
Chlorite	Clasts; Fe-Mg minerals within lithic clasts of basement gneiss have been chloritized (Figure 3-19).	Euhedral to subhedral, bright blue interference colors, often replacing biotite.
Biotite	Clasts; crystals aligned with fabric of gneiss.	Euhedral to subhedral, ≤ 500 µm crystals; seen at hand scale as flaky, black minerals in clasts.
Pyrite	Matrix and clasts; found within the clastic matrix associated with and without carbonate cement, and within the fabric plane of breccia clasts (Figure 3-15 and 17).	Euhedral to anhedral; 3 to 5mm cubes precipitated with carbonates in matrix cement; forming small, irregular veinlets within fine clastic matrix; and small euhedral crystals within fabric plane of gneiss.
Apatite	Clast; crystallized in feldspar phases of breccia clasts, including rim (Figure 3-16).	Anhedral, rounded grains up to 60 µm.

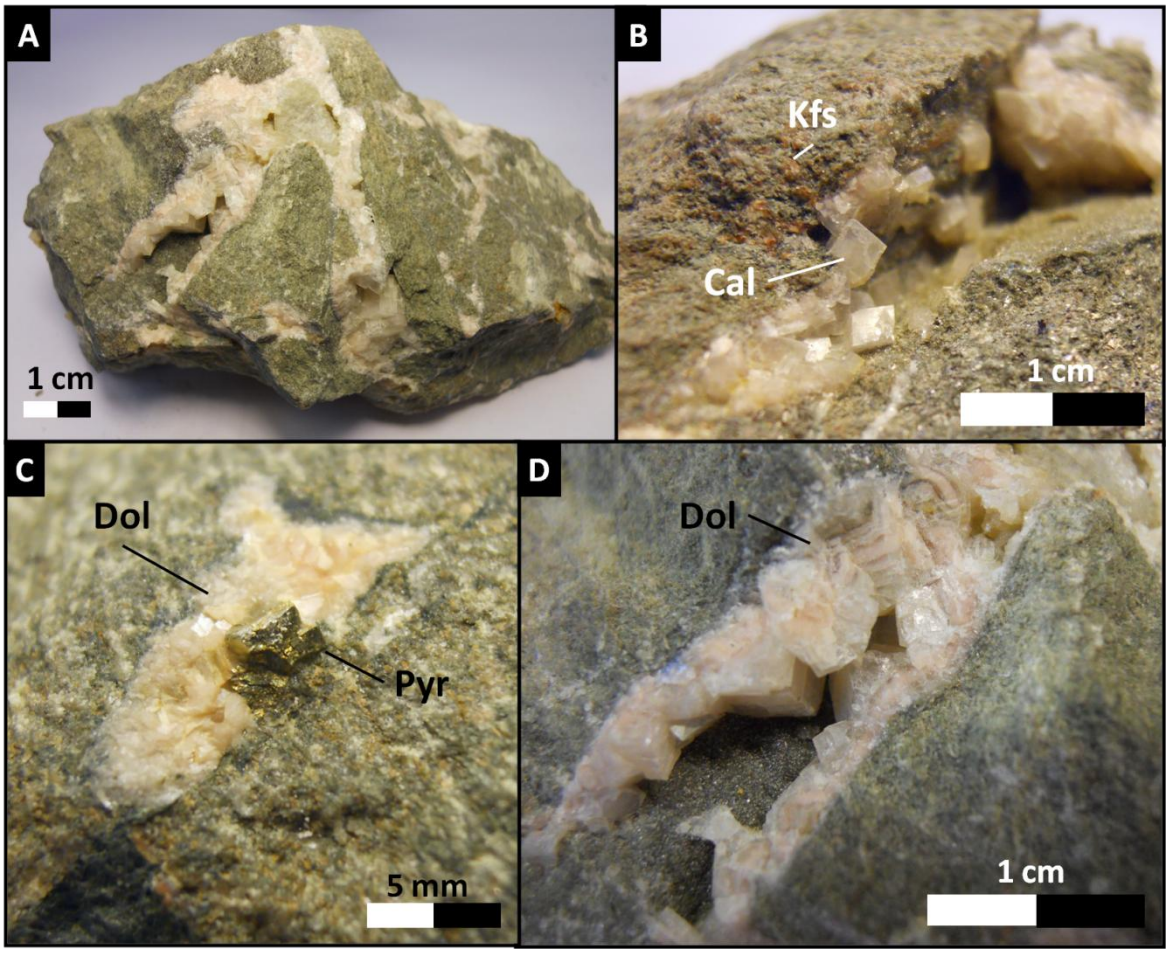

Figure 3-15: Photographs of carbonate and sulphide mineralization within the Champagnac type monomict lithic impact breccia. The K-feldspar in photo B is bright red, characteristic of orthoclase produced as a result of potassic alteration.

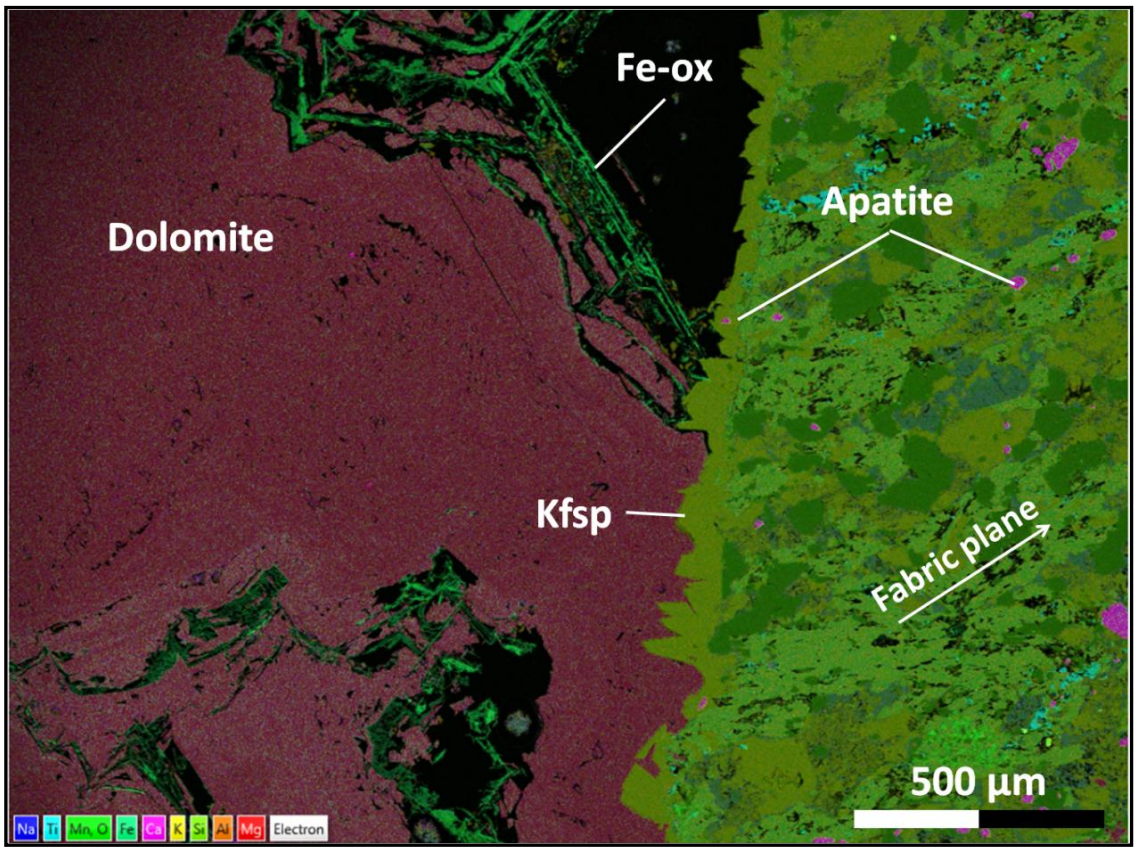

Figure 3-16: EDX map of carbonate cement in monomict lithic breccia; secondary apatite has crystallized within feldspar phases of lithic clasts, including orthoclase rim (Kfsp). Iron-rich rims of dolomite have weathered into iron oxides (Fe-ox).

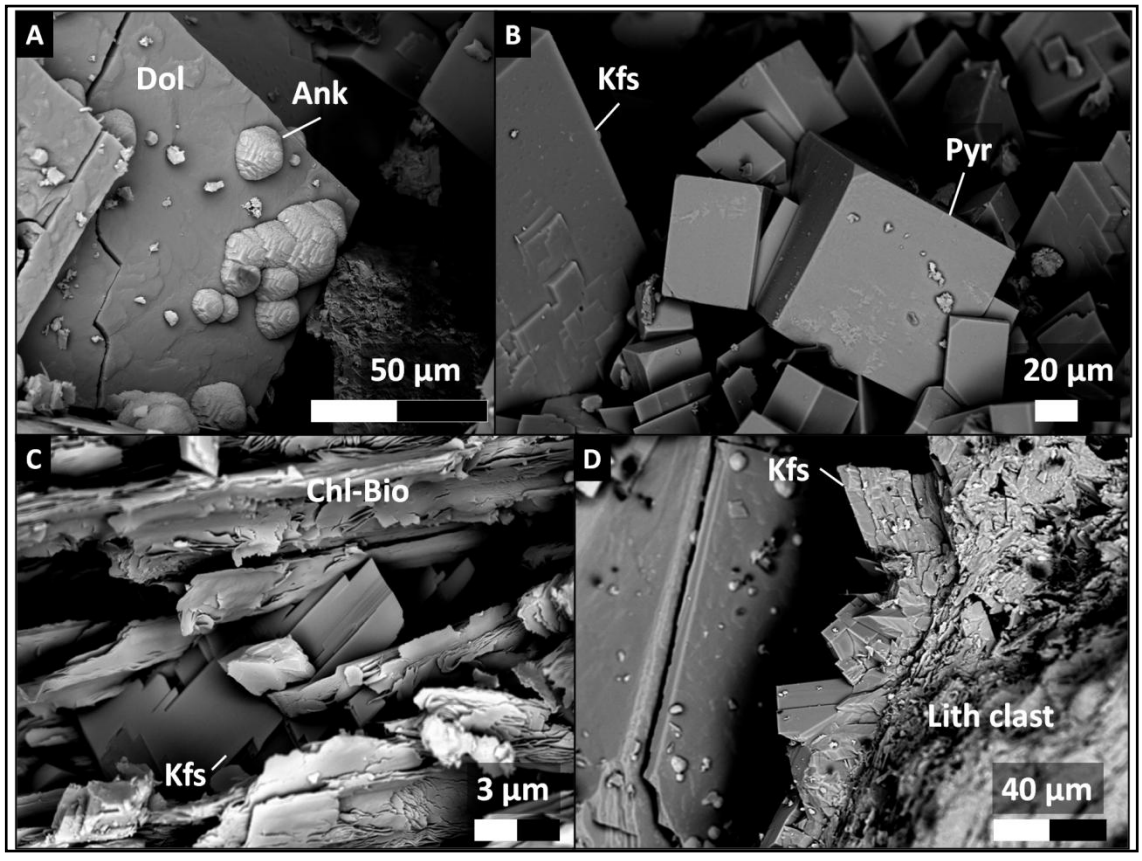

Figure 3-17: SEM AsB images of Au-coated fracture surfaces, showing textural relationships between various alteration minerals (Ank = ankerite; Chl-Bio = chlorite/biotite, Dol = dolomite; Kfs = K-feldspar; Pyr = pyrite).

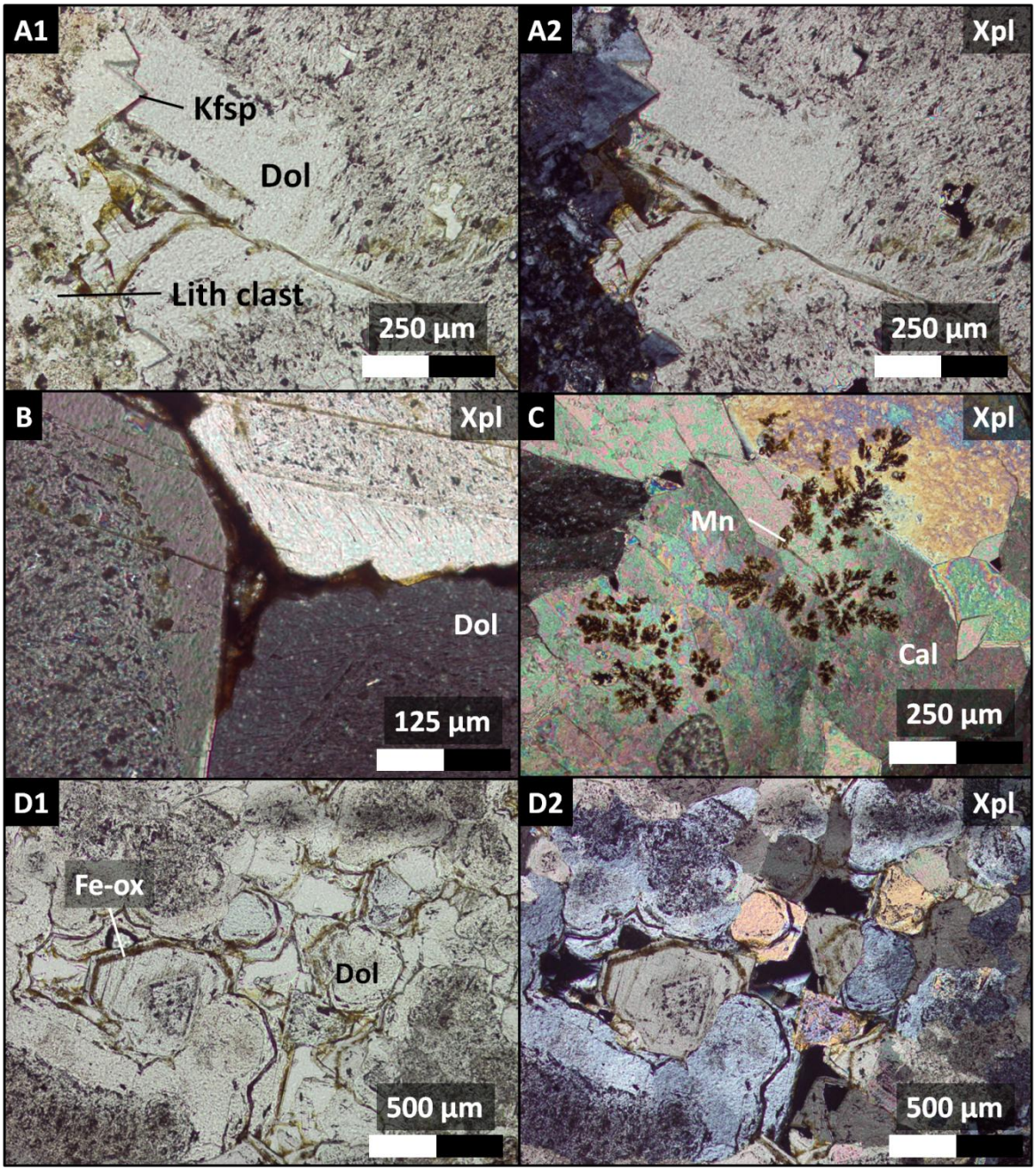

Figure 3-18: Transmitted light microscope images of carbonate cement in the monomict lithic breccia. (A1 and A2) K-feldspar overgrowths on lithic clasts are ubiquitous throughout the monomict breccias. (B) Clean, well-formed crystal exteriors with vuggy interiors forms the characteristic sparry texture. (C) Manganese dendrites are not uncommon in calcite cement. (D1 and D2) In most cases, dolomite crystals contain Fe-rich rims, which are weathered to Fe-oxide.

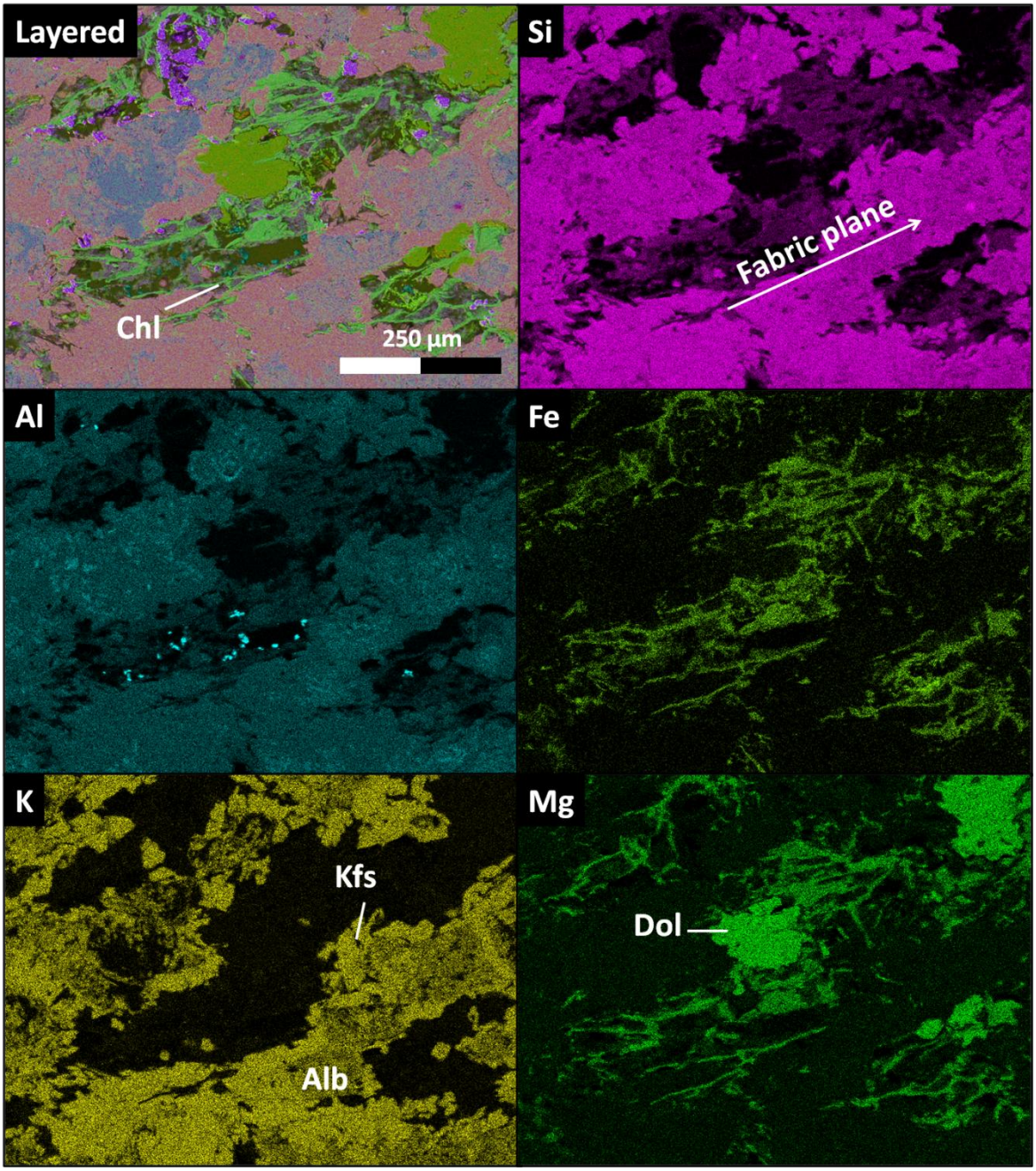

Figure 3-19: EDS element maps of monomict lithic breccia clast, showing distribution of elements Si, Al, Fe, K, Mg and a composite image. Although not as extensive as melt-bearing material, K-metasomatism is still pervasive through the monomict lithic breccia, as seen by the replacement of Na-feldspars by K-rich phases. Carbonate mineralization still penetrates the lithic clasts, and chlorite is aligned with the fabric plane, replacing Fe-Mg minerals within the target gneiss (Alb = albite; Chl = chlorite; Dol = dolomite; Kfs = K-feldspar).

3.3.1.5 Champagnac breccia dike

The polymict melt-bearing dike in Champagnac shows evidence for pervasive potassic alteration, minor H^+ metasomatism and moderate carbonate mineralization. The material surrounding the dike has been highly altered as well, likely due to a combination

of localized heat from melt-bearing material and fluid flow. Some quartz grains within melt-bearing material appear to have been etched (Figure 3-20), creating unusual "honeycomb" texture.

K-metasomatism: Mineral grains, lithic and melt fragments and matrix within melt bearing material have been affected by K-metasomatism (Figure 3-22). Bright red grains of albite replaced by K-feldspar are dispersed throughout finely crystalline melt-bearing material; X-ray maps reveal K-feldspar replacement following cleavages of albite (Figure 3-22, C). Breccia clasts within the surrounding parautochthonous host rock have bright-red to dark-purple-grey reaction rims of K-feldspar, with weathered, soft clay interiors. *Clays:* Smectite overgrows and replaces quartz and feldspar within clasts of host rock (Figure 3-21) and within the melt-bearing intrusion (Figure 3-23). *Carbonates:* Dolomite has precipitated within void space of melt-bearing material, and as coarse cement in parautochthonous material. *White mica:* Muscovite and paragonite are found as replacement minerals within lith and mineral clasts, melt-bearing material and within adjacent rocks.

Table 3-12: Secondary minerals in polymict breccia dike

Mineral	Occurrence	Description
K-feldspar	Matrix and clasts; replacement of albite, overgrowths, void-filling; forms reaction rims on surrounding monomict host clasts.	Euhedral to anhedral, variety of textures and habits; most common as <10µm veins and 50 to 100µm rhombohedral fracture coatings.
Smectite	Matrix and clasts; small overgrowths within the matrix and replacing clast interiors in host rock.	Subhedral to anhedral; <10µm circular patches (Figure 3-23) in SEM.
Carbonate	Matrix and clasts; minor dolomite within melt-bearing matrix, associated with bright red K-feldspar, cement in lith clasts of melt-bearing dike and cement in adjacent monomict material.	Subhedral to anhedral, sparry, up to 200µm-thick in melt material and up to 5mm crystals in parautochthonous host.
White mica	Matrix and clasts; sericitic texture in silicate minerals, may be found in fabric of lith clasts.	Euhedral to anhedral larger up to ~250 µm euhedral crystals to <20 µm replacement along cleavage planes of feldspars.

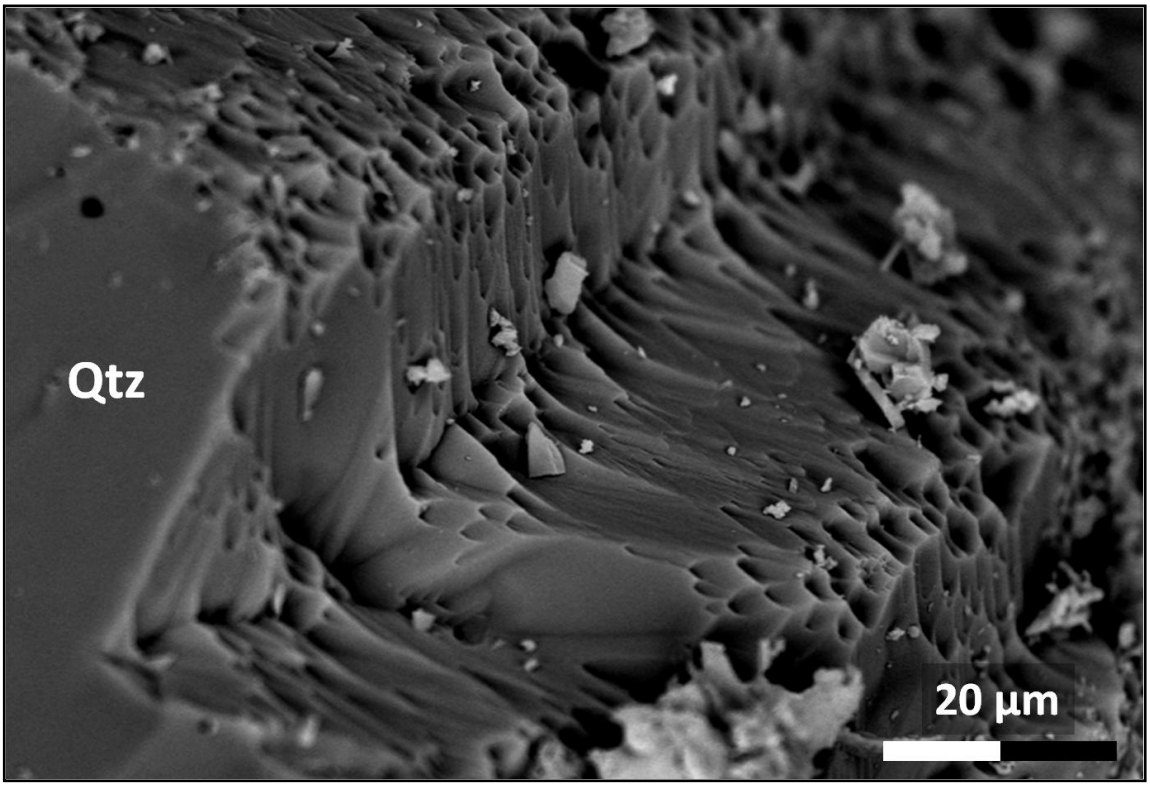

Figure 3-20: SEM AsB image of quartz grain with unusual "honeycomb" texture within the melt-bearing impact breccia dike.

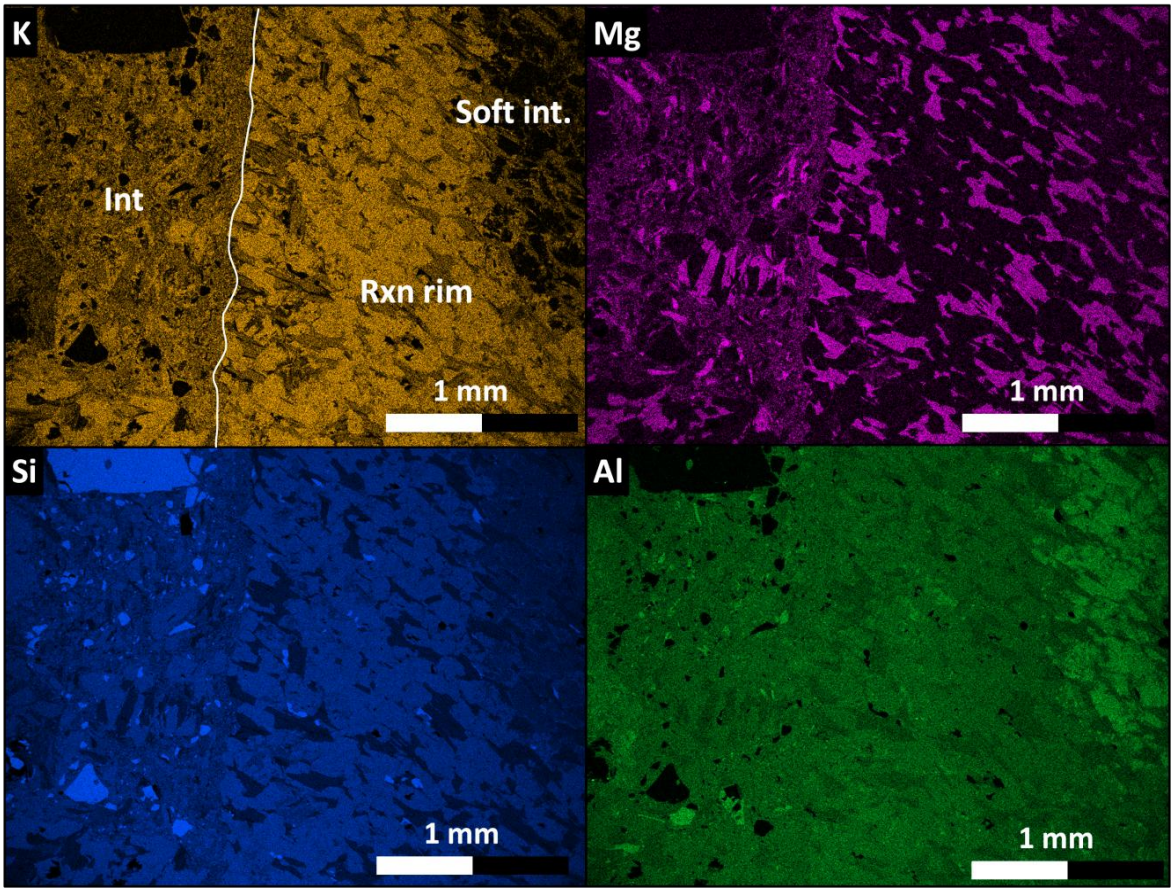

Figure 3-21: EDS maps of K, Mg, Si and Al at interface between the polymict melt-bearing intrusion (labeled "int") and clast of monomict breccia, showing K-feldspar reaction rim ("Rxn

rim") and clay-rich clast interior ("Soft int.") (Al map). Overall, biotites aligned with gneiss clast fabric plane do not appear to have been affected by aqueous alteration; silicates quartz and feldspar within clast interiors have been altered, and overall the melt-bearing material is enriched in K.

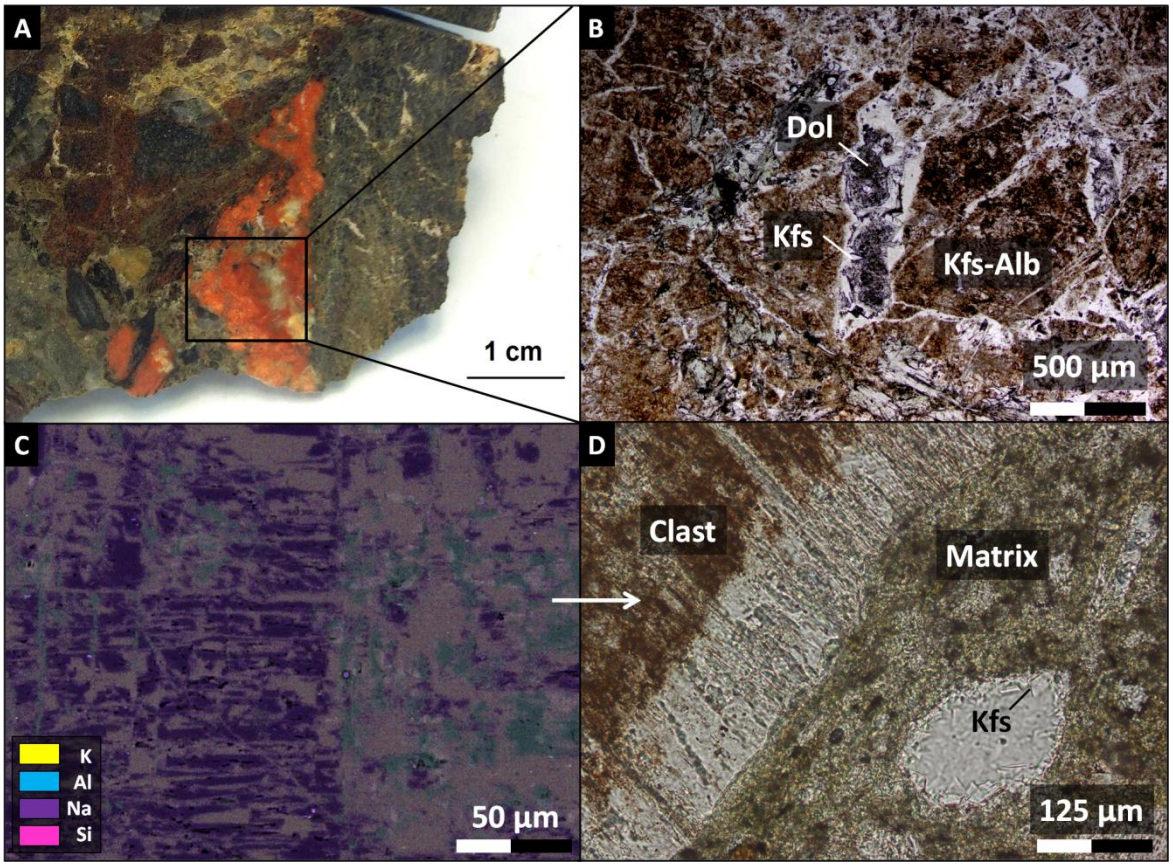

Figure 3-22: (A) Photograph of bright red K-feldspar-albite commonly found in melt-bearing dike. (B) Transmitted light photograph showing carbonate and potassic alteration within bright red mineralization. (C) EDS map showing alteration of albite along cleavage planes by K-rich fluid. (D) Transmitted plane polarized light photograph of potassically altered bright red albite and K-feldspar. (Alb = albite; Dol = dolomite; Kfs = K-feldspar).

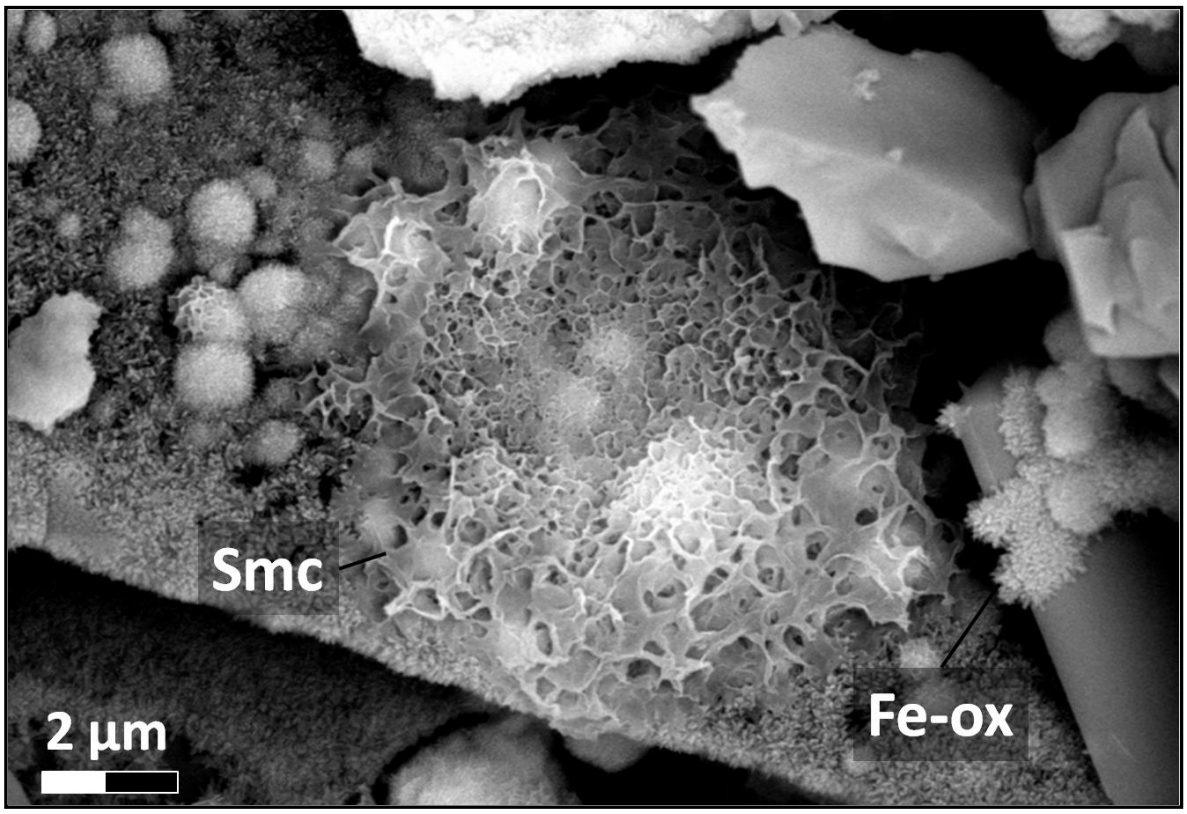

Figure 3-23: SEM AsB image of smectite patch overgrowing iron oxides within melt-bearing dike. (Fe-ox = iron oxides; Smc = smectite).

3.3.1.6 Rochechouart polymict lithic breccia

The polymict lithic breccia has been less affected by K-metasomatism, but is more highly chloritized, when compared to melt rocks. Late stage Fe-oxide staining in secondary porosity created by weathering of clasts is common.

Table 3-13: Secondary minerals in polymict lithic impact breccia, type Rochechouart

Mineral	Occurrence	Description
K-feldspar	Matrix and clasts; rims of lithic clasts commonly contain red-orange reaction rim of K-feldspar, and secondary crystals crystallized in matrix voids.	Euhedral, rhombohedral, up to ~60µm, first order grey crystals.
White mica	Matrix and clasts; sericitic textures in silicates and larger crystals within clast fabrics.	Subhedral to anhedral 10 to 100µm crystals, sometimes forming sericitic texture in smaller silicates.
Chlorite	Matrix and clasts; partially to completely replacing biotite.	Subhedral to euhedral, up to 1mm, often “Berlin blue” high-iron variety.

Fe-oxides	Matrix and clasts; precipitating in and staining area around fractures and secondary porosity.	Anhedral, dark red staining; may form inclusions in feldspars, causing dirty reddish-brown coloring.
Mn-oxides	Matrix and clasts; localized minor amounts of Mn-oxides are found throughout intercrystalline voids.	Irregular, dark brown-black, sometimes fibrous growths.

Silicates: At the microscale secondary, clean, rhombohedral crystals of K-feldspar occur in fractures and intercrystalline void space within the matrix and clasts; bright orange-red reaction rims of orthoclase may be seen on larger felsic lithic clasts. *White mica:* white mica, muscovite and paragonite partially to completely replace quartz and feldspar, sometime forming large, well-crystallized laths, but also affecting tectosilicates on a smaller scale, creating sericitic textures. *Chlorite:* Biotite may be replaced partially to completely by Fe-rich chlorite (Figure 3-25). *Fe-oxides:* accessory hematite throughout matrix and clasts within voids and in framework silicates, often forming inclusions in altered crystals (Figure 3-24) or decorating PDF's in shocked quartz. *Mn-oxides:* minor amounts of fibrous, hair-like growths of manganese oxides, likely pyrolusite, has precipitated within intercrystalline voids (Figure 3-26).

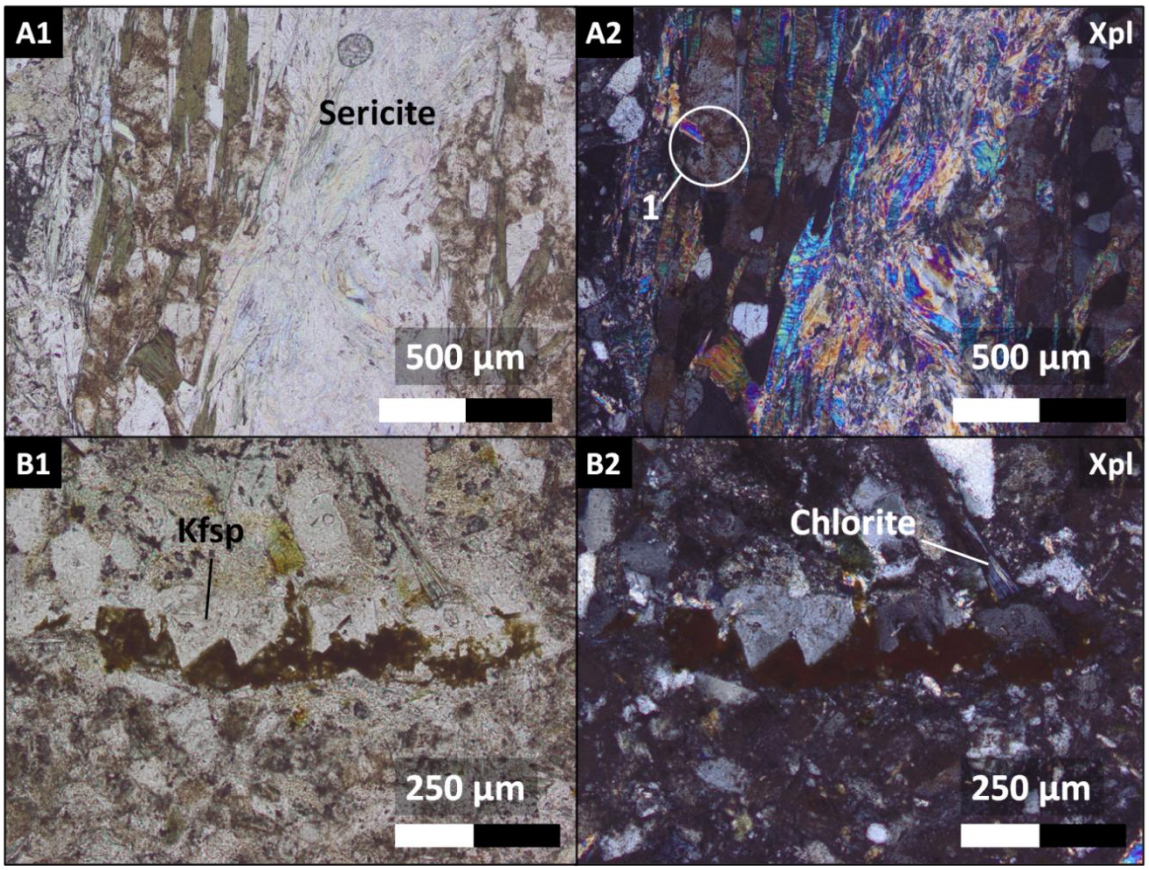

Figure 3-24: Transmitted light microscope images of alteration in the polymict lithic breccia, type Rochechouart. (A1 and A2) Potassic alteration assemblages, sericite and replacement of albite-rich feldspars by orthoclase and accessory Fe-oxides (section 1). (B1 and B2) Secondary orthoclase precipitated within matrix void and chloritized biotite.

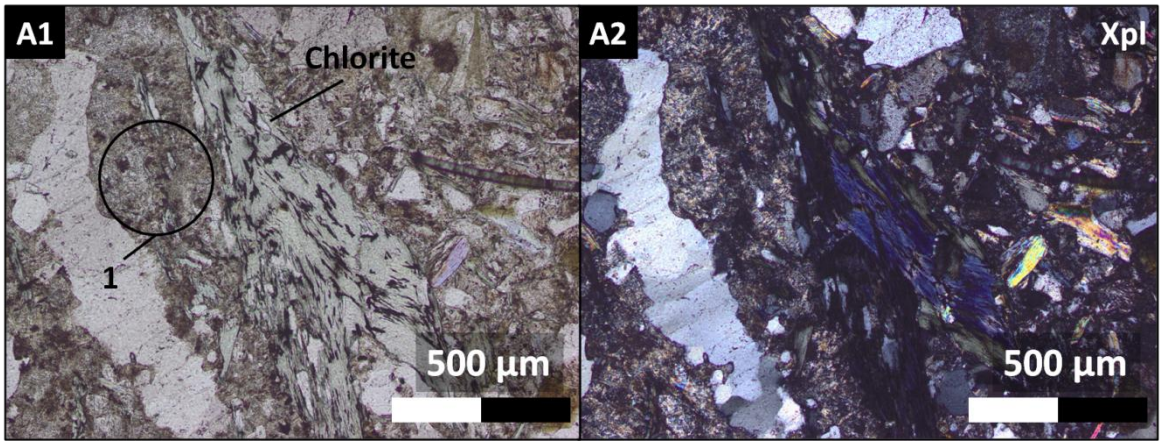

Figure 3-25: Transmitted light microscope images of alteration in the Rochechouart impact breccia; feldspars have been partially sericitized (A1, area 1), and Fe-rich chlorite has completely replaced biotite (A2, Xpl).

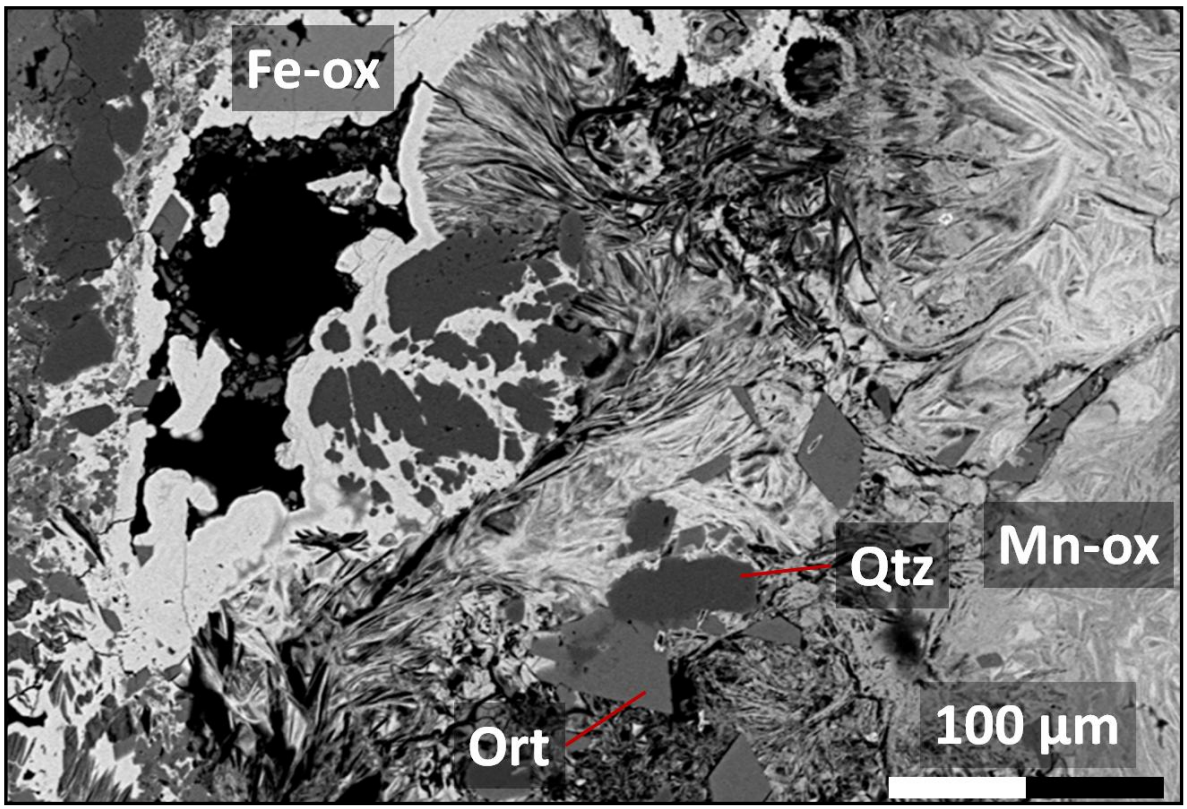

Figure 3-26: SEM AsB image of aqueous alteration in the matrix of the Rochechouart type polymict lithic breccia. (Fe-ox = iron oxides, Mn-ox = manganese oxides, Ort = orthoclase, Qtz = quartz).

3.3.1.7 Melt-bearing impact breccia, type Chassenon

The Chassenon melt-bearing breccia is one of the most extensively altered impact lithologies; in addition to pervasive potassic alteration, minerals have been affected by H^+ metasomatism, especially glasses.

Silicates: Rhombohedral orthoclase has precipitated within intercrystalline matrix voids, and potassic alteration has affected some feldspars within both matrix and lithic fragments. Thin rims of α-quartz are observed on isotropic glass (Figure 3-29, A1 and A2). *Smectite:* The most noticeable alteration within the Chassenon, smectite clays can be observed at both the hand scale, as swelling clays during the preparation of material for thin sections, and at the microscale replacing glass clasts (Figure 3-27 and 28). *White mica:* paragonite and muscovite are found in abundance altering feldspar minerals, creating sericitic textures in smaller crystals; they also form larger crystals in the lithic fragments. *Fe-Ti oxides:* Oxide minerals are observed as small crystal aggregates within both the matrix and lithic clasts, and within devitrified glass clasts (Figure 3-28 and 29).

Table 3-14: Secondary minerals in melt-bearing impact breccia, type Chassenon

Mineral	Occurrence	Description
K-feldspar	Matrix and clasts; precipitated in fractures and intercrystalline voids and replacement of Na-feldspar.	Euhedral, rhombohedral crystals up to ~80 microns, first order grey in transmitted light (Figure 3-29, B1 and B2).
α-quartz	Clasts; devitrification of isotropic glass may lead to quartz overgrowths.	Fibrous, first order grey growths up to ~30μm thick around isotropic glass (Figure 3-29 A1 and A2).
Smectite (nontronite)	Clasts; devitrification of impact glass.	Dark brown, opaque, unresolved material under transmitted light. At hand scale can be seen as soft, dark-green black clasts (Figure 3-27 and 28).
White mica	Matrix and clasts; muscovite and paragonite, replacement of framework silicates. Larger crystals associated with lithic clasts appear to have been shocked, and are likely inherited from the target.	Subhedral to anhedral high interference color crystals, most often seen in lithic fragments; ranges from small, <10μm sericitic alteration of feldspars to large 1 to 2 mm laths in lithic

		clasts.
Fe-Ti oxides	Matrix and clasts; concentrated at grain boundaries, fractures and voids. Often associated with smectite and areas of high H^+ alteration.	Anhedral to subhedral, dark red-brown to opaque crystal aggregates from <5 µm to 500 µm.

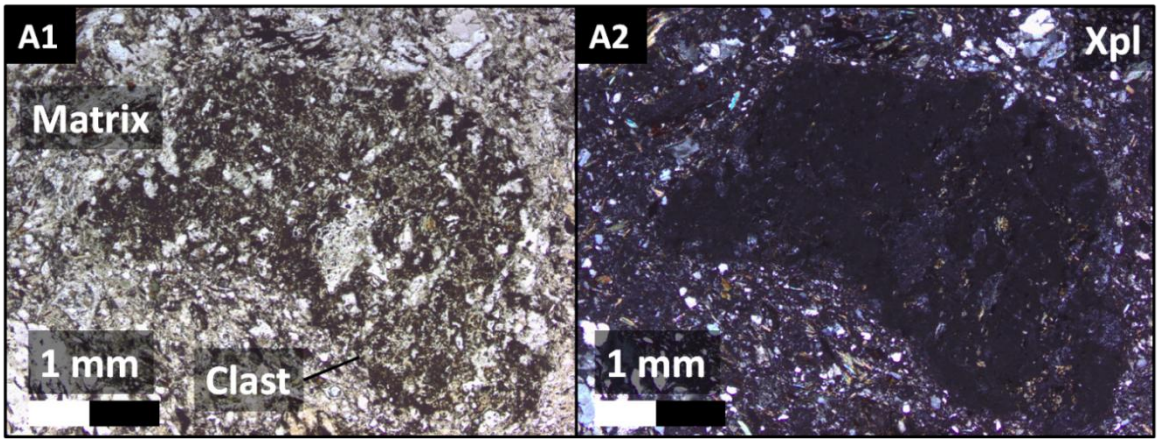

Figure 3-27: Transmitted light microscope images of the soft "green glass" characteristic of the Chassenon melt-bearing breccia; much of the glass has been devitrified to Fe-Mg-K-rich smectite clays.

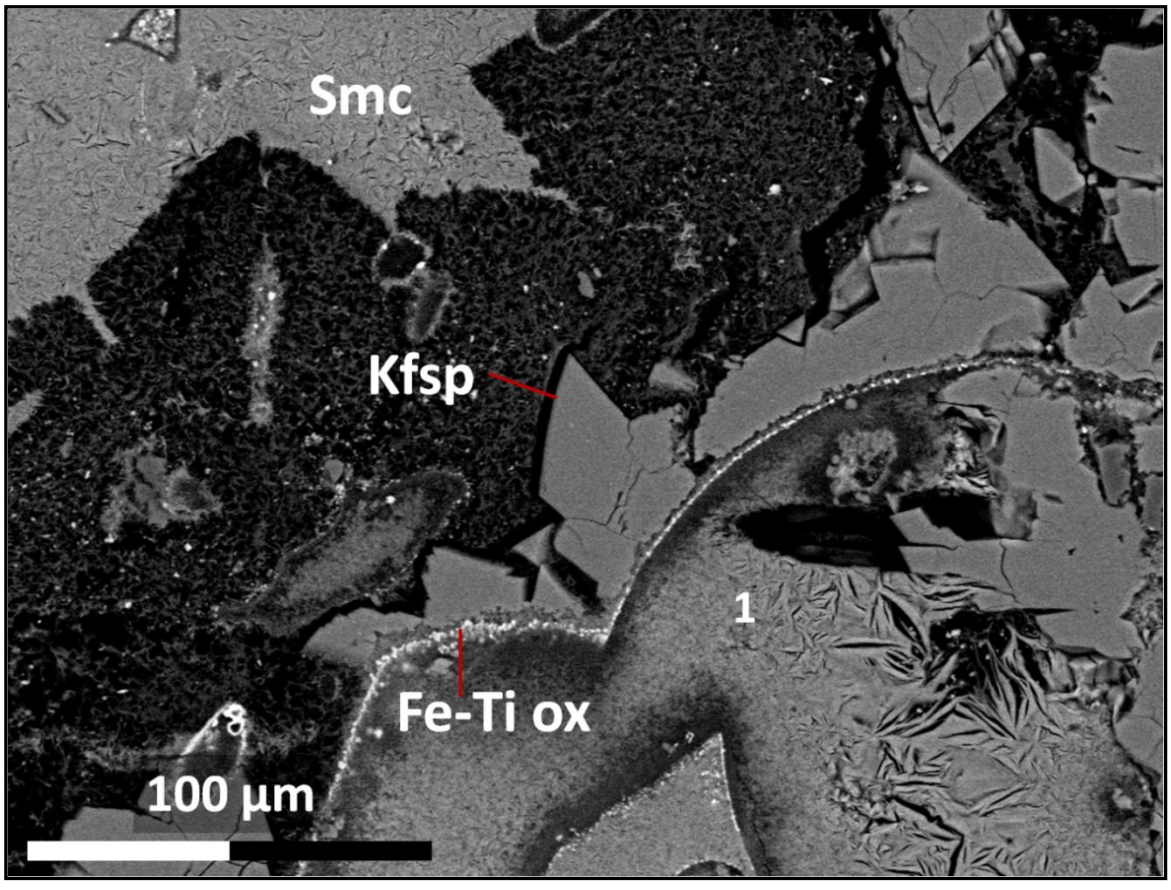

Figure 3-28: SEM AsB image of typical alteration in Chassenon melt-bearing impact breccia; the

rounded clast represented by area “1” is impact glass which has been devitrified to smectite, with Fe-Ti oxides concentrated around the rim and overgrown by orthoclase.

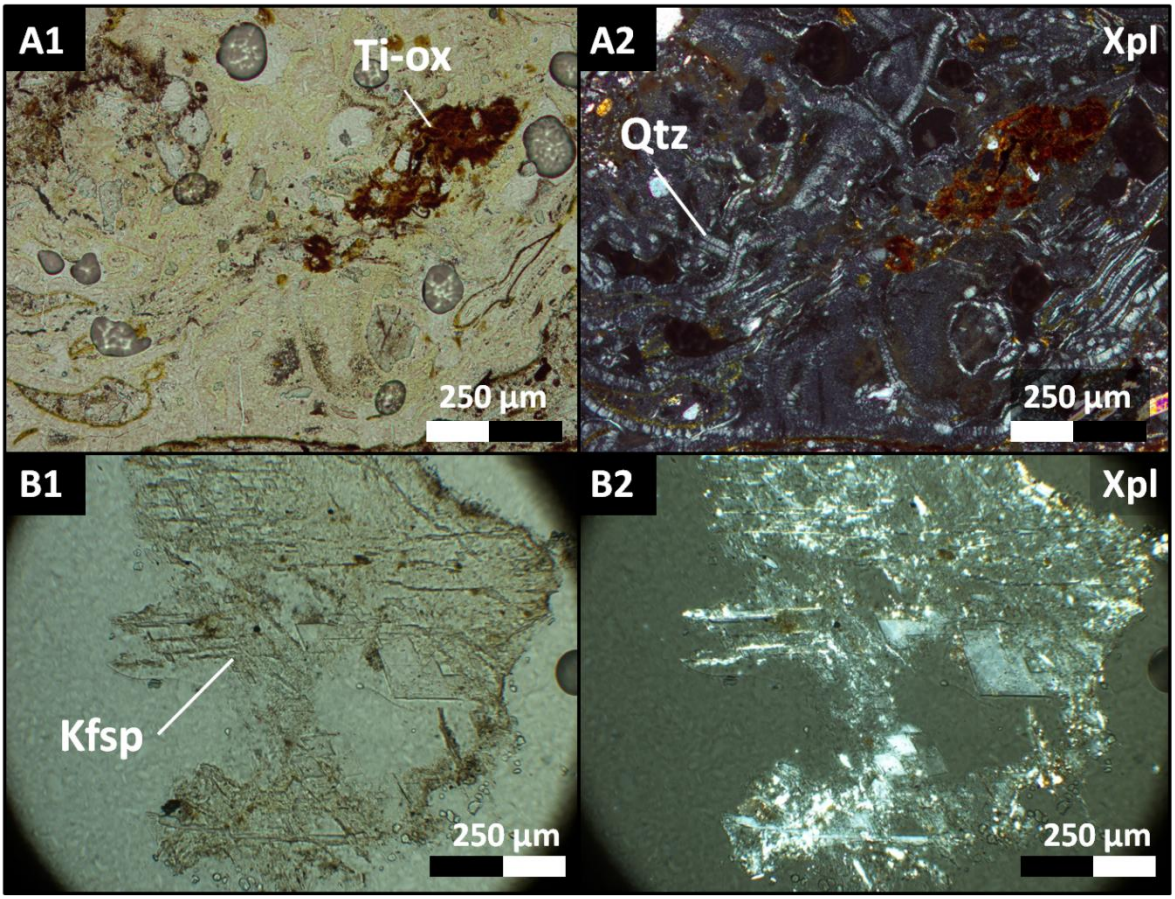

Figure 3-29: Transmitted light microscope images of alteration in the Chassenon melt-bearing impact breccia. (A1 and A2) Fibrous α-quartz recrystallized from impact glass with minor rutile. (B1 and B2) K-feldspar (Kfsp) precipitated within matrix void space.

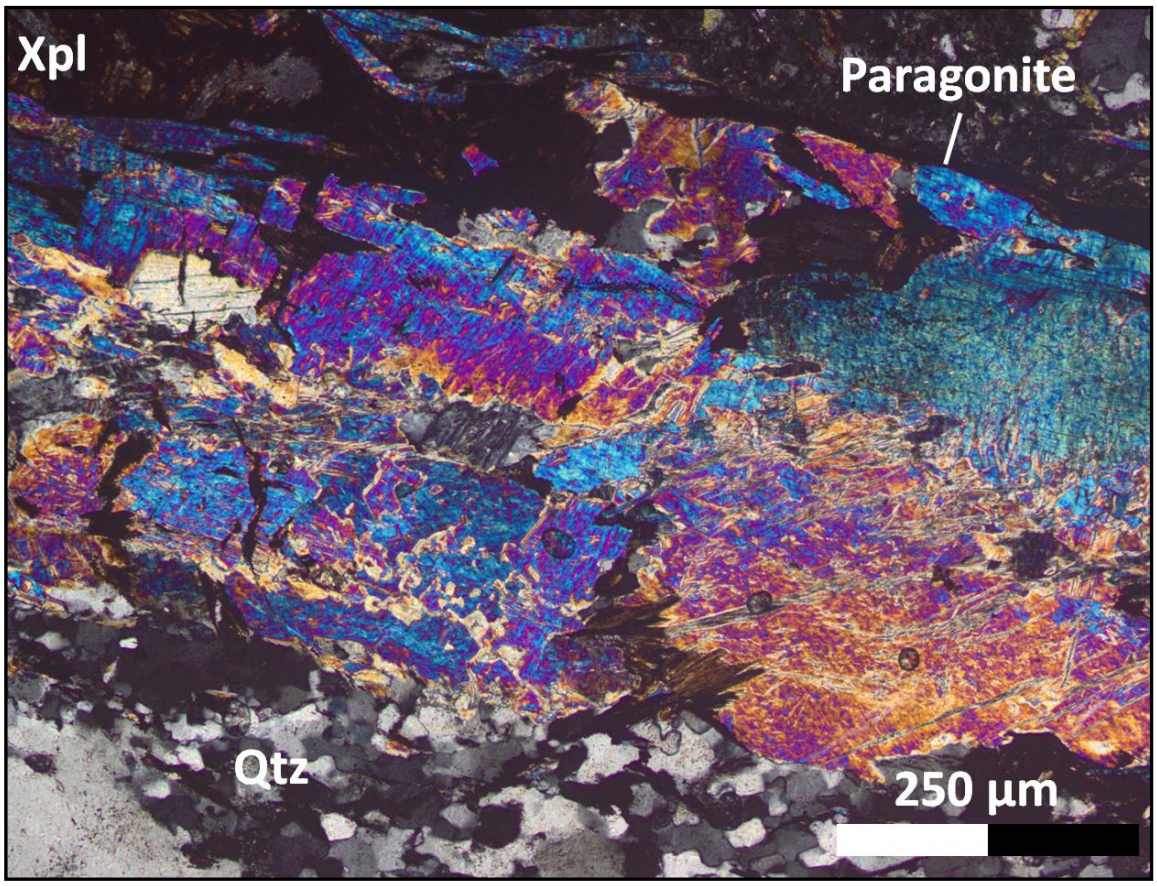

Figure 3-30: Shocked paragonite within a lithic clast of the melt-bearing impact breccia.

3.3.1.8 Particulate impact melt, type Montoume

Both the melt matrix and lithic clasts of the Montoume type particulate impact melt show evidence for pervasive K-metasomatism; K-feldspar and iron oxide are the dominant secondary mineral assemblages and α-quartz may be found replacing higher temperature phases.

Silicates: Secondary, euhedral K-feldspar and quartz crystals up to 120µm line fractures and occur as veins cross-cutting both lithic clasts and matrix. Pervasive potassic alteration as replacement of Na-Ca plagioclase and rhombohedral K-feldspar overgrowth is observed in both lithic clasts and in the melt groundmass. The boundaries of quartz glass clasts may be recrystallized to alpha quartz. *Fe-Ti oxides*: Spherulitic/hemimorphic red-orange hematite clusters up to approximately 50µm and unresolved red-yellow iron oxide staining is common within fractures and along fracture boundaries in both groundmass and clasts. Dark red-brown Fe-Ti oxides are common along grain boundaries within the matrix (Figure 3-31 A; Figure 3-32).

Table 3-15: Secondary minerals in particulate impact melt rock, type Montoume

Mineral	Occurrence	Description
Orthoclase	Matrix and clasts; veins, fracture coating, overgrowth, replacement of Na-plagioclase.	Euhedral, rhombohedral, up to 120 µm, first order grey.
α-quartz	Recrystallization of high temperature polymorphs and glass within the melt matrix.	Radiating, first order grey crystallization along glass boundaries.
Hematite	Matrix and clasts; crystal aggregates in fractures and void space, and general staining.	Subhedral hemimorphic, dark red-brown crystals 20 to 60µm, and anhedral, diffuse staining.
Ilmenite	Matrix and clasts; diffuse within intercrystalline voids and fractures, often associated with orthoclase.	Subhedral opaque crystal aggregates.

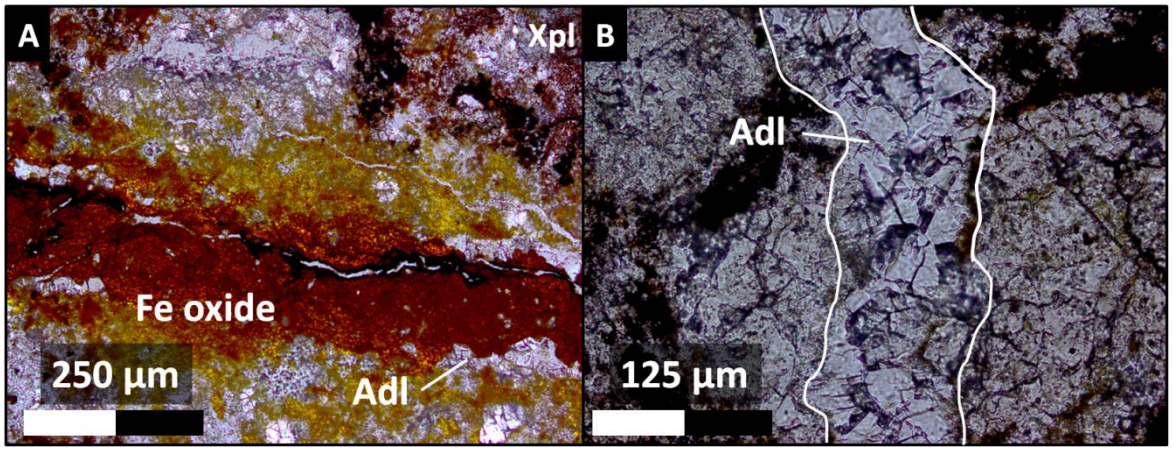

Figure 3-31: (A) Secondary orthoclase and dark-red yellow iron oxide staining along a fracture surface. (B) An orthoclase vein within the matrix of the Montoume type particulate impact melt.

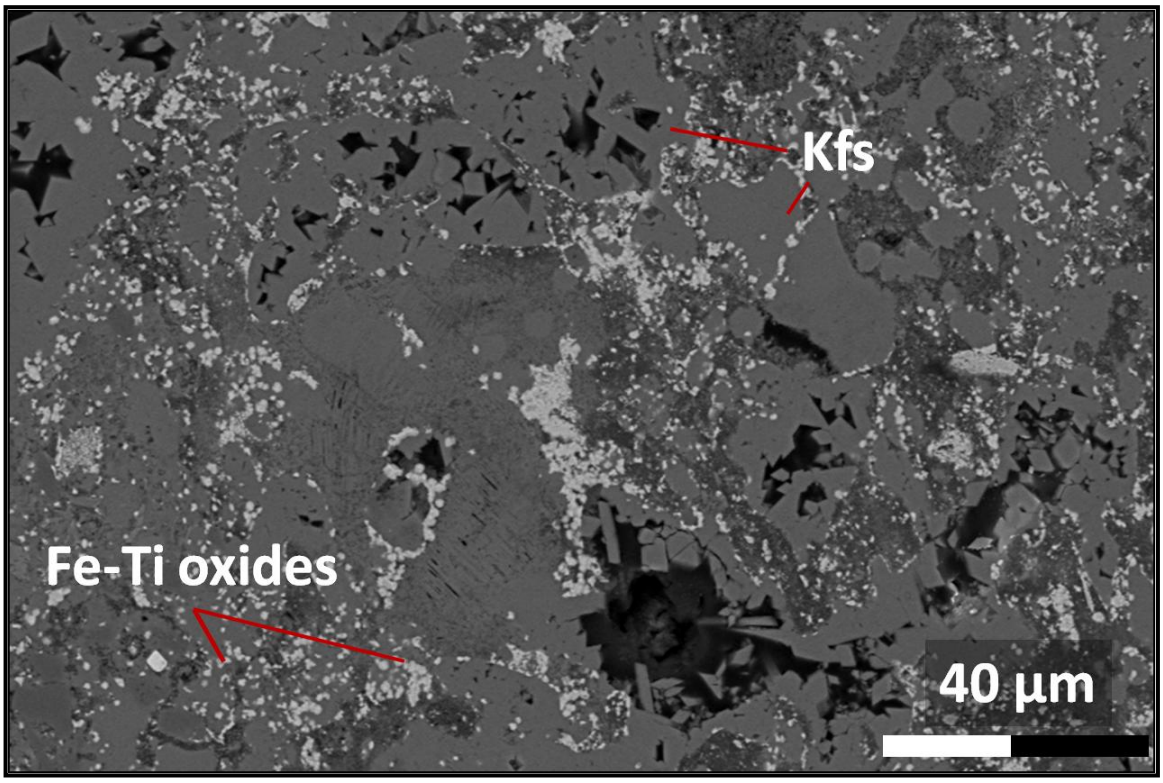

Figure 3-32: SEM AsB images of Montoume melt matrix, showing secondary rhombohedral K-feldspar and Fe-Ti oxides at grain boundaries.

3.3.1.9 Impact melt rock, type Babaudus

Groundmass and lithic and mineral fragments that make up the Babaudus melt rock show evidence for pervasive weathering, K-metasomatism and H^+ metasomatism, and localized late stage sulphate precipitation. Many of the rock-forming minerals are unresolved in transmitted light due to cryptocrystalline textures.

Table 3-16: Secondary minerals in impact melt rock, type Babaudus

Mineral	Occurrence	Description
K-feldspar (orthoclase + adularia)	Matrix and clasts; secondary growth in voids and vesicles and replacement of Na-plagioclase in clasts.	Euhedral, rhombohedral, up to 20 to 50µm, first order grey; alteration of "tartan" twinned microcline in clasts (Figure 3-33)
Smectite	Matrix; vesicle-filling, and replaces rhombohedral K-feldspar.	Yellow-brown, swelling, Fe-Mg clays (nontronite) occluding pores and vesicles; resolved under SEM replacing blocky, rhombohedral K-feldspar (Figure 3-34 A and 35).
Hematite, rutile	Matrix and clasts: lining vesicles and within	Euhedral, up to 10µm tabular rutile and diffuse red staining hematite (Figure 3-34,

	intercrystalline voids	36-B).
Barite	Matrix; Rare, vesicle lining	Euhedral, 5 to 10µm fibrous crystal aggregates

Silicates: Small rhombohedral crystals of adularia line and often completely fill vesicles and voids within the groundmass. The very few lithic and mineral fragments within the matrix often display intense, pervasive potassic alteration, consisting entirely of K-Na feldspars and clays. *Smectite:* Primary K-feldspar in both phase 1 (sanidine, elongated crystallites) and 2 (rhombohedral, euhedral) has been partially to completely replaced by smectite/montmorillonite. At the micro and mesoscale, vesicles are filled and sometimes completely occluded by yellow-brown smectite, often associated with minor amounts of iron oxides. *Fe-Ti oxides*: minor red-orange anhedral hematite and goethite is found lining vesicles in phase two and intercrystalline voids in phase one. Small crystal aggregates of euhedral rutile up to 10µm are found within vesicles and within the matrix of phase one (Figure 3-36, B). *Sulphate:* Euhedral, 5 to 10µm fibrous crystals of barite are rarely observed lining vesicles, both intergrown with and post-dating smectite mineralization (Figure 3-36, A).

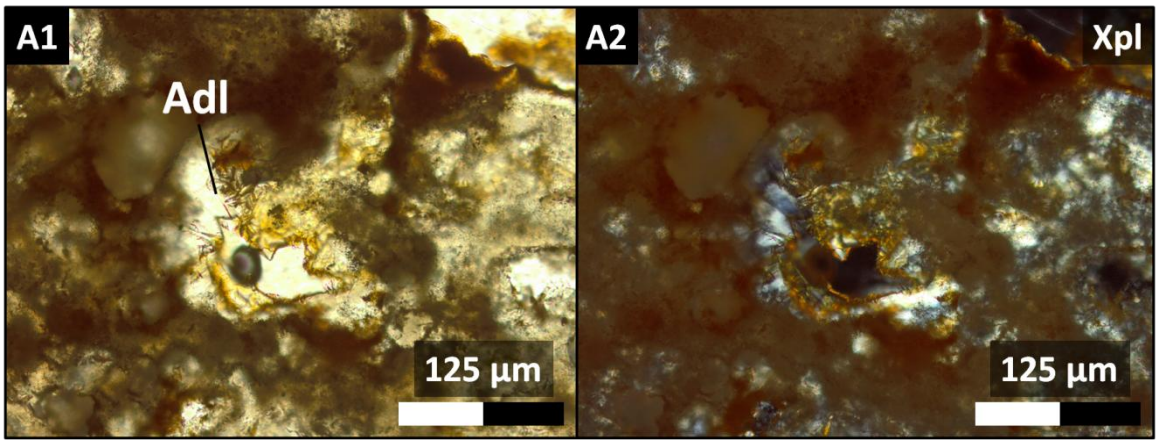

Figure 3-33: Transmitted light microscope images of intercrystalline adularia (Adl) within the Babaudus impact melt.

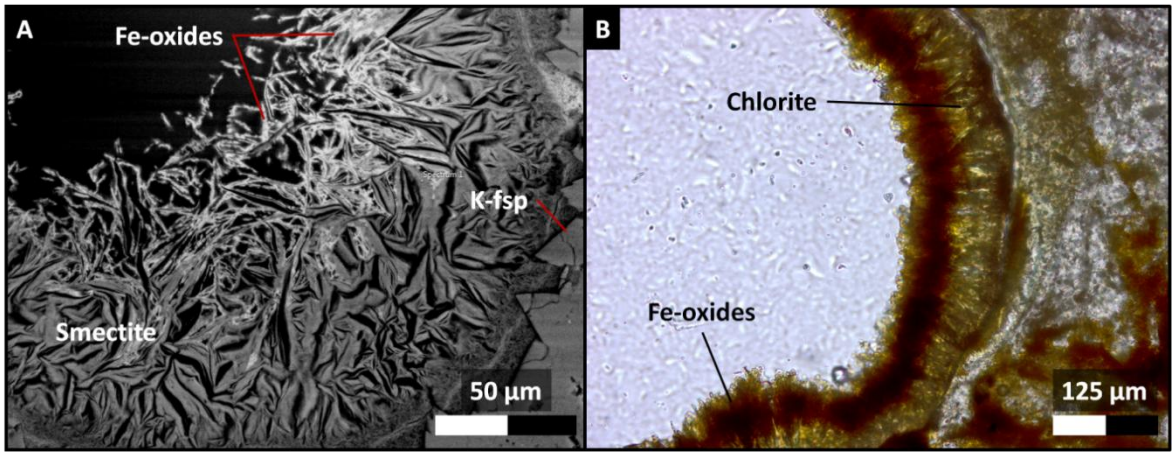

Figure 3-34: (A) SEM AsB image of vesicle lining secondary Fe-Mg-K-rich smectite clay with Fe-oxide coating. (B) Transmitted light microscope image of euhedral chlorite coating vesicle, also with Fe-oxide coating.

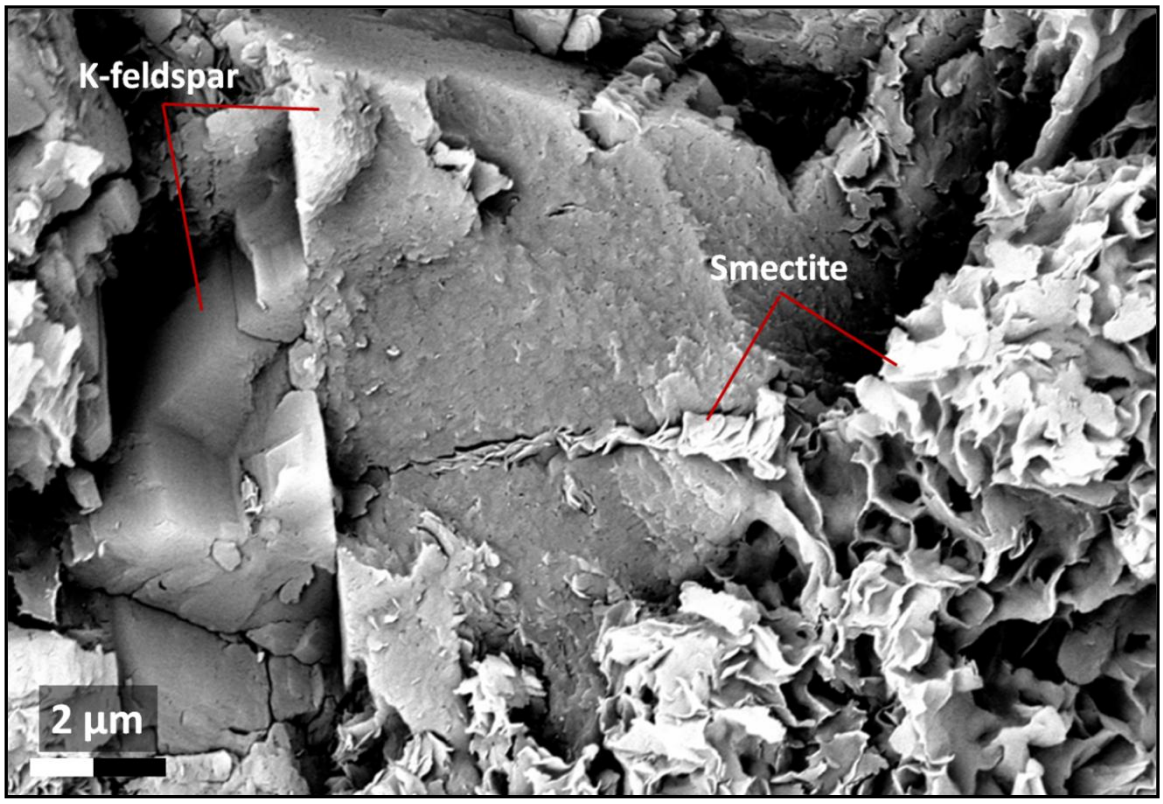

Figure 3-35: SEM AsB image of smectite clays replacing K-feldspar within vesicular impact melt, type Babaudus.

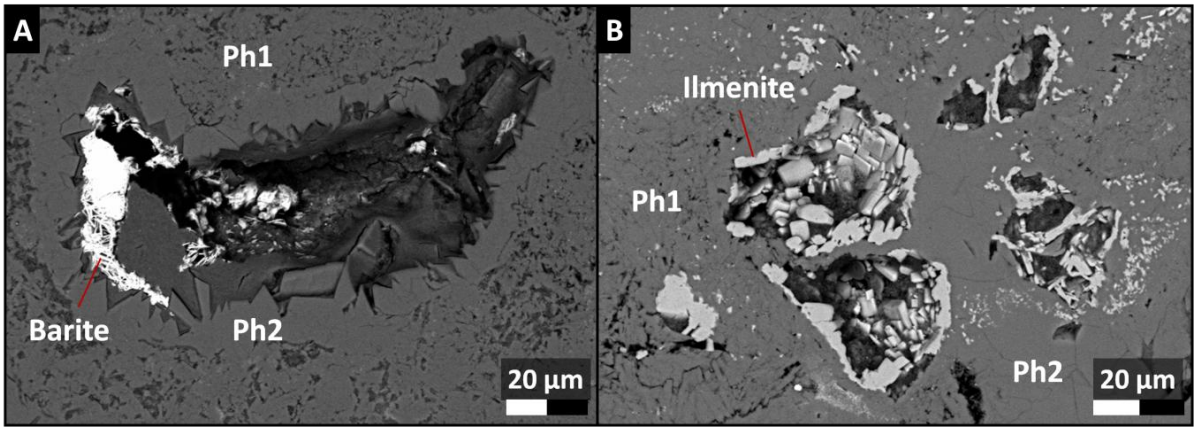

Figure 3-36: (A) SEM AsB images of secondary barite and (B) ilmenite; alteration in both cases post-dates both sanidine (Ph1) and orthoclase (Ph2) matrix within vesicular impact melt rock, type Babaudus.

3.3.2 Stable isotope results

3.3.2.1 $\delta^{13}C$ and $\delta^{18}O$, and $\delta^{34}S$ isotope results: tables

1σ reproducibility is between 0.003 and 0.03‰ for $\delta^{13}C$, 0.002 and 0.033‰ for $\delta^{18}O$, and 0.008 and 0.057‰ for $\delta^{34}S$.

Table 3-17: $\delta^{13}C$ and $\delta^{18}O$ isotope results (‰)

Sample ID	Rock type	$\delta^{13}C_{calcite}$ (VPDB)	$\delta^{18}O_{calcite}$ (VSMOW)	$\delta^{13}C_{dolomite}$ (VPDB)	$\delta^{18}O_{dolomite}$ (VSMOW)
	Basal marine limestones				
TC-1		0.613	30.9	0.320	31.8
TC-2		0.481	30.9	0.789	31.7
	Monomict lithic breccia				
MC-1		-7.66	26.6	-7.55	25.5
MC-2		-8.24	26.9	-8.13	26.0
MC-3		-12.4	26.1	-13.1	25.4
MC-4		-8.25	27.5	-7.94	26.4
MC-5		-11.3	26.1	-12.9	28.7
MC-6		-13.0	24.9	-13.0	23.8
MC-7		-12.2	25.6	-11.9	25.0
	Polymict dike				
PC-1		-10.6	26.8	-11.4	25.8

PC-2		-10.7	26.8	-11.3	25.9
PC-3		-12.4	25.0	-12.0	13.6
	Autochthonous fractures				
AC-1		-5.00	26.2	-4.50	25.4
	Unknown fractures				
UC-1		-4.56	27.5	-5.26	28.6
UC-2		-6.21	27.1	-6.63	25.9
UC-3		-11.2	25.3	-11.0	25.0
UC-4		-11.5	25.1	-11.4	24.4
UC-5		-8.50	24.9	-7.00	24.4

Table 3-18: $\delta^{34}S$ isotope results (‰)

Sample ID	Rock type	Mineral	$\delta^{34}S$ (VCDT)	Sample ID	Rock type	Mineral	$\delta^{34}S$ (VCDT)
	Monomict lithic breccia			ASL-2		Pyr	-24.6
MS-1		Pyr	-10.7	ASL-3		Pyr	-18.5
MS-2		Pyr	-5.60		*Basement*		
MSL-1		Pyr	-1.80	BS-1		Pyr	0.400
MSL-2		Pyr	-1.20	BS-2		Pyr	-3.70
	Autochthonous fractures			BSL-1		Pyr	-1.00
AS-1		Pyr + Mar	-32.0	BSL-2		Pyr	-1.30
AS-2		Pyr + Mar	-31.8	BSL-3		Pyr	-2.70
					Unknown fractures		
AS-3		Pyr + Mar	-32.2				
AS-4		Pyr + Mar	-34.2	US-1		Cpy	-1.70
AS-5		Pyr + Mar	-35.5	US-2		Cpy	-6.90
AS-6		Pyr + Mar	-35.8	US-3		Pyr	-26.2
AS-7		Pyr + Mar	-26.9	US-4		Pyr	-24.2
ASL-1		Pyr	-5.20				

Abbreviations: Cpy = chalcopyrite; Mar = marcasite; Pyr = pyrite.

3.3.2.2 $\delta^{13}C$ and $\delta^{18}O$, and $\delta^{34}S$ isotope results: tables

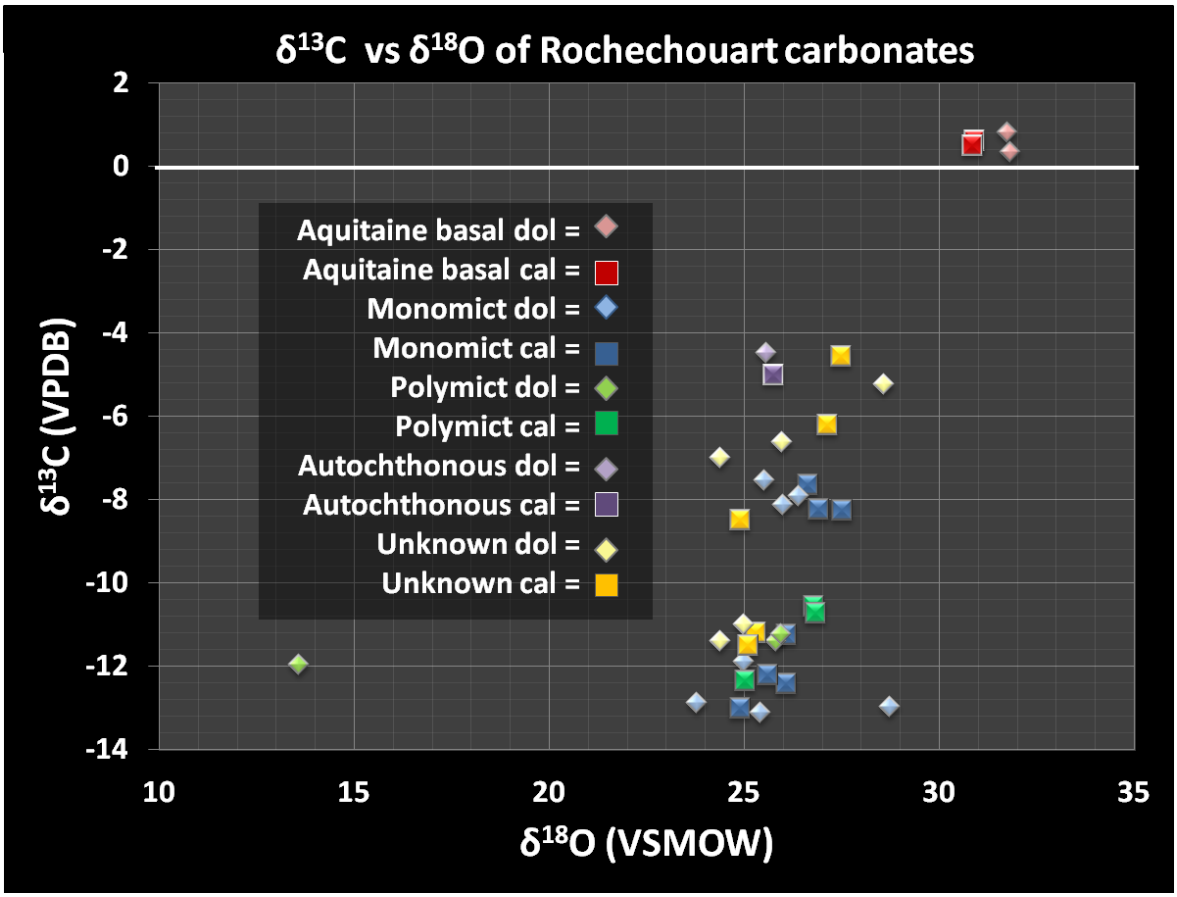

Figure 3-37: $\delta^{13}C$ and $\delta^{18}O$ of all carbonate minerals. $\delta^{13}C$ of impactites varies from -4.5 to -13.1 ‰, while $\delta^{18}O$ remains more consistent, from +23.8 to +28.7 ‰, with the exception of one dolomite reading of +13.5 ‰.

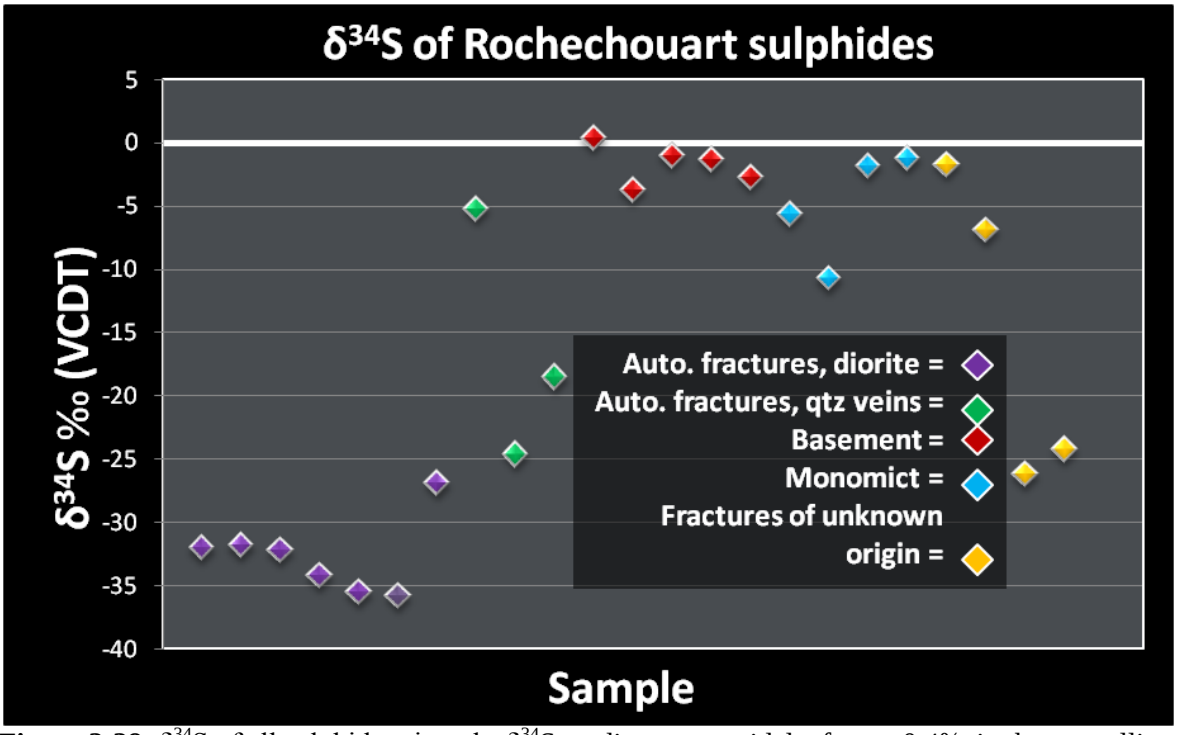

Figure 3-38: $\delta^{34}S$ of all sulphide minerals. $\delta^{34}S$ readings vary widely, from +0.4‰ in the crystalline basement to -35.8‰ in autochthonous fractures.

3.4 Discussion

3.4.1 Distribution and types of alteration in Rochechouart

Overall, these observations are consistent with previous findings concerning hydrothermal alteration in Rochechouart; K-metasomatism affects all lithologies, from the vesicular impact melt to the underlying crystalline basement. The overgrowth, selective alteration and sometimes complete replacement of albite phases by orthoclase, and in many cases orthoclase by sericite (muscovite + paragonite) is present in all lithologies; very little to no An-rich plagioclase is found in melt-rich impactites. H^+ metasomatism is the next most pervasive alteration type; swelling clays, smectite/montmorillonite (nontronite), are most prevalent in melt and glass-bearing lithologies, with decreasing amounts in lithic impactites and basement. Chloritization becomes more common in lithic impactites and the basement as potassic and H^+ alteration decreases. Lastly, there is a stark difference in the intensity of carbonate and sulphide mineralization between melt-bearing and lithic rock types; lithic breccias, autochthonous fractures and basement material have been heavily mineralized, which is rare to absent in melt rocks. Iron oxide and hydroxide staining is common within secondary porosity and fractures of all impactites; iron and titanium are released as a byproduct of K-metasomatism, but in particulate-rich impactites the anhedral, rust-colored staining seen at hand scale is likely a product of surficial weathering.

3.4.1.1 Basement

Similar to the impactites, crystalline gneiss and diorite also have a K-metasomatic overprint. Compared to impact lithologies, the basement rocks display a moderate degree of sericitization of feldspar minerals, a lesser amount of authigenic K-feldspar and even more scarce, carbonate and sulphide-coated fractures.

The diorite contains myrmekitic textures (Figure 3-11), large relict sphene crystals which have been replaced by rutile (Figure 3-11), and a significant quantity of large, mostly unaltered phenocrysts of biotite, none of which is observed in any impactites. Myrmekite is characteristic of sub-solidus Ca-metasomatism during the cooling of a felsic plutonic body (Figure 3-11, A and B); the vermicular quartz in myrmekite is preserved, but the plagioclase has been completely replaced by orthoclase, possibly by post-impact K-metasomatism.

The amphibolite gneiss is much less highly altered. The partial replacement of chlorite by biotite, a sericitic texture in albite, and sulphide-carbonate veins both cross-cutting and within the fabric are the main types of alteration. Stable isotope values from pyrite within the gneiss fabric closely match those within the veins, with only a minor degree of fractionation between the two (+0.4 to -3.7‰).

The origin of fractures in the granodiorite is unknown. The dolomite that coats their surfaces is texturally and compositionally similar to the dolomites in the monomict lithic breccias. Oxygen isotope results from dolomite and calcite within these fractures are not reflective of a Hercynian origin (Fourcade et al., 2012); it is very possible that the fractures are impact-related, or possibly reflect the late-stage fluid event outlined by Cathelineau et al. (2012).

Some types of aqueous alteration related to sub-solidus reactions during plutonic cooling are preserved. However, the overprinted selective removal of calcium and to a lesser degree, sodium, from primary minerals, and enrichment in potassium parallels that found in the impact rocks. It is difficult to know whether the smaller scale effects of potassic alteration, such as sericitization, are a result of regional metamorphic or impact processes.

3.4.1.2Autochthonous impact fractures

Autochthonous fractures in highly altered basement granodiorite contain massive sulphide mineralization and a moderate amount of carbonate, and are marked in outcrop by dark red-orange iron oxide staining. The host granodiorite has been potassically altered, and contains chlorite, K-feldspar, white mica and quartz. The fractured, brecciated nature

of the outcrop, as well as it's field context at the base of the allochthonous lithic impactite unit , and the context of the sulphide minerals, which cross-cut all other minerals in the host rock, confirm that the deposits post-date the impact.

The most striking difference between the autochthonous fractures and any other Rochechouart lithology is the intense sulphide mineralization; 0.5 cm-thick coatings of pyrite and marcasite cover fracture surfaces. Unlike in the monomict breccias, dolomite is much less abundant and appears to have co-precipitated with the sulphides; where dolomite appears to be the substrate for sulphide growth, it is highly weathered. This pattern of mineralization is indicative of fluid pH neutralization; chloride complexes destabilize in near-neutral conditions, hydrogen sulphide readily bonds with metals to form sulphide minerals and a neutralized pH allows for carbonate precipitation.

In addition to textural relationships between the sulphide minerals and host-rock supporting a post-impact timing, stable isotope compositions of sulphide and carbonate minerals indicate cool fluid temperatures expected during late stage impact hydrothermal activity (<150°C) (Naumov, 2005; Osinski et al., 2013), a strongly biological origin for sulphides, and a $\delta^{13}C$ value closer to seawater than any other carbonates in the structure. Previous studies have also shown that hydrothermal fluid flow is controlled by impact fractures; coherent, allochthonous impactites are generally impermeable (~1 mD) and late stage mineralization is predicted to concentrate within impact fractures (Parnell at al., 2010). These findings may have implications for the longevity of the hydrothermal system, and supports the scheme outlined by Naumov (2005) and Osinski et al. (2013) concerning late-stage carbonate-sulphide mineralization in complex impact craters (Naumov, 2005; Pierazzo and Osinski, 2012).

3.4.1.3 Monomict and continuous polymict lithic breccias

Alteration of lithic breccias is distinctly different from melt-bearing lithologies; there is a transition from pervasive smectite-dominated assemblages to chlorite, carbonate and sulphide. Similar to all other Rochechouart lithologies, euhedral adularia in fractures and void spaces and sericitization of feldspar minerals is observed in the polymict and monomict breccias, though is not as pervasive as in melt-bearing impactites.

Bright red reaction rims on lithic fragments are common in polymict breccias, but less so in the monomict material; in some cases the interiors of monomict clasts have been altered to zeolite. This pattern on clasts, an incomplete authigenic, bright red K-feldspar decreasing in intensity from the outside inwards, alludes to a temperature-controlled reaction, and is characteristic of K-feldspar produced as a result of potassium-rich fluids

(Pirajno, 2009).

Champagnac-type monomict breccias have been intensely adularia-carbonate-sulphide mineralized; dolomite, calcite and pyrite locally completely replace the clastic matrix, forming a coarse cement post-dating orthoclase overgrowth on clasts. Oxygen isotope data (Table 3-19) from these carbonates suggest moderate temperatures (up to 135ºC). Sulphide minerals occur within both the fabric of breccia clasts and precipitated with carbonate cement; isotope results reveal a minor to moderate degree of fractionation between the two types, possibly indicating that sulphides in the cement may have been leached from the amphibolite gneiss. Carbonate mineralization has been reported previously within the polymict breccias (Sapers et al., 2014); the monomict breccias studied here are significantly more mineralized than the continuous polymict impactite.

Although there are similarities in the secondary mineral assemblages associated with the monomict and polymict breccias, the parautochthonous unit is significantly more heavily altered. Clast chloritization, authigenic biotite and ubiquitous adularia-carbonate-sulphide cement are all characteristic of the monomict breccia; these minerals occur to a lesser degree in the polymict material. Previous studies have identified the crater cavity-sub crater interface as one of six areas within a complex impact structure suitable for the development of hydrothermal fluid circulation (Pierazzo and Osinski, 2012). The transition from a smectite-dominated assemblage to chlorite downward within the structure and further from the melt sheet is consistent with observations of other impact structures (Naumov, 2005).

3.4.1.4 Champagnac dike

The polymict dike found in Champagnac showcases the effects of localized high temperature perturbations on hydrothermal processes within the sub-crater environment. Monomict clasts proximal to the hot, melt-bearing polymict intrusion display distinctive, bright red-purple reaction rims with weathered, soft clay interiors. No other occurrence of such a pervasive reaction, affecting entire clasts, has been observed during this study apart from those associated with the dike. It would appear, therefore, that this is a localized temperature-controlled reaction assisted by hydrothermal fluid circulation.

Stable isotope results reveal a dramatic temperature difference in carbonate cements within the surrounding parautochthonous impactite; while the majority of carbonates in the monomict material are at most 135ºC, one sample of dolomite yields temperatures over 250ºC (Table 3-19). Bright red K-feldspar mineral fragments are dispersed throughout the melt material; the intense red coloring is caused by small hematite inclusions released

during potassic alteration of the precursor mineral. Overall, the melt material is enriched in K^+ (Figure 3-21). As stated by Naumov (2005), hydrothermal alteration within an impact structure is largely controlled by a lithology's proximity to a heat source; these observations corroborate this claim, showcasing the small-scale effects a melt-bearing dike may have on aqueous alteration in the sub-crater environment.

3.4.1.5 Chassenon melt-bearing breccia

The Chassenon melt-bearing breccia also has evidence for K-metasomatism, as alteration of tectosilicates and precipitation of authigenic K-feldspar in void spaces. Unlike the Montoume or Babaudus melt rocks, the Chassenon contains a large quantity of mafic green and clear quartz impact glass, which has been partially to completely devitrified to Fe-Mg clays and α-quartz. SEM observations reveal authigenic K-feldspar overgrowths associated with devitrified glass; this finding may indicate moderate acid leaching related to H^+ metasomatism, and similar to the melt-rich rocks, has left secondary K-feldspar untouched and glassy phases partially to completely argillized. Fe-Ti oxides, commonly rutile, are associated with both types of devitrified glass.

White mica is found both within larger lithic clasts and replacing smaller mineral grains within the matrix. Some crystals, such as those in Figure 3-30, appear to have been affected by shock metamorphism and are inherited from the target, while sericitization of quartzofeldspathic mineral fragments in the fine matrix is related to post-impact processes.

Alteration patterns within the Chassenon overlap slightly with those in the Babaudus; both rock types have an abundance of smectite clays with a seemingly unaltered phase of adularia. However, the Chassenon, like the Montoume, has much more lithic material than the Babaudus; alteration of mafic minerals in basement clasts may result in iron-rich fluids leading to the alteration of preserved glassy phases to Fe-Mg-rich smectite clays and associated Fe-Ti oxides.

3.4.1.6 Melt rocks: Babaudus and Montoume

Within Rochechouart, melt-bearing lithologies are most affected by K-metasomatism, with primary melt phases consisting of orthoclase as sanidine crystallites and adularia filling in voids, fractures and vesicles. The vesicular Babaudus-type melt rock has significantly higher volumes of smectite clays than the Montoume (Figure 3-35); this may be related to the formation of impact glass, subsequently devitrified by H^+ metasomatism during the early to mid stages of hydrothermal alteration or surficial diagenetic weathering.

Fe-Ti oxide minerals are found in both lithologies and are a common by-product of K-metasomatism (Pirajno, 2009). In the particulate impact melt, the combination of oxide minerals weathering from inherited lithic material combined with aphanitic K-feldspar melt is responsible for the characteristic red coloring. This red coloring is absent from the vesicular impact melt, which is made up almost completely of quartzofeldspathic minerals with very little lithic material inherited from the target. In the Babaudus, there is no evidence for crystallization of primary Fe-Mg phyllosilicates from the initial melt and none were observed in lithic fragments. If these minerals were present initially in the vesicular melt, they were likely broken down by alteration in the early stages of cooling, providing a source for the Fe-Ti oxides observed crystallized in vesicles and staining.

In the Babaudus, minor amounts of very late stage barite occurs in vesicles. The origin is unknown; sulphate minerals are absent from all other Rochechouart impactites except those associated with sulphides in autochthonous fractures.

Alteration assemblages and textures in the vesicular melt rock are characteristic of early stage K-autometasomatism of an impact melt and subsequent H^+ metasomatism, or argillic alteration (Naumov, 2005; Pirajno, 2009). As a granitic melt cools, residual fluids may interact with surrounding rocks to produce a series of subsolidus reactions, marking the early stages of hydrothermal alteration beginning around 600 to 800ºC (Figure 3-39). Base exchange reactions in feldspars (in this case, K^+ for Na^+) result in the development and circulation of alkaline fluids leading to potassic alteration; this process is likely to be responsible for the precipitation of adularia, replacement of albite and sericitization observed in all Rochechouart impactites. Within the Babaudus, alkali metasomatism was followed by H^+ metasomatism; potassic alteration releases H^+, increasing the H^+/K^+ ratio, leading to argillic alteration, acid leaching of aluminosilicates, breakdown of any mafic minerals, leading to the formation of clay minerals such as Fe-Mg smectite (nontronite) and chlorite observed in vesicles (Figure 3-39) (Pirajno, 2009). K-feldspar that precipitated during the preceding stage of K-metasomatism may be preserved during argillic alteration (Pirajno, 2009). This sequence of alteration is also in agreement with the scheme outlined by Naumov (2005) for impact-generated hydrothermal activity; melt-rich lithologies are dominated by a smectite-zeolite zone, which grades into a chlorite-dominated zone in melt-poor to non-melt bearing lithologies.

The vesicular impact melt rock in Rochechouart is highly weathered and argillic alteration occurs over a wide range of temperatures; without further work on the clay minerals, such as using oxygen isotopes to constrain temperatures, it is difficult to say whether the smectites we observe today are a product of surface diagenesis or early acidic

fluids during the cooling period. Similarly, iron oxide staining seen at the hand scale in fractures and vesicles may be a result of surficial weathering.

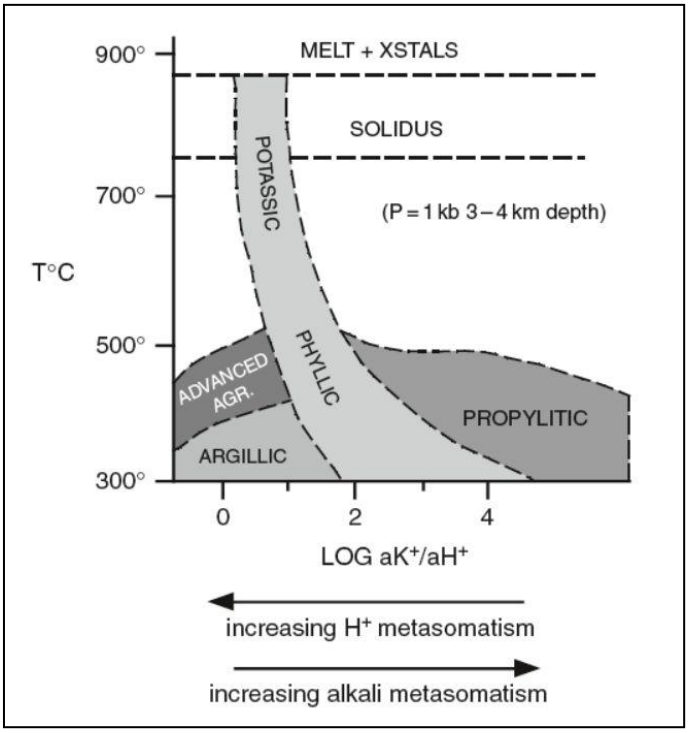

Figure 3-39: Types of aqueous alteration as a function of temperature and K^+/H^+ ratios (Pirajno, 2009). Early stage cooling of a granitic melt body initiates sub-solidus base exchange reactions between potassium and sodium; in Rochechouart, this process likely resulted in the enrichment of fluids in potassium.

3.4.2 Carbon and oxygen stable isotopes

Carbon isotope compositions of Rochechouart lithologies reflect mixing between organic and inorganic reservoirs; values range from -4‰ associated with autochthonous fractures, close to seawater and close to the Aquitaine basal carbonates at around +0.5‰, to a lighter -13‰ in monomict lithic breccias. Oxygen isotopes are relatively invariant, from +23.8 to +28.7‰, with only one outlier at +13‰ within the melt-bearing polymict breccia.

3.4.2.1 *$\delta^{13}C$ as an indicator of fluid reservoir mixing*

Because $\delta^{18}O$ of the starting fluid is unknown, carbonate mineral temperatures can only be estimated using the equations outlined in Section 3.2.3. Following the methods described by Boiron et al. (2002) we will interpret the corresponding carbon isotope associated with a carbonate mineral species to be an indicator of the fluid source. Similarly, secondary mineral assemblages associated with a carbonate mineral allude to the temperature of an environment, and may give clues to the $\delta^{18}O_{fluid.}$

The two major carbon reservoirs in the area which may have contributed to the precipitation of carbonate minerals are inorganic sedimentary, or seawater carbon, and dissolved organic carbon. Seawater $\delta^{13}C$ from 210 to 190 Ma is between -2 and +3‰ (Gradstein et al,. 2012), with the basal Aquitaine carbonates measuring between +0.3 and +0.7‰ (Table 3-17); a value of $\delta^{13}C$ = 0.5‰ will be assigned to represent seawater carbon. Organic carbon from plant material averages at $\delta^{13}C$ = -25‰ (Hoefs, 2009), and will be used to represent a purely organic reservoir. Isotope and fluid inclusion studies on carbonate mineralized Hercynian fractures within the crystalline basement of the Central Massif north of Rochechouart have yielded $\delta^{13}C$ values ranging from -13 to -6‰ (Boiron et al., 2002; Fourcade et al., 2002). This intermediate range of isotopic compositions has been attributed to the mixing of metamorphic and externally derived fluid reservoirs, with $\delta^{13}C$ input from mean crustal carbon (organic) and sedimentary carbon (inorganic) (Section 3.1.5). Similarly, Rochechouart carbonates span a range of $\delta^{13}C$ from -4 to -13‰, also likely representing mixing of multiple fluid reservoirs. This theory is corroborated by sulphide isotope data, which is discussed in Section 3.4.3.

3.4.2.2 Calcite and dolomite temperature estimates

The temperatures of aqueous solutions in equilibrium with calcite and dolomite were estimated using the established fractionation factors between carbonate minerals and water (Section 3.2.3; Section 3.6). Because the $\delta^{18}O$ of the fluid that precipitated the minerals is unknown, temperatures can only be constrained by placing limits on potential fluid sources; the reservoirs considered for this study are seawater and metamorphic fluids (Section 3.4.2.1). Late Triassic seawater $\delta^{18}O_{fluid}$ was between -2 and 0‰ (Gradstein et al., 2012), and metamorphic fluids were $\delta^{18}O_{fluid}$ from +9 to -5‰, using the average +/- 1 standard deviation of the dataset given by Fourcade et al. (2002) for Hercynian fluids. In the late Triassic, Rochechouart was equatorial; present day meteoric water $\delta^{18}O$ at the equator is 0‰ (VSMOW) (Hoefs, 2009; NASA Earth Observatory). Purely meteoric or seawater retaining it's original $\delta^{18}O$ value while infiltrating basement fractures or in this case, an impact crater, without interacting with crustal fluids is highly unlikely. Similar to other impact-hydrothermal studies, waters were likely sourced from a mixture of reservoirs (Chapter 1, Sections 1.3 and 1.4).

Calculated temperatures, with the exception of the polymict breccia dike, are within the range of late stage impact-hydrothermal (Chapter 1, Section 1.3; Naumov, 2005) or diagenetic. It is also worth noting that no suitable fluid inclusions with both a gas and liquid phase were identified for analysis; this would suggest that the fluids which

precipitated the adularia, calcite and dolomite within both impactites and basement lithologies may not have exceeded 100ºC. The exception to this is the dolomite in sample PC-3, which may represent an earlier generation of carbonate cement precipitated as a result of a localized injection of hot, melt-bearing material into the basement.

Table 3-19: Temperature range estimates for calcite and dolomite (ºC) (also see Section 3.6)

Rock type, and dataset or sample	**$\delta^{18}O_{mineral}$**	**$\delta^{18}O_{fluid}$ = seawater**		**$\delta^{18}O_{fluid}$ = metamorphic**	
		Calcite (ºC)	Dolomite (ºC)	Calcite (ºC)	Dolomite (ºC)
Monomict lithic breccia					
δ^{13}C-heavy cluster	Calcite avg = 27‰				
(MC-1, 2 and 4)	Dolomite avg = 25.9‰	25-35	45-55	15-95	25-130
δ^{13}C-light cluster	Calcite = 25.6‰				
(MC-3, 5, 6 and 7)	Dolomite = 25.7‰	25-40	45-55	20-105	25-130
Polymict breccia dike					
	Calcite avg = 26.8‰				
PC-1 and 2	Dolomite avg = 25.9‰	20-35	40-55	10-95	30-115
	Calcite = 25.02‰				
PC-3	Dolomite = 13.6‰	30-45	125-150	20-110	100-250+
Autochthonous fractures					
	Calcite = 26.2‰				
AC-1	Dolomite = 25.4‰	25-35	45-55	15-100	25-150
Basement fractures of unknown origin					
δ^{13}C-heavy cluster	Calcite avg = 26.4‰				
(UC-1, 2 and 5)	Dolomite avg = 26.2‰	25-35	40-50	15-100	25-140
δ^{13}C-light cluster	Calcite avg = 25.2‰				
(UC-3 and 4)	Dolomite avg = 24.9‰	30-45	50-60	20-115	30-155

Monomict breccias: Two data clusters were identified in the monomict lithic breccia carbonates based on corresponding carbon isotopes (Figure 3-45); cluster one, MC-1, 2 and 4, has a slightly heavier δ^{13}C and cluster two, MC-3, 5, 6 and 7, is slightly lighter, reflecting a more organic source. The average δ^{18}O of each cluster was calculated and used to construct the temperature models (Figure 3-45 and 46). Overall, calcite temperatures range from 15-105ºC, and dolomite is slightly hotter at 25-135ºC (Figure 3-46).

Apart from slightly different stable isotope signatures, the minerals associated with both clusters are texturally and compositionally the same. Both datasets reflect some level of organic carbon input, and do not represent purely meteoric, metamorphic or seawater

end members. The differences in carbon compositions of the minerals may reflect changes in fluid composition over the lifetime of the hydrothermal system.

Champagnac dike: Carbonate minerals extracted from the lithic breccia hosting the Champagnac polymict dike reflect the small-scale effects of hot, melt-bearing intrusions on the sub-crater environment. Two generations of dolomite cement were identified (Figure 3-47). PC-1 and 2 indicate relatively cool fluids (30 to 115 ºC) (Figure 3-48), similar to those found in the monomict lithic breccia; Dolomite in PC-3, however, is significantly hotter, with the lowest temperature estimates at 100ºC and the highest above 250ºC (Figure 3-48). Such a large difference in temperature on a small scale agrees with the alteration observed in the host rock; clasts in contact with the melt-bearing material have high temperature reaction rims with weathered clay interiors.

Because one dolomite sample was significantly hotter than the other two temperatures were modeled using the equation given by Zheng (1999), which covers a wider range of temperatures (0-1200°C) than that provided by Vasconcelos et al. (2005) (25-45°C). The differences in results obtained from the two equations are represented graphically in Figure 3-5.

Autochthonous fractures: Carbon isotopes from autochthonous fractures are the closest to seawater $\delta^{13}C$ than any other lithology, at -4‰ (dolomite) and -5‰ (calcite) (Figure 3-49 and 50). Calcite ranges from 15 to 100°C, and dolomite ranges from 25 to 150°C; however, if we consider the corresponding carbon isotope composition and estimate the temperatures assuming Triassic seawater, calcite ranges from 25 to 35°C and dolomite from 45 to 55°C (Figure 3-50). These temperature ranges compliment the corresponding sulphur stable isotopes (Figure 3-41), which strongly support a biological origin for the sulphide minerals co-precipitated with the carbonates.

Unknown basement fractures: The five sets of fractures within the basement are grouped into two clusters based on carbon isotopes (Figure 3-51); samples UC-1, 2 and 5 were isotopically heavy, ranging from -4 to -8‰, and samples UC-3 and 4 were isotopically light, with slightly more organic-rich values of around -11‰. The heavy carbon fractures were slightly cooler than those with a lighter signature, by 5 to 15°C. Calcite temperatures range from 15 to 115°C and dolomites are slightly hotter, ranging from 25 to 155°C (Figure 3-52).

The unknown fractures do not exhibit $\delta^{18}O$ values reflective of Hercynian hydrothermal activity. They may be of impact origin, or they may source from the late stage fluid event outlined in Section 3.1.3. The dolomites are texturally and compositionally similar to those in Rochechouart impactites, with the exception that they

lack both the ubiquitous adularia rim found in monomict breccias, and the intense heavy sulphide mineralization seen in the autochthonous fractures.

3.4.3 Distribution and origin of sulphide minerals in Rochechouart

Sulphur isotope data reflect a high degree of fractionation between impactites and basement material; autochthonous fracture sulphides are as low as $\delta^{34}S$ of -35‰ and pyrite associated with the basement gneiss is as high as 0.4‰.

3.4.3.1 $\delta^{34}S$ of Rochechouart impactites and basement

Pyrite analyzed from within the amphibolite fabric ranges from $\delta^{34}S$ = 0.4‰ to -1.3‰; sulphide veins cross-cutting the gneiss fabric are only slightly fractionated, at -3.7 and -2.7‰ (Figure 3-40). Although these sulphides are considerably heavier than those within the impactites, they are on the lighter range of primary sulphur, supporting a small degree of fractionation. Amphibolite facies metamorphism does not completely obliterate isotopic signatures of monomineralic sulphide species within a protolith (Crowe, 1994); the Upper and Lower Gneiss units contain paragneiss intercalations (Chapter 2, Section 2.5.2.1), therefore the $\delta^{34}S$ recorded may have been inherited from a sedimentary or igneous protolith. Though this unit has not been as pervasively affected by aqueous alteration as other lithologies, sulphides may also have formed during hydrothermal activity associated with regional metamorphism; associated sulphides are not likely a product of impact-hydrothermal fluid circulation within the basement, but an impact origin cannot be ruled out.

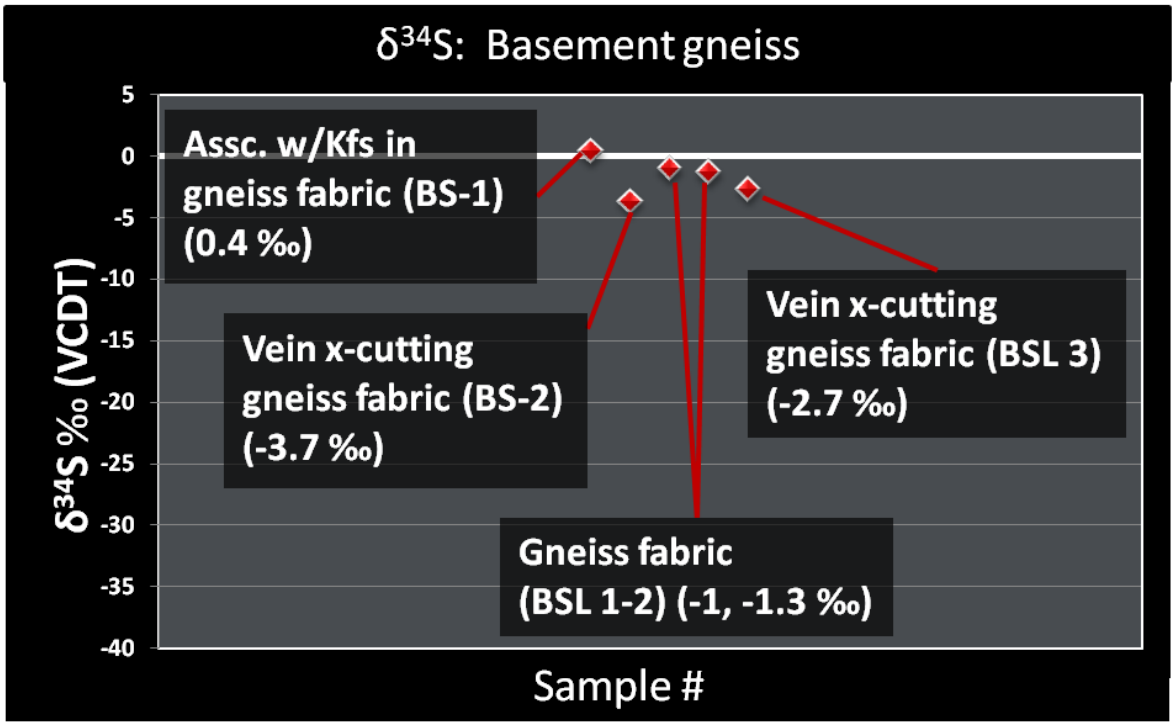

Figure 3-40: $\delta^{34}S$ of sulphides within basement amphibolite gneiss; overall, all samples fall within the range of terrestrial igneous sulphides or sedimentary (Figure 3-6).

Autochthonous granodiorite fractures strongly reflect biological signatures, with $\delta^{34}S$ ranging from -26.9 to -35.8‰ (Figure 3-41); these values also support the hypothesis that seawater infiltrated the structure during the post-impact cooling period. Considering the paleogeography of Rochechouart, seawater is the only sulphate reservoir large enough to support this level of fractionation within a sulphide species. Seawater sulphate $\delta^{34}S$ from 190 to 210 Ma ranges from +13‰ to +19‰; thermochemical sulphate reduction is only capable of reducing parent sulphate by a maximum of 20‰, therefore the lower limit of iron sulphide produced as a result of thermochemical sulphate reduction from a seawater source in this area is -7‰. This conclusion is also corroborated by the corresponding carbonate data; temperatures are well within the realm of biological sulphate reduction and carbon signatures are close to those of seawater (Figure 3-49 and 3-50). $\delta^{34}S$ results from autochthonous fractures within the brecciated basement quartz veins parallel those of the granodiorite fractures. A defining characteristic of biological sulphate reduction is large fractionations over a small scale (Machel, 2001); three measurements were taken from a single vein in one sample set (ASL-1 to 3) which yielded isotope fractionations varying by as much as 20‰.

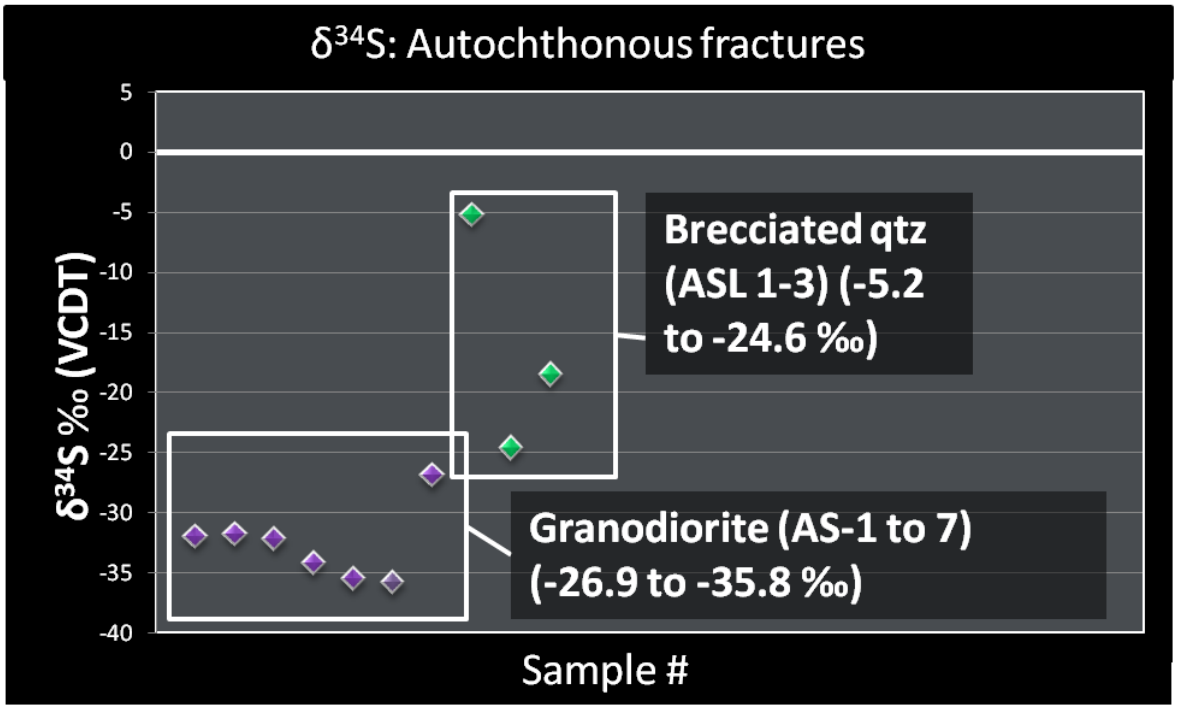

Figure 3-41: $\delta^{34}S$ of sulphides in autochthonous granodiorite-hosted fractures and brecciated basement quartz veins.

Sulphur isotopes from the monomict breccia clast fabric and clastic matrix parallel those values within the crystalline basement gneiss fabric, indicating very little to no fractionation between the two. When compared to the clast fabric pyrite at -1.8‰, pyrite associated with carbonate cement within the matrix shows a minor to moderate degree of fractionation, at -5.6 to -10.7‰, and pyrite not associated with dolomite cement within the clastic matrix shows no degree of reduction, at -1.2‰ (Figure 3-42). Corresponding $\delta^{13}C$ and $\delta^{18}O$ (Figure 3-45 and 46) of carbonate matrix cement indicates a relatively cool origin for the dolomite and calcite (<150°C).

Although post-impact hydrothermal activity has affected the monomict lithic breccia, it appears that it has had little effect on sulphides within the clast fabric or clastic matrix; only sulphides within the matrix carbonate cement have significantly reduced $\delta^{34}S$. Sulphides within the unshocked basement reflect a minor degree of fractionation, possibly by pre-impact processes; sulphides within the breccia cement may be a product of hydrothermal remobilization and minor fractionation of these pre-existing target sulphides.

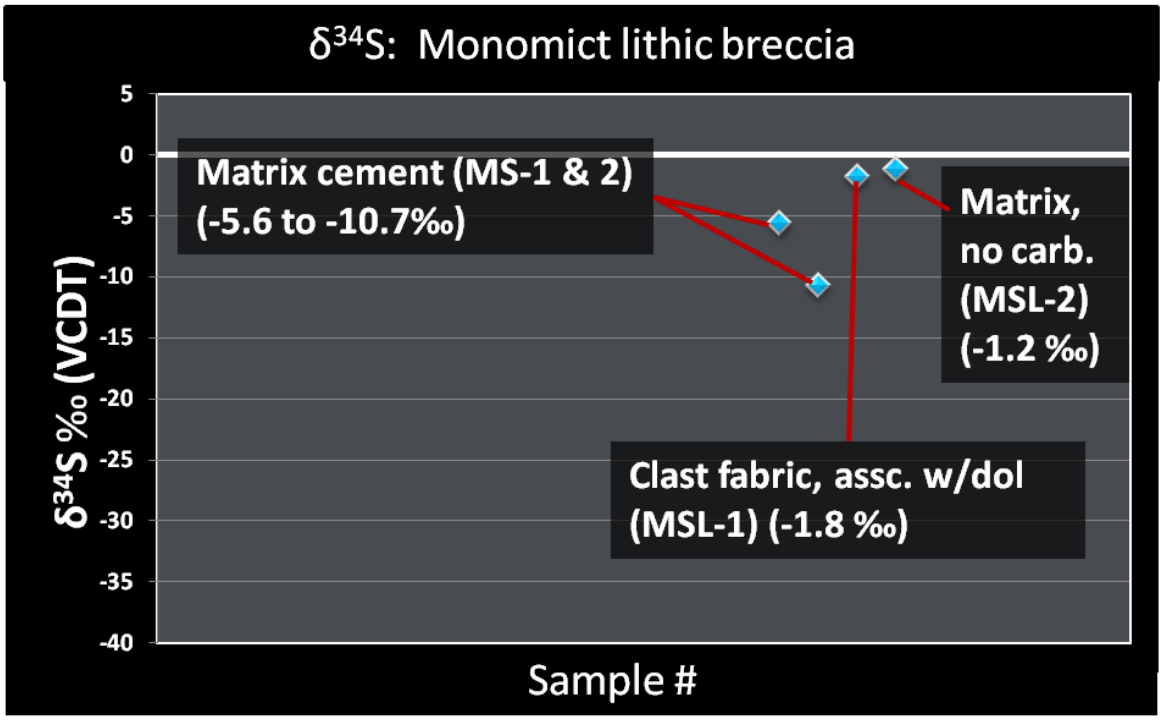

Figure 3-42: $\delta^{34}S$ of sulphides in the monomict lithic impact breccia.

The set of fractures of unknown origin within the basement granodiorite show a wide range of $\delta^{34}S$ values, from -1.7 to -26.2‰ (Figure 3-43). It could be argued that the two samples showing strong evidence for biological sulphate reduction (US-3 and 4) are impact related, as they reflect values similar to those in the autochthonous fractures; however, they come from unshocked crystalline basement, and without chronological constraints their origin and context relative to the impact event is unknown. Temperature models based on corresponding oxygen isotopes associated with samples US-1 and 2 reveal cool conditions (<150°C) and slightly heavier carbon values than those in impact breccias (Figure 3-51 and 52); it is unlikely the fractures are Hercynian, and may represent impact-hydrothermal deposits or late-stage fluid infiltration and brine migration as outlined by Cathelineau et al. (2012).

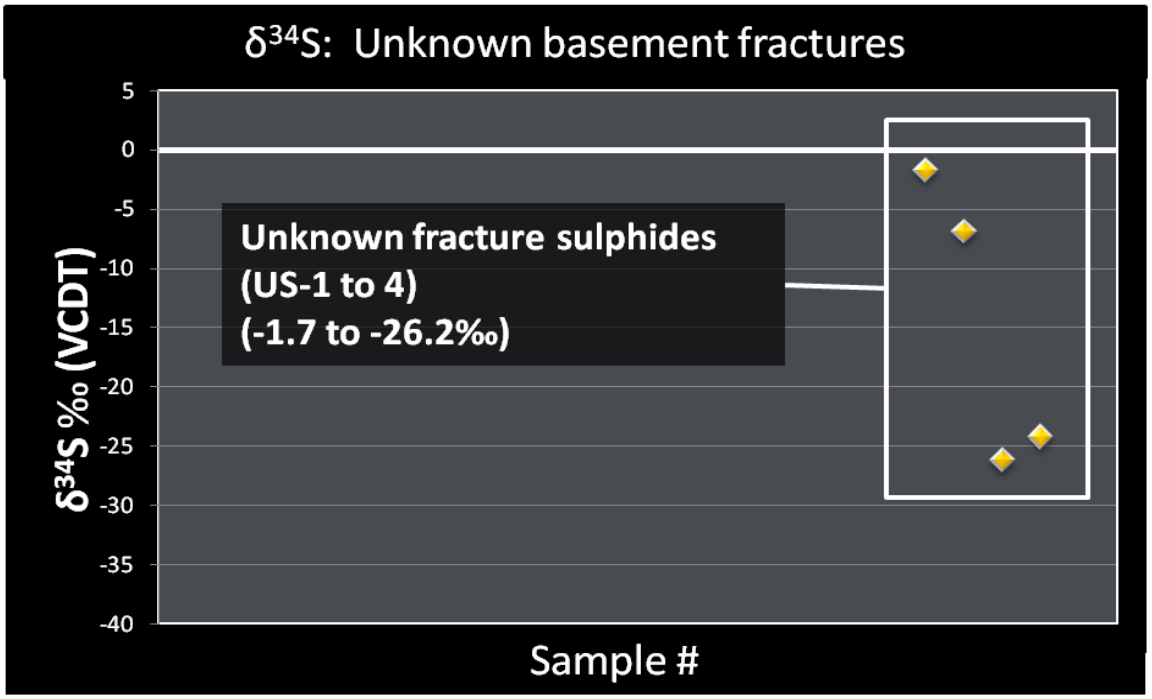

Figure 3-43: $\delta^{34}S$ of sulphides in basement fractures of unknown origin.

3.4.4 Evidence for fluid mixing

Stable isotope and mineralogical evidence supports the concept of mixing of Aquitaine seawater and metamorphic fluid reservoirs within the Rochechouart post-impact hydrothermal environment. $\delta^{13}C$ values reflect a mixture of organic and inorganic carbon sources and $\delta^{34}S$ isotopes of autochthonous sulphides support open system biological sulphate reduction. The ubiquitous presence of dolomite throughout Rochechouart impactites requires an abundant source of magnesium which, at near-surface conditions, is most likely to be provided by seawater.

3.4.4.1 The "dolomite problem" and how to solve it

The most common carbonate mineral in Rochechouart is dolomite. The precipitation of dolomite in a diagenetic environment requires a fluid to be saturated in Mg^{2+}; meteoric water is undersaturated with respect to magnesium and at near-surface conditions seawater is the only fluid source of providing sufficient magnesium for dolomite precipitation (Warren, 2001). Modern day concentrations range from ~1200-1300 ppm (Pirajno, 2009); During the Triassic, levels were approximately one-half to one-third those of today (Horita et al., 2002).

The problem of dolomite precipitation, however, is not one of ion saturation, but kinetics. The hydration barrier between magnesium and water is much stronger than that of calcium, and can only be overcome kinetically. Dolomite precipitation is also inhibited by

the presence of sulphate, which is a major ion in seawater at present day concentrations of 2600-2700 ppm (Pirajno, 2009); during the Triassic, seawater sulphate concentration was approximately half of modern day values (Horita et al., 2002). The kinetic inhibitors on dolomite precipitation in an Mg-saturated fluid can be overcome by heating or cooling, the introduction of a fluid with a different salinity or reducing the amount of dissolved sulphate (Warren, 2001; Boiron et al., 2002); these conditions are met when we consider a mixing model for hydrothermal fluid reservoirs, and the evidence provided by sulphur isotopes that sulphate-reducing bacteria were present within the system. This model is supported further by the oxygen isotopes of carbonates, which reveal temperatures suitable to support colonization by thermophilic sulphur-reducing bacteria.

The fluctuations in carbon isotopes throughout all impactites may reflect the evolution of fluids over the lifetime of the system. Autochthonous fractures, which reveal values close to seawater carbon, may represent early stage mineralization before fluids equilibrated with the organic-rich metamorphic fluids.

3.5 Conclusion

3.5.1 Overview of hydrothermal activity in Rochechouart and event overprinting

Mineralogical and stable isotope data indicate a cool (<300°C), retrograde hydrothermal environment typical of impact systems (Naumov, 2005; Osinski and Pierazzo, 2012; Osinski et al., 2013) where alteration assemblages and patterns are largely controlled by host rock melt content (heat source). Hydrothermal alteration related to Variscan metamorphism and plutonic activity may be detected from small scale mineralogical observations of unshocked basement material; however, the pervasive K-metasomatic overprint in all impactites also extends into the crystalline basement, and without chronological constraints it's provenance cannot be determined. No carbonate mineralization related to Hercynian metamorphism was detected; the basement fractures of unknown origin contain carbonates that gave palaeotemperatures too cool to represent regional or plutonic hydrothermal mineralization, therefore an impact origin may be considered. Stable isotope data supports the mixing of multiple fluid reservoirs within the system, with considerable input from seawater. Sulphide mineralization within lithic impactites covers a wide range of values, reflecting inheritance from the target with minimal fractionation, as well as open system biological sulphate reduction. Lastly, late stage brine migration along the unconformity identified by Cathelineau et al. (2012) and Boiron et al. (2002) must be considered a fluid source for carbonate precipitation within

the structure (Chapter 4).

3.5.5.1 Hydrothermal model overview

The potassic overprint in Rochechouart is derived from the granitic melt sheet; during the early stages of cooling, subsolidus exchange reactions enriched fluids in potassium, which have affected all lithologies. The pervasiveness of the alteration on a small scale, as well as subsequent alteration types, correlates with melt content and therefore heat source. This model agrees with the scheme outlined by Naumov for impact-hydrothermal systems (2005); in addition to K-metasomatism, melt and glass-bearing impactites contain smectite-silicate dominated assemblages, which decrease with melt content and grades into chlorite-carbonate-sulphide in lithic breccias and autochthonous material. These observations are consistent with alteration patterns observed in other endogenous geologic settings; as a granitic melt cools, autometasomatism produces K-rich fluids and potassic alteration. In Rochechouart, subsequent H^+ metasomatism lead to silicate hydrolysis, which attacks highly shocked glass and melt-bearing phases, producing argillic dominated assemblages as seen in the Babaudus, Chassenon and Montoume melt-bearing and melt-rich rocks. Argillic alteration may spare secondary K-feldspar (Pirajno, 2009); ultimately, melt rocks end up enriched in K_2O with Na_2O and CaO removed from primary impact products. Waters become near-neutral to alkaline and are saturated with ions as a result of early stage H^+ uptake.

Chloritization of mafic minerals in particulate impactites and the continued precipitation of adularia in all lithologies marks the intermediate stage of hydrothermal alteration. This stage is reflected in the lithic breccias and autochthonous material; while still showing evidence for K-metasomatism, smectite clays are mostly absent and chloritization dominates. The bright-red K-feldspar observed throughout all Rochechouart impactites is characteristic of potassic alteration; iron oxides are produced as a by-product, and may form small inclusions in feldspars. The replacement of albite by orthoclase, and orthoclase by muscovite and paragonite, is characteristic of alteration by K-rich fluids which continues through the intermediate phase (Naumov, 2005).

The last stage of hydrothermal alteration in Rochechouart is marked by carbonate-sulphide precipitation in lithic impactites and autochthonous fractures. Carbon and oxygen stable isotope results reveal a cool, (<150°C) environment. As temperatures decrease and pH becomes more neutral to alkaline, chloride complexes carrying metals destabilize and calcite, dolomite and pyrite precipitate (Figure 3-52). The exception to this pattern is the autochthonous fractures, which contain marcasite, pyrite and considerably less dolomite

than other impactites, indicating slightly more acidic conditions. The reduced sulphur isotopes also support the mediation of sulphate-reducing bacteria.

The Champagnac site represents an area within impact structures suitable for the development of hydrothermal circulation, as outlined by Osinski et al. (2012). Observations reveal this area to be one of dynamism; fluctuations in heat, fracturing, porosity and stable isotope results from this study reveal the sub-crater environment to be an ideal place to search for extremophile life in impact structures, and certainly an area suitable for later-stage hydrothermal circulation.

A mixture of metamorphic and marine fluid reservoirs is proposed on the basis of three observations; carbon isotopes reflect organic and inorganic reservoirs; sulphide minerals are highly reduced, requiring an open-system and prolonged supply of sulphate to reach such high fractionations; and the omnipresence of dolomite, whose precipitation requires specific conditions not met without a mixing model.

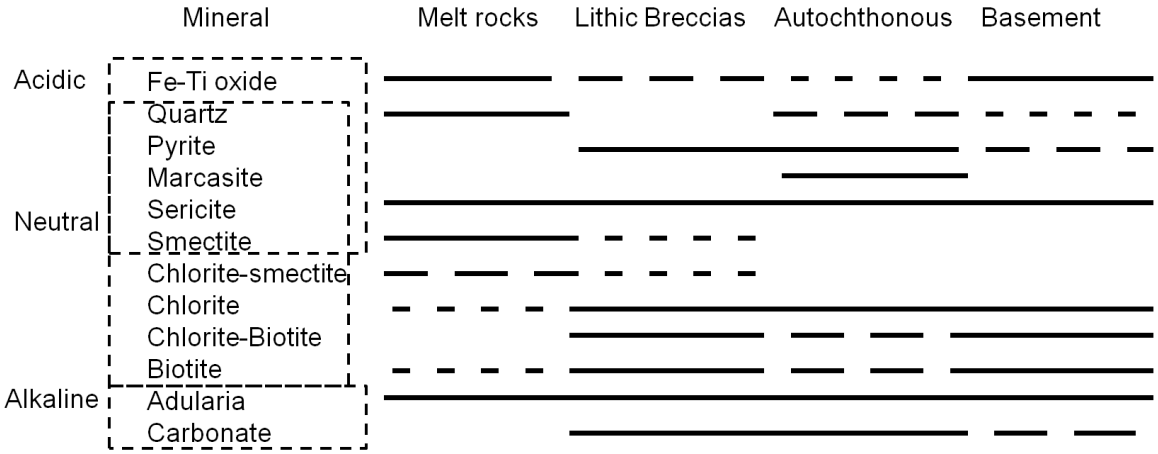

Figure 3-44: Overview of dominant hydrothermal mineral assemblages as a function of fluid pH and rock type in Rochechouart. Modified after Pirajno, 2009.

3.5.5.2 Pre-impact metamorphic vs impact-hydrothermal

No Hercynian carbonates were unambiguously identified in this study; however, mineralogical evidence does allow for some differentiation of metamorphic and plutonic pre-impact alteration within the granodiorite. There is evidence for K-metasomatism affecting plutonic hydrothermal assemblages within the granodiorite; An-plagioclase in myrmekite has been altered, leaving only K-feldspar, albite and quartz. Similarly Fe-Mg phyllosilicates within the gneiss unit contain K-rich rims and albite has been partially altered to K-feldspar which may also display a sericitic texture; this mineralogy may represent post-impact K-metasomatism, or possibly late stage regional metasomatism

during the Variscan orogeny.

3.5.5.3 Late stage fluid event and brine migration, and unknown fractures

Carbonates precipitated during the late stage fluid event outlined by Fourcade et al. (2002), Boiron et al. (2002) and Cathelineau et al. (2012) contain similar isotope values to those in all Rochechouart carbonates. The "fluid event" is a result of the percolation and mixing of Mesozoic seawater with metamorphic and meteoric fluids at the Aquitaine unconformity, precipitating dolomite, adularia, fluorite, quartz and sulphides in basement fractures.

Mineralogically and isotopically, the origin of the Rochechouart carbonates in lithic impactites (post-impact hydrothermal or late stage diagenetic) cannot be distinguished. The temperatures and fluid sources for the two events are almost identical; radiometric dating of adularia or secondary apatites would answer this question. It is also possible that diagenetic carbonates overprint impact-hydrothermal carbonates; growth patterns and crystal textures in dolomites may allude to "resetting" during a later fluid phase (Warren, 2000).

3.6 Supporting figures for $\delta^{13}C$ and $\delta^{18}O$ results: $\delta^{13}C$ vs $\delta^{18}O$ and temperature models

The following figures show $\delta^{13}C$ vs $\delta^{18}O$ plots for carbonate minerals (Figures 3-45, 47, 49 and 51), and temperature estimates based on the known fractionation factors (α) between dolomite and water, and calcite and water, as a function of temperature, drawn using the equations outlined in Section 3.2.3 (methods) (Figure 3-46, 48, 50 and 52). Because the starting fluid $\delta^{18}O$ is unknown, but the $\delta^{18}O_{mineral}$ is known (measured during this study), temperatures (x-axis) are estimated relative to possible fluid reservoirs in Rochechouart (y-axis) (discussed in Sections 3.4.2.1 and 3.4.2.2); the limit of Hercynian metamorphic fluid (Fourcade et al. 2002) is outlined in blue and late Triassic seawater (Gradstein et al., 2012) in yellow. The arrows drawn from the equation lines down to the x-axis denote the upper and lower temperature limits for each carbonate data set. A summary of the calculated temperatures is listed in Figure 3-19. For further information on oxygen isotope fractionation and applications within the carbonate mineral-water system, see Section 3.1.6.

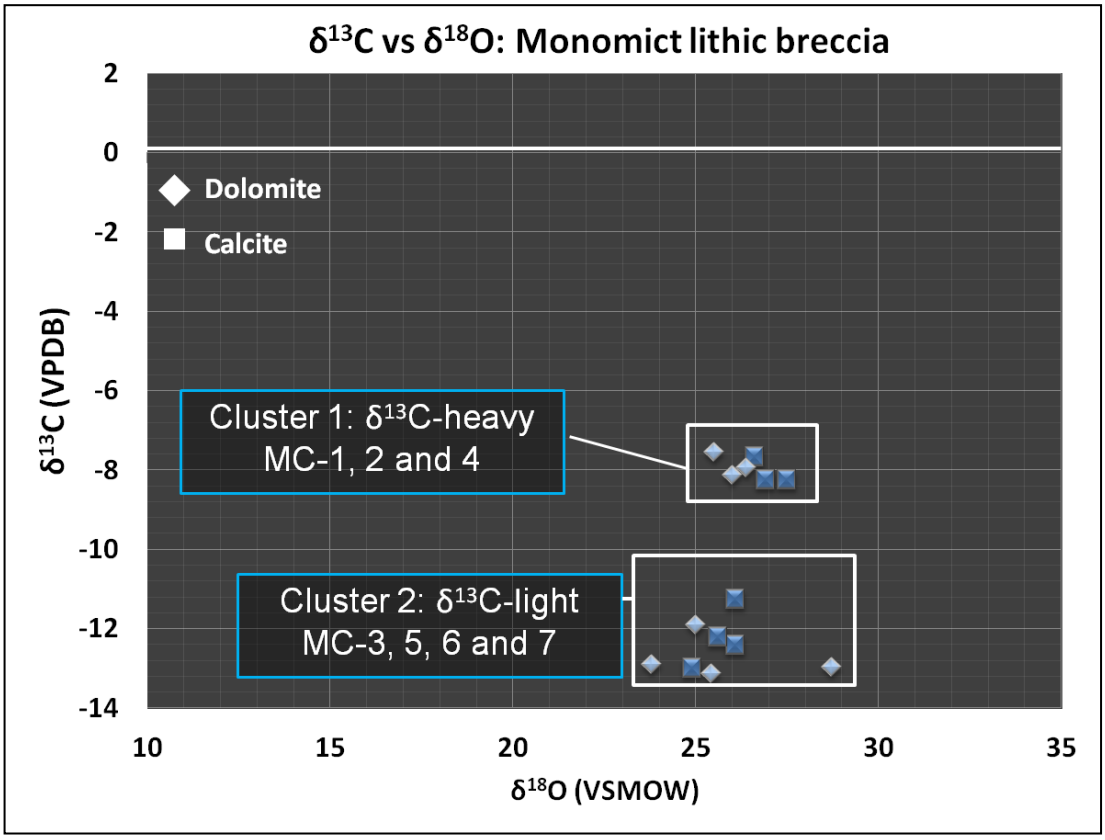

Figure 3-45: $\delta^{13}C$ vs $\delta^{18}O$ of monomict carbonates. Samples were divided into two clusters based on carbon isotopes compositions; cluster one, $\delta^{13}C$-heavy samples, has carbon isotope ranges from -7.5 to -8.2‰, and cluster two, which is $\delta^{13}C$-light from -11.2 to -13.1‰. Overall, cluster two is slightly hotter than cluster one, with the exception of one outlier with a $\delta^{18}O$ of 28.7‰. Corresponding temperature estimates are in Figure 3-46.

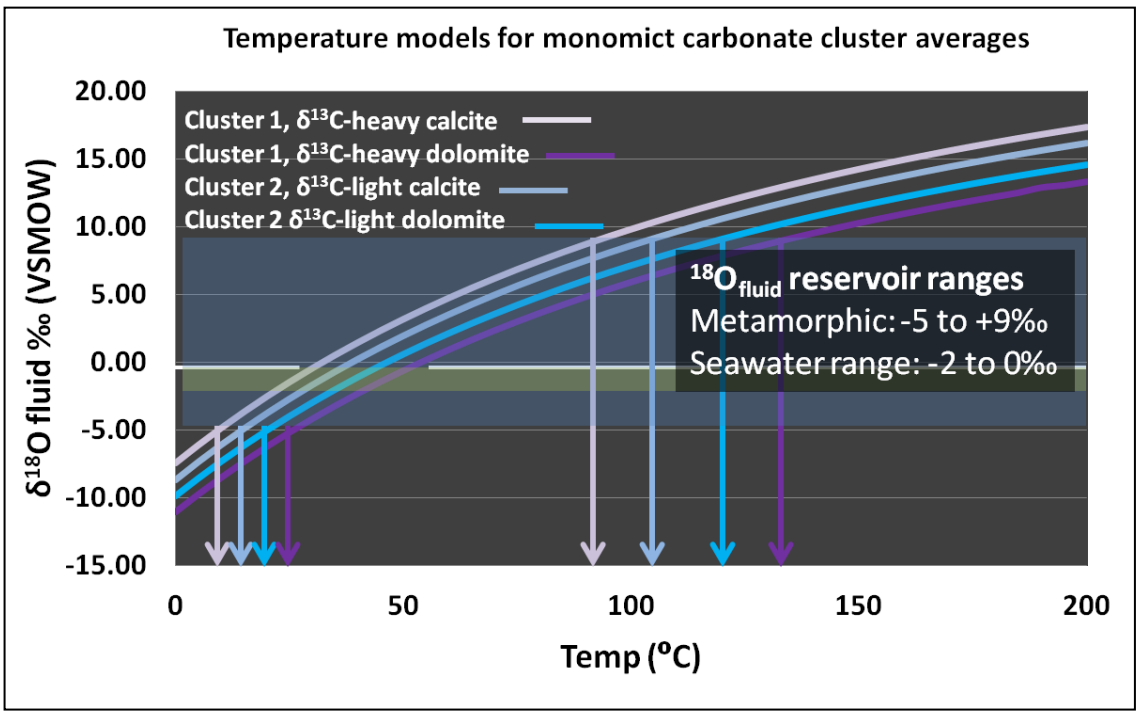

Figure 3-46: Temperature models constructed using the average $\delta^{18}O$ for both clusters of monomict

lithic breccia carbonates (Figure 3-45); arrows extending to x-axis (temperature) denote overall limits for each dataset. Monomict lithic breccia carbonate temperatures are fairly invariant, and reflect a cool (<150ºC), late stage hydrothermal regime, with contribution from organic carbon. For a detailed discussion, see Section 3.4.2.2.

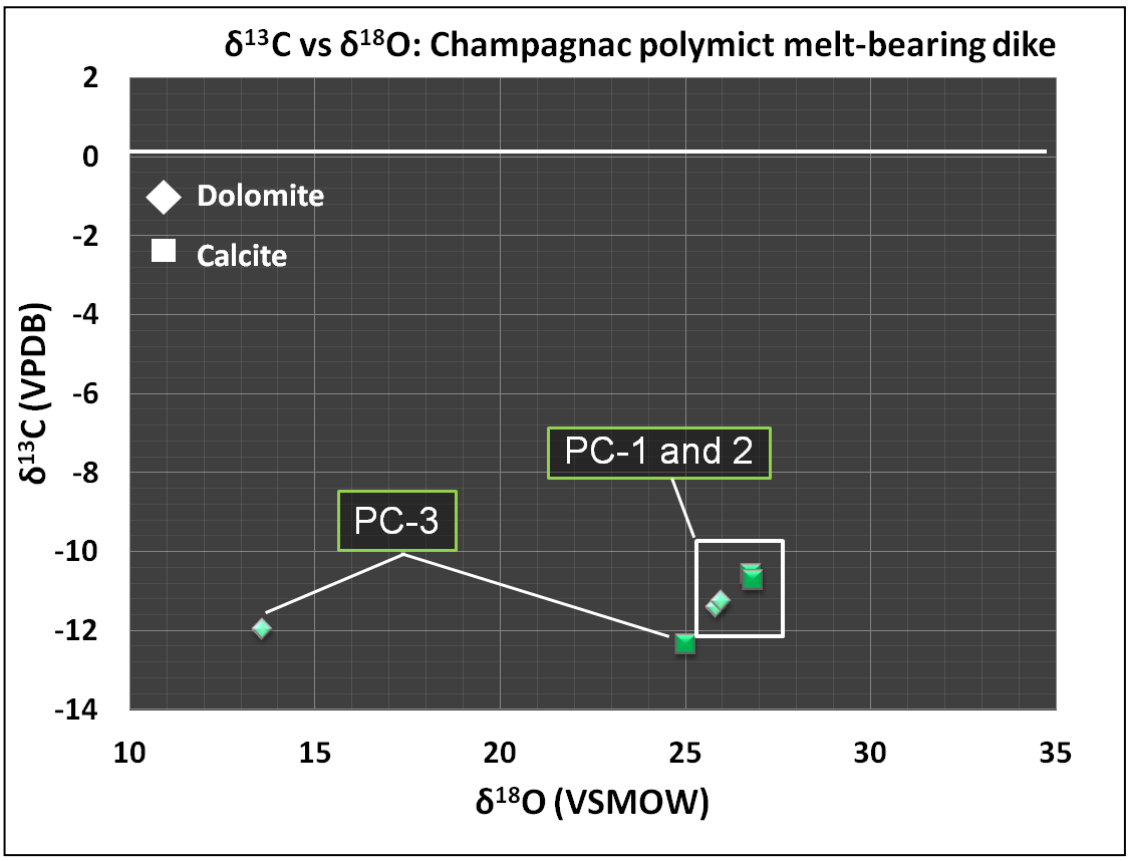

Figure 3-47: $\delta^{13}C$ vs $\delta^{18}O$ of carbonate minerals associated with the polymict dike; PC-1 and 2 are very similar and were averaged for the temperature models in Figure 3-48. Carbon isotopes vary little between all samples, ranging from -10.3 to -12.5‰, reflecting contribution from an organic source.

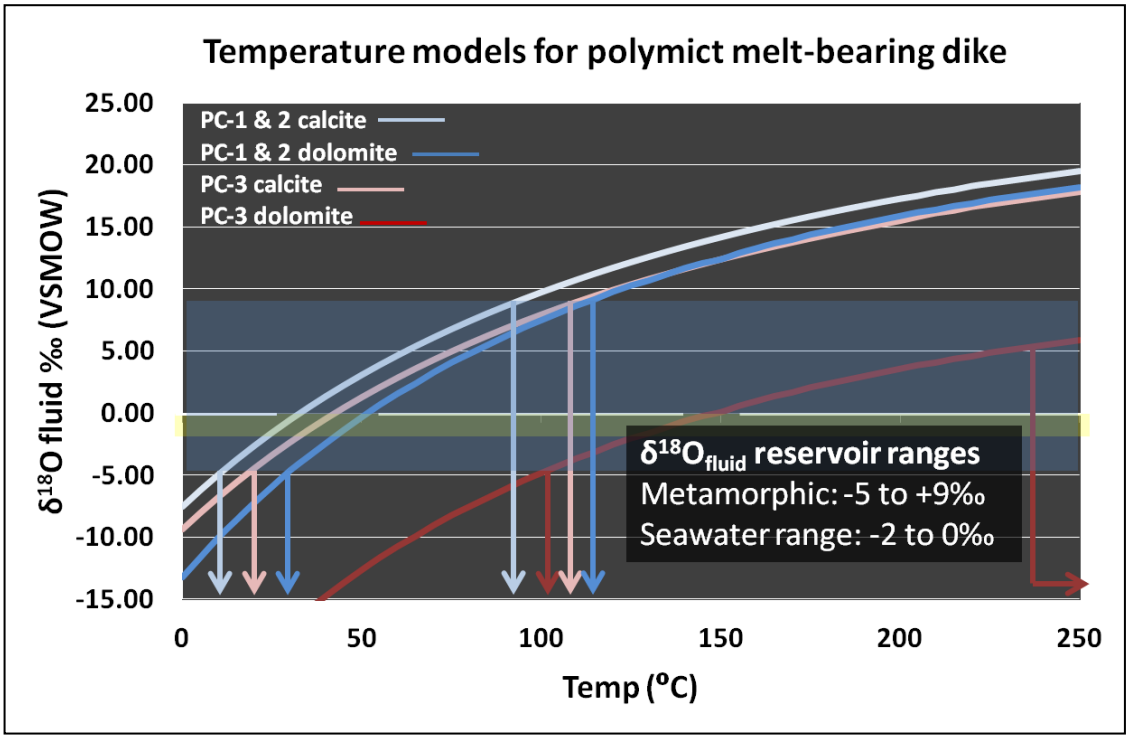

Figure 3-48: Temperature models constructed using the average $\delta^{18}O$ of calcites and dolomites from PC-1 and 2 (Figure 3-47), and PC-3; arrows extending to x-axis (temperature) denote overall limits for each dataset. PC-3 dolomite is significantly hotter than any other carbonates in the Rochechouart field area analyzed during this study (+250ºC) (Figure 3-19).

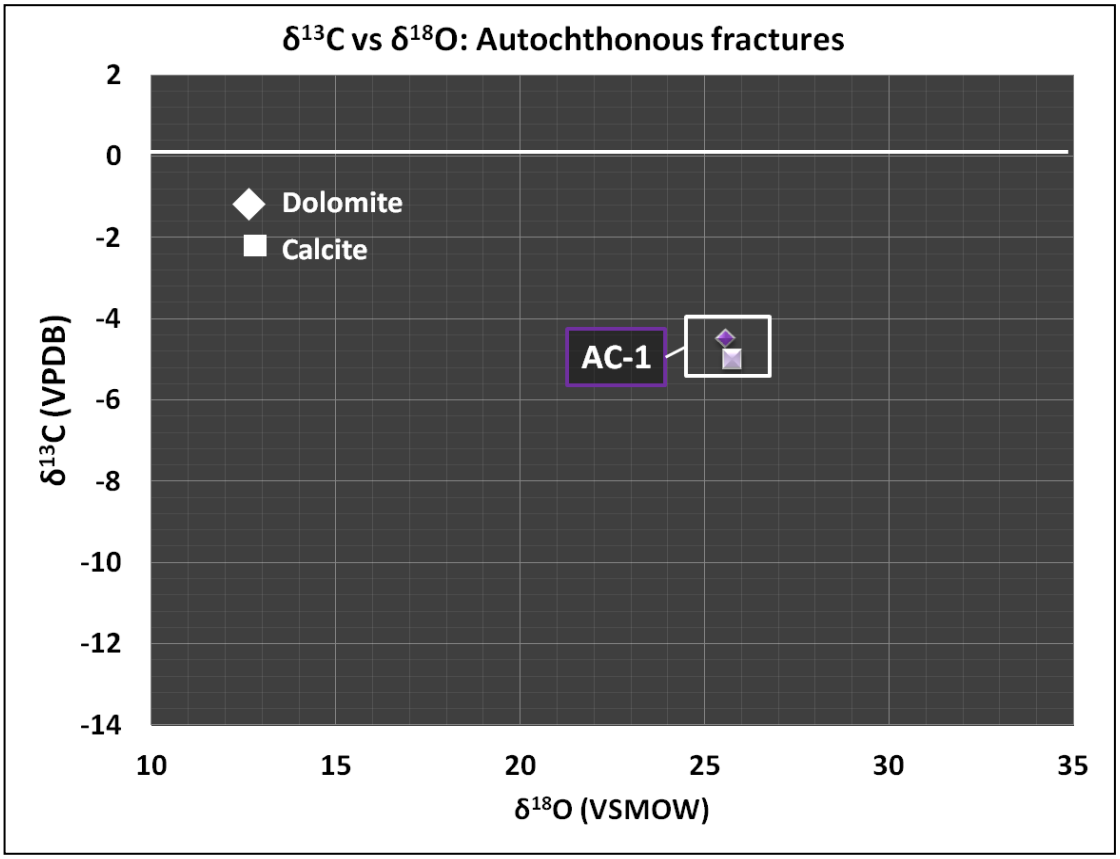

Figure 3-49: $\delta^{13}C$ vs δ^{18} for carbonates precipitated within the autochthonous impact fractures, based on models in Figure 3-45.

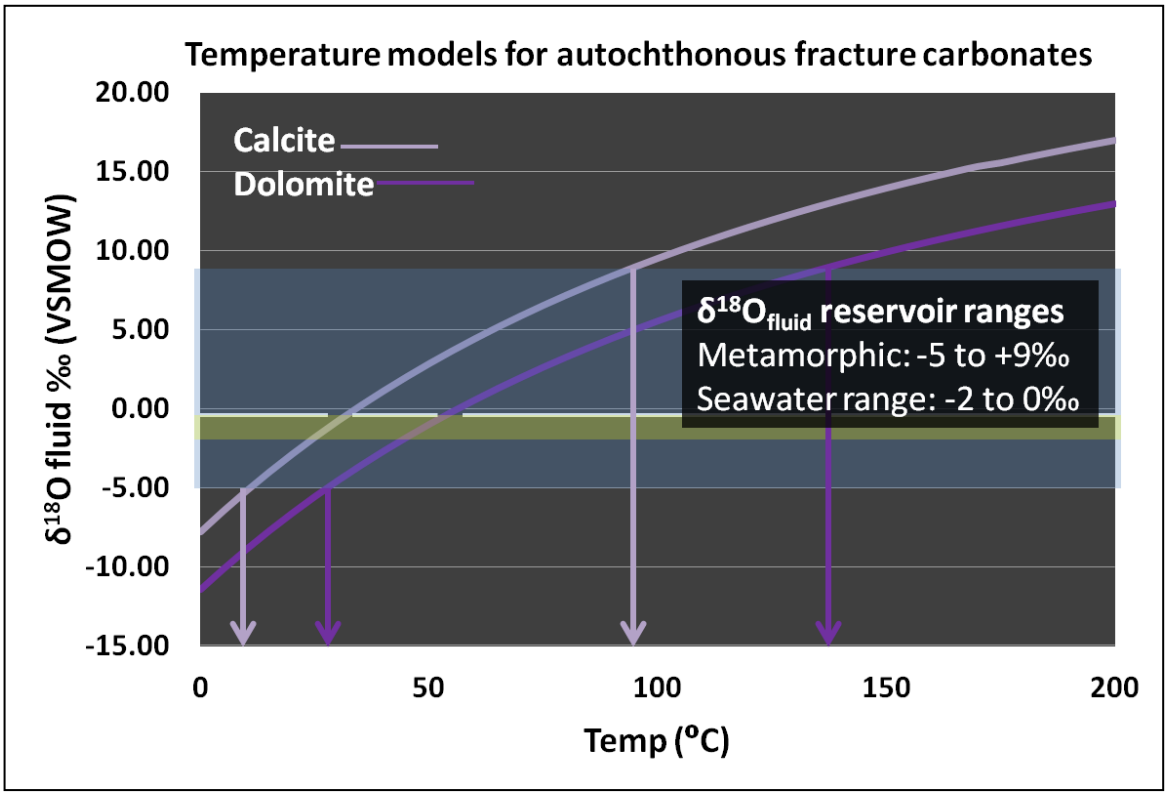

Figure 3-50: Temperature models for autochthonous impact fracture calcite and dolomite; arrows extending to x-axis (temperature) denote overall limits for each dataset. Considering the heavy

carbon isotope signature, which is close to that of seawater, autochthonous carbonates may have precipitated from hydrothermal solutions reflecting more input from seawater than metamorphic (Figure 3-41).

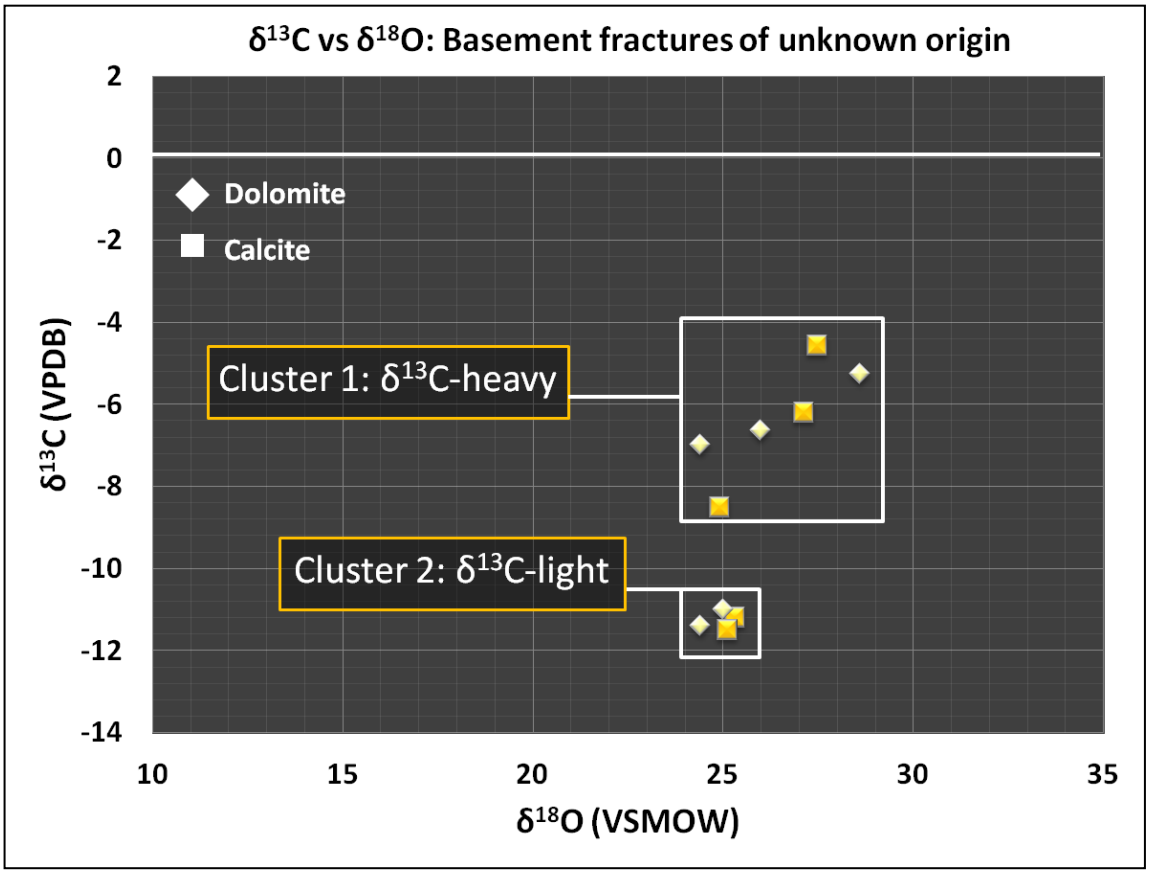

Figure 3-51: $\delta^{13}C$ vs $\delta^{18}O$ for the basement fractures of unknown origin. Data sets were grouped based on their carbon isotope, both of which reflect a mixture of fluid reservoirs. Oxygen isotopes do not reflect a Hercynian origin (Figure 3-52).

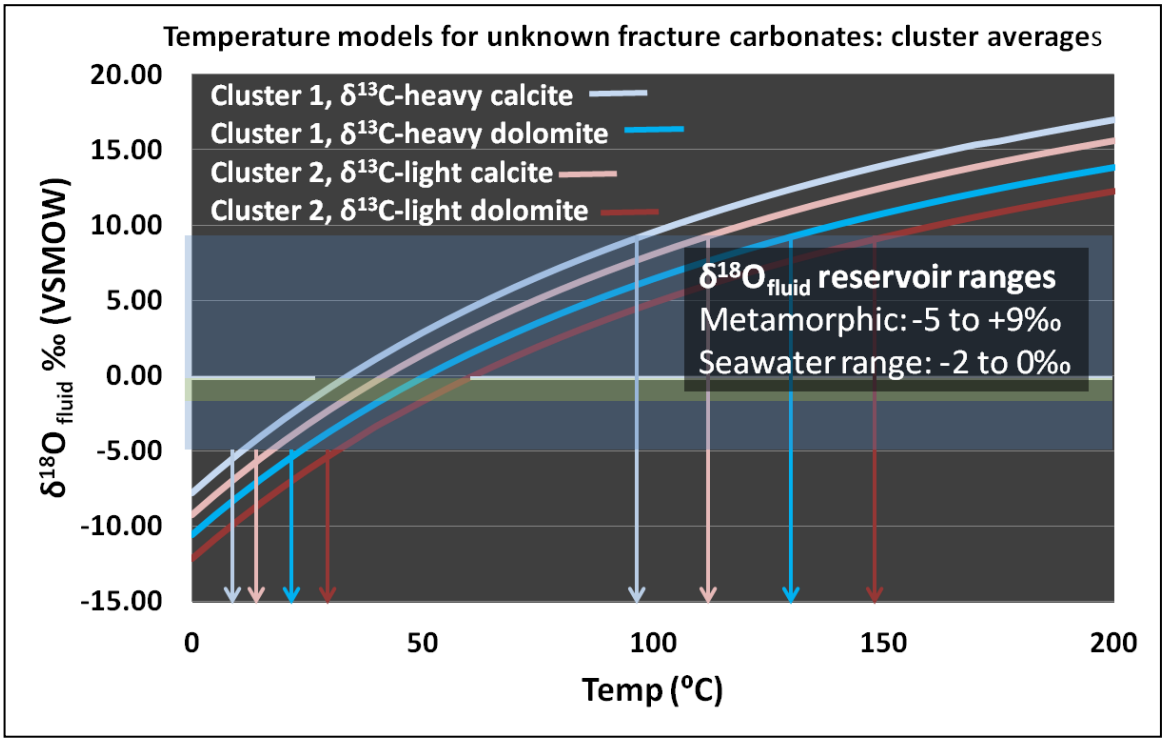

Figure 3-52: Temperature models for the two sets of basement fractures of unknown origin; arrows extending to x-axis (temperature) denote overall limits for each dataset. It is very unlikely that these fractures are Hercynian, as even at the upper limits of a purely metamorphic fluid, they are much cooler than what would be expected for regional metamorphic or magmatic hydrothermal activity (Fourcade et al., 2002; Boiron et al., 2002).

3.7 References

Al-Aasm, I.S., Taylor, B. E., South, B., 1990, Stable isotope analysis of multiple carbonate samples using selective acid extraction, *Chemical Geology,* 80, p. 19-125.

Boiron, M. C., Cathelineau, M., Banks, D. A., S. Buschaerta, Fourcade, S., Coulibaly, Y., Michelot, J. L., Boyce, A., 2002, Fluid transfers at a basement/cover interface Part II. Large-scale introduction of chlorine into the basement by Mesozoic basinal brines, *Chemical Geology* 192, 121– 140.

Bureau de recherché géologiques et minières, Maps: number 686: La Rochefoucauld, 1982; number 687: Rochechouart, 2012. 1:50,000. BRGM.

Cathelineau, M., Boiron, M. C., Fourcade S., Ruffet, G., Clauer, N.,
Belcourt, O., Coulibaly, Y., Banks, D. A., Guillocheau, F., 2012, A major Late Jurassic fluid event at the basin/basement unconformity in western France: 40Ar/39Ar and K–Ar

dating, fluid chemistry, and related geodynamic context, *Chemical Geology*, 322–323, pp 99–120.

Cockell, C. S., Bland, P. A., 2005, The evolutionary and ecological benefits of asteroid and comet impacts, *Trends in Ecology and Evolution*, Vol. 20 No. 4.

Fourcade S., Michelot J. L., Buschaert S., Cathelineau M., Freiberger R., Y. Coulibalyc,f, J.F. Aranyossy, 2002, Fluid transfers at the basement/cover interface Part I. Subsurface recycling of trace carbonate from granitoid basement rocks (France), *Chemical Geology*, 192, p. 99– 119.

Galli, M. T., Jadoul, F., Bernasconi, S. M., Weissert, M., 2005, Anomalies in global carbon cycling and extinction at the Triassic/Jurassic boundary: evidence from a marine C-isotope record, *Palaeogeography, Palaeoclimatology, Palaeoecology*, 216, 203– 214.

Gradstein, F., Ogg, J. G., Schmitz, M.D., Ogg, G. M., 2012, The Geological Time Scale, *Elsevier BV* (ISBN 978 0 44 459425 9).

Hoefs, J., 2009, Stable isotope geochemistry, 6th edition, Springer-Verlag Berlin Heidelberg, ISBN: 978-3-540-70703-5.

Holli Riebeek, 2005, Paleoclimatology: The Oxygen Balance, (electronic) *NASA Earth Observatory*,http://earthobservatory.nasa.gov/Features/Paleoclimatology_OxygenBalance/, (accessed Jun 01, 2015).

Horita, J., Zimmermann, H., Holland, H. D., 2002, Chemical evolution of seawater during the Phanerozoic: Implications from the record of marine evaporites, *Geochimica et Cosmochimica Acta*, Vol. 66, No 21, p. 3733-3756.

IAEA, 2001, *GNIP Maps and Animations, International Atomic Energy Agency, Vienna*. Accessible at *http://isohis.iaea.org*. Accessed 21 Jan, 2015.

Lafuente, B., Downs, R. T., Yang, H., Stone, N., (2015) The power of databases: the RRUFF project. *Highlights in Mineralogical Crystallography*, T Armbruster and R M Danisi, eds. Berlin, Germany, W. De Gruyter, pp 1-3.

Lambert P., 1977, The Rochechouart Crater: Shock Zoning Study, *Earth and Planetary Science Letters*, 35 p. 258-268.

Lambert, P., 1981, Breccia dikes - Geological constraints on the formation of complex craters Multi-ring basins: Formation and evolution; *Proceedings of the Lunar and Planetary Science Conference, Houston, TX, November 10-12 1980*, p. 59-78.

Lambert, P., 2010, Target and impact deposits at Rochechouart impact structure, France *Geological Society of America*, Special Paper 465.

Machel, H. G., 2001, Bacterial and thermochemical sulfate reduction in diagenetic settings - old and new insights, *Sedimentary Geology*, 140, p. 143-175.

Muttik, N., Kirsimäe, K., Vennemann, W. T., 2010, Stable isotope composition of smectite in suevites at the Ries crater, Germany: Implications for hydrous alteration of impactites, *Earth and Planetary Science Letters*, 299, 190–195.

Naumov, M., 2005, Principal features of impact-generated hydrothermal circulation systems: mineralogical and geochemical evidence, *Geofluids*, 5, p 165-184.

Oneill, J. R., Clayton, R. N., Mayeda, T. K., 1969, Oxygen isotope fractionation in divalent metal carbonates, *Journal of Chemical Physics*, v. 52, p. 5547-5558.

Osinski G. R., Spray, J. G., and Lee, P., 2001, Impact-induced hydrothermal activity within the Haughton impact structure, arctic Canada: Generation of a transient, wet warm oasis. *Meteoritics and Planetary Science*, 36, No. 731-745.

Osinski, G. R., Lee, P., Parnell, J., Spray, J. G. and Baron, M., 2005, A case study of impact-induced hydrothermal activity: The Haughton impact structure, Devon Island, Canadian High Arctic, *Meteoritics and Planetary Science*, Vol. 40, No. 12, pp. 1859-1877.

Osinski, G. R. and Pierazzo, E., 2012, Impact Cratering: Processes and Products, *John Wiley & Sons, Ltd*, Chichester, UK. doi: 10.1002/9781118447307.ins

Osinski, G. R., Tornabene, L. T., Banerjee, N. R., Cockell, C. S., Flemming, R., Izawa, M. R., McCutcheon, J., Parnell, J., Preston, L. J., Pickersgill, A. E., Pontefract, A., Sapers, H. Southam, G., 2013, Impact-generated hydrothermal systems on Earth and Mars, *Icarus*, 347-363.

Parnell, J.,Taylor W. C.,Thackrey, S., Osinski, G. R., Lee, P., 2010, Permeability data for impact breccias imply focussed hydrothermal fluid flow, *Journal of Geochemical Exploration,* 106, p. 171-175.

Parnell, J., Boyce, A., Thackrey, S., Muirhead, D., Lindgren, P., Mason, C.,Taylor, C., Still, J., Bowden, S., Osinski, G. R., and Lee, P., 2010, Sulfur isotope signatures for rapid colonization of an impact crater by thermophilic microbes, *Geology*, Vol. 38, No. 3, pp. 271-274.

Pirajno, F., 2009, Hydrothermal processes and mineral systems, 1st edn., *Springer & Geological Survey of Western Australia.* doi: 10.1007/978-1-4020-8613-7.ins

Robinson, B.W. & Kusakabe, M. (1975). Quantitative preparation of sulphur dioxide for $^{34}S/^{32}S$ analyses from sulphides by combustion with cuprous oxide. Analytical Chem. 47, 1179–1181

Sapers H. M., Osinski G. R., Banerjee N., 2009, Re-evaluating the Rochechouart impactites: petrographic classification, hydrothermal alteration and evidence for carbonate bearing target rocks, *40th Lunar and Planetary Science Conference.*

Sapers H. M., Osinski G. R., Banerjee N. R., Ferriere L., Lambert P., Izawa M. R., 2014, Revisiting the Rochechouart impact structure, France, *Meteoritics and Planetary Science*, 1-17

Schmeider M., Buchner E., Schwarz W. H., Trieloff M., Lambert P., 2010, A Rhaetian $^{40}Ar/^{39}Ar$ age for the Rochechouart impact structure (France) and implications for the latest Triassic sedimentary record, Meteoritics & Planetary Science 45, Nr 8, 1225-1242.

Scottish Universities Environmental Research Centre, East Kilbride, United Kingdom. Address: Scottish Enterprise Technology Park/Rankine Av, Glasgow G75 0QF.

Seal II, R. R., 2006, Sulfur Isotope Geochemistry of Sulfide Minerals, *USGS Staff Published Research.* Paper 345.

Spray J. G., Kelley S. P., and Rowley D. B., 1998, Evidence for a late Triassic multiple impact event on Earth, *Nature*, vol. 392.

Tagle R., Schmitt R. T., Erzinger J., 2009, Identification of the projectile component in the impact structures Rochechouart, France and Saaksjarvi, Finland: Implications for the impactor population for the earth, *Geochimica et Cosmochimica Acta*, vol 73 p. 4891–4906

Vasconcelos, C., McKenzie, J. A., Warthmann, R., Bernasconi, S. M., 2005, Calibration of the $\delta^{18}O$ paleothermometer for dolomite precipitated in microbial cultures and natural environments, *Geology*, Vol. 33; no. 4; p. 317–320.

Wagner, T., Boyce, A. J. Fallick A. E., 2002, Laser combustion analysis of ^{34}S of sulfosalt minerals: Determination of the fractionation systematics and some crystal-chemical considerations, *Geochimica et Cosmochimica Acta*, Vol. 66, No. 16, pp. 2855–2863.

Warren, J., 2001, Dolomite: occurrence, evolution and economically important associations, *Earth Science Reviews*, 52, p 1-81.

Zhang, J., Quay, P. D., Wilbur, D. O., 1995, Carbon isotope fractionation during gas-water exchange and dissolution of CO_2, *Geochimica and Cosmochimica Acta*, Vol. 59, No. 1, pp. 107 to 117.

Zheng, Y. F., 1999, Oxygen isotope fractionation in carbonate and sulfate minerals, *Geochemical Journal*, 33, pp. 109-126.

Chapter 4: Closing

In this chapter

4.0 Closing

4.1 Conclusions

Results from this study confirm the hypothesis that post-impact hydrothermal activity in Rochechouart was pervasive and follows the phases of hydrothermal cooling and alteration for complex craters with crystalline targets outlined by Naumov (2005) and Osinski et al. (2013). The type and extent of hydrothermal alteration in Rochechouart lithologies is controlled by heat source (melt content) and therefore rock type; alteration in melt and glass-rich rocks is dominated by pervasive K-metasomatism and H^+ metasomatism, while alteration in lithic breccias and autochthonous fractures is less pervasive and dominated by chlorite-biotite-carbonate-sulphide assemblages. As outlined by Naumov (2005) and Pirajno (2009), during the early stages of cooling in hydrous crystalline targets, autometasomatism of quartzofeldspathic melt rocks supplies alkali-rich fluid; these early reactions consequently leads to the pervasive K-metasomatic overprint observed in all Rochechouart impact lithologies. The origin of the many clays in glass-bearing impactites is unknown; both surficial weathering and hydrothermal alteration by acidic fluids can produce smectite clays. Further work, possibly using stable isotopes, could reveal their origin.

Carbon and oxygen isotope results are ambiguous and without further information on the oxygen isotope composition or salinity of the fluid that precipitated the carbonate minerals, which could possibly be obtained by fluid inclusion analysis, temperatures are relatively open to interpretation; the oxygen isotope results in this thesis give a fairly wide range (up to approximately 250°C) of temperatures, but it is not possible to narrow these

ranges without further analyses.

The sulphur isotope results are more robust. Isotope values for the various representative terrestrial sulphur reservoirs is much more constrained than that of carbon and oxygen (Hoefs, 2009), and the comparison of various sulphide minerals extracted from Rochechouart rocks representing a continuum of meso- and macroscopic brittle shock deformation and mixing allows for a more definitive conclusion on their origin, and therefore a hydrothermal model.

The results slightly contradict those of Parnell et al. (2010) concerning impact breccia porosity and permeability. While autochthonous fractures show strong evidence for hydrothermal fluid flow, the monomict lithic breccias in the Champagnac site of Rochechouart are also locally highly porous; isotope results from lithic breccias reveal the majority of carbonates have precipitated at relatively low temperatures (<150°C), reflective of intermediate to late stage cooling. The exception to this regime is the localized carbonates precipitated proximal to the melt-bearing intrusion, which were relatively hot (≥250°C).

Stable isotope data of all carbonate and sulphide minerals confirms the hypothesis that seawater was a contributing fluid reservoir for hydrothermal circulation during the post-impact cooling period. Carbon isotopes reflect a mixture of organic and inorganic reservoirs, likely indicating mixing with metamorphic fluids, which may have a lighter carbon isotope signature as a result of containing organic crustal carbon (Figure 4-1) (Cathelineau et al., 2012). The hypothesis that seawater infiltrated the structure is also evidenced by corresponding sulphur isotopes of sulphide minerals co-precipitated with carbonates in autochthonous fractures, which have a strongly biological signature. The negative sulphur values observed in autochthonous sulphide minerals can only be reached biologically with an open system and steady supply of sulphate for metabolic reduction. Large fractionations (>20‰) are observed on a very small scale, which is also indicative of biological, as opposed to thermochemical, sulphate reduction. Today, there is no sedimentary cover to indicate that the Mesozoic sea inundated the structure after the impact; however, considering that impact fracturing may extend up to 3 crater radii from the center of an impact site, it is possible seawater infiltrated the crater from the nearby sea, the shoreline of which today preserved only 5km from outside the structure, through autochthonous basement fractures.

Secondary sulphide minerals in lithic breccias do not have as strong a biological signature as the autochthonous fractures. Sulphur isotope values of sulphide minerals extracted from unshocked, unaltered basement amphibolite are close to $\delta^{34}S = 0‰$.

Similarly, sulphides within the fabric of monomict lithic breccia amphibolite gneiss clasts and within the matrix, not associated with carbonate cement, are also close to $\delta^{34}S = 0‰$; these results show no significant degree of fractionation as a result of post-impact hydrothermal alteration. Sulphides associated with carbonate minerals in the matrix of the lithic breccias show a moderate to minor degree of fractionation

In this study, no pre-impact Hercynian carbonates were detected isotopically; all hydrothermal calcite and dolomite from the basement fractures of unknown origin were relatively cool fluids (<250°C), and like the impactites, reflect carbon isotope contribution from both organic and inorganic reservoirs. Magmatic-hydrothermal alteration can be detected texturally and mineralogically in the granodiorite and amphibolite gneiss (Chapter 3). However, the origin of the K-metasomatic overprint pervading basement rocks cannot be determined without age constraints.

4.1.1 Implications for longevity of hydrothermal activity in sub-crater environment

Prolonged hydrothermal circulation at and below the transient crater floor is evidenced by mineralogical and isotopic results presented in this study. In the Champagnac site of Rochechouart, hydrothermal fluids were focused within the porous network of impact fractures and lithic breccias, which were overlain by hot, relatively slow-cooling, impermeable melt rocks. This model agrees with predictions concerning hydrothermal fluid flow within a complex impact crater (Parnell et al., 2010). The majority of carbonate and sulphide mineralization is characteristic of cooler (<150°C), late stage hydrothermal activity in an impact crater (Naumov, 2005; Osinski et al., 2013); temperature models given by calcite and dolomite oxygen isotope results in this study are within this range. Based on the evidence that secondary mineralization found in lithic impactites is reflective of late-stage hydrothermal circulation, the conclusion can be made that in Rochechouart, autochthonous fractures and lithic breccias hosted hydrothermal circulation for relatively long periods of time, well into the latest stages of cooling.

4.2 Astrobiological implications and impact-hydrothermal systems on Mars

Results presented in this study support the hypothesis that the fractured and brecciated basement beneath complex craters with hydrous minerals or free water-bearing targets may provide an ideal environment for the development of extremophile microbial communities on other terrestrial planets and satellites. Hydrothermal fluids carry nutrients and provide heat to support the growth of thermophilic microbial communities; the conditions fossilized in the Champagnac site reflect an environment with prolonged fluid

circulation, which is further evidenced by the strong biological signatures reflected in sulphur isotopes.

The primary conditions limiting the development of impact-hydrothermal systems are the generation of a sustainable heat source and the presence of sufficient volatiles within a target (Naumov, 2005; Osinski et al., 2013). On Earth, these conditions are satisfied; on planets such as Mars, as outlined by Pope et al. (2006), long-lived, complex hydrothermal systems are likely less common due to the rarity of large, coherent melt-sheet production in impact craters and the lack of crustal volatiles. The majority-basaltic crust of Mars is considerably denser than that of Earth, and therefore higher shock pressures are required (~80 to 100 GPa) to induce melting (Pope et al., 2006). Clast and glass-rich impact melt rocks cool faster than clast-poor and clast-free impact melt (Pope et al., 2006) and the generation of a thick, coherent melt sheet provides a longer-lasting heat source than localized and dispersed melt bodies. Due to Mars' lower gravity than Earth, and therefore lower impact velocities, and drier crust, the generation of coherent melt sheets is estimated to be limited to the largest craters (>400km). The contradiction to this theory is the recent discovery of the hydrous phyllosilicate-rich ~40km Toro crater on Mars, which contains melt-bearing impactite and a central uplift, and shows promising geochemical and geomorphological evidence for impact-hydrothermal activity (Marzo et al., 2010).

Results from this study show that the sub-crater environment within complex impact structures in majority or mixed-crystalline, volatile-rich targets, which show evidence for the generation of a sustainable heat source, are ideal research targets in the search for exolife.

4.3 Outstanding questions and future work

Even at the extrema given by the temperature models in Chapter 3, the majority of $\delta^{13}C$ and $\delta^{18}O$ isotopic results from carbonate minerals in this study reveal temperatures and fluid sources reflective of seawater mixing during intermediate-late stage impact-hydrothermal activity (<150°C), similar to conditions surrounding the late stage fluid event outlined by Cathelineau et al. (2012) attributed to brine migration along the Aquitaine unconformity. There is isotopic evidence for initially hot (≥250°C) temperatures at the transient crater floor-basement interface, which is also reflected in lithic breccia reaction rims; however, it is possible that late stage impact-hydrothermal carbonates were overprinted by unconformity brine migration at the Jurassic-Cretaceous boundary. In addition, the pervasive potassic alteration in coherent unshocked basement rocks may be a result of pre-impact hydrothermal alteration; this further complicates the identification of

post-impact alteration, as the Variscan K-metasomatic assemblages may have been incorporated into impactites and later altered by hydrothermal fluids. To discern the timing and origin of fluid events recorded in all Rochechouart lithologies, this study would greatly benefit from geochronological constraints on secondary alteration, such as $^{40}Ar/^{39}Ar$ on the ubiquitous adularia or fission track dating on secondary apatite associated with calcite and dolomite in lithic breccias.

The origin of smectite clay minerals in all lithologies, particularly those in glass and melt-rich impactites, remains unknown; clays are produced over a wide range of temperatures (>200°C to ambient conditions in epithermal systems; Pirajno, 2009), and their origin as a product of early impact-generated H^+ metasomatism or surface diagenesis is unknown. Previous studies in the Ries crater (Muttik et al., 2010) have utilized $\delta^{18}O$ isotopes to determine the provenance of smectite clays in suevites, which might also be applicable to Rochechouart impactites. Fluid inclusion analysis on carbonate and silicate minerals would reveal further temperature information, as well as salinity.

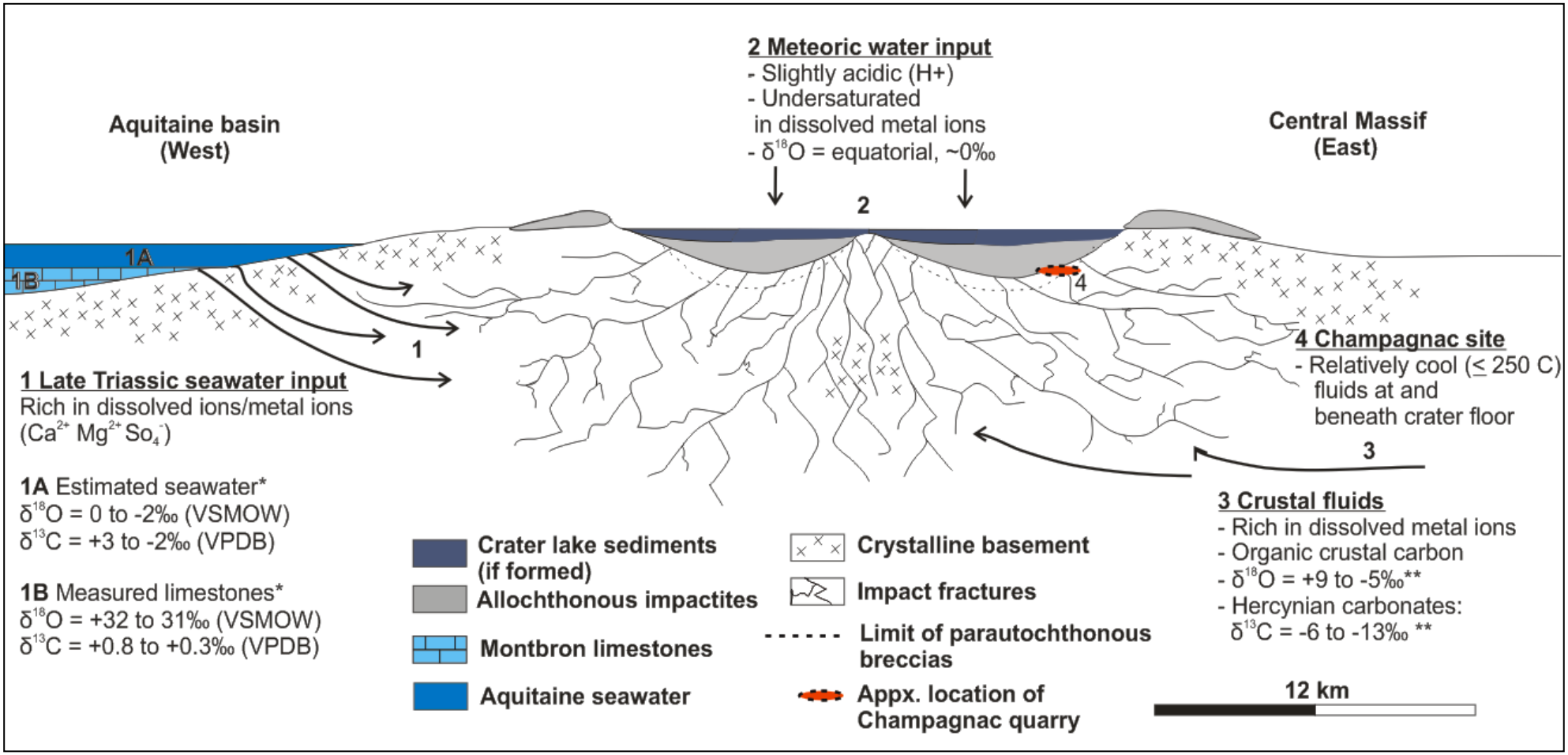

Figure 4-1: Hypothetical cross-section through the Rochechouart impact structure shortly after the impact, around 201 Ma, showing various fluid reservoirs contributing to hydrothermal circulation within the structure, and their respective oxygen and carbon isotope values (modified from Naumov, 2005). Late Triassic seawater estimates are given by Gradstein et al. (2012), and metamorphic values are given by Cathelineau et al. (2012).

4.4 References

Cathelineau M., Boiron M. C., Fourcade S., Ruffet G., Clauer N., Belcourt O., Coulibaly Y., Banks D. A., Guillocheau F., 2012, A major Late Jurassic fluid event at the basin/basement unconformity in western France: $^{40}Ar/^{39}Ar$ and K–Ar dating, fluid chemistry, and related geodynamic context, *Chemical Geology*, 322–323, p. 99–120.

Gradstein, F., Ogg, J. G., Schmitz, M.D., Ogg, G. M., 2012, The Geological Time Scale, *Elsevier BV* (ISBN 978 0 44 459425 9).

Marzo, G. A., Davila, A. F., Tornabene, L. L., Dohm, J. M., Fairén, A. G., Gross, C., Kneissl, T., Bishop, J. L., Roush, T. L., McKay, C. P., 2010, Evidence for Hesperian impact-induced hydrothermalism on Mars, *Icarus*, 208, 667-683.

Muttik, N., Kirsimäe, K., Vennemann, W. T., 2010, Stable isotope composition of smectite in suevites at the Ries crater, Germany: Implications for hydrous alteration of impactites, *Earth and Planetary Science Letters*, 299, 190–195.

Naumov, M., 2005, Principal features of impact-generated hydrothermal circulation systems: mineralogical and geochemical evidence, *Geofluids*, 5, p 165-184.

Osinski, G. R., Tornabene, L. T., Banerjee, N. R., Cockell, C. S., Flemming, R., Izawa, M. R., McCutcheon, J., Parnell, J., Preston, L. J., Pickersgill, A. E., Pontefract, A., Sapers, H. Southam, G., 2013, Impact-generated hydrothermal systems on Earth and Mars, *Icarus*, 347-363.

Parnell, J.,Taylor W. C.,Thackrey, S., Osinski, G. R., Lee, P., 2010, Permeability data for impact breccias imply focussed hydrothermal fluid flow, *Journal of Geochemical Exploration,* 106, p. 171-175.

Pirajno, F., 2009, Hydrothermal processes and mineral systems, 1st edn., *Springer & Geological Survey of Western Australia.*

Pope, K. O., Kieffer, S. W., Ames, D. E., 2006, Impact melt sheet formation on Mars and its implication for hydrothermal systems and exobiology, *Icarus*, 183, p 1-9.

Appendix

All raw calcite CO_2 was corrected using the fractionation factor (lnα) between calcite and 100% phosphoric acid at 25°C (1.01025) (Friedman and O'neil, 1977); raw dolomite CO_2 was corrected using the fractionation factor (lnα) of dolomite and 100% phosphoric acid at 100°C (1.00901) (Rosenbaum and Sheppard, 1986).

For conventional extraction from sulphide minerals, standard corrections were applied to raw $\delta^{66}SO_2$ to produce corrected $\delta^{34}S$ values (Wagner et al., 2002). Non-conventional laser combustion produces a significant degree of fractionation between $\delta^{34}S_{mineral}$ and the $\delta^{34}S_{gas}$; all data is corrected using $\delta^{34}S_{pyrite}=\delta^{34}S_{gas} + 0.8‰$ (Wagner et al., 2002).

1σ reproducibility is between 0.003 and 0.03‰ for $\delta^{13}C$, 0.002 and 0.033‰ for $\delta^{18}O$, and 0.008 and 0.057‰ for $\delta^{34}S$.

Summary of standards (‰)

Standard ID	Mineral	$\delta^{34}S$ (CDT)	
CP1	Chalcopyrite	-4.30	
NBS123	Sphalerite	17.0	
IAEAS-3	Argentite	-3.60	
Standard ID	Mineral	$\delta^{13}C$ (VPDB)	$\delta^{18}O$ (VPDB)
MAB	Calcite	+2.50	-2.40

$\delta^{13}C$ and $\delta^{18}O$ isotope analysis; summary of data (‰)

Sample ID	Mass Spec ID	Sample wt (mg)	ASG (mb)	Raw carbon (δ^1)	σ	Raw oxygen (δ^2)	σ	$\delta^{13}C_{calcite}$ (VPDB)	$\delta^{18}O_{calcite}$ (VPDB)	$\delta^{18}O_{calcite}$ (VSMOW)
Calcite										
TC-1	MC0155	13.4	81.4	26.742	0.005	17.636	0.006	0.6130	-0.0050	30.900
TC-2	MC0148	12	73.1	26.614	0.009	17.528	0.110	0.4810	-0.0600	30.848
MC-1	MC0147	17.1	31.0	18.654	0.005	13.379	0.012	-7.656	-4.159	26.623
MC-2	MC0145	21	46.0	18.104	0.006	13.683	0.006	-8.237	-3.876	26.914
MC-3	MC0158	2.8	5.50	14.048	0.030	12.852	0.008	-12.426	-4.685	26.080
MC-4	MC0152	32.1	64.4	18.106	0.009	14.261	0.010	-8.254	-3.307	27.500
MC-5	MC0157	23.6	47.3	15.184	0.003	13.013	0.008	-11.251	-4.529	26.241
MC-6	C21580A	22.4	50.6	n/a	n/a	n/a	n/a	-13.000	-5.800	24.900
MC-7	C21583A	21.3	39.4	n/a	n/a	n/a	n/a	-12.200	-5.200	25.600
PC-1	MC0150	48.3	51.0	16	0.004	13.539	0.009	-10.572	-4.013	26.773
PC-2	MC0154	15.8	39.4	15.712	0.012	13.591	0.004	-10.721	-3.962	26.826
PC-3	MC0153	52.1	18.2	14.083	0.006	11.804	0.005	-12.355	-5.716	25.017
AC-1	MC0151	21.2	1.50	21.192	0.009	12.977	0.230	-5.003	-4.577	26.191
UC-1	MC0146	36.2	67.1	20.065	0.005	13.901	0.010	-6.206	-3.666	27.131
UC-2	MC0156	36.1	15.9	21.661	0.009	14.252	0.009	-4.558	-3.324	27.483
UC-3	C21579A	21.9	71.4	n/a	n/a	n/a	n/a	-11.20	-5.400	25.300

UC-4	C21581A	23.6	105	n/a	n/a	n/a	n/a	-11.5	-5.700	25.100
UC-5	C21582A	21.5	63.9	n/a	n/a	n/a	n/a	-8.5	-5.800	24.900
Dolomite										
TC-1	MC0155B	13.4	52.7	26.45	0.007	17.31	0.008	0.32	0.9030	31.841
TC-2	MC0148B	12.0	40.1	26.898	0.006	17.215	0.004	0.789	0.8080	31.743
MC-1	MC0147B	17.1	133	18.682	0.007	11.06	0.008	-7.549	-5.237	25.511
MC-2	MC0145B	21.0	179	18.141	0.004	11.55	0.007	-8.128	-4.753	26.01
MC-3	MC0158B	2.80	19.9	13.316	0.005	10.968	0.007	-13.125	-5.316	25.43
MC-4	MC0152B	32.1	160	18.336	0.006	11.927	0.009	-7.938	-4.382	26.393
MC-5	MC0157B	23.6	180	13.557	0.015	14.225	0.033	-12.982	-2.109	28.763
MC-6	C21580B	22.4	145	n/a	n/a	n/a	n/a	-12.9	-6.900	23.800
MC-7	C21583B	21.3	39.5	n/a	n/a	n/a	n/a	-11.9	-5.800	25.000
PC-1	MC0150B	48.3	58.1	14.97	0.003	11.35	0.008	-11.418	-4.943	25.814
PC-2	MC0154B	15.8	85.3	15.134	0.004	11.493	0.016	-11.252	-4.803	25.959
PC-3	MC0153B	52.1	68.6	14.063	0.006	0.694	0.008	-11.962	-16.804	13.586
AC-1	MC0151B	21.2	161	21.6	0.005	10.969	0.006	-4.513	-5.332	25.413
UC-1	MC0146B	36.2	289	19.578	0.009	11.528	0.009	-6.633	-4.778	25.985
UC-2	MC0156B	36.1	303	20.985	0.006	14.101	0.006	-5.256	-2.246	28.594
UC-3	C21579B	21.9	150	n/a	n/a	n/a	n/a	-11	-5.700	25.000
UC-4	C21581B	23.6	122	n/a	n/a	n/a	n/a	-11.4	-6.300	24.4
UC-5	C21582B	21.5	111	n/a	n/a	n/a	n/a	-7	-6.3	24.4

Conventional $\delta^{34}S$ isotope analysis; summary of data (‰)

Sample ID	Mass Spec ID	Sample wt (mg)	Cu_2O (mg)	Bara (mb)	Raw $\delta^{66}SO_2$	$\delta^{34}S$ (CDT)	σ
MS-1	MAT2587	5.1	n/a	n/a	-16.84	-10.7	0.014
MS-2	MAT3153	4.0	204	47.8	-12.172	-5.60	0.009
AS-1	MAT3145	9.8	225	112.3	-37.628	-32.0	0.016
AS-2	MAT3148	12	194	over	-37.451	-31.8	0.021
AS-3	MAT3149	8.3	200	94.4	-37.808	-32.2	0.017
AS-4	MAT3144	14	207	over	-39.786	-34.2	0.021
AS-5	MAT3152	10	201	113.2	-40.865	-35.5	0.012
AS-6	MAT3155	8.4	204	80.9	-41.336	-35.8	0.017
AS-7	MAT3154	9.2	200	111.9	-32.774	-26.9	0.057
BS-1	MAT3146	6.5	215	75.9	-6.389	0.400	0.035
BS-2	MAT3147	5.5	203	78.2	-10.338	-3.70	0.008
US-1	MAT3152	9.0	200	115.5	-8.446	-1.70	0.009
US-2	MAT3151	6.2	214	70.7	-13.492	-6.90	0.490
US-3	MAT2588	8.0	n/a	n/a	-29.98	-24.2	0.022
US-4	MAT2589	7.4	n/a	n/a	-31.87	-26.2	0.016

Laser combustion $\delta^{34}S$ isotope analysis; summary of data (‰)

Sample ID	MS ID	O_2 (mb)	CO_2 (mb)	SO_2 (mb)	Raw $\delta^{66}SO_2$	Corrected $\delta^{34}S$ (CDT)
ASL-1	LS9798	24	0.500	0.550	-13.27	-5.20
ASL-2	LS9799	23	0.100	2.50	-31.22	-24.6
ASL-3	LS9800	24	n/a	0.750	-25.58	-18.5
BSL-1	LS9793	24	0.080	1.30	-9.390	-1.00
BSL-2	LS9794	24	0.040	1.10	-9.670	-1.30
BSL-3	LS9795	24	0.050	1.75	-10.97	-2.70
MSL-1	LS9796	24	n/a	2.10	-31.22	-24.6
MSL-2	LS9797	24	n/a	1.20	-25.58	-18.5

Friedman, I., O'Neil, J., 1977, Compilation of stable isotope fractionation factors of geochemical interest, Data of Geochemistry, 6th edition, *United States Geological Survey.*

Rosenbaum, J., Sheppard, S. M. F., 1986, An isotopic study of siderites, dolomites and ankerites at high temperatures, Geochimica and Cosmochimica Acta, Vol. 50, p. 1147-1150.

Wagner, T., Boyce, A. J. Fallick A. E., 2002, Laser combustion analysis of ^{34}S of sulfosalt minerals: Determination of the fractionation systematics and some crystal-chemical considerations, *Geochimica et Cosmochimica Acta*, Vol. 66, No. 16, pp. 2855–2863.